Dissertation
for the degree of *PhilosophiæDoctoris (PhD)*

Properties on column density structure of molecular clouds based on probability density function of the column density and star-forming activities

A Dissertation submitted for the Degree of Ph.D.
March 2023

Graduate School of Science & Engineering
Kagoshima University

Takeru MURASE

ABSTRACT

This Ph.D. dissertation is about the effect of massive star-forming regions on the surrounding molecular clouds and the statistical properties of the molecular clouds based on column density histograms. In this study, we used the Nobeyama 45-m radio telescope. This dissertation consists of five chapters.

Chapter 1 reviews previous studies of the interstellar medium. In particular, we focused on knowledge from observational studies. First, we summarized the layer structure of the interstellar medium with different temperatures and densities, the formation pathways of molecular hydrogen, and the phase transition mechanisms that form the layer structure. Next, we reviewed the characteristics of molecular gas clouds and summarized the properties of molecular clouds revealed by the previous statistical studies. Then, the properties of massive stars and their impact on the surrounding environment are described. And finally, we summarize the questions that motivated this study based on this background and describe the structure of this paper.

Chapter 2 presents ammonia mapping observations towards the W33 complex used to study feedback effects from the massive star-forming regions. Massive stars affect the surrounding interstellar medium through expanding HII regions, strong outflows, strong stellar winds, and intense ultraviolet radiation. In addition, this feedback from high-mass stars influences subsequent star formation. Therefore, we focused on the gas temperature distribution in molecular clouds to investigate how much star formation activity affects the surrounding molecular gas. We performed mapping observations in ammonia emission lines toward the W33 massive star-forming region. Consequently, the molecular gas surrounding the HII region located at W33 Main exhibited a higher temperature (> 20 K) than the rest of the observed area. The size of the influence area was estimated at approximately 1.25 pc.

In Chapter 3, we discussed the hierarchical density structure of molecular clouds based on column density histograms. The column density histogram is called the column density probability distribution function (N-PDF). In this study, we considered the N-PDF using multi-log-normal distributions. We identified molecular clouds from the Nobeyama 45-m Cygnus X CO survey and conducted N-PDF analysis on the obtained molecular clouds.

As a result, we found that the N-PDF could be well-fitted with one or two log-normal distributions. We also found that the N-PDF shape was less correlated with the star-forming activity.

In Chapter 4, we extended the analytical methods used in Chapter 3 to the molecular clouds in the Milky Way mid-plane. We performed N-PDF analysis on 96 molecular clouds decomposed from the FUGIN (FOREST Unbiased Galactic plane Imaging survey with Nobeyama 45m telescope) survey data. Consequently, we found that N-PDFs can well-fit with at most three log-normal distributions. In addition, the diffuse structures that form the bulk of the molecular clouds have relatively consistent properties in the arms of the Milky Way galaxy. In this chapter, we summarize the statistical investigation of the properties of molecular clouds using the parameters obtained from the N-PDF fitting.

In Chapter 5, we summarized this dissertation.

ACKNOWLEDGEMENTS

With this doctoral dissertation, I conclude my nine years at Kagoshima University. I want to thank all the people I have shared my memories with at Kagoshima University during my bachelor's and Ph.D. My life in Kagoshima was the span that most nurtured my values.

I sincerely thank Prof. Hiroshi Imai and Prof. Takahiro Nagayama for supporting my Ph.D. study. I am very grateful to my supervisor, Prof. Toshihiro Handa, for his dedicated instruction and valuable advice, which nurtured my enthusiasm for my studies. In addition to research activities, we laughed together on various topics at home parties and coffee breaks. I feel fortunate to have you instructing me at Kagoshima University. If not for the values you have instilled in my life, I would not be the person I am today.

My study would not have been possible without the data from the Nobeyama 45-m radio telescope. I would like to thank the people at Nobeyama Radio Observatory. My first visit to NRO in May 2017 was the first day of my life as a researcher. I will never forget this stay. I learned much about radio telescopes at the VERA Iriki station. I would like to thank all staff of the VERA project group for providing me with the opportunity to operate the radio telescope.

My life in Kagoshima would not have been as enjoyable without my supportive friends and colleagues. I cannot introduce all their names here, so I would like to thank them for their friendship and support during all these years. Doing a Ph.D. was one of the most important events in my life. My Ph.D. was a fascinating and enjoyable period and has shaped my worldview. This experience will contribute to everything I do for the rest of my life.

Finally, I am deeply thankful to my parents and family for supporting my stress-free life in Kagoshima. I could not have asked for better parents.

Special thanks!!
BAR JOE-COOL, Caffe Bar JIMLAN, Korimoto Hot Spring, Nagano Wine, Sushi restaurant Mekkemon, The Karaage Honpo, and The spa of Lofty Korimoto.

Contents

List of Figures

List of Tables

Chapter 1

Overview and Introduction

When we look up at the night sky, we see starlight from countless stars. These are mostly the stars close to Earth, but they also include planets, nebulae, and galaxies. The space between the stars in a galaxy is called interstellar space, and the medium that fills it is called the interstellar medium (ISM). The discovery of the ISM is one of the most significant discoveries of modern astronomy.

The ISM is extremely diffuse. If the ISM were uniformly distributed in the Milky Way, the average density would be about 1 cm^{-3}. However, because of the vastness of interstellar space, the ISM has the mass to form many stars and planets.

1.1 Interstellar Medium

The total mass of the ISM in the Milky Way is 10^{10} $M_\odot$ (Kalberla & Kerp, 2009). The ISM is composed of gas (gas phase) and dust (solid phase), and their mass ratio is thought to be about 100:1 (e.g. Bohlin et al., 1978; Lombardi et al., 2014). The total mass of gas-phase ISM is composed of about 70% hydrogen and 28% helium, with a much smaller amount of heavy elements such as oxygen and carbon (Draine, 2011).

1.1.1 Multi-phase structure

The gas phase of the ISM can be divided into phases of different temperatures and densities. Figure 1.1 shows a summary of the properties of the gases in

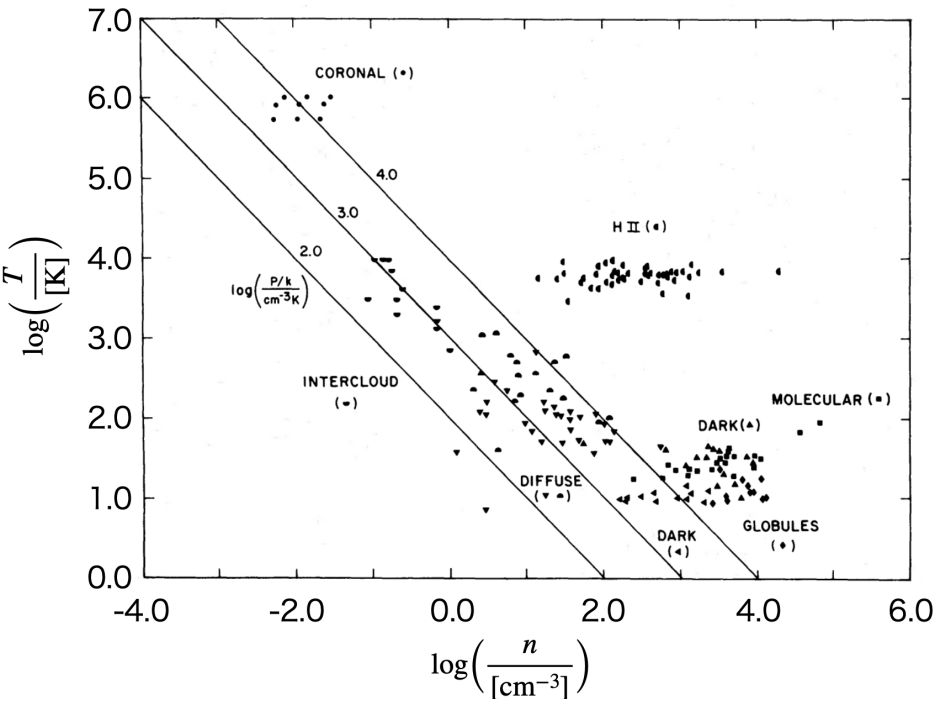

Figure 1.1: Interstellar gas temperature–density diagram. The straight line indicates that the hydrogen number density and gas temperature are constant (pressure equilibrium). This figure has been taken from Myers (1978).

each of the phases (Myers, 1978). These phases are described below (see Wolfire et al., 2003, and SKA-JP Science book).

1. Hot Ionized medium (HIM)

   The HIM is the hottest ionized gas in the ISM (10^6 K) with a density of 10^{-2} cm^{-3}. It is known to occupy about half of the volume of interstellar space in the Milky Way (Spitzer, 1956; Ferrière, 2001). The HIM is very diffuse and has a limited mass. Thermal bremsstrahlung from free electrons and emission lines from ionized heavy elements can be detected in the soft X-ray range. We can observe HIM as coronal gas in galactic halos and as high-temperature plasma associated with supernova remnants.

2. Ionized medium (HII region)

   The HII region consists of ionized gas produced by ultraviolet radiation from massive stars (> 8 M$_\odot$). The typical temperature is about 10^4

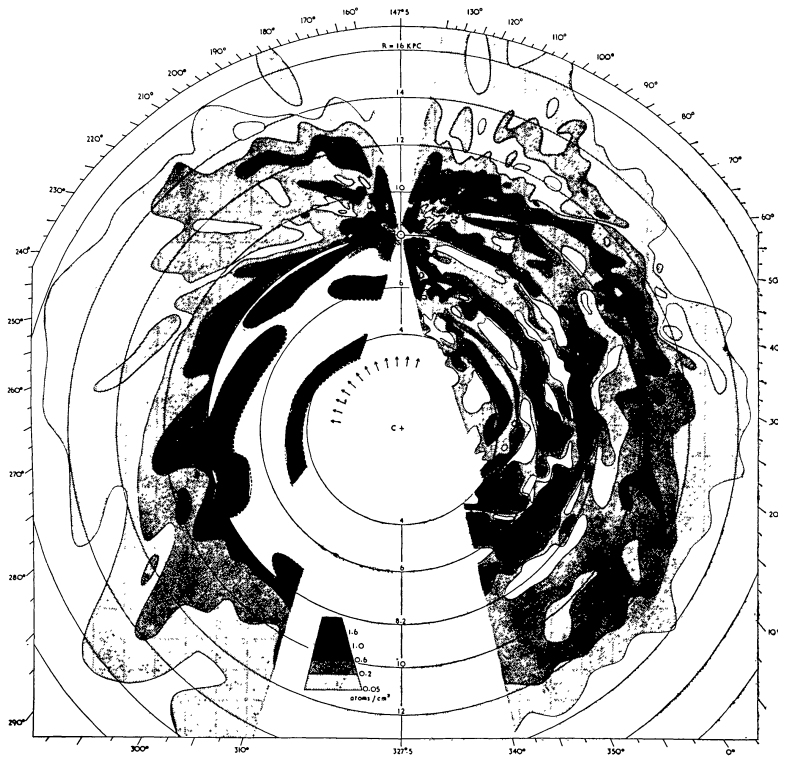

Figure 1.2: Map of the neutral atomic hydrogen in the Milky Way. The location of the Sun is in the upper part of the plot at 8 kpc. This figure has been taken from Figure 1 of Oort et al. (1958).

K and the density is 10–10^3 cm^{-3}. Although classical studies on HII regions have used emission lines in visible light, including Hα, continuum emission with free radiation and hydrogen recombination lines can be detected beyond optical wavelengths to radio wavelengths.

3. Warm Neutral Medium (WNM)

   The WNM is a diffuse (10^{-1} cm^{-3}) neutral atomic hydrogen gas (HI) at a temperature of 10^3–10^4 K. In spiral galaxies such as the Milky Way, the WNM is reported to be distributed along spiral arms (e.g. Oort et al., 1958). The tracers of the WNM are HI 21 cm lines at 1420 MHz due to hyperfine structure transitions. Observational studies of 21 cm lines have revealed the structure of the Milky Way, the galactic rotation curve, and other properties of the galactic gas disk (Figure 1.2).

4. Cold Neutral Medium (CNM)

   The CNM is a cold (10^1–10^2 K) and dense (1–10^3 cm^{-3}) neutral atomic hydrogen gas compared to the WNM. Observing the gas in this phase is challenging because it does not have strong emission lines. The CNM is usually associated with compact molecular clouds and is detected by HI absorption lines against a background of continuum sources (e.g. Mebold et al., 1982; Mohan et al., 2004; Roy et al., 2006; Murray et al., 2015).

5. Molecular Medium (MM)

   The MM is the molecular gas with the lowest temperature (10 K) and highest density (10^2–10^5 cm^{-3}) in the ISM. Such gases are also called molecular clouds because they are thought to be spatially concentrated. The molecular cloud is mainly composed of H_2 molecules. The ideal observational study of molecular gas is the direct observation of H_2 lines. However, due to the symmetric structure of H_2, it has no electric dipole emission. Furthermore, the upper energy level of the lowest rotational transition (S(0)) is $E/k = 510$ K. Therefore, H_2 emission is considered too cold to be visible at the typical temperature of molecular clouds. In general, observational studies have used the CO isotope, which is the second most abundant after H_2. Since the detection of CO emission lines from interstellar space by Wilson et al. (1970), observational studies of the molecular medium have developed rapidly.

Table 1.1: A list of the main physical properties of each ISM phase. Adapted from Ferrière (2001) and Girichidis et al. (2020).

Component	Temperature [K]	Density [cm^{-3}]	Volume fraction [%]
HIM	$\sim 10^6$	$\sim 10^{-2}$	30–70
HII region	$\sim 10^4$	10 – 10^3	< 1
WNM	10^3–10^4	$\sim 10^{-1}$	10–20
CNM	10^1–10^2	1–10^3	~ 4
MM	~ 10	10^2–10^5	a few

Table 1.1 shows the physical properties of each ISM phase. The characteristic feature of the gas phase ISM is that it consists of multiple phases (see also Field et al., 1969; McKee & Ostriker, 1977).

1.1.2 H_2 formation

In this subsection, we will review the processes by which molecular gas is formed (or destroyed). This is because star formation generally takes place in molecular clouds.

The chemically simplest way to form H_2 is the radiative association of two hydrogen atoms,

$$H + H \rightarrow H_2 + \gamma. \tag{1.1}$$

However, since the rate coefficient of this reaction is extremely small, very little H_2 is formed (Latter & Black, 1991). Another pathway, the ion-neutral reactions

$$H^- + H \rightarrow H_2 + e^- \tag{1.2}$$

and

$$H_2^+ + H \rightarrow H_2 + H^+ \tag{1.3}$$

are also inefficient. Furthermore, the photodesorption of H^- by photons from the interstellar radiation field and the photodissociation of H_2^+ render these pathways less effective (Glover, 2003). Consequently, the formation of H_2 in the gas phase is extremely inefficient under typical ISM conditions. However, we can observe a large amount of H_2 molecules in the Milky Way clouds. Therefore, we need to consider other indirect mechanisms for the formation of molecular hydrogen.

In the Milky Way and nearby galaxies, most of the H_2 is formed on interstellar dust grains (e.g. Gould & Salpeter, 1963; Draine, 2011). Association reactions between hydrogen atoms adsorbed on the interstellar dust readily occur on the surface of the dust grains. This reaction is exothermic; the energy released is partly absorbed by the interstellar dust and partly converted into the internal and kinetic energy of H_2 (Bron et al., 2014). The formation rate of H_2 is limited only by the velocity of the hydrogen atoms adsorbed on the surface. The formation rate under typical Milky Way conditions is

$$R_{H_2} \sim 3 \times 10^{-17} n \; n_H \; [s^{-1} \; cm^{-3}], \tag{1.4}$$

where n is the total number density of gas particles and n_H is the number density of atomic hydrogen (Jura, 1975). In atomic hydrogen gas, the amount of n and n_H are equal if the contributions from helium and possibly metals are ignored.

We also need to consider the destruction of the H_2 molecules. The most dominant process for destroying H_2 is photodissociation. When H_2 absorbs ultraviolet photons with energy $E > 11.2$ eV, it ends up in an excited electronic state. The excited H_2 then undergoes a radiative transition back to the electronic ground state. When the transition to the vibrational continuum occurs, the molecule dissociates.

Because H_2 photodissociation occurs in a specific energy band, the photodissociation rate of H_2 in the ISM is highly sensitive to self-shielding. Indeed, Lyman-Werner photons (91–110 nm) are mainly absorbed by H_2 molecules at the surface of the molecular cloud. As a result, the photodissociation rate of H_2 in a whole molecular "cloud" is lower than in optically thin gases. This is particularly noticeable for hydrogen column densities above $N(H_2) \sim 10^{14}$ cm^{-2}. The visual extinction required to reduce the photodissociation rate of H_2 by a factor of 10 is $A_V \sim 0.65$, corresponding to a total hydrogen column density of $N \sim 10^{21}$ cm^{-2} in the diffuse ISM (see Girichidis et al., 2020).

1.1.3 Thermal instability

In the ISM recycling process, the phase transition from WNM to CNM is the first step in extracting molecular gas from the diffuse ISM in interstellar space. Therefore, we review the latest research on instabilities that occur in the atomic gas phase.

Inoue & Inutsuka (2012) summarize the heating and cooling rates based on various processes and their equilibrium states in the density-pressure diagram (Figure 1.3). The growing region on the left corresponds to the WNM region, and the growing region on the right corresponds to the CNM which should become molecular cloud regions. These intermediate regions (density around 1–30 cm^{-3}) are thermally unstable and characterized by a negative pressure gradient for the volume density (called unstable neutral medium (UNM)).

One of the most prominent heating processes in diffuse ISM is photoelectric heating. This is driven by the emission of photoelectrons from interstellar dust, which absorbs UV photons. On the other hand, Lyα photons, oxygen atoms, [OI], and single ionized carbon, [CII], are essential cooling mechanisms (see Wolfire et al., 2003).

The thermal instability is due to the weak temperature dependence of UNM, which has a density of about 1–30 cm^{-3}. More precisely, the instability

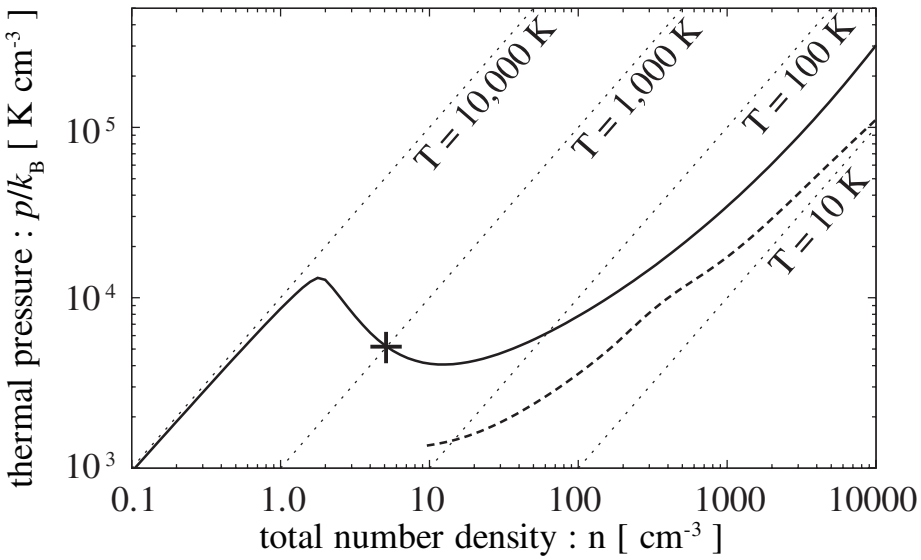

Figure 1.3: Thermal pressure as a function of the total number density of the ISM. The thick solid and dotted lines indicate the medium of $A_v = 0$ and $A_v = 1$, respectively. The dotted guidelines are isotherms of $T = 10^4$, 10^3, 10^2 and 10 K, respectively. This figure has been taken from Inoue & Inutsuka (2012).

arises because cooling is proportional to the square of the density (radiative de-excitation of the coolant caused by collisions), and heating is simply proportional to the density. Consequently, as soon as the WNM enters the thermally unstable region, it begins to contract toward the CNM. This implies a contraction of about 1/100 of the density from Figure 1.3.

The typical scale of thermal instability growth is determined by thermal conduction and radiative cooling and is called the "Field Length" (Field, 1965). The Field Length of a typical ISM is 1 pc for WNM and 0.1 pc for CNM. This means that the composite structure of the sub-pc scale with WNMs and CNMs is formed due to thermal instability. These formed sub-pc scale ($\sim$ 0.1 pc) CNM structures are critical as precursors to the molecular clouds, which are the direct sites of star formation.

1.2 Molecular clouds and cloud statistics

The molecular cloud is the coldest and densest region of the ISM. Typical temperatures of molecular clouds are approximately 10–20 K and sizes range between $\sim$ 1–200 pc. Based on spatial size and mass, molecular gas has a

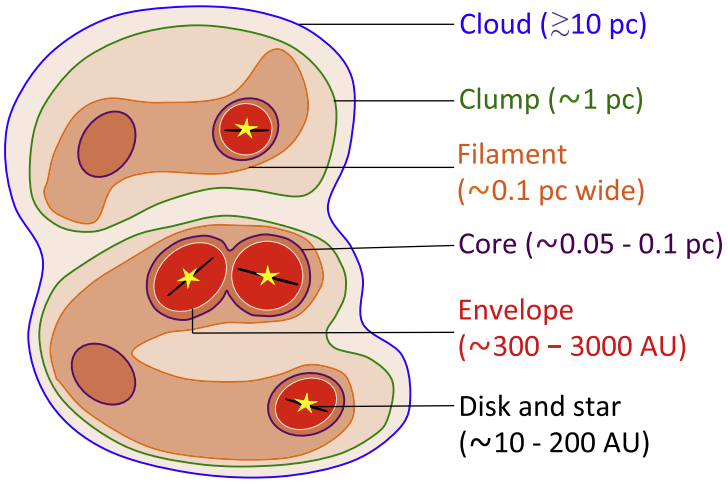

Figure 1.4: Schematic representation of the hierarchical structure of the interior of molecular clouds from cloud scale to protostellar object. This image has been taken from Pokhrel et al. (2016).

hierarchical structure as follows. (i) giant molecular clouds (GMCs): $> 10^5$ $M_\odot$, $\sim$ 30 pc and up to 100–200 pc, (ii) molecular clouds (MCs): 10^2–10^4 $M_\odot$ and 10–20 pc, (iii) clump: 10–10^2 $M_\odot$ and a few pc, (iv) core : 10 $M_\odot$ and 0.1 pc or less (e.g. Blitz, 1993; Heyer & Dame, 2015). However, these terminologies can mislead us about the actual structure; we can find spatial structures of all sizes, down to the resolution limit of the telescope (such as "envelope" and "disk"). This has been interpreted as a fractal property of the molecular gas in the ISM (Scalo, 1990; Falgarone et al., 1991, 2009). Figure 1.4 shows the hierarchical structure in a GMC.

The morphological structure of the ISM is also complex. The filamentary structures have been established by *Herschel* imaging surveys at nearly all length scales ($\sim$ 0.5 pc to 100 pc) of MCs in the Milky Way (e.g. André et al., 2010; Henning et al., 2010; Palmeirim et al., 2013; Wang et al., 2015). Most of the *Herschel* prestellar cores are in thermally supercritical high-density filaments, suggesting that filament fragmentation is universal in the formation of star-forming cores. (e.g. Schisano et al., 2014; Könyves et al., 2015). Thus, many researchers discuss filamentary structures.

After many investigations to understand MCs, many questions are still open. What determines the interior structure of MCs, what is the role of filaments and cores in the evolution of MCs, what is the part of physical

processes (e.g. turbulence, magnetic fields, and galaxy dynamics) in each evolutionary process, and what are the implications of the scaling relations between mass and internal velocity dispersion and size? These questions may be due to the complexity of the spatial structure, and we have not yet found the observational parameters that are simple enough to discuss.

To overcome this situation and understand the molecular clouds, we consider the following two types of *statistical* analysis in this dissertation. (i) investigations using statistical parameters obtained from a single molecular cloud (Chapter 3), (ii) investigations based on a large number of molecular clouds (Chapter 4). In the following, we summarize the critical properties of MCs: the scaling relations between mass and velocity dispersion, the mass spectrum of the clouds, and the probability distribution of column densities.

1.2.1 Scaling Relations

Previous studies of MCs have found some scaling relationships between the mass, radius, and internal velocity dispersion of each cloud. One of the pioneering works was carried out by Larson (1981). Larson (1981) used millimeter-wave data to show that MCs have the following scaling relations (see also Lombardi et al., 2010).

1. Cloud length L and its velocity dispersion σ_v have a power-law relation ($\sigma_v \propto L^{0.38}$).

2. Molecular clouds are approximately virial equilibrium ($2GM/\sigma_v^2 L \sim 1$).

3. A relationship between molecular cloud density and length is $n \propto L^{-1.1}$ (i.e., the column density of molecular clouds is relatively constant).

These relationships are empirical laws derived from observational studies. Here, it should be noted that the cloud length L is calculated as the equivalent area radius of the cloud projected onto the plane of the sky.

It is well known that the molecular lines emitted from MCs are much broader than the thermal linewidth (~ 0.2 km s^{-1} at a gas temperature of 10 K). This broad linewidth is thought to be due to supersonic turbulence. The existence of the above $L - \sigma_v$ relation for cloud ensembles over four to five orders of magnitude in size suggests that supersonic turbulence is a universal dynamical feature of molecular clouds (e.g. Larson, 1981; Heyer & Brunt, 2004; Falgarone et al., 2009). The exponent of 0.38 obtained by Larson (1981)

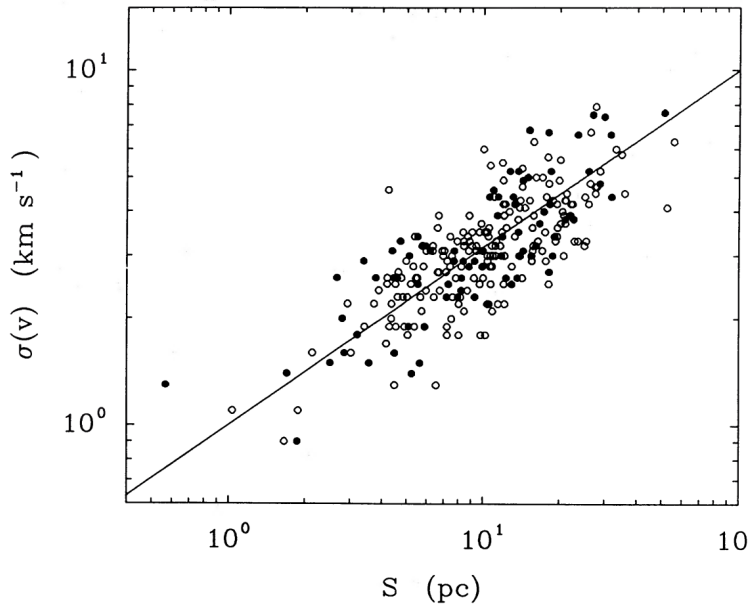

Figure 1.5: Molecular cloud size–velocity dispersion relation. The filled circles indicate the clouds with known distances. The open circles indicate the clouds with resolved near-far distance ambiguity. Figure from Solomon et al. (1987).

is close to that predicted by Kolmogorov (1941) for incompressible (subsonic) turbulence. Larson (1981) interprets it as incompressible turbulence in the MCs.

From an analysis of 273 nearby clouds using ^{12}CO data from the University of Massachusetts-Stony Brook (UMSB) Galactic Plane Survey, the exponent of the velocity dispersion–size relation was updated to ~ 0.5 (e.g. Solomon et al., 1987). The velocity dispersion–size correlation diagram is shown in Figure 1.5. This value is theoretically expected in a shock dominated turbulent field (see Passot et al., 1988; Vázquez-Semadeni, 1999; McKee & Ostriker, 2007). In observational studies, however, the detailed slope of the velocity dispersion-size relation has not yet been established. In some cases, exponents smaller than 0.5 (e.g. Caselli & Myers, 1995; Plume et al., 1997; Shirley et al., 2003; Traficante et al., 2018; Ma et al., 2021), negative exponents (Wu et al., 2010) and larger than 0.5 (e.g. Shetty et al., 2012; Kauffmann et al., 2017; Tanaka et al., 2020; Krieger et al., 2020) have been reported. Moreover, the analysis with the addition of the massive core has shown that the power-law relationship is lost (Ballesteros-Paredes et al.,

2011). The lack of a consistent correlation has been suggested to be because the dense gas tracers trace only a small fraction of the mass and volume of the cloud (Ballesteros-Paredes & Mac Low, 2002; Heyer & Brunt, 2004). However, there is a clear trend that high column density cores still have a large velocity dispersion (e.g. Ballesteros-Paredes et al., 2011, 2018, 2020). This result is expected as gravitational collapse and local feedback in the core increases the velocity dispersion in the core (Ballesteros-Paredes et al., 2018).

1.2.2 Cloud mass spectrum

The mass function of molecular clouds is called the cloud mass spectrum. This spectrum is defined by

$$dN = f(M)dM, \tag{1.5}$$

where dN is the number of MCs found within a mass range $[M,\ M + dM]$. It is governed by the physical processes in the molecular cloud or in its formation; thus, the mass spectra of the clouds provide a clue to the formation mechanisms of the objects. Estimates of GMC mass spectra have been reported from CO and dust continuum surveys. The results indicate that the mass distribution has no characteristic mass and follows a power law with a negative exponent (e.g. Stutzki & Guesten, 1990; Dobashi et al., 1996; Yonekura et al., 1997; Kramer et al., 1998). In general, the resulting mass spectrum is recognized as a function that follows a power law,

$$f(M) = \frac{dN}{dM} \propto M^{-\gamma}. \tag{1.6}$$

The values of γ for GMC, MC, and clump based on CO and dust continuum observations ranged between 1 and 2 (e.g. Stutzki & Guesten, 1990; Dobashi et al., 1996; Yonekura et al., 1997; Heyer & Terebey, 1998; Heithausen et al., 1998; Kramer et al., 1998; Motte et al., 1998; Johnstone et al., 2000; Heyer et al., 2001; Johnstone et al., 2001; Alves et al., 2007; Rosolowsky et al., 2010; Könyves et al., 2015; Ohashi et al., 2016). However, there is some controversy about analyses based on mass spectral exponents because the estimated γ values may be biased by the used method. Possible reasons include line-of-sight contamination, opacity effects, CO depletion in

dense cores, and clump identification algorithms. In particular, it should be noted that analyses based on interferometric observations may loose the large-scale structures that affect the slope of the mass function (i.e., missing flux). In addition, we should consider the intermediate density range. In fact, if one looks carefully at the mass functions of previous studies (e.g. Johnstone et al., 2000; Motte et al., 2001; Alves et al., 2007; Könyves et al., 2015), one can also fit the log-normal function instead of the power law, as pointed out by Ballesteros-Paredes et al. (2006) and Könyves et al. (2015).

1.2.3 Probability distribution function

The probability distribution function (PDF) is one of the basic concepts of statistics, expressing the probability that a random variable is found within a given range. Under the stationary state of an ergodic system, the PDF is equal to the histogram of the variable of the system at any instant. In observational studies of ISM, the word PDF is used as histograms of volume (ρ-PDF) or column density (N-PDF). The shape of these volume and column density PDFs is determined by the physical processes that dominantly contribute to the density structure in the molecular gas (e.g. Vázquez-Semadeni, 1994; Passot & Vázquez-Semadeni, 1998; Federrath et al., 2008; Kainulainen et al., 2009; Kritsuk et al., 2011; Ballesteros-Paredes et al., 2011). As a result, ρ-PDF and N-PDF are recognized as effective tools for investigating the properties of molecular clouds, which are believed to be affected by various physical processes. However, it should be noted that the density histograms obtained from observations are not required to reflect the physical processes behind the PDF, since the histogram is equal to the PDF only if the system is steady and ergodic (Vázquez-Semadeni & García, 2001; Tassis et al., 2010). Nevertheless, we can assume the steadiness and ergodicity of ISM in the most observational study. In addition, we should be careful to use the word "PDF"; some works say PDF is the volume density histogram and others use it as the column density histogram.

The shapes of the ρ-PDF are determined by the dominant physical processes governing the density structure of MCs. Theoretical studies of supersonic turbulence suggest that the probability density function of the gas density, or the ρ-PDF, of turbulence-dominated clouds exhibits a log-normal distribution (e.g. Vázquez-Semadeni, 1994; Passot & Vázquez-Semadeni, 1998; Ostriker et al., 2001; Federrath et al., 2008; Burkhart et al., 2015; Nolan

et al., 2015). This feature is mainly attributed to the application of the central limit theorem to the hierarchical density fields formed by multiplicative processes. The reason is the following (see Vázquez-Semadeni, 1994; Passot & Vázquez-Semadeni, 1998; McKee & Ostriker, 2007; Ballesteros-Paredes et al., 2020). The first step is that isothermal shocks with Mach number $\mathscr{M}$ produce a density enhancement proportional to $\mathscr{M}^2$ for the mean density ρ, $\delta\rho/\rho \propto \mathscr{M}^2$. Next, in isothermal turbulent fluids with Mach number $\mathscr{M}$, the amplitude of the density fluctuation is generated by the random successive passage of the shock. This results in a random distribution of multiplicative (additive in logarithm) density enhancement. As a result, the central limit theorem generates a normal (Gaussian) distribution function in the logarithmic density scale or log-normal function. It should be noted, however, that this result assumes that each line of sight is independent. If the dominant process is asymmetric in density evolution, such as gravitational collapse, its ρ-PDF will have an excess tail on the high-density side. This leads many researchers to interpret the power-law tail of the ρ-PDF at the high-density end (e.g. Klessen, 2000; Ballesteros-Paredes et al., 2011; Kritsuk et al., 2011; Collins et al., 2012; Federrath & Klessen, 2013; Burkhart et al., 2015). However, it is difficult to obtain the ρ-PDF of a MC from observations. This is because the length of the MC in the line of sight (LoS) direction is almost impossible due to the projection effect, and therefore the fraction of the volume occupied by the gas giving the emission lines is also unknown. Therefore, observational studies of molecular gas have mainly been discussed using the PDF of the column density, or N-PDF.

Three tracers have been used in observational N-PDF studies: dust extinction in the near-infrared (e.g. Goodman et al., 2009; Kainulainen et al., 2009), dust emission in the mid/far-infrared (e.g. Goodman et al., 2009; Schneider et al., 2012, 2013, 2015a,b,c; Könyves et al., 2015; Lombardi, Marco et al., 2015), and optically thin molecular line emission (e.g. Goldsmith et al., 2008; Goodman et al., 2009; Schneider et al., 2016b; Ma et al., 2020, 2021, 2022). Previous studies using these three tracers have shown that the N-PDFs of many quiescent clouds are log-normal, while those of active star-forming clouds consist of two components: a log-normal and a pronounced power-law tail in the high-density region (e.g. Goodman et al., 2009; Kainulainen et al., 2009; Schneider et al., 2013; Ma et al., 2021; Lewis et al., 2022). However, we should take into account that approximately 70% of the clouds in the second and third quadrants of the Milky Way mid-plane

were log-normal N-PDF (Ma et al., 2021, 2022). This means that most MCs are dominated by turbulence. In addition, they pointed out that the N-PDF having an excess tail is not necessarily related to the star-forming activity.

High-resolution FIR observations and simulations reveal a third component: another tail at the highest density (Kritsuk et al., 2011; Schneider et al., 2015a; Pokhrel et al., 2016; Jaupart & Chabrier, 2020; Khullar et al., 2021). Simulations of isothermal gravitational turbulence performed by Khullar et al. (2021) suggested that the resulting PDF has one log-normal and two power-law tails. The first power-law tail in the intermediate-density range with a steeper slope is due to the onset of self-gravity, and the second tail in the denser range is due to the onset of rotational support. However, it is unclear whether the three components of an observational N-PDF correspond to the components due to these physical processes (e.g. Tremblin et al., 2014; Schneider et al., 2015a; Pokhrel et al., 2016).

The analysis of the N-PDF needs to be performed only for contours that are closed on the column density map, as pointed out by Alves et al. (2017). This is because including data beyond the closed column density contours will give an N-PDF that is underestimated in lower-density bins from an unobserved part of the cloud. When referring to the results of numerical simulations, we should pay attention to their physical specifications (see also Ballesteros-Paredes et al., 2020). In numerical simulations, the boundary of the statistics is set to be the whole box for the calculation. This corresponds to an open-density contour. The size and mass of the numerical box are finite. Because of this, if the PDFs from these simulations often show the maximum value and decrease with lower densities, they may differ from the observed histograms obtained from interstellar gas. In addition, the observed histogram calculated from the intensity of the ISM is affected by the thermal noise at the low-density end. We, therefore, should not overestimate the simulation results to fit and analyze the N-PDF in observational studies.

1.3 Star formation

The star formation process can be described as the physical process of converting diffuse ISM into stars. Stars are considered to be formed by the gravitational contraction of the densest part of the MC, called the molecular cloud core. The Sun, for example, has a mass of 2×10^{33} g, corresponding

to 10^{57} hydrogen nuclei. If we were to distribute these nuclei at the average density of the Milky Way (1 cm^{-3}), we would need a volume of about 10^{19} cm^3 ($\sim$ 3 pc^3). The formation of a star requires the collection of ISM in the above volume. In this section, we review the properties of stars and focus on massive star formation.

1.3.1 Initial Mass Function

Mass is one of the most important properties of a star. The evolution of a star is strongly dependent on its mass of the star. The simplest way to make a statistical study of stellar masses is to obtain the stellar mass function. This is called the initial mass function (IMF). Note that the luminosity function is obtained from observations, not the mass function. Since the lifetime of a star depends on its mass, a model that corrects for the stellar lifetime is required to investigate the IMF.

The IMF is defined as the relative frequency of stars within a mass range $[m, m + \delta m]$ being born in a single cluster and can be described by

$$\int_{m_{\mathrm{min}}}^{m_{\mathrm{max}}} m\phi(m)dm = 1\mathrm{M}_{\odot}, \tag{1.7}$$

where m_{min} and m_{max} are the minimum and maximum stellar mass limits, respectively. Salpeter (1955) conducted pioneering observational work on the IMF. He found from optical observations in the solar neighborhood that the IMF can be fitted with a power law with an exponent of -2.35. However, the power law with a single negative exponent is unrealistic because of the divergence as it approaches zero (implying an infinite number of extremely low-mass stars). In the low-mass range, the abundance is expected to decrease. Observations of stars in clusters and the Large Magellanic Cloud (LMC) have extended the work on stars below one solar mass (e.g. Scalo, 1990; Massey, 1998; Kroupa et al., 2001; Kroupa & Boily, 2002; Muench et al., 2002). Consequently, it was shown that the IMF is a combination of power laws with different exponents in different mass ranges (broken power law). The currently recognized IMF is as follows (Kroupa et al., 2001),

$$\phi(m)dm \simeq m^{-2.3}dm \ : \ m \geq 0.5 \ \mathrm{M}_{\odot}, \tag{1.8}$$

$$\phi(m)dm \simeq m^{-1.3}dm \ : \ 0.5 \ \mathrm{M}_{\odot} \geq m \geq 0.08 \ \mathrm{M}_{\odot} \tag{1.9}$$

and

$$\phi(m)dm \simeq m^{-0.3}dm \ : \ 0.08 \ \mathrm{M}_{\odot} \geq m \geq 0.01 \ \mathrm{M}_{\odot}. \tag{1.10}$$

On the other hand, it has been proposed that the IMF can be fit by a log-normal distribution or a combination of log-normal plus power law (e.g. Padoan & Nordlund, 2002; Chabrier, 2003, 2005; Maschberger, 2013; Offner et al., 2014, and references therein). The form of the IMF is still under discussion. The difference between the two function types (power-law and log-normal) in the high-mass range is whether one considers star formation to be a continuous process or whether there is a dominant physical process in a particular region. However, it is not necessary to construct a model that uniformly reproduces the IMF in all mass ranges. This is because the formation mechanisms of low- and intermediate-mass stars are thought to be different from those of massive stars.

1.3.2 Massive star formation

In general, a star with a mass larger than 8 $\mathrm{M}_{\odot}$ is called a massive star. Massive stars are rare (10% of the total mass of stars, or 0.2% in number). However, the energy emitted by massive stars can play an essential role in the evolution of their host galaxies (see Kennicutt, 2005). One of the main characteristics of massive stars is that hydrogen fusion reactions begin before mass accretion is complete. In this section, we will focus on the challenges of observational studies of massive star-forming regions.

Observational studies of massive star formation are limited compared to those of low-mass stars. This problem is mainly due to the following reasons. First, as mentioned above, since massive stars are rare, massive star-forming regions are generally far away from observers. For instance, the nearest massive star-forming region is the Orion cloud at a distance of $\sim$ 400 pc (Hirota et al., 2007). Most massive star-forming regions are at distances of a few kpc (e.g. Reid et al., 2009). In contrast, the distance of the low-mass star-forming region, the Taurus cloud, is $\sim$ 140 pc (Rebull et al., 2004). This implies that high spatial resolution is difficult to achieve in observations. The second is the evolutionary timescale. Massive stars form in an extremely short time compared to low-mass stars. Consequently, the observational period for massive star formation is very limited. The final problem is that massive stars form almost exclusively in compact OB clusters or large OB associations. This means that extremely high spatial resolution is required to

Table 1.2: A list of the classification of HII regions. Adapted from Habing & Israel (1979) and Kurtz (2002).

Class	n_e [cm^{-3}]	size [pc]	EM^*[cm^{-6} pc]	Ionized mass [M$_\odot$]
Hypercompact	10^6	< 0.05	10^9	10^{-3}
Ultracompact	$> 3 \times 10^3$	< 0.15	$> 10^6$–10^7	10^{-2}
Compact	$> 10^3$	0.1–1	$> 10^6$	1
Classical	$\sim 10^2$	1–30	10^4–3×10^6	10
Giant	3–50	10–300	$< 5 \times 10^5$	500–5×10^6
Supergiant	10	> 100	$< 10^5$	10^6–10^8

* Emission measure, EM, is defined as the square of the number density of free electrons integrated over the LoS of the ionized gas, $EM = \int_0^s n_e^2 ds$.

separate the properties of individual massive star formation sites and massive stars. At the center of the Orion Nebula cluster, the stellar density is 10^5 pc^{-3} and the typical interstellar distance is 0.02 pc (Hillenbrand & Hartmann, 1998), corresponding to approximately 10″ for a distance of 400 pc. Most massive star-forming regions require a spatial resolution of a few arcsec. Furthermore, a typical dense clump-forming massive cluster has a mass of a few thousand M$_\odot$, a radius of about 1 – 2 pc, and a surface density of ~ 1 g cm^{-2} (e.g. McKee & Tan, 2003; Myers et al., 2013). This corresponds to $A_V \sim$ 200 mag (Güver & Özel, 2009). For most massive star formation processes, only mid-infrared, sub-millimeter, and radio observations are possible. Radio interferometers can only achieve high resolution at such long wavelengths.

Previous observational studies suggest that massive stars form in the following evolutionary stages. (i) infrared dark clouds (size $\sim$ 0.1 pc, mass $\sim$ 10 M$_\odot$–100 M$_\odot$), (ii) hot core ($T \sim$ 100–200 K), (iii) HII region (typical temperature $\sim 10^4$ K, size $\sim$ 0.01 pc–10 pc). Table 1.2 shows the classification of HII regions based mainly on the spatial size (see also Habing & Israel, 1979; Kurtz, 2002).

1.3.3 Triggered star formation

Massive stars affect their surroundings through the expansion of HII regions, powerful outflows, strong stellar winds, and large amounts of radiation. These feedback mechanisms are reviewed in Krumholz et al. (2014). The feedback from the massive stars is considered to influence the subsequent star formation activity. For example, feedback from massive stars causes

strong shocks in the surrounding molecular gas, which compresses the gas and triggers star formation (e.g. Urquhart et al., 2007; Shimajiri et al., 2008; Thompson et al., 2012; Deharveng et al., 2015; Duronea et al., 2017; Paron et al., 2021). In other cases, feedback heats the surrounding molecular gas and suppresses the fragmentation of cores or filaments. This is thought to be a contributing factor in the formation of massive stars (e.g. Bate, 2009; Hennebelle & Chabrier, 2011; Deharveng et al., 2012; Bate & Keto, 2015; Hennebelle et al., 2020). These positive feedbacks that promote or accelerate star formation are called triggered or induced star formation. The mechanisms of feedback-induced star formation have been actively studied. The collect and collapse (C&C) model and the radiation-driven implosion (RDI) model are representative (see Elmegreen & Lada, 1977; Bertoldi, 1989).

The C&C model was proposed by Elmegreen & Lada (1977). Figure 1.6 shows a simplified representation of the structure of the MC associated with the OB subgroup. In this model, a shell of warm ionized gas expanding from the HII region forms a cold, dense gas region at the edge of the shell. If enough gas is compressed for a long enough time, this dense region can start to form stars. Indeed, infrared sources, maser sources, and compact continuous sources have been detected at expected locations of shock fronts (e.g. Habing et al., 1972; Lada et al., 1976; Deharveng et al., 2003). In the RDI model, shock waves from ionized gas enter the MC. As a consequence, the stable clumps become unstable due to external pressure, and stars are formed (Bertoldi, 1989). Bertoldi & McKee (1990) performed numerical calculations using the RDI model and showed that shocks induced by ionized gas cause the formation of dense regions that collapse to form the next generation of stars.

Although it is easy to define the mechanisms of triggered star formation, it is difficult to identify different types of mechanisms from observational studies. In some cases, while there is observational evidence for the formation of low- and intermediate-mass stars under the influence of the expansion of HII regions, the evidence for massive star formation is limited. Thompson et al. (2012) suggest that between 14% to 30% of massive stars were triggered by star formation, and the remainder formed in a different scenario. The study of these massive star-forming regions and their star formation histories is very active (e.g. Chibueze et al., 2013; Nakano et al., 2017; Duronea et al., 2017; Bobotsis & Fich, 2019; Dewangan et al., 2020b; Pandey et al., 2022).

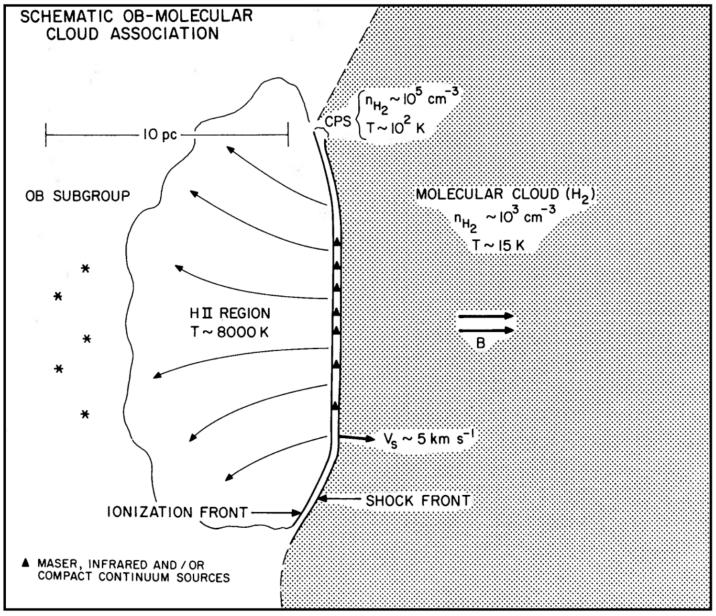

Figure 1.6: Schematic representation of the C&C model. This figure has been taken from Elmegreen & Lada (1977). The asterisk (*) marks indicate the OB stars. In the thin layer between the molecular cloud and the HII region, it becomes gravitationally unstable and forms new stars. The formed stars can be indirectly evidenced by maser spots, infrared sources, and compact continuum sources, indicated by filled triangle (▲) marks.

1.4 Motivation for this dissertation

As discussed in the previous section, there are many phases of the ISM, such as ions, atoms, and molecules. The molecular gas phase is one of them. These phases are not isolated from each other; the ISM is changing and cycling through all these phases.

Many mechanisms can contribute to the formation processes from ISM to stars at each stage. Along the time evolution of the ISM, the standard scenario is the following. First, thermal instability should be the major mechanism from the WNM to the CNM. Next, molecular gas fragments formed from the CNM evolve into MCs in GMCs through hierarchical agglomeration, and converging flows. The passage of spiral arms and cloud-cloud collisions should help these processes through shock waves, and large-scale instabilities (see Section 2 in Ballesteros-Paredes et al., 2020).

In the process shown in the previous paragraph, the first stage, i.e. how to densify the diffuse molecular gas is still unexplored. After the discovery of the MC with CO observations in the 1970s, observational studies have been focused on the later stages of the star formation process on smaller scales by observations in shorter wavelengths and with higher spatial resolution. This has allowed us to make great progress in understanding the last stage of star formation. However, the process in the earlier stages is still an open question. Someone thinks that the process before the molecular dense core formation is a different business for star formation, but the process to form MCs must have a physical connection. To address this "wilderness", sensitive wide-field observations with a high spatial resolution enough to resolve the interior of a MC are required. Fortunately, since the 2010s, large-scale surveys with a sensitive and high spatial resolution ($< 1'$) of the galactic mid-plane with radio telescopes have been conducted, and huge amounts of molecular emission line data have been published (e.g. Heyer & Dame, 2015; Rigby et al., 2016; Schuller et al., 2017; Umemoto et al., 2017; Hogge et al., 2018; Yamagishi et al., 2018; Su et al., 2019; Kohno et al., 2022; Mazumdar, 2022). Such large-scale surveys have allowed us to investigate the spatial distributions of temperature, column density, and the velocity dispersion of a MC for many MCs.

To change the physics between cloud-scale and local star formation activity, we focus on the spatial structure of a whole cloud and investigate the properties of individual clouds. Our goal is to find out between the physical

properties of cloud-scale properties and the star formation process in it.

It is widely known that a star formation activity affects the properties of its mother molecular cloud. We, therefore, have to estimate the effects and spatial scales of star formation activity in a massive star-forming region by the results shown in this dissertation and the previous works done by our colleagues (e.g. Chibueze et al., 2013; Murase et al., 2022). After then, we investigated the relationship between the statistical structure of MCs and the star-forming activity.

1.5 Structure of this dissertation

This dissertation consists of five chapters, including this introduction. The main topics of this dissertation are (i) the measurement of the influence of massive star-forming regions on the surrounding molecular gas (Chapter 2) and (ii) a statistical analysis of the properties that characterize MCs (Chapters 3 and 4). These studies focus on molecular gas and are performed using molecular emission lines that can be obtained in the radio range. In Chapter 2, we have used emission lines from multiple excited states of NH_3 to investigate the extent of feedback from massive stars. In Chapters 3 and 4, to probe the large-scale structure of the cloud, we used ^{12}CO (J=1–0) and ^{13}CO (J=1–0). These data were obtained with the Nobeyama 45-m radio telescope.

In Chapter 5 we summarize this dissertation and its conclusions, followed by appendices.

Chapter 2

Star formation feedback on dense molecular gas in the W33 complex

The contents of this chapter were originally published as a proceeding ""KAGONMA" NH_3 mapping observations of molecular clouds with Nobeyama 45m telescope" in *Origins: From the Protosun to the First Steps of Life. Proceedings of the International Astronomical Union* (Murase et al., 2020) and a paper "Kagoshima galactic object survey with the Nobeyama 45-meter telescope by mapping in ammonia lines (KAGONMA): star formation feedback on dense molecular gas in the W33 complex" in *Monthly Notices of the Royal Astronomical Society* (Murase et al., 2022). The author has changed the layout of the paper to accommodate this dissertation format.

2.1 Introduction

Massive stars (> 8 $M_\odot$) affect the surrounding environment through expansion of the HII regions, powerful outflows, strong stellar winds, and large amounts of radiation. Consequently, they ultimately play a key role in the evolution of the host galaxy (see Section 1.3.3). In this study, we focus on the effects of the formation processes of massive stars on the molecular cloud environment.

Several recent observations of the James Clerk Maxwell Telescope (JCMT)

Gould Belt survey (Ward-Thompson et al., 2007) have quantified the effect of radiative feedback from OB stars on molecular clouds. Using the dust color temperature derived from the flux ratios of 450- and 850-μm continuum emission, they found that the dust temperature around OB stars can rise to 40 K, with effects on scales of several parsec (Rumble et al., 2021). They reported that heating the dust may raise the Jeans mass and enhance the stability of the cores of filaments against gravitational collapse (Hatchell et al., 2013; Rumble et al., 2015, 2016, 2021). In addition to dust data, the gas temperature map can be obtained using molecular lines (e.g. CO, NH_3, N_2H^+, etc.). Large surveys of nearby star-forming regions in NH_3 revealed that the average gas temperature in molecular clouds with inactive star formation is around 15 K. In contrast, active star-forming cores have temperatures above 20 K (e.g. Urquhart et al., 2015; Friesen et al., 2017; Hogge et al., 2018; Billington et al., 2019; Keown et al., 2019; Tursun et al., 2020). In the range of hydrogen number densities $n(H_2) \gtrsim 10^4$ cm^{-3}, the dust and gas temperatures are expected to be well coupled due to the frequent collision of dust grains and gas (e.g. Goldsmith, 2001; Seifried et al., 2017).

Most stars are recognized to form in cluster mode (Lada & Lada, 2003; Krumholz et al., 2019). The heating of molecular gas by radiation feedback from massive stars in the cluster may impact the properties of core mass function and the types of stars formed (e.g. Bate, 2009; Rumble et al., 2015). In order to study the impact of radiative feedback, it is important to investigate the effects and scales of star-forming regions of various evolutionary stages on the surrounding environment.

There are several techniques to measure the temperature of the ISM. The dust temperature $T_{\rm dust}$ can be estimated by fitting a single-temperature graybody model to the observed spectral energy distribution (SED) of the dust continuum thermal emission (Hildebrand, 1983). However, there are uncertainties in the assumptions of the dust emissivity coefficient κ, and dust emissivity index β, which affect the accuracy of the derived dust temperature. CO emission lines are commonly used for molecular gas observations. In particular, the gas excitation temperature can be easily obtained from the brightness temperature of ^{12}CO (J=1–0) by assuming the opacity thick and the filling factor in the observed beam is unity. While it should be noted that the physical parameters in the center of high-density cores may not reflect this due to optical thickness and the freezing out onto dust grains (e.g. Willacy et al., 1998; Tafalla et al., 2002; Christie et al., 2012; Feng

et al., 2020).

NH_3 has long been recognized as a good thermometer for the ISM (Ho & Townes, 1983) and its line observations have the advantage of the ability to derive physical parameters such as column density and optical depth from the splitting of the inversion transition into hyperfine structure lines with only reasonable assumptions that the main transitions of the molecule are emitted under similar excitation conditions. The rotational temperature can also be estimated from the relationship between the intensity ratio of two different inversion transition lines and the optical depth. In addition, the inversion transitions in the lowest metastable rotational energy levels are easily excited in the typical temperatures of molecular clouds. Moreover, NH_3 molecules are abundant in the gas phase in cold and high-density environments (e.g. Bergin & Langer, 1997; Tafalla et al., 2002).

Previous observational studies in NH_3 lines have predominantly been single beam pointings toward infrared dark clouds (IRDCs), young stellar objects (YSOs) and the centers of HII regions (e.g. Wilson et al., 1982; Rosolowsky et al., 2008; Dunham et al., 2010; Urquhart et al., 2011; Wienen et al., 2018), and mappings at scales of few parsec (e.g. Keto et al., 1987; Mangum et al., 1992; Toujima et al., 2011; Chibueze et al., 2013; Urquhart et al., 2015; Nakano et al., 2017; Billington et al., 2019; Burns et al., 2019). These studies have related the physical conditions of active star-forming cores to the surrounding environment. Recently, large surveys with the Green Bank Telescope (GBT) have been conducted to study the relationship between the kinematics of dense gas and star formation in entire molecular clouds. These observations cover giant molecular clouds (K-band Focal Plane Array (KFPA) Examinations of Young STellar Object Natal Environments (KEYSTONE); Keown et al., 2019), the Gould Belt star-forming regions (the Green Bank Ammonia Survey (GAS); Friesen et al., 2017) and the galactic plane (the Radio Ammonia Mid-Plane Survey (RAMPS); covering $10^\circ \leq l \leq 40^\circ$, $\mid b \mid \leq 0^\circ.5$; Hogge et al., 2018). These large surveys were made with the On-The-Fly (OTF) mapping mode. However, these unbiased surveys are rather shallow, since NH_3 line observations require a large amount of time to detect weaker emissions. Therefore, we conducted a high-sensitivity NH_3 imaging survey targeting dense molecular cores and the regions around them.

For our survey, we identified dense molecular cores based on the $C^{18}O$ (J=1–0) imaging data obtained as a part of FUGIN (FOREST Unbiased Galactic plane Imaging survey with the Nobeyama 45-m telescope; Umemoto

Table 2.1: A list of KAGONMA sources which have already been observed.

KAGONMA name	l [degree]	b [degree]	$v_{\rm LSR}(C^{18}O)$ [a] [km s^{-1}]	associated object
KAG1	44.312	+0.039	+56.9	G044.3103+00.0416*
KAG35	14.613	−0.565	+18.5	G14.628–0.572
KAG39	14.565	−0.603	+18.7	G14.555–0.606
KAG45	14.454	−0.102	+40.4	G014.481–00.109*
KAG64	12.798	−0.202	+35.6	W33 Main *
KAG71	224.274	−0.833	+18.0	CMa OB1
KAG72	201.446	+0.638	+6.5	G201.44+00.65

[a] Umemoto et al. (2017)
* HII region

et al., 2017). By using the *Clumpfind* algorithm (Williams et al., 1994), we cataloged 72 molecular cores / clumps in part of 1st and 3rd quadrants of the Galactic plane (i.e. $10° \leq l \leq 50$ °, and $198° \leq l \leq 236°$, $\mid b \mid \leq 1°$). This catalog includes Infrared Dark Clouds (IRDCs), massive star-forming regions and HII regions. We have already finished the mapping observations towards 7 cores or clumps, which are listed in Table 2.1. In this dissertation, we present the results of the W33 massive star-forming region, identified as KAGONMA 64.

Figure 2.1 shows the *Spitzer* -GLIMPSE 8.0 μm (Benjamin et al., 2003) image of the W33 region. W33 has six dust clumps defined in the ATLASGAL (Atacama Pathfinder Experiment (APEX) Telescope Large Area Survey of the GALaxy) 870 μm survey (Schuller et al., 2009; Contreras et al., 2013; Urquhart et al., 2014), which are W33 Main, W33 A, W33 B, W33 Main 1, W33 A1, and W33 B1 (see Figure 2.1). Immer et al. (2014) reported that these 6 dust clumps are at various stages (Massive protostellar object, Hot core, compact HII region) in star-forming processes based on their spectral energy distributions (SEDs) from centimeter to far-infrared. In Table 2.2, the evolutionary stage of each dust clump is listed in order of earliest to latest. W33 Main harbors a compact HII region found by radio continuum observations (Ho & Townes, 1983), indicating massive star formation. Water and methanol maser emission has been detected in W33 A, W33 Main and W33 B (i.e. Haschick et al., 1990; Menten, 1991; Immer et al., 2013), and OH maser sources have been detected in W33 A and W33 B (i.e. Caswell, 1998; Colom et al., 2015).

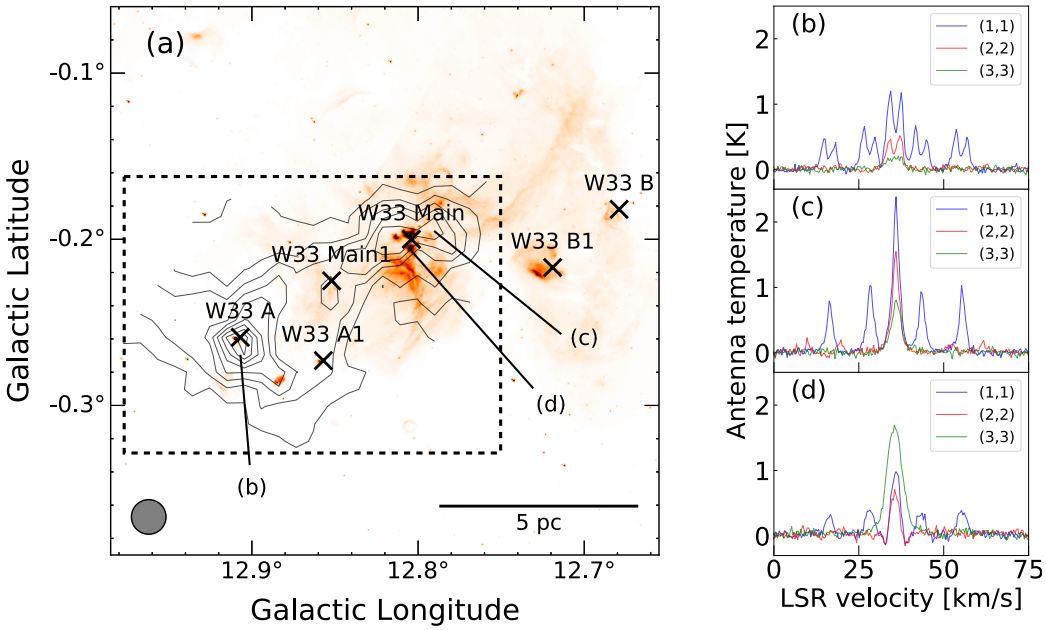

Figure 2.1: (a): The NH_3 (1,1) integrated intensity map of the W33 complex in contours over the *Spitzer* - GLIMPSE 8.0 μm image. The lowest contour and contour steps are 0.8 K km s^{-1} and 1.2 K km s^{-1} (30σ), respectively. The cross marks indicate the dust clumps reported by the ATLASGAL 870 μm survey (e.g. Contreras et al., 2013; Urquhart et al., 2014). The dashed rectangle shows our observed area. The NRO 45-m beamsize (FWHM) is indicated by the gray circle shown in the lower left corner in panel (a). The (b)–(d) labels indicate the positions for the profiles shown in panels (b)–(d).

Table 2.2: Evolutionary stages of dust clumps.

Source	l [degree]	b [degree]	$T_{\rm ex}(C^{18}O)$ [a] [K]	Evolution Stage [b]
W33 A1	12.857	−0.273	18	Massive protostellar object
W33 B1	12.719	−0.217	23	Massive protostellar object
W33 Main1	12.852	−0.225	19	Massive protostellar object
W33 A	12.907	−0.259	18	Hot core
W33 B	12.679	−0.182	17	Hot core
W33 Main	12.804	−0.200	34	compact HII region

[a] Kohno et al. (2018)
[b] Haschick & Ho (1983); Immer et al. (2014)

The distance to the W33 complex, based on annual parallax, was established as 2.4 kpc using VLBI water maser observations (Immer et al., 2013). W33 is located in the Scutum spiral arm of the Milky Way. Some CO line observations covering the entire W33 region were conducted (e.g. Stier et al., 1984; Sridharan et al., 2002; Kohno et al., 2018; Liu et al., 2021). Kohno et al. (2018) reported W33 A, W33 Main, and W33 B1 are at a radial velocity of $\sim +35$ km s^{-1} and W33 B has a velocity of $\sim +58$ km s^{-1}, while Immer et al. (2013) reported that these clumps exist within a single molecular cloud because these clumps have the same parallactic distance.

This chapter is organized as follows: in Section 2.2 we describe the set-up of our observations and data reduction. In Section 2.3 we present the results and estimated physical parameters of the observed area. We evaluate the influence of star formation feedback based on the rotational temperature distribution of NH_3 lines in Section 2.4. In Section 2.5, we summarize our results and our conclusions.

2.2 Observations

2.2.1 NH_3 and H_2O maser observations

We made mapping observations covering a $12' \times 12'$ area including W33 A and W33 Main with the Nobeyama 45-m radio telescope from 2016 December–2019 April. We observed the NH_3 (J,K) = (1,1), (2,2), (3,3) and H_2O maser lines simultaneously. From February 2019, we observed NH_3 (3,3), (4,4), (5,5) and (6,6) lines at positions where the (3,3) emission line was detected ($> 20\,\sigma$). The (3,3) emission line was observed again for relative calibration. We used the H22 receiver, which is a cooled HEMT receiver, and the SAM45 (Spectral Analysis Machine for the 45-m telescope: Kuno et al., 2011; Kamazaki et al., 2012), which is a digital spectrometer to observe both polarization for each line simultaneously. The bandwidth and spectral resolution were 62.5 MHz and 15.26 kHz, respectively. At the frequency of NH_3 these correspond to a velocity coverage and resolution of 400 km s^{-1} and 0.19 km s^{-1}, respectively. The telescope beam size was $75''$ at 23 GHz, which corresponds to 0.87 pc at 2.4 kpc. The pointing accuracy was checked every hour using a known H_2O maser source, M16A at $(\alpha, \delta)_{J2000}$=($18^{\rm h}15^{\rm m}19^{\rm s}.4$, $-13°46'30''.0$), and was better than $5''$. The map centre was $(l, b) = (12.°820, -0.°194)$. The OFF reference position was taken at $(l, b) = (13.°481, +0.°314)$

Table 2.3: Transition frequencies and excitation temperatures.

Transition	Frequency[a] [GHz]	E_u/k_B[a] [K]
H_2O 6_{12}-5_{12} (maser)	22.235080	-
NH_3 (1,1)	23.694495	23.3
NH_3 (2,2)	23.722633	64.4
NH_3 (3,3)	23.870129	123.5
NH_3 (4,4)	24.139416	200.5
NH_3 (5,5)	24.532988	295.6
NH_3 (6,6)	25.056025	408.1

[a] From the JPL Sub-millimeter, Millimeter, and Microwave Spectral Line catalog (Pickett et al., 1998). E_u is the energy of the upper level above the ground.

where neither $C^{18}O$ (J=1-0), NH_3 nor H_2O maser was detected.

We observed 280 positions using a 37″.5 grid in the equatorial coordinates using the position switch method. For efficient observation, three ON positions were set for each OFF position, and integrations were repeated for 20 seconds at each position. To obtain a uniform map noise, the scans were integrated until the RMS noise level for each polarization of each observed line was reached below 0.075 K. The typical system noise temperature, T_{sys}, was between 100 and 300 K. The antenna temperature, T_a^*, was calibrated by the chopper wheel method (Kutner & Ulich, 1981). We summarise the parameters for the NH_3 and H_2O maser line observations in Table 2.3.

2.2.2 Data reduction

For data reduction, we use the java NEWSTAR software package developed by the Nobeyama Radio Observatory (NRO). Baseline subtraction was conducted individually for all spectra using a line function established using emission-free channels. By combining dual circular polarisations, the RMS noise level was typically 0.04 K at each position. A conversion factor of 2.6 Jy K^{-1} was used to convert the antenna temperature to flux density.

In this dissertation, the intensities are presented as antenna temperature in kelvins. The NH_3 lines have five hyper-fine components consisting of one main line and four satellite lines. In our observations, these satellite lines

were detected only in the (1,1) transition. The number of map positions in which $\geq 3\sigma$ detections were achieved in all (1,1), (2,2) and (3,3) lines were 260, 231, and 172, respectively. No emission from transitions higher than (3,3) was detected.

The NH_3 profiles obtained in our observations can be categorized into three types (Figure 2.1 (b)-(d)). Figure 2.1-(b) shows double peak profiles detected around W33 A. The double-peak profiles were detected at 46 positions (The enclosure in Figure 2.2-(a)). The single peak profiles shown in Figure 2.1-(c) are typical NH_3 profiles. The intensity of these two types of profiles becomes weaker with higher excitation, while the (3,3) was detected more strongly than low excitation lines of the center of W33 Main, where a compact HII region is located (Figure 2.1-(d)). In this region, we found absorption features at 33 km s^{-1} and 39 km s^{-1} in (1,1) and (2,2) lines (see Section 2.4.3 for detail).

2.3 Results

2.3.1 Spatial distribution of NH_3 emission

Figure 2.2 shows the integrated intensity maps of the (1,1), (2,2) and (3,3) lines in our observed region. The velocity range of each map is between 32.0 and 40.0 km s^{-1}. NH_3 (1,1) emission is extended over a region of $12' \times 12'$, or 10×10 pc at 2.4 kpc. Two NH_3 clumps were detected at W33 Main $(l, b) = (12.^\circ804, -0.^\circ200)$ and W33 A $(l, b) = (12.^\circ907, -0.^\circ259)$.

Although maps of both the NH_3 (1,1) and (2,2) line show two peaks in W33 Main with a separation of about $2'$, the (3,3) map shows a single peak between them. After checking the profiles of the (1,1) and (2,2) lines there, we found hints of an absorption signature. Therefore, the actual column density structure of W33 Main has only a single clump with an apparent gap inside if caused by the absorption of emission at the midway point. We will further discuss the absorption feature in Section 2.4.3.

2.3.2 Linewidth correlations

Figure 2.3 shows the correlation plots of linewidths in the NH_3 (1,1), (2,2) and (3,3) emission lines. In Figure 2.3, we only used the observed positions where single peak profiles were obtained (except for the enclosed positions

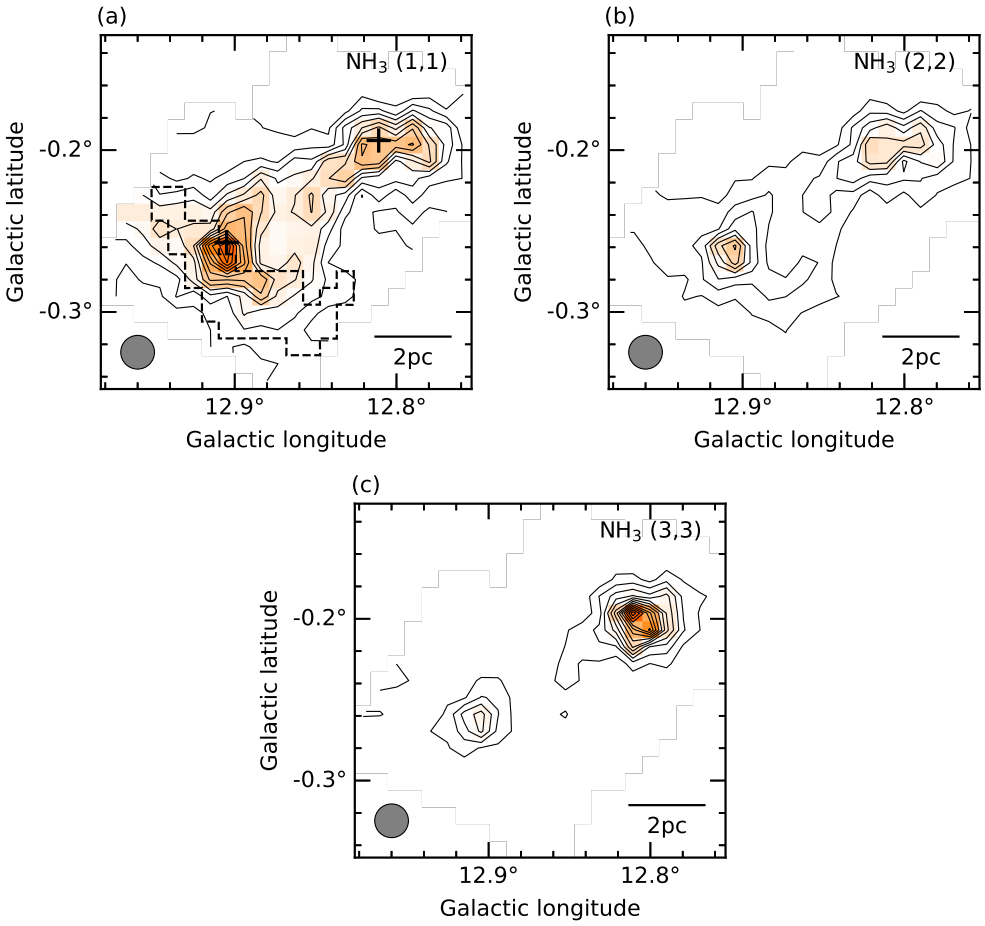

Figure 2.2: (a): Integrated intensity map of NH_3 (1,1). (b): in (2,2). (c): in (3,3). The NRO45 beamsize is indicated by the gray circle shown in the lower-left corner of each panel. The lowest contour and contour steps are 20σ (0.8 K km s^{-1}) in T_a^*, respectively. Plus marks indicate the positions of H_2O maser emission. The black dashed enclosure shows the region where double-peak profiles were detected.

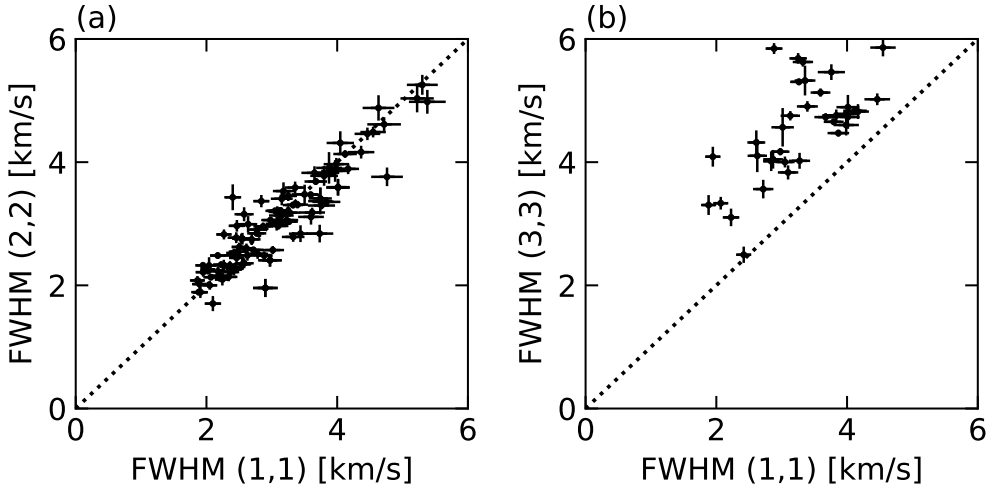

Figure 2.3: Scatter plots of FWHM linewidth of NH_3 (1,1), (2,2) and (3,3) emission. The solid lines indicate the line of equality.

in Figure 2.2-(a)). In our observations, the range of linewidths for each NH_3 line was 2 to 6 km s^{-1}, which is broader than the expected thermal linewidth for temperatures in W33 (approximately 0.2 km s^{-1} at a gas temperature of $\sim$ 20 K). These broader linewidths may be due to internal gas kinematic motions such as turbulence, outflows and stellar winds. While the linewidths of (1,1) and (2,2) emission show strong correlations, (3,3) emission tends to have systematically broader linewidths than the lower excitation transitions (see also Figure 11 in Urquhart et al., 2011). As shown in Table 2.3, the NH_3 (3,3) lines require approximately 5 times higher excitation energies than (1,1) lines. Therefore, the emission regions of higher transitions of NH_3 lines are considered warmer and more turbulent gas than (1,1) lines. These results are similar to single-beam observations toward the centers of MYSOs and HII regions (Urquhart et al., 2011; Wienen et al., 2018). Our results, therefore, show that such linewidth correlations in NH_3 can also be seen on larger scales than the core scale.

2.3.3 Deriving physical properties from NH_3 lines

Using NH_3 line profiles we can derive several physical properties at each observed position, such as optical depth, rotational temperature and column density.

Currently, there are two major methods for deriving the optical depth and

rotational temperature (see Wang et al., 2020, for details). They are known as the *Intensity ratio* and *Hyper-fine fitting* methods. The first method is derived from the intensity ratio between two different excitation lines, assuming a Boltzmann distribution (e.g. Ho & Townes, 1983; Mangum et al., 1992). The other method is generating a model spectrum from the radiative transfer function and searching for parameters that match the observed profiles (e.g. Rosolowsky et al., 2008; Urquhart et al., 2015). The common point in these methods is that the physical conditions along the velocity axis are assumed to be uniform. In general, however, molecular lines have a velocity structure, and the shape of profiles is asymmetric. Therefore, we used a method to derive physical parameters for each velocity channel based on the *Intensity ratio* method (see Appendix 2.6.1 for more details).

The equation for deriving the optical depth and rotation temperature using the *Intensity ratio* method is described below. The optical depth is derived from the line intensity ratios of the main and satellite lines in the (1,1) transition (Ho & Townes, 1983). The excitation energy differences between the hyper-fine components are very small. This allows us to assume that the main beam efficiencies, beam filling factors and excitation temperatures for all hyper-fine components are identical. Therefore, we can use

$$\frac{T_a^*(\mathrm{main})}{T_a^*(\mathrm{sate})} = \frac{1-\exp(-\tau)}{1-\exp(-a\tau)}, \tag{2.1}$$

where the values of a are 0.27778 and 0.22222 for the inner and outer satellite lines, respectively (Mangum et al., 1992).

Assuming that excitation conditions of gas emitting (1,1) and (2,2) lines were the same, the rotational temperature, T_{rot} can be estimated from the intensity ratio of the (2,2) to (1,1) and optical depth at each observed position (Ho & Townes, 1983) using

$$T_{\mathrm{rot}}(2,2;1,1) = -41.1 \Big/ \ln\Big(\frac{-0.282}{\tau(1,1,m)} \times \ln\left[1-\frac{T_{\mathrm{a}}^*(2,2,m)}{T_{\mathrm{a}}^*(1,1,m)} \times [1-\exp(-\tau(1,1,m)])\right]\Big), \tag{2.2}$$

where $\tau(1,1,m)$ is the optical depth of the NH_3 (1,1) main line.

Under the local thermal equilibrium (LTE) condition, the column density of the NH_3 in the (1,1) state can be estimated using the optical depth,

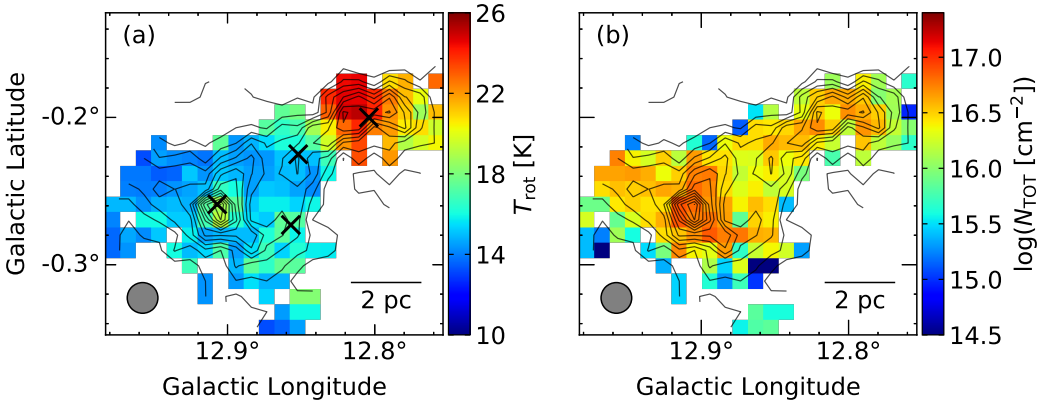

Figure 2.4: Spatial distributions of the physical parameters described in Section 2.3.3. The plotted values are representative along the velocity axis. (a): the rotational temperature. (b) : the total column density of NH_3 gas. Contours indicate the NH_3 (1,1) integrated intensity map which are the same as in Figure 2.2-(a). The NRO45 beamsize is indicated by the gray circle shown in the lower-left corner of each panel. Cross marks are the same as inside the dashed rectangle in Figure 2.1-(a).

$\tau(1,1,m)$ and the rotational temperature, $T_{\rm rot}$ (Mangum et al., 1992).

$$N(1,1) = 2.78 \times 10^{13} \tau(1,1,m) \left(\frac{T_{\rm rot}}{\rm K}\right) \left(\frac{\Delta v_{1/2}}{\rm km\,s^{-1}}\right), \tag{2.3}$$

where $\Delta v_{1/2}$ is the velocity width defined as the full width at half-maximum (FWHM) of the main line. The column densities were derived by using physical parameters at each observed position. When all energy levels are thermalized, the total column density, $N_{\rm TOT}(NH_3)$, can be estimated by

$$N_{\rm TOT}({\rm NH_3}) = N(1,1) \sum_J \sum_K \left(\frac{2 g_{\rm J} g_{\rm I} g_{\rm K}}{3} \exp\left[\frac{23.3 - E_{\rm u}(J,K)/k_{\rm B}}{T_{\rm rot}} \right] \right) \tag{4}$$

where $k_{\rm B}$ is the Boltzmann constant, g_J is the rotational degeneracy, g_I is the nuclear spin degeneracy, g_K is the K-degeneracy, and $E(J,K)$ is the energy of the inversion state above the ground state.

2.3.4 Molecular gas properties

In this subsection, we will report the spatial distribution of the derived physical parameters in W33 (Figure 2.4), which were solved in each velocity

channel. The physical parameters at each position were derived when the signal-to-noise ratio (S/N) of all peaks of NH_3 (1,1) hyper-fine components and (2,2) main line are above 3σ. The optical depth and rotational temperature errors were estimated to be $\pm$ 0.10 and $\pm$ 0.4 K, respectively (see Appendix 2.6.2).

The derived optical depth ranges from 1 to 2, and its mean value over all observed positions was 1.24 $\pm$ 0.10. The optical depth distribution was not significantly different at each position.

Maps of the rotational temperature and total column density are shown in Figure 2.4. The range of rotational temperature was between 12 and 25 K (Figure 2.4-(a)). We found a clear difference between the galactic east and west parts, corresponding to W33 A and W33 Main, respectively. All pixels in W33 A were colder than 18 K, and most pixels in W33 Main were warmer than 20 K. In our NH_3 observations, the temperature change was a particularly noticeable characteristic. We will discuss the relationship between the molecular gas temperature and star formation feedback in Section 2.4.2.

The value of total column density ranges between 2×10^{15} to 8×10^{16} cm^{-2} as shown in Figure 2.4-(b). The peak total column density of W33 Main and W33 A was $(5.1 \pm 0.1) \times 10^{16}$ cm^{-2} and $(7.5 \pm 0.1) \times 10^{16}$ cm^{-2}, respectively. In contrast to the difference in the rotational temperature, there was no significant difference in the total column density between W33 Main and W33 A. A weak dip in the measured column density at the center of W33 main is apparently due to the compact HII region.

2.3.5 H_2O maser detection

In our observations, H_2O maser emission was detected in W33 A on the 21st May in 2017 with 26.3 Jy at (l, b)=(12.°905, $-$0.°257) and W33 Main on the 07th May in 2016 with 10.7 Jy at (l, b)=(12.°811, $-$0.°194). These masers are positionally consistent with those reported in the parallax observations of Immer et al. (2013). H_2O maser emission is believed to be a signature of star formation in its early evolutionary stages (e.g. Sunada et al., 2007; Urquhart et al., 2011). Therefore, the detection indicates both W33 A and W33 Main host star-forming activity.

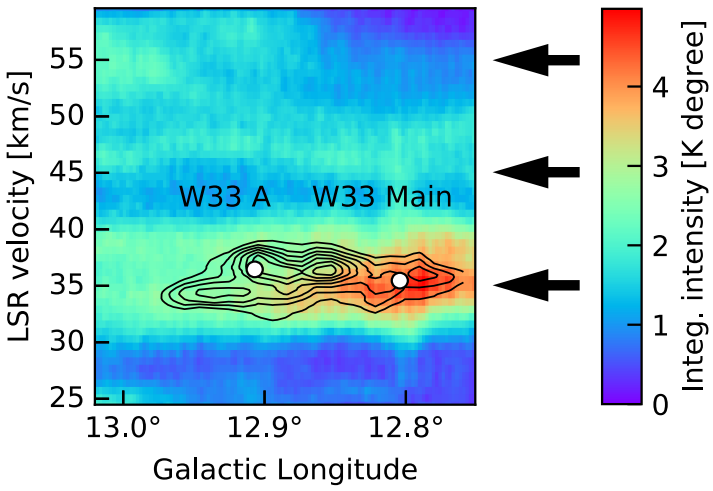

Figure 2.5: Longitude-velocity diagram of the ^{12}CO (J=1–0) emission using FUGIN data (color image) and the NH_3 (1,1) main line emission (contour). The white circles indicate the peak velocity of W33 A and W33 Main in the C^{18}O (J=1–0) emission line (Umemoto et al., 2017; Kohno et al., 2018). The arrows show the three velocity components at +35 km s^{-1}, +45 km s^{-1} and +55 km s^{-1}. The lowest contour level and contour intervals are 0.06 K degree and 0.03 K degree, respectively.

2.4 Discussion

2.4.1 Velocity components in W33 complex

Kohno et al. (2018) and Dewangan et al. (2020a) reported three velocity components at +35 km s^{-1}, +45 km s^{-1} and +55 km s^{-1} in the W33 region from FUGIN CO survey data [1]. The +35 km s^{-1} and +55 km s^{-1} velocity components exhibit similar spatial distributions (see Figure 6 in Kohno et al., 2018). On the other hand, the +45 km s^{-1} velocity component shows weak emission extended over the wider W33 complex, and its spatial distribution is not exclusively associated with the W33 complex. Kohno et al. (2018) concluded that the +45 km s^{-1} velocity component is unrelated to the star formation activity in W33 complex. Figure 2.5 shows the longitude–velocity diagram using our data and FUGIN ^{12}CO (J=1–0) data [2] integrated over galactic latitudes between $-0.^\circ35$ to $-0.^\circ12$, where contours indicate the NH_3

[1]The +55 km s^{-1} component is reported as +58 km s^{-1} in Kohno et al. (2018), and +53 km s^{-1} in Dewangan et al. (2020a).

[2]http://jvo.nao.ac.jp/portal/nobeyama/

(1,1) main line. The dominant emission in CO and NH_3 is detected at +35 km s^{-1} and gas at this velocity is considered to be a molecular cloud related to the star formation activity in W33.

Figure 2.6 shows the longitude–velocity diagram of the our NH_3 (1,1) data and rotational temperature. In the remainder of this dissertation, we focus on the +35 km s^{-1} velocity component. Figure 2.6 shows that there are three velocity sub-components centered on +35 km s^{-1}. In particular, we can find that NH_3 splits into two velocity components at W33 A (an easternmost component at +34.5 km s^{-1}, and the main component of W33 A at +36.0 km s^{-1}). These components with different velocities give rise to the double-peak profiles at positions shown in Figure 2.2-(a) and have different properties as shown below. From Figure 2.1-(b), the intensity of the satellite lines are differed between the two velocity components, although the peak intensities of the NH_3 (1,1) main line components are approximately the same. It suggests that the optical depths are different in these components since the intensity ratio of the main and satellite lines depends on optical depth. The mean optical depth of each velocity component was 1.39 (+34.5 km s^{-1}) and 1.50 (+36.0 km s^{-1}), respectively. We also investigated temperature differences between these two components. The emission at the +34.5 km s^{-1} is colder than 16 K, while the +36.0 km s^{-1} component is about 18 K. However, within each velocity component, the temperature is almost uniform (Figure 2.5), suggesting there is no direct interaction between these components. In addition, there was no change in the temperature in the region between these two velocity components. We obtained no evidence of interaction such as collisions between these components in our observations. On the other hand, the NH_3 emission associated with W33 Main at $v_{\rm LSR}$ = +35 km s^{-1} is warmer than 20 K and will be discussed further below.

2.4.2 Star formation feedback traced by gas temperature

In Section 2.3.4, we show that the temperature changes more significantly in the W33 complex than in the other physical parameters. In this section, we use the temperature distribution to discuss the influence range of star formation activity.

The rotational temperature in W33 Main is higher than the other sub-components (Figures 2.4-(a) & 2.6). This suggests that embedded

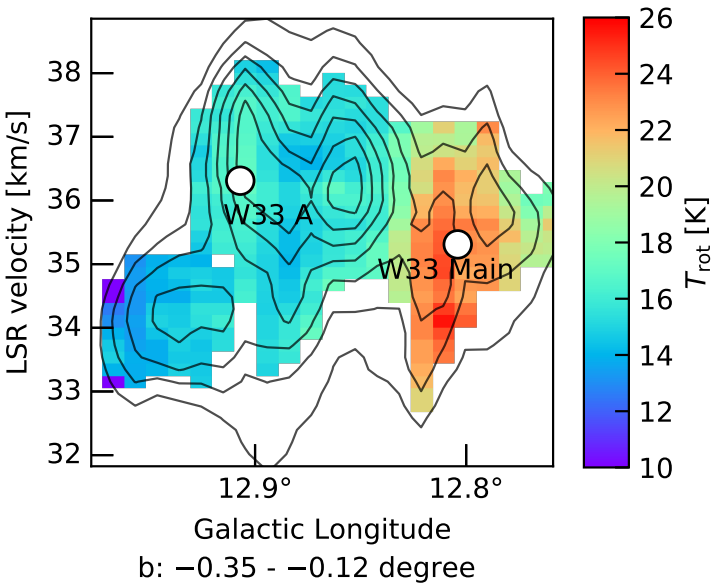

Figure 2.6: The longitude-velocity diagram of the rotational temperature. White circles, lowest contour level and contour interval are the same as in Figure 2.5.

compact HII regions are having an impact on the physical conditions of the surrounding molecular gas. This feature of temperature distribution is also seen in some IRDCs, MYSOs and HII regions (Urquhart et al., 2015; Billington et al., 2019). Previous studies measuring molecular gas temperature have reported that quiescent regions exhibit temperatures of 10 – 15 K, while active star-forming regions associated with massive young stellar objects and HII regions show temperatures higher than 20 K (e.g. Urquhart et al., 2015; Friesen et al., 2017; Hogge et al., 2018; Billington et al., 2019; Keown et al., 2019). In this study, the observation points that measured temperatures higher than 20 K are defined as the region under the influence of star-formation feedback.

Using Figure 2.4-(a), we estimated the size of the influenced area. The projected area showing more than 20 K was estimated from the sum of the grid points (each of $37''.5 \times 37''.5 = 0.19$ pc^2), resulting in a total size of 4.92 pc^2. Its equiareal radius was 1.25 pc. The apparent size of the compact HII region is $12''.6 \times 4''.6$ based on the 5 GHz continuum map obtained by White et al. (2005) with the VLA, which corresponds to 0.15 pc × 0.05 pc at 2.4 kpc. The heated area is several times larger than the compact HII region.

In a previous study by our group, we investigated the size of a molecular

gas cloud affected by the HII region at the edge of the Monkey Head Nebula (MHN) (Chibueze et al., 2013). They reported no apparent impact of the extended HII region of the MHN. However, the molecular gas around the compact HII region S252A has higher temperatures and the size of the heating area was 0.9 pc. We can expect that there may be a relationship between the size of the heating area and the properties of the heating source, although the continuum size of S252A is unknown. To make more certain statements about any possible relationship, observations of more regions are required.

No temperature increase was obtained in W33 A, where the strong NH_3 emission was detected. In several previous studies, a large-scale outflow was reported in the center of W33 A (Galván-Madrid et al., 2010; Kohno et al., 2018). Using ^{12}CO (J=3–2) and (J=1–0) data, Kohno et al. (2018) investigated the intensity ratio, $R_{3-2/1-0}$, for the three velocity components at +35 km s^{-1}, +45 km s^{-1} and +55 km s^{-1}. A high $R_{3-2/1-0}$ was found in W33 A and W33 Main. These results are understood to be due to the outflows from protostellar objects and heating by massive stars (Kohno et al., 2018). However, in our results, the temperature distribution estimated by NH_3 showed no evidence of heating the molecular cloud around W33 A. We consider that gas heating by outflow is not effective, or the size of the gas heated by outflows in W33 A is significantly smaller than our beam size (75″). High-resolution observations may be required to investigate the impact of such stellar feedback in more detail.

2.4.3 Comparison of emission and absorption components

We tried to reproduce the profile shown in Figure 1-(d) using a combination of emission and absorption using a multi-component Gaussian profile with positive and negative peaks for each of the five hyperfine lines in (1,1) and the main line in (2,2). Then we took the peak intensity, linewidth, and central velocity of each hyperfine line as free parameters. Figure 2.7 shows our result for the (1,1) - (3,3) lines. In this result, the peak velocities of both components are consistent within the error.

High angular resolution observations toward W33 Main with the GBT, the Max Planck Institute for Radio Astronomy (MPIfR) 100 -m radio telescope and Very Large Array (VLA) also detected the absorption feature (Wilson et al., 1982; Keto & Ho, 1989; Urquhart et al., 2011). NH_3 gas in front of

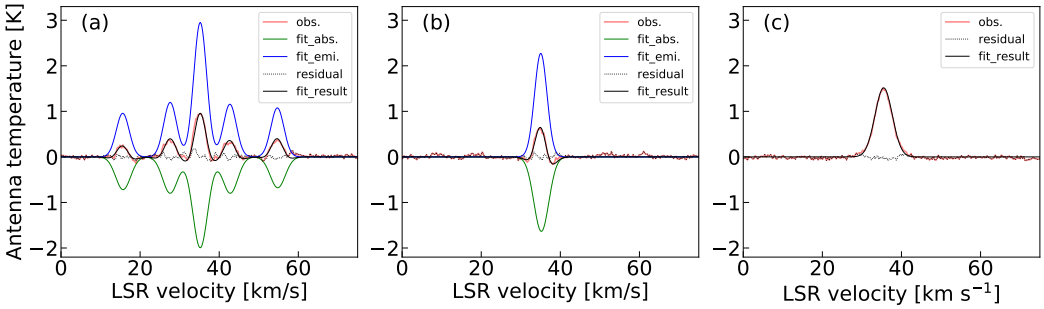

Figure 2.7: The profile in Figure 2.1-(d) is reproduced by a multi-component Gaussian. (a) shows the fit results of the NH_3 (1,1) profile, (b) shows the (2,2) profile, and (c) shows the (3,3) profile. The blue dash-dotted lines, green lines, red lines, and black dashed lines indicate the observed profile, absorption component, emission component, and fitting result profile, respectively. The dotted lines show the residual profile in the same color. Since no absorption feature was found in the (3,3) profile, we apply only an emission component.

a bright continuum source is seen as an absorption feature (e.g. Keto et al., 1987; Henkel et al., 2008). The GBT profile shows the absorption feature more clearly (see Figure A1 of Urquhart et al., 2011). This suggests that the size of the continuum sources is smaller than the beamsize of the NRO 45-m. Interferometric observations of the radio continuum also support our interpretation (e.g. Haschick & Ho, 1983; Immer et al., 2014). However, in the (3,3) line, neither observations with NRO -45m, MPIfR, nor GBT showed an absorption feature. We will discuss this further in the next subsection.

The decomposed line profiles show an interesting property in Figure 2.7. Previous studies in NH_3 lines have reported the combination of absorption and emission lines with different peak velocities such, as a P-Cygni or inverse P-Cygni profiles, in all observed transitions (e.g. Wilson et al., 1978; Urquhart et al., 2011). In W33 Main, the peak velocity of the emission and absorption exhibited consistent velocities within their errors (see NH_3 (1,1) and (2,2) spectra in Figure 2.7). We also compared the line-width of both components (Figure 2.8). The *absorption* components in (1,1) and (2,2) lines show the same line-width as the *emission* in the (3,3) line. Suggesting they originate in the same gas cloud. In many molecular cores, the higher transitions of NH_3 emission lines are thought to be emitted from more compact regions and also show broader line-widths (Urquhart et al., 2011, and see also Section 2.3.2 of this dissertation). Our results may indicate that the absorption component traces more turbulent gas close to the continuum sources.

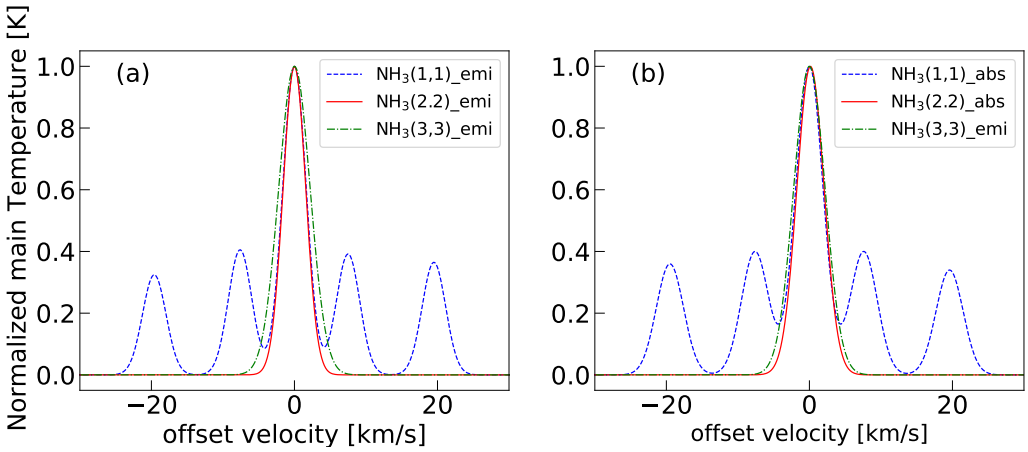

Figure 2.8: Comparison of the emission and absorption components obtained by Gaussian fitting. The horizontal axis indicates the offset velocity from the central velocity of each transition main line. The vertical axis shows the relative intensity normalized by each main line peak. (a) shows the NH_3 (1,1)–(3,3) emission profiles. (b) shows the comparison between the negative-intensity profiles of the absorption components of (1,1) and (2,2), and the positive-intensity profile of (3,3).

Because an absorption feature delineates the physical properties of gas in front of a continuum source, it can be used to can separate the physical properties along the line of sight and within an observed beam. The estimated optical depth and rotational temperature are $\tau = 0.89 \pm 0.10$ and $T_{\rm rot} = 20.9 \pm 0.4$ K in the emission component, $\tau = 0.91 \pm 0.10$ and $T_{\rm rot} = 21.1 \pm 0.4$ K in absorption component. The physical parameters of the two components are the same within the error. This suggests that the physical conditions of NH_3 gas surrounding the continuum sources are the same. Therefore, the HII region located in the center of W33 Main may still be embedded in dense molecular gas with the same motion as the surrounding environment.

2.4.4 Absence of the absorption in NH_3 (3,3)

An absorption feature must be located in front of a continuum background and be affected by its brightness. As mentioned in Section 2.4.3, the continuum source size is smaller than the beamsize of the NRO 45-m. Previous studies have reported objects that show P-Cygni and inverse P-Cygni profiles in all inversion transitions in NH_3 (e.g. Wilson et al., 1978;

Burns et al., 2019). In models assuming a spherically symmetric molecular gas cloud with the continuum source in its center, these features can reveal the expansion or contraction of the gas motion in front of the continuum source. The emission and absorption features of NH_3 (1,1) and (2,2) lines obtained in our observations are detected with the same line-of-sight velocity. However, for the (3,3) transition, only the emission component was detected, without any hint of absorption. We tried to explain all transition profiles in our observations consistently, but failed under the spherically symmetric model after considering the following three possibilities.

An absorption feature requires a bright continuum background. Therefore, we estimated the brightness temperature of the HII region in W33 Main using an electron temperature and emission measure of 7800 K and 1.5×10^6 pc cm^{-6} from observations at 15.375 GHz with the National Radio Astronomy Observatory (NRAO) 140-foot telescope (Schraml & Mezger, 1969). The expected brightness temperature of the continuum emission at our observed frequency, $T_{\rm cont}$, is calculated to be about 6 K which is sufficient to produce an absorption feature. Since the absorption features are detected both in (1,1) and (2,2) lines, and since NH_3 inversion transitions are detected in a narrow frequency range, the continuum brightness temperature is almost the same for all observed NH_3 lines. The value of $T_{\rm cont}$ at the frequency of NH_3 (3,3) is therefore also strong enough to produce an absorption feature.

The spatial distribution of the NH_3 gas observed in the (3,3) line may differ from the other lines. If no NH_3 gas for producing absorption is located in front of the continuum source, we would not observe any absorption feature which contradicts the detection of absorption features at NH_3 (1,1) and (2,2). It is unlikely that the distributions of the same molecular species are vastly different at different excitation levels. Wilson et al. (1982) observed the center of W33 Main with the MPIfR 100-m radio telescope in the NH_3 (1,1), (2,2), (3,3), and (4,4) lines. They detected absorption features only in para-NH_3 lines (see Figure 1 of Wilson et al., 1982). They also failed to explain the absence of absorption in (3,3) line under LTE assumption in all four levels even when considering two molecular clouds with different temperatures.

NH_3 maser emission is another possibility. The NH_3 (3,3) maser has been detected in star-forming regions (e.g. W51: Zhang & Ho (1995); G030.7206–00.0826: Urquhart et al. (2011); G23.33–0.30: Walsh et al. (2011); Hogge et al. (2019)), which has been reported to have a narrow line-width. Wilson et al. (1982) proposed a similar model; only (3,3) in a

state of population inversion. However, this requires coincidental masking of the absorption component by maser emission over the full velocity width, because the (3,3) emission line has a linewidth the same as or broader than the thermal excitation line of NH_3 (1,1) and (2,2) lines as shown in Figure 2.8. Therefore, this possibility is not realistic.

High-angular resolution and high sensitivity multi-transition NH_3 observations are required to investigate an explanatory model in more detail. It should be possible with the Square Kilometre Array (SKA) and next-generation Very Large Array (ngVLA).

2.5 Conclusions

We performed mapping observations toward the W33 massive star-forming region in NH_3 (1,1), (2,2), (3,3) and H_2O maser transitions using the Nobeyama 45-m radio telescope. Our observations detected only a single velocity component around +35 km s^{-1}. NH_3 (1,1) and (2,2) lines are extended over the observed region. From these observations, the distribution of the physical parameters of the dense molecular gas was obtained. Consequently, the molecular gas surrounding the HII region located at W33 Main exhibited a higher temperature (> 20 K) than the rest of the observed area. The size of the influence area is estimated at approximately 1.25 pc. The heating source of the molecular gas is considered to be the compact HII region in W33 Main. Strong NH_3 emission was also detected in W33 A, however, no temperature increase in its molecular gas was obtained.

Molecular gas in front of the compact HII region in W33 Main was detected as an absorption feature. Gaussian fitting of the emission and absorption components reveals that the peak velocities of both components are almost the same. This suggests that the continuum source located in the center of W33 Main may still be embedded in the dense molecular gas. Curiously, the absorption feature was detected only in the NH_3 (1,1) and (2,2) transitions but not in the (3,3) transitions. We tried to explain these NH_3 profiles using spherically symmetric models but concluded that any simple model could not explain the observed profiles in all three transitions towards W33 Main. It is possible that the spatial distributions of NH_3 (3,3) emitted region and the continuum sources may be different.

2.6 A technical description to estimate the physical parameters

2.6.1 The 'CLEAN' procedure for an NH_3 profile

In many investigations using NH_3 the integrated or peak intensity of lines is used to derive the gas physical parameters. However, for objects with velocity structure this procedure may not be ideal because of the non-linearity of the equations in derivation. Therefore, we should estimate the physical parameters in each velocity component at first.

In this subsection, we describe the method used in this dissertation to derive the physical parameters based on the CLEAN algorithm. The CLEAN algorithm was devised by Högbom (1974) and is the most used iterative method to improve radio interferometer images. In general, CLEAN is used in a two-dimensional map with a fixed dirty beam over the whole imaging field. In our method, we assumed that the detected intensities of each channel are a Dirac delta function for each velocity component. However, the NH_3 inversion transition line exhibits a hyperfine structure and the observed five-line intensities depend on the optical depth. We employ the hyperfine structure pattern with an optical depth as the dirty beam for each delta function component.

Our method is composed of the following 6 steps (Figure 2.9).

1. Find the peak intensity and velocity of the main line from the input profile (Figure 2.9, panel (a)). The frequency and corresponding velocity offsets between the NH_3 (1,1) main line to the other four satellite lines are fixed as shown in Table 2.4. This can give the five hyper-fine line intensities (indicated as red points in panel (a)). From this dataset, the four intensity ratios between the main line and satellite

Table 2.4: The velocity offset between the main line and four satellite lines in NH_3 (1,1) (Krieger et al., 2017; Ho & Townes, 1983)

transition	$F_1 = 0 \rightarrow 1$	$F_1 = 2 \rightarrow 1$	$F_1 = 1 \rightarrow 1$ $2 \rightarrow 2$	$F_1 = 1 \rightarrow 2$	$F_1 = 1 \rightarrow 0$
offset [MHz]	0.92	0.61	0	−0.61	−0.92
offset [km s^{-1}]	−19.48	−7.46	0	7.59	19.61

lines are obtained.

2. Estimate the optical depth using each intensity ratio following equation 2.1. To get the optical depth for a single velocity component, we take the median of the estimated four optical depths. (black dots in panel (e)).

3. Using the estimated optical depth and the main line intensity after step (ii) we reproduce the intensity of each satellite line.

4. Subtract the scaled reproduced main and satellite lines from the original profile. We call the scaling factor of the reproduction as a *gain factor* $G < 1$ (indicated as blue bars in panel (b)). This *gain factor* corresponds to the *loop gain* in the CLEAN algorithm. In this dissertation, we adopted a *gain factor* of 0.2.

5. The steps (ii) through (iv) are iterated until one of the five hyper-fine intensities fall below a 3 σ noise level (panel (c)). In one velocity channel, it is typically iterated 3 to 5 times. The resultant profile is used as the *input* profile in step (i). (blue horizontal line in panel (f) shows the median value of the optical depth for a channel).

6. The steps from (i) to (v) are iterated n times for the subtracted profile. We recommend limiting the velocity range to the main line and searching for the peak intensity (which corresponds to the *cleanbox* in the CLEAN). These steps (i) to (v) continue until the peak intensity of the residual main line is below a 3 σ noise level (panel (d)).

Figure 2.9, panels (d) and (g) show the final resulting profile and optical depth of each velocity channel. Using the optical depths and the intensity ratio of NH_3 (1,1) and (2,2) at each velocity channel, the rotational temperature can be estimated.

2.6.2 Error Estimation by the Monte Carlo method

Evaluating the error of observed parameter estimation is important. Although the error is straightforward when calculating the value from direct measurement, an indirect parameter derived through non-linear equations is complicated. Instead of non-linear error propagation analysis, we used a

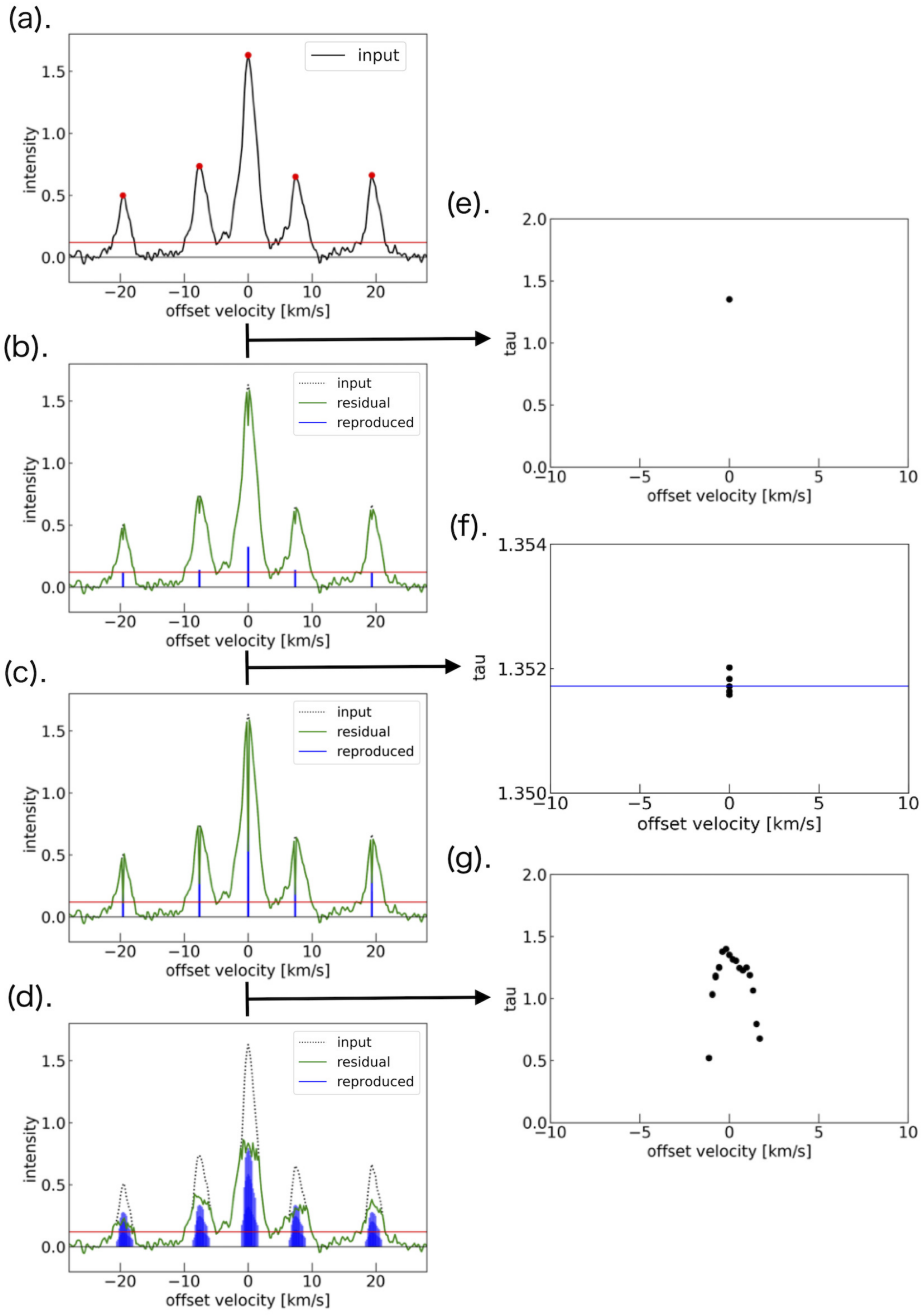

Figure 2.9: The workflow of our method, based on an observation position at (l, b)=(12.801, −0.196). Panel (a) ∼ (d) and (e) ∼ (g) show the profiles, and the estimated optical depth in each step, respectively. The red line in panel (a) ∼ (d) indicates the 3 σ level. Read the main text for further detail.

Monte Carlo method in this dissertation. For the sample data of NH_3 (1,1), we adopt a noise-free Gaussian profile assuming a constant optical depth in the line-of-sight direction. Here, we used an optical depth value of 1.24 (the average value across the W33 complex). The peak intensity of the (1,1) main line was 1.0 (Figure 2.10-(a)). For the (2,2) data, we used a Gaussian profile with half the intensity of the (1,1) emission. Using equation 2.2, the value of the rotational temperature was derived to be 17.83 K adopting $\tau = 1.24$ and $R_{(2,2)/(1,1)} = 0.5$. The line-width of (1,1) and (2,2) profiles were assumed to be the same. We added Gaussian noise ($\sigma_{\rm noise} \simeq 0.04$) to these profiles and sampled 10^5 times.

Figure 2.10-(c) and (d) show histograms of the distributions of the sampled optical depth and rotational temperature, respectively. These distributions are close to Gaussian. (black lines in Figure 2.10-(c) and (d)). The standard deviation of the resultant optical depth and rotational temperatures for samples were 0.092 and 0.330 K, respectively. In this dissertation, we determined the error of these physical parameters were $\pm$ 0.10 and $\pm$ 0.4 K, respectively.

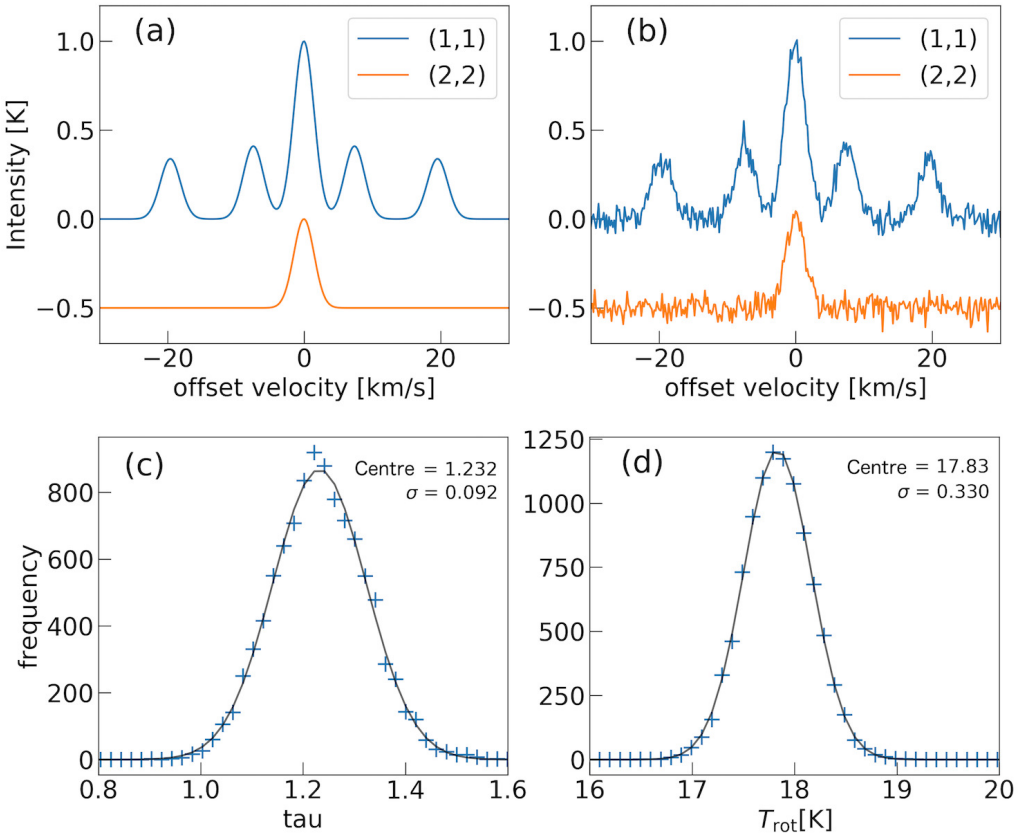

Figure 2.10: The result of error estimate in our method. (a) shows the model profile of NH_3 (1,1) (blue) and (2,2) (orange). (b) shows profiles with Gaussian noise (RMS 0.04 K) added to the model profile shown in panel (a). Panel (c) and (d) indicate the frequency distributions of the optical depth and rotational temperature, respectively. The black line shows the best-fit log-normal function.

Chapter 3

Multi log-normal density structure in Cygnus-X molecular clouds: A fitting for N-PDF without power-law

The contents of this chapter were originally published as a proceeding "The density structure of molecular cloud scales: A fitting for N-PDF with multi log-normal functions" in *Resolving the Rise and Fall of Star Formation in Galaxies. Proceedings of the International Astronomical Union* (Murase et al., accepted.) and a submitted paper "Multi log-normal density structure in Cygnus-X molecular clouds: A fitting for N-PDF without power-law" to *Monthly Notices of the Royal Astronomical Society.* The author changed the layout of the paper to accommodate this dissertation format.

3.1 Introduction

MCs are an important evolutionary stage in star formation scenarios; they contain dense regions directly linked to star formation and diffuse regions (e.g. Larson, 1994, 1995; Stutzki et al., 1998; Elmegreen, 2000). Although gravitational collapse is an essential mechanism, it is still open to evolving from an initial density fluctuation to a dense core; the proposed initial processes are turbulence, self-gravity, and massive star feedback (McKee & Ostriker, 2007).

As mentioned in section 1.2.3, the ρ PDF has been used as a powerful tool to study the density structure of MCs affected by different physical processes (e.g. Vázquez-Semadeni, 1994; Vázquez-Semadeni & García, 2001; Ostriker et al., 2001; Ballesteros-Paredes et al., 2011; Federrath & Klessen, 2013; Federrath et al., 2016; Jaupart & Chabrier, 2020; Khullar et al., 2021). It is determined by the dominant physical processes governing the density structure of MCs; for example, turbulence and self-gravity should give the log-normal distribution and the excess tail, respectively.

Previous observational studies have shown that the N-PDFs of many quiescent clouds are log-normal, whereas those of active star-forming clouds consist of two components: a log-normal and a pronounced power-law tail in the high-density range (e.g. Goodman et al., 2009; Kainulainen et al., 2009; Schneider et al., 2013; Lewis et al., 2022). However, as mentioned in section 1.2.3, it has been pointed out that most MCs in the Milky Way are dominated by turbulence, and the power-law N PDFs are not necessarily related to star formation activity (Ma et al., 2021, 2022).

We highlight that the scale size of structures attributed to the power-law N-PDF is different between observations and numerical simulation studies in order of magnitude (see Section 3.4.1 in detail). Therefore, the "so-called" power-law components of the observed N-PDF may not be of power-law origin. These may be segments of a single log-normal component. Only a few observational studies on N-PDF have used multi-log-normal fitting. Tremblin et al. (2014) have successfully performed a two log-normal plus one power-law tail fitting for N-PDFs of four clouds associated with HII regions using *Herschel* dust continuum data (Motte et al., 2010, 2012). They interpreted the components of an N-PDF as follows: the log-normal in the lowest-density range comes from the turbulence of a molecular gas, the log-normal in the intermediate-density range comes from the compressed area induced by the expansion of the HII regions into the first component, and the power-law tail comes from the gravitationally collapsing cores (Tremblin et al., 2014). However, no investigation of N-PDF using multi-log-normal functions has been performed on MCs in various environments. Are HII regions required to produce the second log-normal of the N-PDF for a MC? Are power-law tails required for an N-PDF, even when we employ multi-log-normal components? To investigate this, we performed an N-PDF study of MCs based on a fit using a multi-log-normal distribution.

Observations of dust continuum emission have been used in N-PDF

studies. However, since a large number of clouds are located near the galactic plane, it is very difficult to study the N-PDF by continuum emission because of the large contamination by foreground and background emission. We made N-PDFs from the molecular line data instead of the dust continuum. This is because the molecular line emission provides kinematic information about the MCs, allowing the separation of overlapping clouds by projection effects.

The remainder of this chapter is organized as follows. First, we describe the decomposition of the molecular line emission into individual clouds and the procedure for creating an N-PDF for each MC (Section 3.3). We present the fit results using the multi-log-normal functions in Section 3.4. Using the fit results, we discuss the relationship between the shape of the N-PDF and the star-forming activity in the interior of a cloud, as well as the parameters that form the N-PDF. In Section 3.5, we summarize our results and conclusions.

3.2 Target and data sets

3.2.1 Cygnus X complex

Cygnus X is a GMC complex in the Milky Way. The distance to the Cygnus X complex based on annual parallax was established as 1.4 kpc using VLBI water maser observations (Rygl et al., 2012). Previous observational studies have conducted large-scale CO surveys (e.g. Schneider et al., 2006, 2007, 2016b; Yamagishi et al., 2018). The total mass of the molecular gas was estimated to be 3×10^6 $M_\odot$ based on observations of ^{13}CO (J=2–1) (Schneider et al., 2006).

The Cygnus X complex contains nine OB associations (Humphreys, 1978). The most active star-forming region, which contains 169 OB stars, is the Cygnus OB2 association located in the center of the Cygnus X complex (Wright et al., 2015). The Cygnus X complex is divided into northern and southern cloud complexes, where the gas masses traced by ^{13}CO (J=2–1) are 2×10^5 $M_\odot$ and 3×10^5 $M_\odot$, respectively (Schneider et al., 2006). In this study, the border between the northern and southern regions of Cygnus X was determined at a galactic longitude of 80°.2, as Takekoshi et al. (2019).

Previous studies have reported that these molecular cloud complexes have different star formation properties (e.g. Schneider et al., 2006, 2007, 2011,

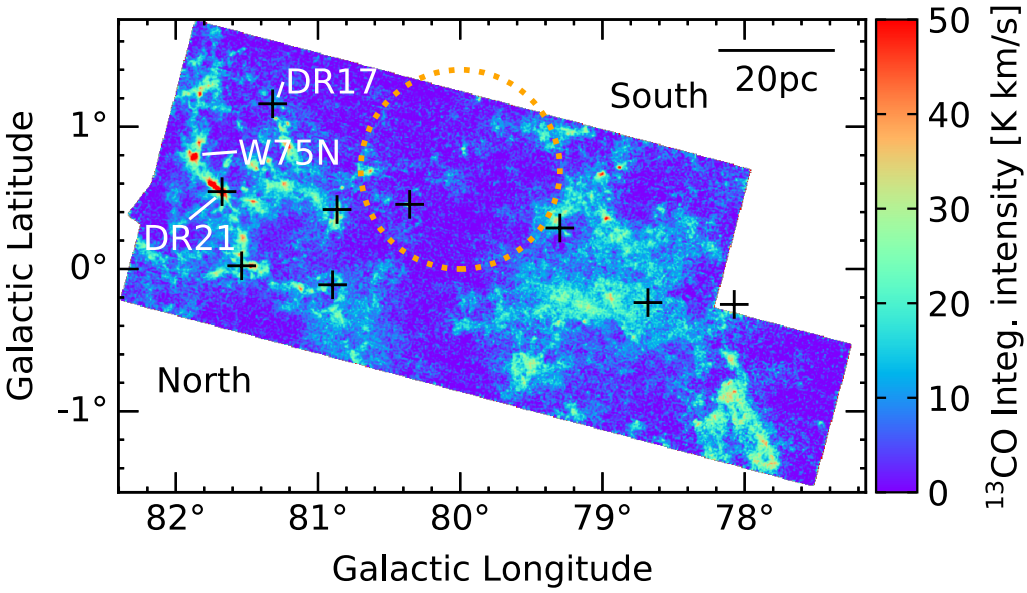

Figure 3.1: Integrated intensity map in ^{13}CO (J=1–0) obtained by the Nobeyama 45-m Cygnus X survey (Yamagishi et al., 2018; Takekoshi et al., 2019). The integrated velocity range is between -20 km s^{-1} and $+20$ km s^{-1}. The orange dashed line indicates the position of the Cygnus OB2 association. Plus marks indicate the positions of 5 GHz radio continuum sources as identified by Downes & Rinehart (1966).

2016b; Yamagishi et al., 2018; Takekoshi et al., 2019). Takekoshi et al. (2019) has investigated the statistical properties of dense clumps associated in both regions using C^{18}O emission. Consequently, they found that the average radius and the velocity dispersion of the dense clumps were similar in both regions. However, the H_2 density was significantly higher in the northern region. This statistical difference suggests a reflection of the star-forming activities in the northern and southern regions (see Figure 4 in Takekoshi et al., 2019).

In the northern part of the Cygnus X complex, many filamentary structures have been identified in dust and molecular gas tracers (e.g. Schneider et al., 2006; Motte et al., 2010; Hennemann et al., 2012; Schneider et al., 2016b,a; Yamagishi et al., 2018, and see also Figure 3.1). In addition, there are well-known star-forming regions such as DR17, DR21, and W75N, which are composed of numerous fragmentary structures and massive dense cores that can form high-mass stars. The southern part of the Cygnus X complex exhibits a diffuse structure (Figure 3.1). Although

the southern part of Cygnus X exhibits weaker star-forming activity than the northern part, the presence of a large amount of molecular gas suggests the possibility of star cluster formation (Schneider et al., 2006; Yamagishi et al., 2018). As described above, the Cygnus X complex contains various star-forming environments. Therefore, this target is suitable for investigating the relationships between the density structure of MCs and star-formation activities.

3.2.2 Data sets

We used ^{12}CO (J=1–0) and ^{13}CO (J=1–0) line data from the Nobeyama 45-m Cygnus X CO Survey[1] (hereafter, Cygnus X Survey) (Yamagishi et al., 2018; Takekoshi et al., 2019). These data were obtained using a multi-beam receiver, FOur-beam REceiver System on the 45-m Telescope (FOREST; Minamidani et al., 2016) and a Spectral Analysis Machine for the 45-m telescope (SAM45; Kuno et al., 2011; Kamazaki et al., 2012). Figure 3.1 shows the integrated intensity map of ^{13}CO (J=1–0). The observation area was 9 deg^2 by connecting 1 $\times$ 1 deg^2 mosaic submaps, which covered the Cygnus X north and south regions, as well as the Cygnus OB2 association. The On-The-Fly (OTF) mapping scan parameters were the same as those of the FUGIN survey (Umemoto et al., 2017). The effective angular resolution of the data cubes was 46″, which corresponded to 0.31 pc at 1.4 kpc. The velocity resolution was 0.25 km s^{-1}. The Cygnus X Survey data were calibrated using the main beam temperature ($T_{\rm mb}$). The typical noise levels of ^{12}CO and ^{13}CO data were 0.88 K and 0.36 K in $T_{\rm mb}$ scale, respectively. More detailed information on the observations and data reduction are described in Yamagishi et al. (2018).

To investigate the distributions of dense molecular cores and radio continuum sources, we used the C^{18}O core catalog obtained from the Cygnus X Survey (Takekoshi et al., 2019) and the radio continuum source catalog of the Red Midcourse Space Experiment (MSX) Source (RMS) survey (Urquhart et al., 2009), respectively. Urquhart et al. (2009) performed continuum observations at 4.86 GHz toward the RMS sources with the Very Large Array (VLA). There were 38 radio continuum sources identified within the observation area of the CO data used in this study, which were classified as compact or ultra-compact HII regions. The mean size of these radio

[1]The data sets are publicly available at https://cygnus45.github.io

continuum sources was $2'' \times 1''$, which corresponded to 0.014 pc $\times$ 0.007 pc at 1.4 kpc.

3.3 Analysis and results

3.3.1 Identification of molecular clouds in ^{13}CO data

Because ^{13}CO lines generally trace molecular cloud structures better than ^{12}CO lines (e.g. Umemoto et al., 2017; Li et al., 2018; Ma et al., 2021), we decomposed the molecular line intensity map into individual MCs from ^{13}CO data cube using DENDROGRAM (Rosolowsky et al., 2008) and SCIMES (Colombo et al., 2015) algorithms. In this study, we used the `astrodendro` Python-based package to analyze the dendrograms of the emission line intensity cube. DENDROGRAM is an algorithm that constructs a tree representing a hierarchy of structures comprising a trunk, branches, and leaves (for more information on the DENDROGRAM algorithm, see Rosolowsky et al., 2008). This algorithm requires three input parameters: the `min_value`, `min_delta`, and `min_npix`. Here, `min_value` is a threshold to distinguish between line emission and noise, `min_delta` represents the threshold for separating two 'leaves', and `min_npix` is the minimum number of pixels to identify an individual 'leaf' structure. We set `min_value` $= 3\sigma$ and `min_delta` $= 2\sigma$, where σ is the RMS noise level of the ^{13}CO data. We also set `min_npix` $= 64$, corresponding to $4 \times 4 \times 4$ pixels along each of the position-position-velocity (PPV) space.

Next, we applied SCIMES using the output of the DENDROGRAM algorithm. SCIMES is an algorithm that identifies clustered structures (see Colombo et al. (2015) in detail). This analysis used the 'volume' as a clustering criterion for the SCIMES algorithm. The outputs from SCIME are PPV mask cubes of the identified clustered structures and a catalog containing the physical information of each clustered structure. In this dissertation, we call the clustered structure identified by SCIMES an 'individual cloud'.

Based on DENDROGRAM and SCIMES analyses, 131 clustered structures were identified. However, seven compact clusters (extracted area $<$ 100 pixels, corresponding to 1.5 pc^2) located at the edge of the map were excluded as noise structures because they were affected by bad channels in

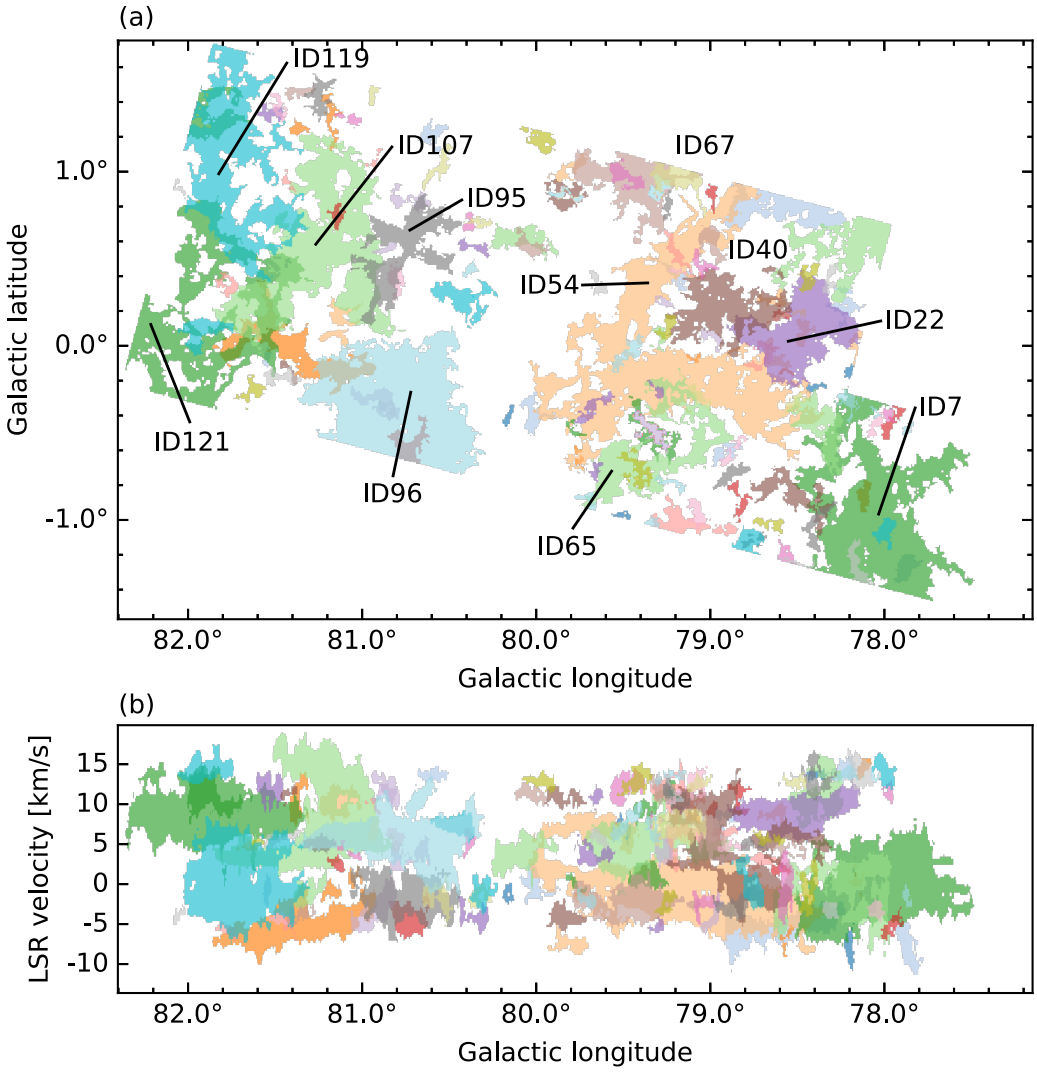

Figure 3.2: ^{13}CO emission segmentation performed using DENDROGRAM and SCIMES algorithms. (a) *l*-*b* space map and (b) *l*-*v* space map. Each color shows an individual identified cloud. The segmentation maps use the same color scheme in panels (a) and (b). ID indicates clouds with an extract projected area over $\sim$ 4000 pixels.

Table 3.1: Cloud parameters identified using SCIMES.

ID	l [deg.]	b [deg.]	$v_{\rm LSR}$ [km s^{-1}]	σ_v [km s^{-1}]	$S_{\rm exact}$ [pix.^{2}]
7	78.063	−1.009	−0.15	2.34	14202
22	78.479	+0.105	+8.63	1.30	5915
40	78.916	+0.223	+4.06	4.58	4492
54	79.235	−0.036	−0.16	2.92	21290
65	79.400	−0.636	+4.68	1.48	5631
67	79.457	+0.938	−2.32	1.08	3937
95	80.776	+0.511	−1.97	1.40	4231
96	80.801	−0.337	+5.48	1.74	13787
107	81.243	+0.621	+7.89	4.90	14139
119	81.734	+0.964	+0.11	3.04	11051
121	81.839	+0.255	+8.65	1.66	12211

Notes: Only a small portion of this table is provided here; the full table is shown in Table A.1.

the map-making process. Hence, 124 clustered structures were identified as MCs. We present the resulting decomposition of the ^{13}CO data cube in Figure 3.2. The cloud properties are summarized in Table 3.1.

3.3.2 Deriving column density maps and N-PDFs

We estimated the column density of ^{13}CO (J=1–0) based on the assumptions that the MCs are under local thermodynamic equilibrium (LTE) with ^{12}CO (J=1–0) and the beam filling factors of both lines are unity. We estimated the excitation temperature $T_{\rm ex}$ in K using the following equation:

$$T_{\rm ex} = 5.53 \Big/ \ln\left(1 + \frac{5.53}{T_{\rm mb}^{\rm peak}(^{12}{\rm CO}) + 0.819}\right), \tag{3.1}$$

where $T_{\rm mb}^{\rm peak}(^{12}{\rm CO})$ is the ^{12}CO peak intensity in K for each pixel, which was derived from

$$T_{\rm MB} = J_{12}(T_{\rm ex}) - J_{12}(T_{\rm CMB}), \tag{3.2}$$

where $J_{12}(T)$ is the brightness temperature in the Rayleigh-Jeans approximation of radiation from a body with temperature T at the ^{12}CO (J=1–0) frequency, and $T_{\rm CMB}$ = 2.7 K is the temperature of the cosmic background

radiation. We assumed $T_{\rm ex}$ was uniform along the line-of-sight (LoS). At this $T_{\rm ex}$ in K, we estimated the optical depth of ^{13}CO at velocity v, $\tau_v(^{13}{\rm CO})$, using the following equation:

$$\tau_v(^{13}{\rm CO}) = -\ln\left[1 - \frac{T_{\rm mb}(^{13}{\rm CO})/5.29}{1/\{e^{5.29/T_{\rm ex}} - 1\} - 0.164}\right], \tag{3.3}$$

which was derived from

$$T_{13} = (J_{13}(T_{\rm ex}) - J_{13}(T_{\rm CMB}))\,(1 - e^{-\tau(^{13}{\rm CO})}), \tag{3.4}$$

where $J_{13}(T)$ is the brightness temperature at ^{13}CO (J=1–0) frequency. From the velocity-integrated optical depth to the column density $N(^{13}{\rm CO})$ in cm^{-2}, we used the following equation:

$$N(^{13}{\rm CO}) = 2.42 \times 10^{14} \frac{T_{\rm ex} + 0.88}{1 - e^{-5.29/T_{\rm ex}}} \int \tau_v(^{13}{\rm CO}) dv, \tag{3.5}$$

where v is in km s^{-1}. This was derived from Einstein's coefficient model with CMB and LTE assumption for all ^{13}CO excitation levels. Note that we used the ^{12}CO data cube applied to the PPV mask cube obtained from ^{13}CO because the shapes of the spectra of ^{12}CO and ^{13}CO are generally similar (e.g. Heyer & Dame, 2015; Umemoto et al., 2017; Li et al., 2018; Takekoshi et al., 2019). Here, Eq. (3.1) assumes that the ^{12}CO emission is optically thick. The estimated $N(^{13}{\rm CO})$ was converted into the molecular hydrogen column density, $(N({\rm H_2}))$, assuming the relative abundances of $[^{12}{\rm C}/^{13}{\rm C}] = 70$ (derived from local ISM in Wilson & Rood, 1994) and $[{\rm H_2}/^{12}{\rm CO}] = 1.1 \times 10^4$, derived from the Taurus molecular cloud (Pineda et al., 2010). Consequently, we used $[{\rm H_2}/^{13}{\rm CO}]$ abundance of 7.7×10^5 in this study. Note that the resultant N-PDF shifts only along the abscissa if the abundance value is different.

To obtain an accurate N-PDF, we chose 11 clouds with an extracted projected area of over $\sim$ 4000 pixels, i.e., 0.4 deg^2. We show the optical depth, excitation temperature, column density map, and N-PDF of one of the 11 clouds in Figure 3.3. In Figure 3.3-(a), most areas were found to be optically thin ($\tau(^{13}{\rm CO}) < 0.5$) and some pixels were optically thick ($\tau(^{13}{\rm CO}) > 1$). Such pixels with large optical depth may refer to clumps and cores. The influences on the N-PDF are considered to be small because of the small surface fraction of the cloud. The median optical depth of each cloud ranged

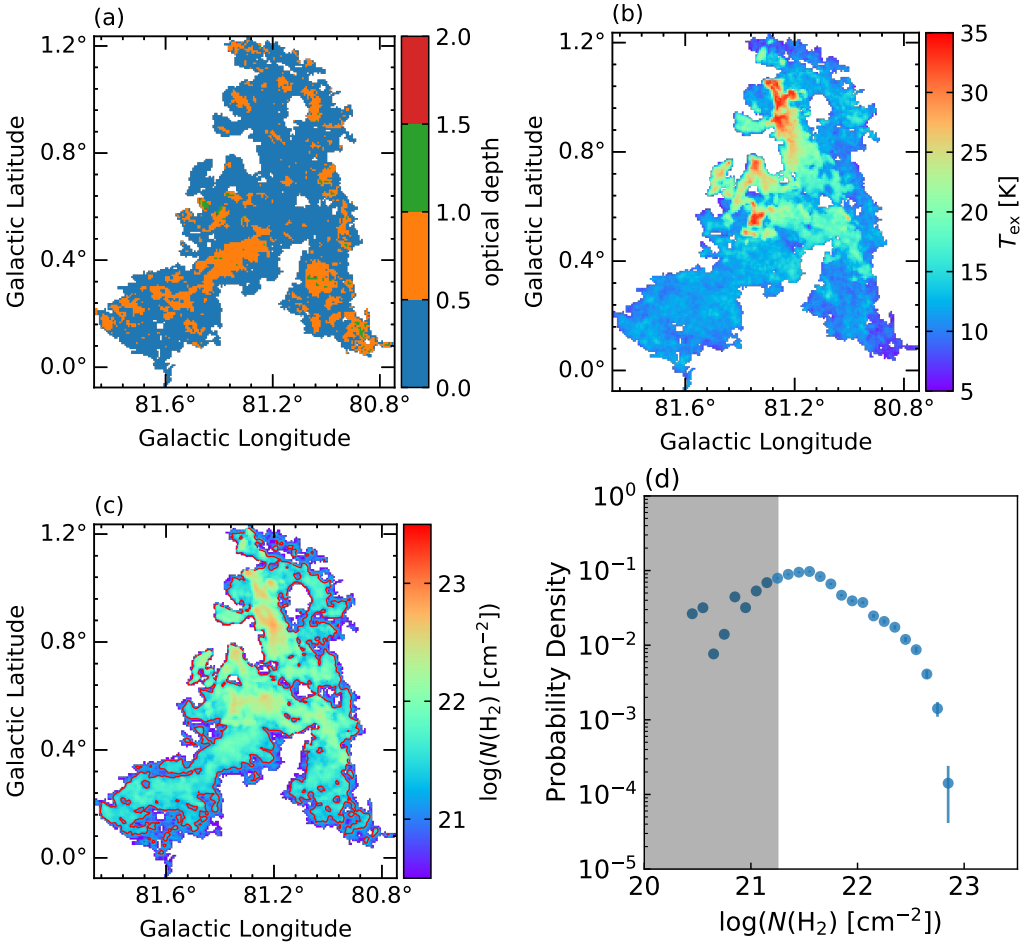

Figure 3.3: The optical depth, excitation temperature, column density maps of ID107 cloud and its N-PDF. (a) Optical depth map. The colors indicate the optical depth in increments of 0.5. (b) Excitation temperature map obtained from ^{12}CO (J=1–0) line. (c) H_2 column density map (see column density maps of other selected clouds in Figure 3.5). The red contour indicates the completeness limit of H_2 column density ($\log(N(H_2)) = 21.25$) for the ID107 cloud. (d) N-PDF is derived from the H_2 column density map of the panel (c). The gray-shaded areas correspond to column densities out of the completeness limit.

from 0.3 to 0.5 (Column 2 in Table 3.2). Figure 3.3-(b) shows the excitation temperature map. The range of excitation temperature was between 4 and 33 K. We can find that regions with relatively high temperatures ($T_{\rm ex}$ > 25 K) are concentrated. Such regions are considered to be star formation regions (e.g. Urquhart et al., 2014; Murase et al., 2022). We summarized the physical parameters of the 11 clouds in Table 3.2.

Schneider et al. (2015b) reported that the size of bins and angular resolution did not affect the N-PDF parameters (e.g. mean column density and width). In this study, we used a bin size of 0.1 dex. To obtain the correct N-PDF, it is necessary to consider the completeness limit of the column-density map. Alves et al. (2017) have recommended that the completeness limit is determined by the lowest closed contour of the column density map (see also Lombardi, Marco et al., 2015; Körtgen et al., 2019). Therefore, we manually determined the completeness limit of the column density map for each cloud. As a result, we found the contours at $\log(N(\mathrm{H_2}))$ = 21.25, which are indicated by the red contours in Figure 3.3-(c), was almost closed. The clouds near the edge of the observation area had almost closed contours at $\log(N(\mathrm{H_2}))$ = 21.5. It should be noted that the completeness limit has to be set to a higher column density for a column density map that includes the edge of the observation area. Even though the contour at the completeness limit was not completely closed, the effect on the PDF shape was considered small because the number of pixels contained in the column density bin around the completeness limit was large (see Figure 3.4). Five out of the eleven clouds were detached from the edge of the observation area and had closed boundaries (Column 12 in Table 3.2). It supports us in making an appropriate N-PDF fitting, as shown in the next subsection.

On the other hand, it should be noted that MCs that contain the edge of the observation area do not have correct N-PDFs due to missing samples (see also Alves et al., 2017). This effect is seen in the N-PDFs of ID7, ID96, and ID119 clouds in the low-density range. Furthermore, we found a cutoff feature in the N-PDF of ID119 cloud at $\log(N(\mathrm{H_2}))$ > 23. The ID119 cloud contains an active massive star-forming region DR21. In such a region, local heating or photodissociation by UV radiation from the star-forming activity can have a significant influence on the CO abundance (Ripple et al., 2013). For these reasons, the ID119 cloud is not used in the following discussion.

At low temperature (T < 20 K) and high volume density ($n(\mathrm{H_2})$ > 10^4 $\mathrm{cm^{-3}}$) regions, such as the infrared dark clouds (IRDCs), the abundance of

CO molecules in the gas phase is affected by adsorption effects on the dust grains (e.g. Willacy et al., 1998; Tafalla et al., 2002). However, Hernandez & Tan (2011) reported that the ratio of the mass surface density obtained from ^{13}CO (J=1–0) and dust extinction observations at IRDC is approximately constant.

3.3.3 Fitting the N-PDFs with multi log-normal distributions

We found that some of the N-PDFs of our clouds had excess from a single log-normal distribution. Although the densest plots exhibited a steeper decline, the excess component of the N-PDFs was not straight but had a curvature on the log-log plane (Figure 3.4). In this study, we fitted the N-PDFs with multi-log-normal distributions. The N-PDFs were fitted to the following equation:

$$p(N) = \sum_{i=1} \frac{p_i}{\sqrt{2\pi}\sigma_i} \exp\left(\frac{-(\log N - \log \bar{N}_i)^2}{2\sigma_i^2}\right), \tag{3.6}$$

where $\bar{N}_i$ is the mean column density of each log-normal distribution. The first component ($i = 1$) is the lowest density log-normal distribution, and the following components ($i > 1$) correspond to higher column density log-normal distributions. We first performed the fitting using a single log-normal and then increased the log-normal components for MCs with significant residuals. All parameters of the N-PDFs were fitted using the least-squares method (Levenberg Marquardt algorithm) from the `astropy.modeling` module for Python (Astropy Collaboration et al., 2013, 2018). The best-fit curves and parameters of all N-PDFs of the clouds are shown in Figure 3.4 and Table 3.2.

We found that the N-PDF could be well-fitted using one or two log-normal distributions (Figure 3.4). The adjusted coefficient of determination, R_f^2, for each N-PDF was above 0.95. Low-density and high-density log-normal distributions were referred to as LN1 and LN2, respectively. In this nonlinear fitting analysis, we set the initial value of the parameter $\bar{N}_1$ to be around the peak value of the low-density component and that of $\bar{N}_2$ to be $\log(N(\mathrm{H_2})) = 22.5$. We confirmed that the fitting result was insensitive to the initial values of $\bar{N}_1$ and $\bar{N}_2$. The column density map of each cloud indicates that the size of the high column density region ($\log(N(\mathrm{H_2})) > 22.5$), which mainly forms

LN2, was $\sim 1 - 5$ pc (see Figure 3.5).

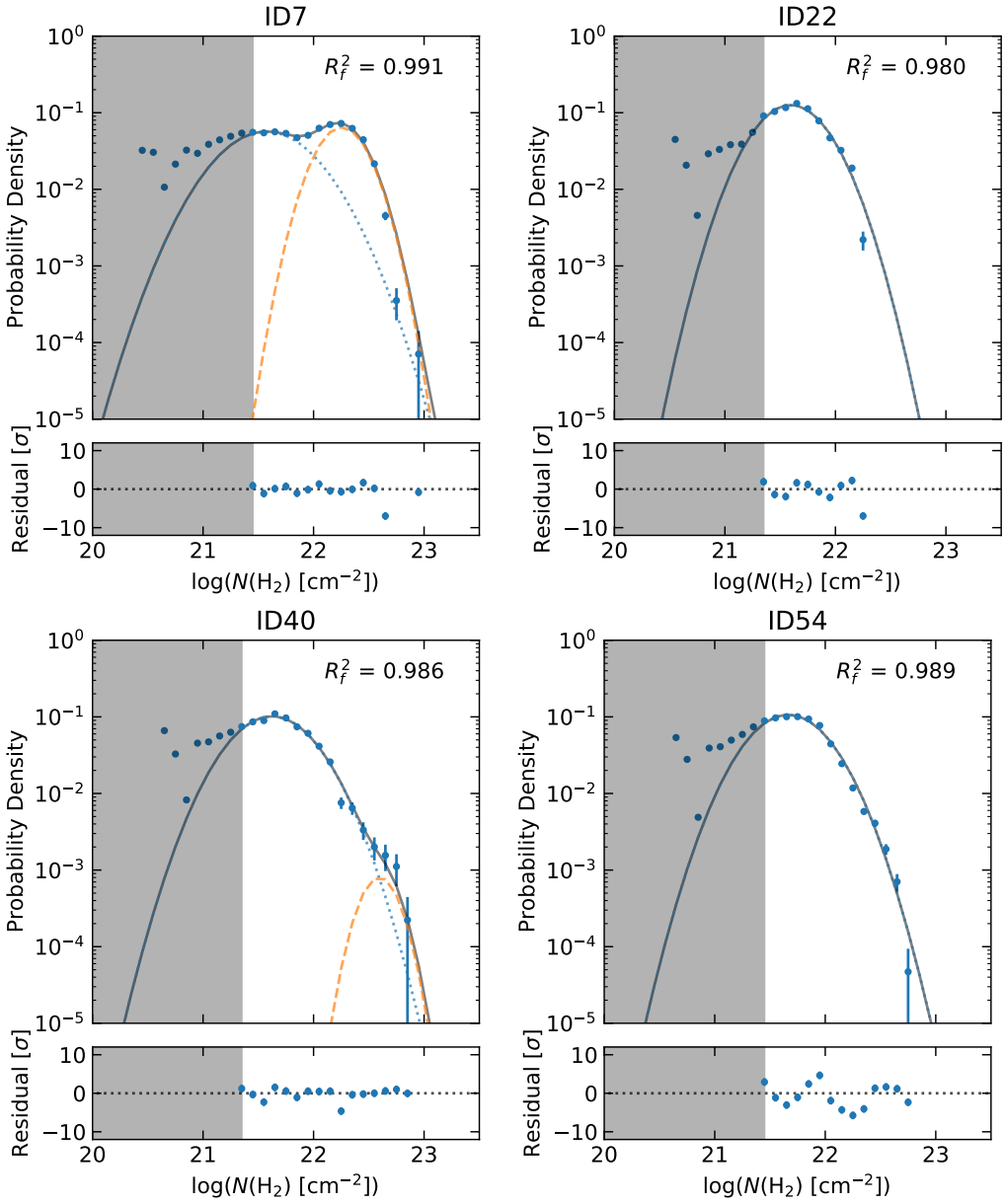

Figure 3.4: N-PDFs and their best-fit curves for all clouds. The blue dotted curves and orange dashed curves indicate the low-density and high-density components, respectively. The black curve is the sum of the two log-normal distributions. The error bars were estimated using Poisson statistics. The adjusted coefficient of determination (R_f^2) for the fitting is shown in each panel of the figure. The gray shaded area corresponds to column densities out of the completeness limit. The sub-panels at the bottom of each panel are the residuals of the fitting. The vertical axis is the Poisson noise at each bin.

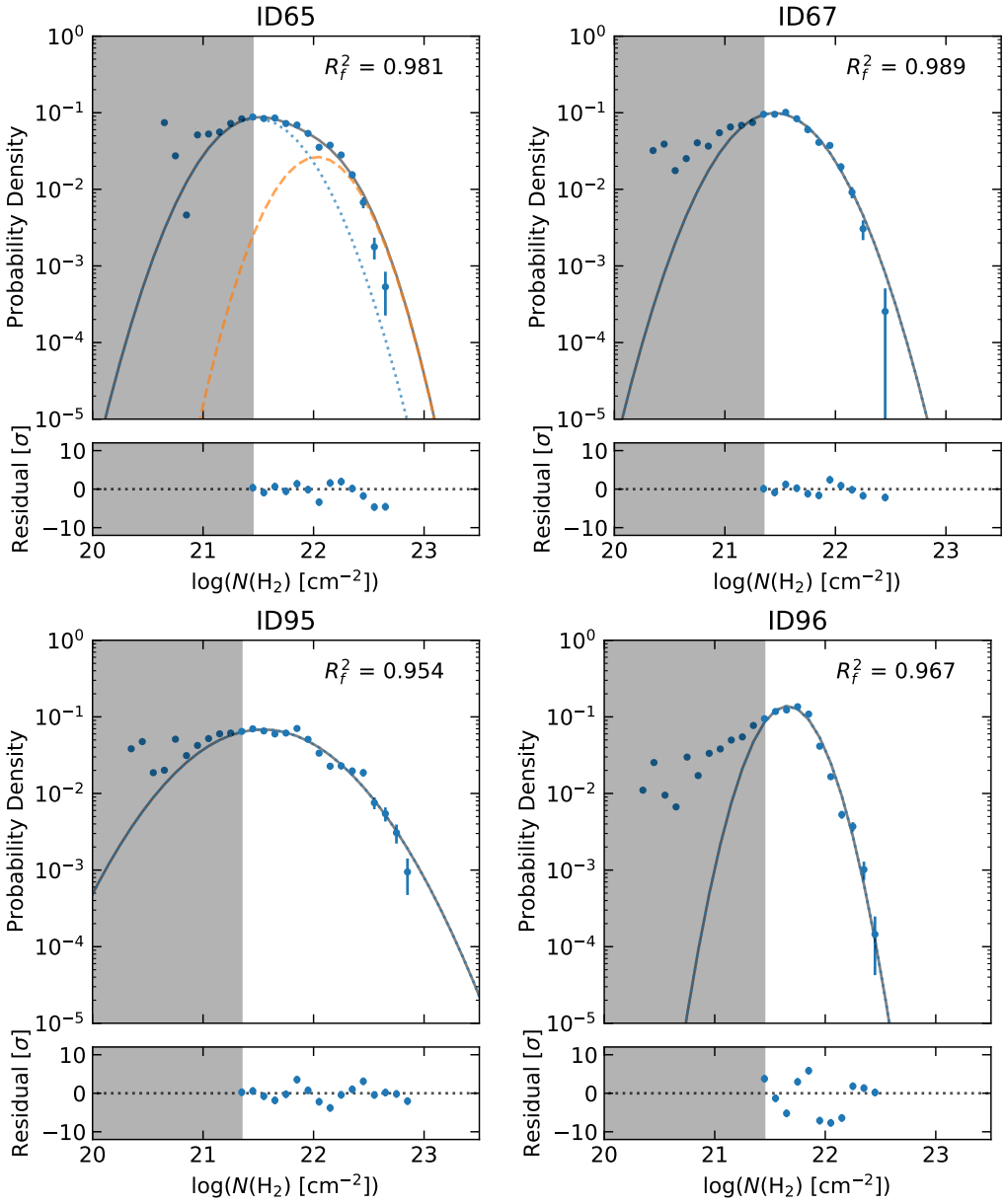

Figure 3.4: *continued*

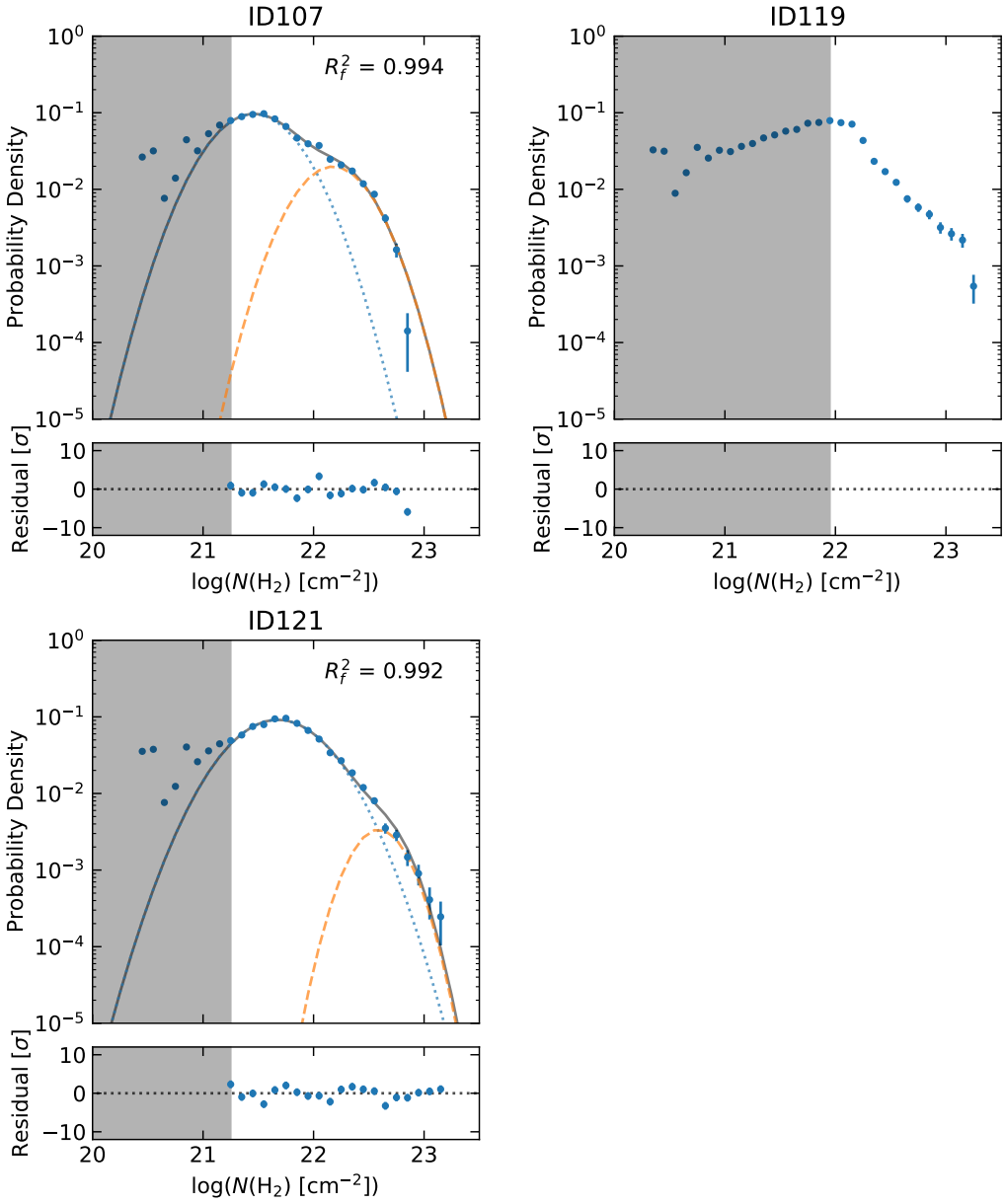

Figure 3.4: *continued*

Table 3.2: Cloud properties and N-PDF fitting parameters of all selected clouds.

ID	$\tau(^{13}\mathrm{CO})^{a}$	$T_{\mathrm{ex,median}}$ [K]	N($C^{18}O$ clump)[b]	p_1	$\bar{N}_1$	σ_1	p_2	$\bar{N}_2$	σ_2	region	Edge
7	0.325	14.94	32	0.051	21.57	0.352	0.032	22.25	0.194	South	Y
22	0.382	12.64	10	0.085	21.60	0.268	–	–	–	South	N
40	0.417	12.41	2	0.080	21.62	0.312	< 0.001	22.60	0.148	South	N
54	0.469	11.62	28	0.085	21.65	0.316	–	–	–	South	Y
65	0.394	13.32	5	0.076	21.51	0.353	0.009	22.12	0.225	South	N
67	0.373	10.55	2	0.080	21.45	0.322	–	–	–	South	Y
95	0.288	13.62	7	0.084	21.54	0.490	–	–	–	North	N
96	0.384	10.74	9	0.073	21.66	0.211	–	–	–	North	Y
107	0.362	12.06	13	0.074	21.46	0.302	0.013	22.17	0.261	North	N
119	0.304	16.16	19	–	–	–	–	–	–	North	Y
121	0.314	14.44	14	0.082	21.68	0.359	0.001	22.70	0.148	North	Y

[a] The median optical depth from ^{13}CO data.
[b] The $C^{18}O$ clumps were identified by Takekoshi et al. (2019).

3.4 Discussion

3.4.1 Absence of power-law distribution

In this section, we discussed the observed N-PDF shapes. Why do our clouds not present a power-law tail? We focused on the size of structures that exhibit power-law tails.

Ma et al. (2021) obtained the N-PDFs for 40 clouds identified in the Milky Way Imaging Scroll Painting (MWISP) project (Su et al., 2019). They reported that power-law tails are formed from structures approximately 1 pc in size. In contrast, Chen et al. (2018) reported that the power-law tail of the N-PDF was the sum of the N-PDFs of the sub-structures inside the MC. The spatial size of these sub-structures was approximately 0.5 pc. This structure size which formed a power-law tail is also supported by numerical studies (e.g. Chen et al., 2018; Khullar et al., 2021). We can consider that the size of the structure forming the power-law component is less than 1 pc from previous N-PDF studies. Here, it should be noted that the N-PDF analysis requires a pixel resolution of one order of magnitude better than the size of the structure to be discussed because each N-PDF requires approximately 10^2 pixels. For dense and compact structures that form power-law tails to affect statistics, such as PDF, we consider that a spatial resolution of 0.01 pc is required. Therefore, the spatial resolution of the Cygnus X Survey data ($\sim$ 0.3 pc) is too poor to discuss the spatial structures and their background mechanism in the high-density regime of the N-PDF.

In this analysis, it is impressive that the N-PDFs obtained from the molecular gas tracer could be well-fitted with one or two log-normal distributions. This means that the "power-law" component reported in previous observational studies could be the second component of our study. This result suggests an alternative density structure of MCs based on the conventional picture (see Section 3.4.3).

3.4.2 Relation between N-PDF and star-forming activity

Previous studies have suggested that the shape of the N-PDF is related to its star-forming activity in the interior of the MC (e.g. Kainulainen et al., 2009; Pineda et al., 2010; Ballesteros-Paredes et al., 2011; Schneider et al., 2013;

Tremblin et al., 2014; Lombardi, Marco et al., 2015; Ma et al., 2021; Lewis et al., 2022). In this section, we discussed the shape of the N-PDFs and star-forming activity using MCs with mainly closed boundaries. We investigated the relationship between the shape of the N-PDFs and star-forming activity by comparing the column density and spatial distributions of high-density clumps and radio continuum sources in each cloud. The following three cases were considered:

Figure 3.5 shows the center positions of the $C^{18}O$ clumps identified by Takekoshi et al. (2019), superimposed on each column density map. These clumps were classified as prestellar and starless cores, which are indicated by circles and crosses in the figures, respectively. Column 4 in Table 3.2 shows the number of associated $C^{18}O$ clumps for each cloud. We found no simple correlation between the number of $C^{18}O$ clumps associated with MCs and the shape of the N-PDF. The ID40 and ID65 clouds had an excess component in the high-density range. However, these clouds had a few $C^{18}O$ clumps. In contrast, the ID22 and ID54 clouds had more $C^{18}O$ clumps than the ID40 and ID65 clouds, although its N-PDF had a single log-normal distribution.

Next, we investigated the relationship between the N-PDF and star-formation activity in each cloud. In addition to the positions of the $C^{18}O$ clumps, the positions of the continuum sources identified by Urquhart et al. (2009) are shown on each column density map as indicators of high-mass star formation (square marks in Figure 3.5). These continuum sources have been classified as compact and ultra-compact HII regions. The ID40, ID65, and ID107 clouds shown in Figure 3.5 indicate LN1 plus LN2 shape. However, there were no continuum sources associated with the clouds at ID40 and ID65. In addition, the ID107 cloud shows a poor positional correlation between the high-density region and the continuum sources. It suggests that both clouds have only a weak correlation between high-density regions and star-forming activity. The reverse cases are found. The ID95 cloud showed only a single log-normal N-PDF, even though the continuum sources were located in high-density regions. The ID54 cloud, in which many prestellar cores are located, also exhibited a single log-normal. Therefore, we suggest that there is little relationship between the star formation activity and N-PDF.

We then investigated the relationship between the star formation stages of the molecular cloud complexes and the N-PDFs of the MCs contained within them. We found no correlation between the star formation stage of the molecular cloud complexes and the density structures of the MCs. As

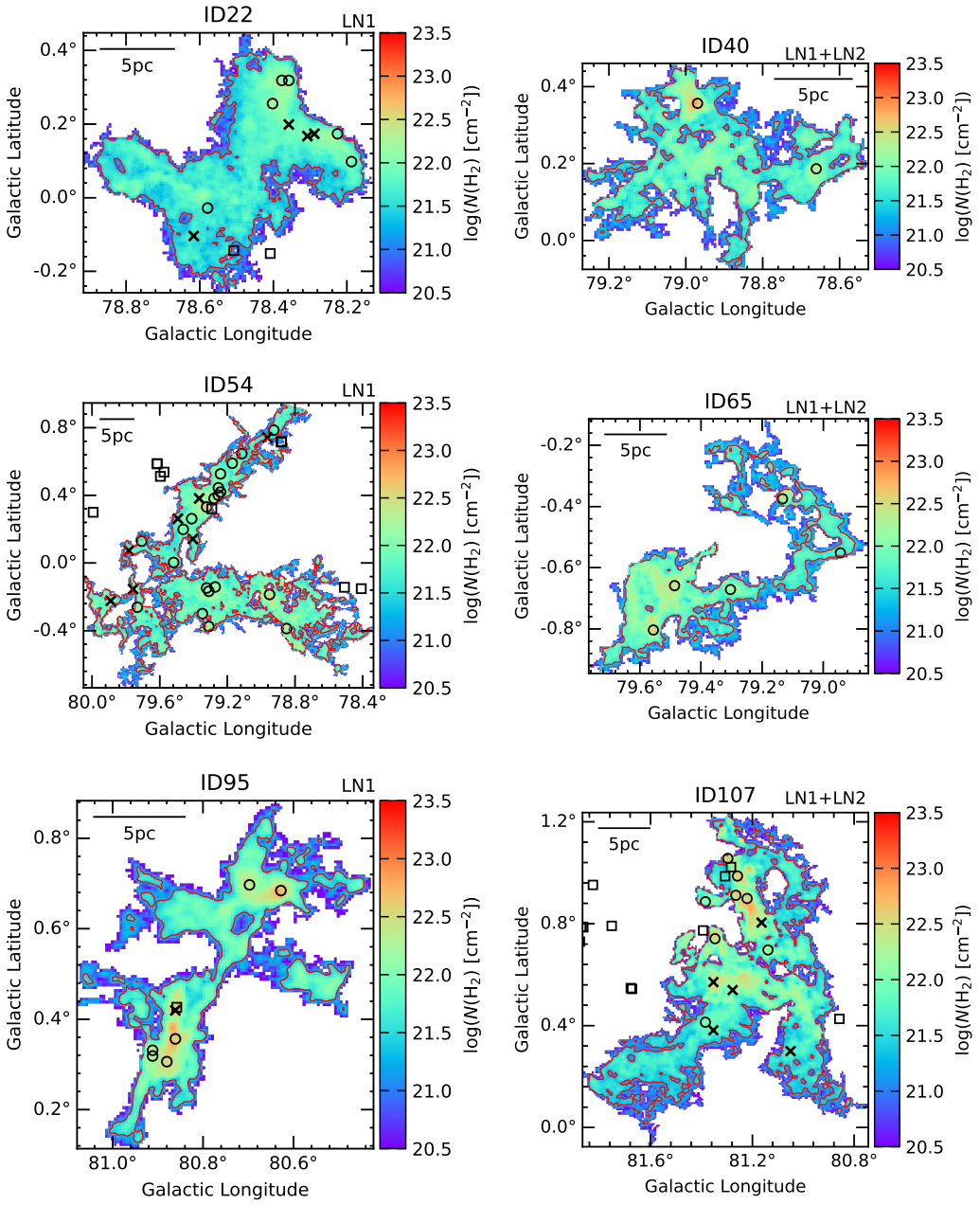

Figure 3.5: H_2 column density maps of some clouds in our sample. The red contour indicates the completeness limit. The circles and crosses indicate the positions of the prestellar and starless cores identified by Takekoshi et al. (2019) from $C^{18}O$ intensity maps, respectively. The square marks indicate the center positions of the radio continuum sources obtained by Urquhart et al. (2009).

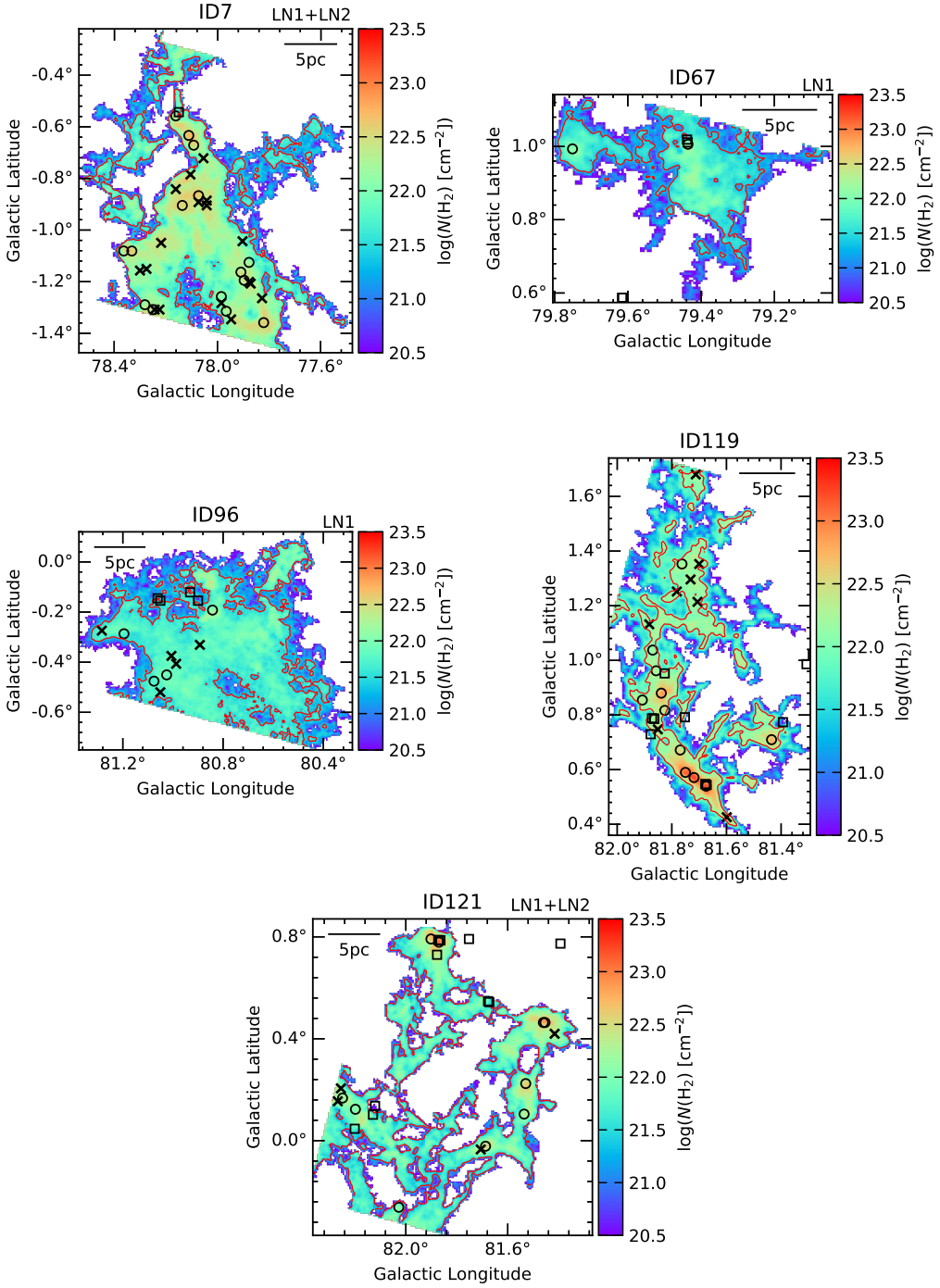

Figure 3.5: *continued.* H_2 column density maps of other selected clouds. The red contour indicates the completeness limit. These clouds include the edge of the observation area.

mentioned in Section 3.2.1, the Cygnus X complex has been reported to exhibit different star-forming stages in the northern and southern regions. Table 3.2 presents a molecular cloud complex and the N-PDF parameters to which the identified cloud belongs. In this study, the number of N-PDFs with excess components was almost the same in both regions. In addition, the log-normal N-PDF parameters (e.g. mean column density and width of log-normal distribution) of the clouds obtained in Section 3.3.3 exhibited no prominent differences in both northern and southern complexes (see Section 3.4.3 for details).

In conclusion in Section 3.4.2, we found that the shape of the N-PDF is not necessarily related to star formation activity. Although more investigations are needed to obtain more robust results, we consider the N-PDF reflects the relationship between the density structure and the turbulent structure of the MC.

3.4.3 Hierarchical density structure in molecular clouds

We performed a statistical investigation of the N-PDF using the fitting parameters of the N-PDF shown in Section 3.3.3. In this study, we focused on the correlation between the surface fraction and width of the log-normal distribution with the mean column density.

Panels (a) and (b) of Figure 3.6 show the best-fit curves for LN1 and LN2, respectively, obtained from our clouds. In these panels, we found that ten clouds had peak column densities of $\sim 10^{21.5}$ cm^{-2} for LN1 and one (ID119) had $10^{22.01}$ cm^{-2} ; LN2 exhibited various curves (Table 3.2). This suggests that the physical properties of LN1 are universal and independent of the molecular cloud characteristics.

Panels (c) and (d) of Figure 3.6 show the correlation plots of the N-PDF parameters. Circles and squares indicate LN1 and LN2, respectively. To evaluate the effect of the completeness limit, we used closed and open symbols for closed and unclosed contours at the completeness limit, respectively (see Section 3.3.2). Figure 3.6-(c) shows the correlation between the mean column density and surface fractions of the log-normal components for each cloud. We found that the higher mean column density shows a smaller fraction. This is consistent with the hierarchical spatial and density structures in a MC (e.g. Larson, 1994; Stutzki et al., 1998; McKee & Ostriker, 2007). Figure 3.6-(d)

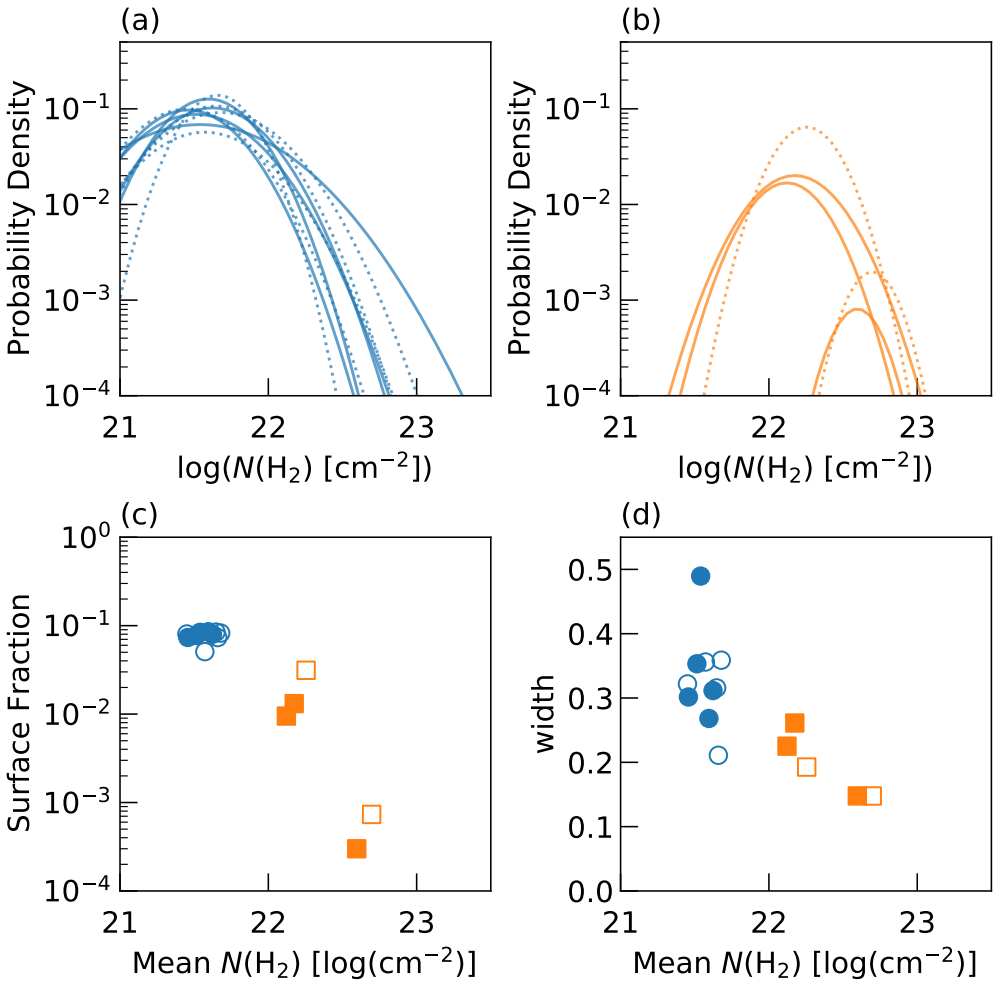

Figure 3.6: Fitting results of N-PDFs of our clouds. Panels (a) and (b) indicate the best-fit curves for the LN1 and LN2 shown in Figure 3.4, respectively. The solid lines and dotted lines indicate the completeness limit contours were closed and the other clouds, respectively. Panels (c) and (d): correlation diagrams between the mean column density and surface fraction, and (d) between the mean column density and half-width of LN components, respectively. The blue circles and orange squares indicate LN1 and LN2, respectively. The filled symbols indicate the clouds of which the completeness limit contours were closed, and the open symbols indicate the other clouds.

shows the correlations between the mean column density and the widths of LN1 and LN2. All plots of LN1 show a large dispersion by a factor of 2.3 (from 0.211 to 0.490) along the width axis. The plots for the closed contour clouds show a similar dispersion by a factor of 1.83 within a 0.16 dex range of the peak column density. In contrast, the plots of LN2 show systematically smaller widths than LN1, which were narrower than 0.27. Through both components, we found a systematic correlation: a component with a larger peak density had a narrower width.

The two correlations shown in Figure 3.6 suggest that a component with higher density has a smaller volume fraction and weaker turbulence within each structure. Previous observational studies have reported that interstellar matter has a hierarchical structure consisting of small dense regions within a less dense and larger envelope. It is not a single stage, but many layers over a wide range of scales from kpc to sub-pc (e.g. Falgarone et al., 1991; Blitz, 1993; Larson, 1994; Armstrong et al., 1995; Larson, 1995; Stutzki et al., 1998; Elmegreen, 2000; Williams et al., 2000; Elmegreen & Scalo, 2004; Chepurnov & Lazarian, 2010). In addition to this spatial hierarchical structure, we found a turbulence hierarchical structure at the cloud scale (Figures 3.4 and 3.6).

What is the origin of these log-normal components? Numerical simulations have been performed to investigate the thermal evolution of a multiphase ISM with supersonic turbulence (Kobayashi et al., 2022). They found that the shocked inhomogeneous ISM exhibited density distribution functions composed of several log-normal distributions with different peak densities and widths corresponding to different temperature ranges (see also Figure 4 in Kobayashi et al., 2022). The spatial structure induced by thermal instability has also been reported. It has dense cold clumps with weak turbulence embedded in diffuse warm interclump gas dominated by stronger turbulence. However, it should be noted that the density and temperature ranges observed in this study were different from the numerical simulations, such that Kobayashi et al. (2022). They focused on MCs during the early evolutional stages when HIgas still dominated.

As noted in Section 3.4.1, it is unclear why the density structures of MCs can be fitted only by two log-normal distributions. To clarify this, observational studies with higher spatial resolution using various ISM probes and numerical simulations of the multiphase ISM at later evolutional stages are required.

3.5 Conclusions

We investigated the N-PDF based on molecular emission lines using the Nobeyama 45-m Cygnus X CO survey data. Using the DENDROGRAM and SCIMES algorithms, MCs were identified, and the N-PDF properties were investigated for extended clouds (> 0.4 deg^2). The main results of this study are as follows:

1. We found that the N-PDFs obtained from ten out of the eleven selected clouds could be well-fitted with one or two log-normal distributions. However, it should be kept in mind that star formation activity in the interior of MCs has a significant impact on the CO abundance, especially for low-J transitions of CO isotopes.

2. We found that the shape of the N-PDF in cloud scale had less correlation with the star-forming activity in the interior of the MC.

3. From the fitting of the N-PDFs, we found that LN1 had almost the same mean column density ($\sim 10^{21.5}$ cm^{-2}) regardless of the features of the individual cloud.

4. We found the correlations between the parameters which characterize the N-PDFs. The width of the log-normal distribution decreased as the mean column density of the structure increased. This tendency implies that the turbulence inside the structure weakened when the mean column density increased.

Although the statistical results are not robust, the log-normal distribution in the low-density part (LN1) exhibited common physical properties, regardless of the molecular cloud characteristics. The LN2 indicated different properties depending on the MC. These results are interesting for studying the scale from MCs to star-forming cores.

Chapter 4

Multi log-normal density structure in the Milky Way mid-plane molecular clouds

To discuss the dependence of the column density structure of MCs on the Galactic environment, we studied MCs on the Galactic plane in the first quadrant of the Milky Way using the N-PDF approach described in Section 3.3.3. We used the data from the FUGIN survey, one of the Nobeyama 45-m legacy projects. In this chapter, we present the results of the study conducted during the span of the Ph.D. dissertation.

4.1 Data set

We analyzed data from the ^{12}CO (J=1–0) and ^{13}CO (J=1–0) lines obtained from the FUGIN survey[1], one of the legacy projects of the Nobeyama 45-m telescope (see Umemoto et al., 2017, for a full description). The FUGIN survey was conducted from March 2014 to April 2017. The observation area covered the first quadrant ($10^\circ \leq l \leq 50^\circ$, $|b| \leq 1^\circ$) and the third quadrant ($198^\circ \leq l \leq 236^\circ$, $|b| \leq 1^\circ$) of the galactic plane and was observed in the On-The-Fly mapping mode (Sawada et al., 2008). The submap size was $1^\circ \times 1^\circ$. In this survey, the J = 1–0 transitions of ^{12}CO (115.271202 GHz), ^{13}CO (110.201354 GHz), and C^{18}O (109.782176 GHz) were observed

[1]The data sets are publicly available at http://jvo.nao.ac.jp/portal/nobeyama/fugin.do

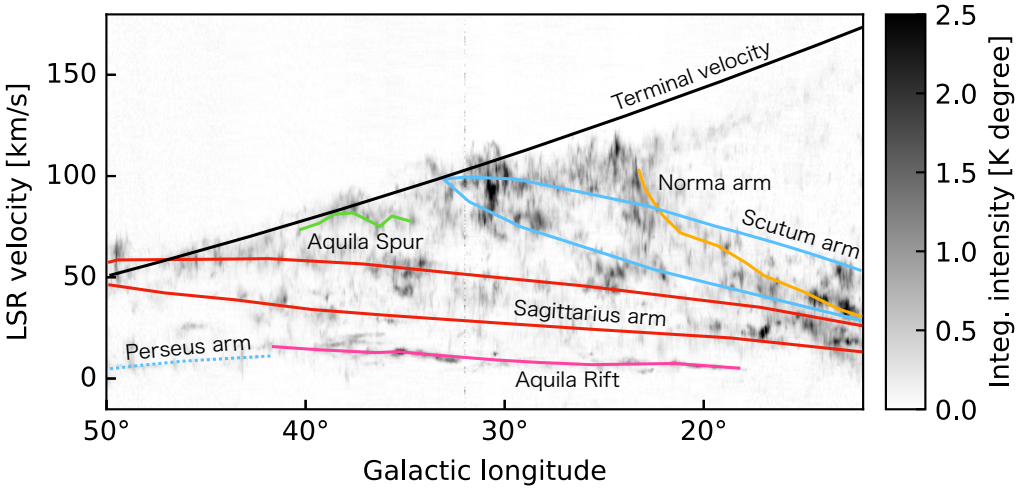

Figure 4.1: Longitude–velocity map in ^{13}CO (J=1–0) datacube for the FUGIN survey analyzed in this dissertation. The galactic longitude range is between l = 12° and l = 50°. The integration range in b is ± 1°. The colored lines indicate the spiral arm at the first quadrant (Reid et al., 2016). The solid black curve shows the terminal velocities. The vertical feature around l = 32° are the spurious structures.

simultaneously. The ^{12}CO line traces molecular gas with a density of approximately 10^2 cm^{-3}, including diffuse regions of MCs, and the ^{13}CO and C^{18}O lines are optically thin, tracing molecular gas with a density of $10^3 \sim 10^4$ cm^{-3} (Scoville & Solomon, 1974; Goldreich & Kwan, 1974; Scoville, 2013). Thus, this unbiased survey allows us to simultaneously analyze the structure of both diffuse and dense gas in MCs. These CO data were obtained using a multi-beam receiver, the FOREST (Minamidani et al., 2016) and a SAM45 (Kuno et al., 2011; Kamazaki et al., 2012). In this analysis, we used data sets obtained in the first quadrant of the galactic plane ($10° \leq l \leq 50°$, $|b| \leq 1°$). The longitude-velocity map of the contiguous ^{13}CO data was shown in Figure 4.1.

The effective angular resolution of the published data is 20″ and 21″ for ^{12}CO and ^{13}CO, respectively, and the velocity resolution is 1.3 km s^{-1}. The spatial and velocity grid sizes are 8″.5 and 0.65 km s^{-1}, respectively. The absolute intensity calibration was performed using $T_{\rm mb} = T_a^*/\eta_{\rm mb}$ with main beam efficiencies of 0.45 ± 0.02 and 0.43 ± 0.02 at 110 GHz and 115 GHz, respectively. The relative intensity uncertainties are 10% ∼ 20% for ^{12}CO and ∼ 10% for ^{13}CO based on observations of the standard source M17 SW

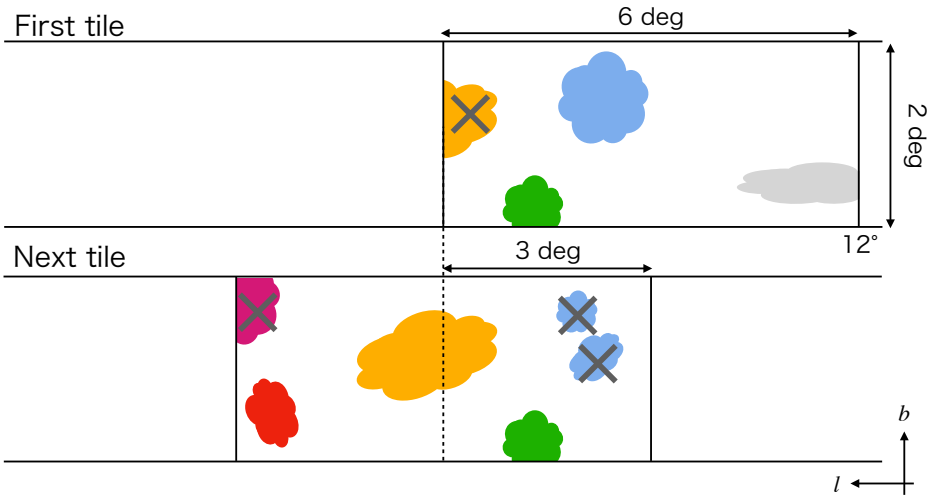

Figure 4.2: Schematic representation of the procedure for deciding cloud from the two overlapping 6° × 2° tiles. In this figure, individual clouds were shown in different colors. The black vertical solid line indicates the edge of each tile. Any clouds at the longitudinal edge were excluded because their boundaries were not closed. The clouds containing longitude edges (l = 12° and l = 50°) were exceptions.

(Umemoto et al., 2017). The published CO data suffer from scan effects. To remove this feature and improve sensitivity, the datacubes were smoothed by convolving with a 2-D Gaussian function to achieve a spatial resolution of 40″. The grid size was resampled to 17″. The smoothed RMS noise levels ranged from 0.5 to 0.8 K and 0.2 to 0.3 K for ^{12}CO and ^{13}CO, respectively.

4.2 Analysis and Results

4.2.1 Making input files and Decomposition of the line emission into individual cloud

Before identifying MCs, we created 12 tiles of 6° × 2°, shifted by 3° on the galactic longitude axis, using MONTAGE[2] software. We ran the DEN-

[2]MONTAGE is funded by the National Science Foundation under Grant Number ACI-1440620, and was previously funded by the National Aeronautics and Space Administration's Earth Science Technology Office, Computation Technologies Project, under Cooperative Agreement Number NCC5-626 between NASA and the California Institute of Technology.

DROGRAM (Rosolowsky et al., 2008) and SCIMES (Colombo et al., 2015) algorithms on relatively small datacubes because it would be computationally expensive (and memory intensive) to generate dendrograms from a single full FUGIN datacube and run the SCIMES analysis.

As in Section 3.3.1, we performed cloud identification on the ^{13}CO datacubes using the DENDROGRAM and SCIMES algorithms. The datacube from $l = 10°$ to $l = 12°$ had a large variation in thermal noise levels for each $1° \times 1°$ sub-map. To identify structures with consistent criteria throughout, this region ($10° \leq l \leq 12°$) was excluded from our analysis. Although the spatial smoothing effectively eliminated the scan effect, the feature remained in some regions. This effect is expected to be stronger in relatively weak emitting regions. Therefore, the parameters used in DENDROGRAM were set to `min_value` $= 5\sigma$, `min_delta` $= 2\sigma$, and `min_npix` $= 64$.

We adopted 'volume' as the clustering criterion for the SCIMES algorithm. To handle overlapping cluster structures appearing in adjacent tiles, we adopted a method similar to that used by Colombo et al. (2019) and Duarte-Cabral et al. (2021). Figure 4.2 shows the schematic representation of our method for deciding cluster structures from the overlapping tiles. We first exclude structures that contain the edge of a tile on the longitude axis, because the cluster structure boundary is not closed. We retain the larger clouds when overlapping or splitting structures between two overlapping tiles. However, we made an exception for structures containing the first ($l = 12°$) and last ($l = 50°$) longitude edges. Finally, to obtain a robust N-PDF, we extracted cluster structures with a projected area larger than 4000 pixels. As a result, we obtained 96 cluster structures identified as MCs. We present the decomposition of the ^{13}CO datacubes in Figures 4.3 and 4.4. The properties of the identified clouds are summarized in Table 4.1.

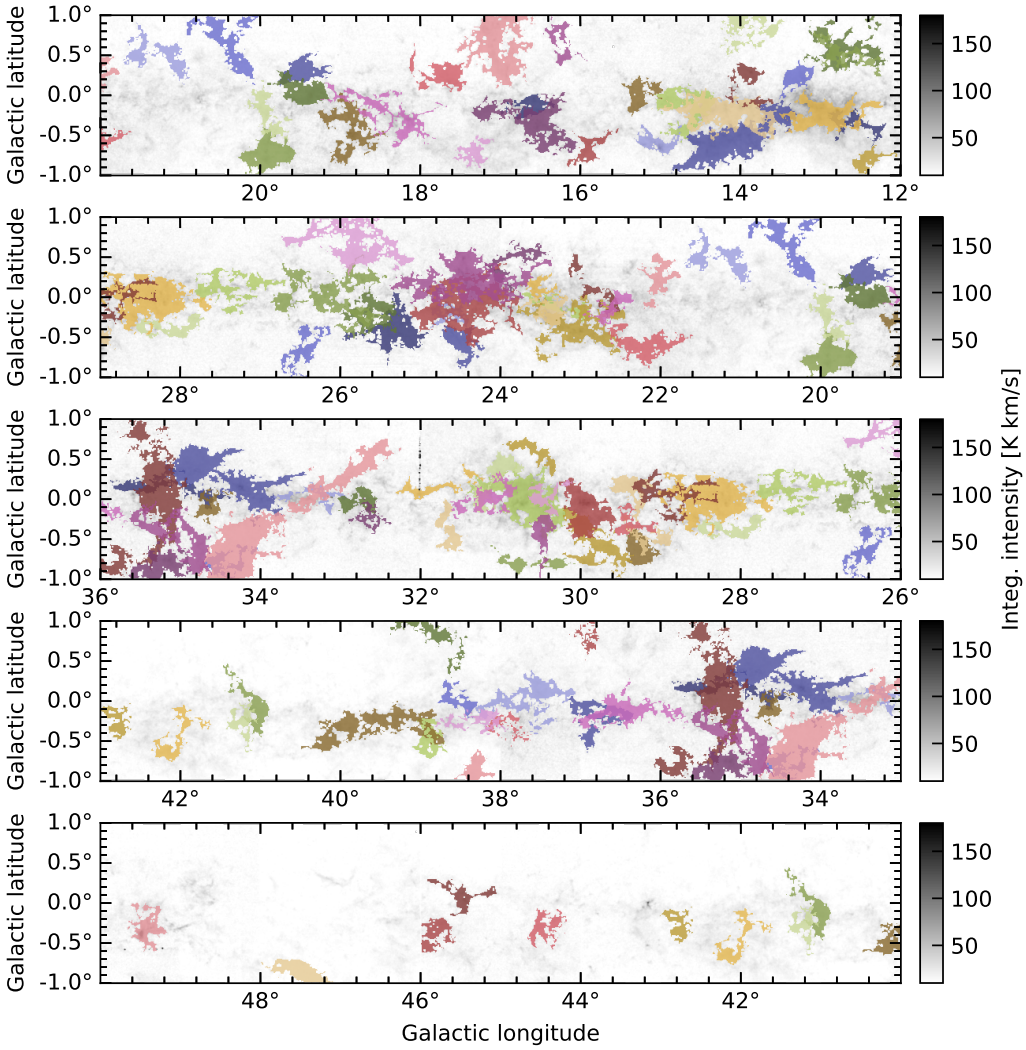

Figure 4.3: The spatial distribution map of the resulting decomposition of the ^{13}CO datacubes using the DENDROGRAM and SCIMES algorithms. The gray scale shows the integrated intensity map of ^{13}CO (J=1–0) with the integrated velocity range of -100 km s^{-1} $\sim$ $+200$ km s^{-1}. The color shows the individual cloud masks with a projected area of over 4000 pixels. The vertical feature at $l = 32°$, $0° \leq b \leq 1°$ are the spurious structures.

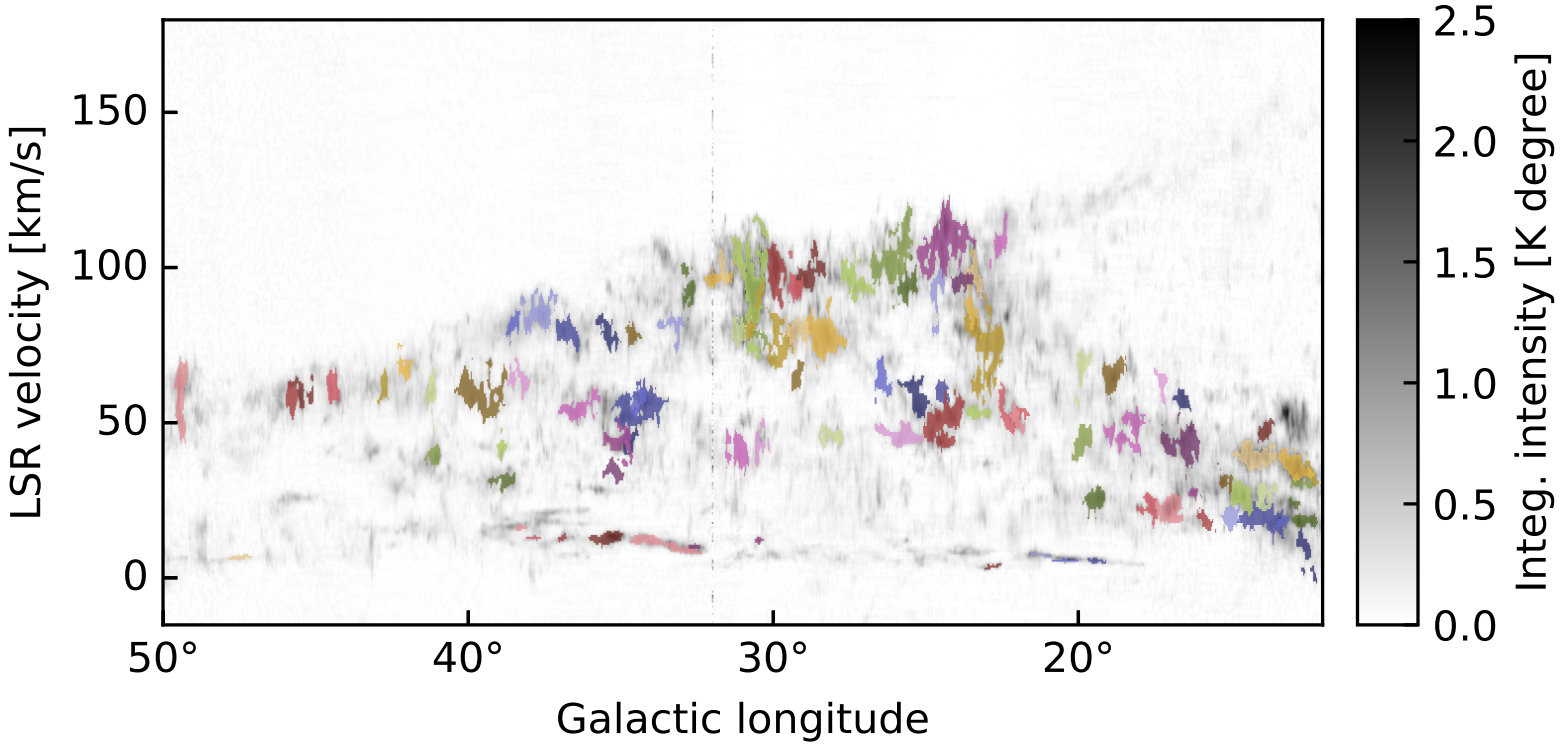

Figure 4.4: Longitude–velocity map of the resulting decomposition of the ^{13}CO datacubes using DENDROGRAM and SCIMES algorithms. The gray scale shows the ^{13}CO integrated intensity (Figure 4.1). The integration range in b is $\pm$ 1°. Identified molecular clouds use the same color scheme in Figure 4.3.

Table 4.1: Cloud parameters identified using SCIMES.

Source name	l [deg.]	b [deg.]	$v_{\rm LSR}$ [km s^{-1}]	$\tau_{^{13}\rm CO}$ [a]	$T_{\rm ex}$ [a] [K]	$S_{\rm exact}$ [pix.^{2}]
FGN12.405–0.814	12.405	−0.814	+34.15	0.479	11.67	4047
FGN12.589–0.358	12.589	−0.358	+8.58	0.431	10.05	6084
FGN12.711+0.549	12.711	+0.549	+19.32	0.406	14.61	14375
FGN12.738+0.497	12.738	+0.497	+31.34	0.520	10.72	7755
FGN12.943–0.260	12.943	−0.260	+36.39	0.550	15.46	19723
FGN13.315+0.207	13.315	+0.207	+18.33	0.375	15.52	4835
FGN13.910+0.160	13.910	+0.160	+47.46	0.392	12.24	5938
FGN13.916+0.817	13.916	+0.817	+26.80	0.407	9.59	9705
FGN14.083–0.543	14.083	−0.543	+20.00	0.367	16.97	26297
FGN14.226–0.210	14.226	−0.210	+39.50	0.483	15.05	22290
...	...	...	...	...	...	...
FGN39.614–0.327	39.614	−0.327	+60.30	0.404	10.43	20686
FGN41.093–0.072	41.093	−0.072	+39.25	0.417	9.53	7176
FGN41.211–0.252	41.211	−0.252	+59.49	0.334	12.38	5160
FGN42.063–0.472	42.063	−0.472	+68.21	0.464	9.64	7517
FGN42.785–0.252	42.785	−0.252	+61.81	0.438	9.72	4534
FGN44.458–0.286	44.458	−0.286	+61.59	0.611	8.96	6227
FGN45.446+0.085	45.446	+0.085	+59.53	0.450	10.91	5460
FGN45.805–0.355	45.805	−0.355	+58.62	0.966	7.12	6042
FGN47.489–0.849	47.489	−0.849	+7.05	0.525	8.94	6901
FGN49.424–0.328	49.424	−0.328	+58.44	0.422	14.59	7132

Notes: The source name starts with "FGN" and is named in the Galactic coordinates of the molecular cloud. Only a small portion of this table is provided here; the full table is shown in Table B.1.

[a] The median value of the optical depth and the excitation temperature.

4.2.2 Physical parameters of extended molecular clouds

The statistical properties of MCs provide knowledge about their dependence on the Galactic environment and the processes that control the evolution of molecular clouds (e.g. Williams et al., 1994; Dame et al., 2001; Ballesteros-Paredes & Mac Low, 2002; Yoda et al., 2010; Dobbs et al., 2014; Colombo et al., 2019; Duarte-Cabral et al., 2021; Spilker et al., 2021). In this section, we derive the physical parameters of the identified clouds.

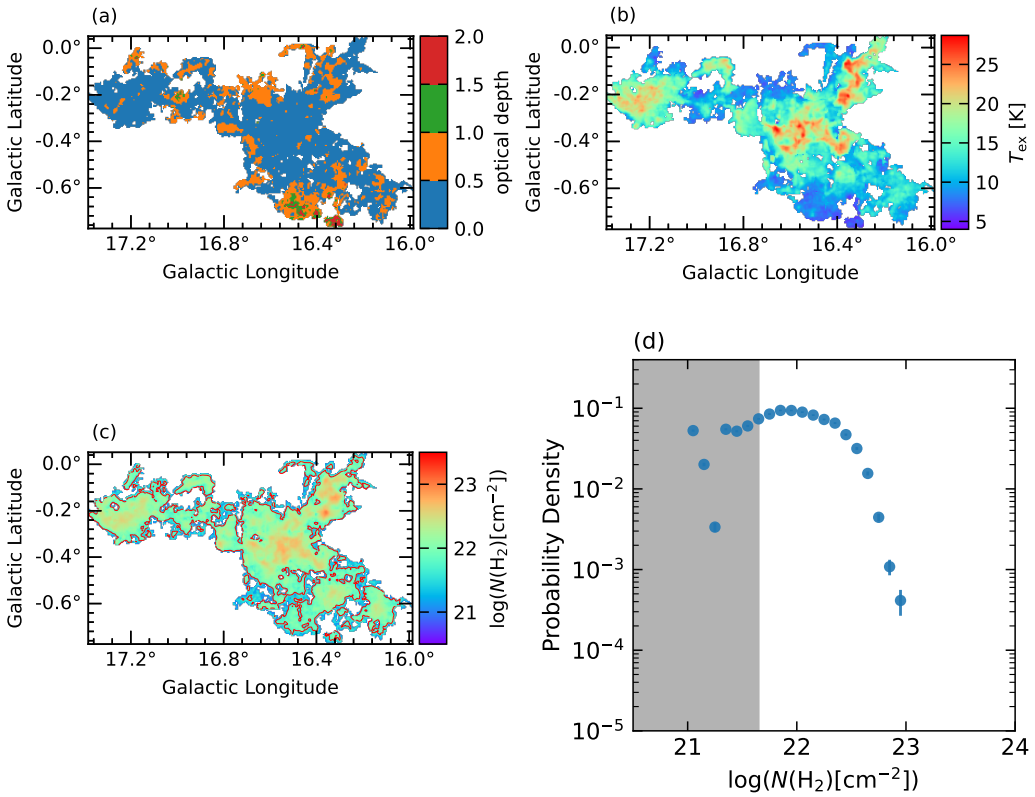

Figure 4.5: An example of the physical parameter maps of FGN16.620–0.313 cloud and its N-PDF. (a) Optical depth map. The colors indicate the optical depth in increments of 0.5. (b) Excitation temperature map obtained from ^{12}CO (J=1–0) line. (c) H_2 column density map. The red contour indicates the completeness limit of H_2 column density ($\log(N(H_2)) = 21.65$) for the FGN16.620–0.313 cloud. (d) N-PDF is derived from the H_2 column density map of the panel (c). The gray-shaded areas correspond to column densities out of the completeness limit.

To estimate the physical properties of identified clouds, it is essential to know the distances. The most reliable method is the measurement of the annual parallax using a maser source, which has been obtained for several star-forming regions in previous observational studies (e.g. Reid et al., 2009; Rygl et al., 2010; VERA Collaboration et al., 2020). Currently, annual parallax-based distances have been measured for a small fraction of our sample. The kinematic distance is most commonly applied to a large-scale survey such as FUGIN. The kinematic distance assumes a galactic rotation model and estimates the distance of objects in the Milky Way disk based on their radial velocities $v_{\rm LSR}$. However, an essential issue with the kinematic distance is that there are two solutions for each radial velocity. This issue is known as *Kinematic Distance Ambiguity* (KDA). These two distances are equally spaced on either side of the tangent position. They are generally referred to as "*near*" and "*far*" in order of proximity to the Sun. Since most of the MCs identified in this study are located in the inner Galaxy, the KDA applies to many of our samples.

On the other hand, the kinematic distance can be uniquely determined at the terminal radial velocity of the galactic rotation. The kinematic distance at terminal radial velocity is referred to as $d_{\rm tan}$. Using the IAU standard parameters (the distance to the Galactic center, $R_0 = 8.5$ kpc and the circular rotational velocity, $\theta_0 = 220$ km s^{-1}), the range of $d_{\rm tan}$ is approximately 5.5 – 8.2 kpc in this analysis coverage ($12^\circ \leq l \leq 50^\circ$). However, Figure 4.4 shows that the identified clouds exhibit a complex velocity structure. We considered that it is not easy to uniquely determine the central velocity for each cloud. Therefore, in this analysis, we avoid using distance-dependent properties of MCs (such as surface density, size of clouds, and the virial parameter) in the following discussion. Recently, a new distance measurement method based on machine learning has been proposed (Fujita et al., 2022). In the future, we believe it will be possible to estimate the distance-dependent properties of MCs identified from large-scale surveys such as FUGIN.

The method for estimating the physical parameters of each cloud is described in Section 3.3.2. Essentially, the excitation temperature, optical depth, and column density of each cloud were derived using a procedure that assumes the LTE condition. The estimated $N(^{13}{\rm CO})$ was converted to $(N({\rm H_2}))$, assuming the relative abundances of $[{\rm H_2}/^{13}{\rm CO}] = 7.7 \times 10^5$ (Wilson & Rood, 1994; Pineda et al., 2010). These physical parameters of the MC are summarized in columns 5 and 6 in Table 4.1. Figure 4.5 shows the optical

depth, excitation temperature, H_2 column density map, and N-PDF of one of the identified clouds.

4.2.3 Multi log-normal fitting of N-PDFs

We fitted N-PDFs obtained from MCs within the analysis area. As mentioned in Section 3.3.2, it is necessary to consider the completeness limits of the column density map to obtain a correct N-PDF (see also Alves et al., 2017). In addition, it should be noted that MCs containing the edges of the observed area do not have a correct N-PDF due to missing samples. In this analysis, 12 clouds contain the edge of the observed area (column 12 in tables 4.2 and B.2). We then manually determined the completeness limit of the column density map for each cloud (see Section 3.3.2). This completeness limit is indicated by the red contours in each column density map (e.g. Figure 4.5-(c)).

We performed the N-PDF fitting using the least squares method (Levenberg-Marquardt algorithm) in the `astropy.modeling` module for Python (Astropy Collaboration et al., 2013, 2018). The initial values of the parameters $\bar{N}_1$, $\bar{N}_2$, and $\bar{N}_3$ were set around the peak of the low-density component, $\log(N(H_2)) = 22.5$ and $\log(N(H_2)) = 23.0$, respectively. The fitting parameters for each N-PDF of identified cloud are listed in Table 4.2. The N-PDF of each molecular cloud was fitted with single or multi-log normal functions, depending on its shape (see Section 3.3.3). The number of log-normal distributions was determined based on the smallest residuals between the N-PDF and the fitted function. The number of log-normal distributions should be as small as possible. In this dissertation, they were referred to as LN1, LN2, and LN3 in the order of the low-density log-normal distributions. We found that the N-PDF can be divided into four categories according to the shape of the N-PDF, i.e., LN1 type (single LN type), LN1+LN2 type (double LN type), LN1+LN2+LN3 type (triple LN type). The complex N-PDF shape was determined to be an unclear type (UN type). Figure 4.6 shows examples of clouds for each N-PDF type. In this analysis, 46 clouds were single LN type, 42 clouds were double LN type, 5 clouds were triple LN type, and 3 clouds were UN type (see also Tables 4.2 and B.2).

Using the parameters obtained from the N-PDF fitting, we plotted the correlation plots between the mean H_2 column density and the surface fraction, the mean H_2 column density, and the half-width of each LN

component (Figure 4.7). In Figure 4.7, the open symbols indicate clouds containing the edge of the observation area. As a result, we obtained a similar correlation for the Cygnus X complex shown in Figure 3.6. We can assume that the systematic correlation between the small and narrow N-PDF and the larger mean column density component is a universal feature of MCs in the Milky Way. However, it should be noted that our sample includes clouds at different distances. In particular, the smaller projection size and larger column density structures are strongly affected by distance effects (see also Ma et al., 2021).

Table 4.2: Properties of the N-PDFs of identified clouds from FUGIN survey.

Source name	N-PDF type	p_1	$\bar{N}_1$	σ_1	p_2	$\bar{N}_2$	σ_2	p_3	$\bar{N}_3$	σ_3	Edge
FGN12.405–0.814	LN1	0.181	21.81	0.220	–	–	–	–	–	–	N
FGN12.589–0.358	LN1	0.112	21.77	0.274	–	–	–	–	–	–	N
FGN12.711+0.549	LN1+LN2	0.104	21.76	0.296	0.017	22.40	0.213	–	–	–	N
FGN12.738+0.497	LN1+LN2	0.127	21.80	0.229	0.007	22.58	0.125	–	–	–	N
FGN12.943–0.260	UN	–	–	–	–	–	–	–	–	–	N
FGN13.315+0.207	LN1	0.132	22.01	0.208	–	–	–	–	–	–	N
FGN13.910+0.160	LN1	0.103	21.67	0.418	–	–	–	–	–	–	N
FGN13.916+0.817	LN1+LN2	0.118	21.56	0.259	0.024	22.06	0.104	–	–	–	Y
FGN14.083–0.543	LN1+LN2	0.083	22.06	0.318	0.062	22.52	0.162	–	–	–	N
FGN14.226–0.210	LN1+LN2+LN3	0.091	22.00	0.288	0.044	22.44	0.173	0.016	22.83	0.100	N
...	...	...	...	...	...	...	...	...	...	...	...
FGN39.614–0.327	LN1	0.113	21.94	0.219	–	–	–	–	–	–	N
FGN41.093–0.072	LN1	0.134	21.78	0.162	–	–	–	–	–	–	N
FGN41.211–0.252	LN1+LN2	0.097	21.72	0.304	0.030	22.18	0.240	–	–	–	N
FGN42.063–0.472	LN1	0.114	21.69	0.314	–	–	–	–	–	–	N
FGN42.785–0.252	LN1	0.139	21.71	0.224	–	–	–	–	–	–	N
FGN44.458–0.286	LN1+LN2	0.082	21.69	0.244	0.068	22.19	0.208	–	–	–	N
FGN45.446+0.085	LN1+LN2	0.081	21.68	0.272	0.061	22.21	0.234	–	–	–	N
FGN45.805–0.355	LN1	0.118	21.95	0.260	–	–	–	–	–	–	N
FGN47.489–0.849	LN1	0.179	21.49	0.197	–	–	–	–	–	–	Y
FGN49.424–0.328	LN1+LN2+LN3	0.080	22.02	0.246	0.052	22.60	0.190	0.007	23.15	0.332	N

Notes: Only a small portion of this table is provided here; the full table is shown in Table B.2.

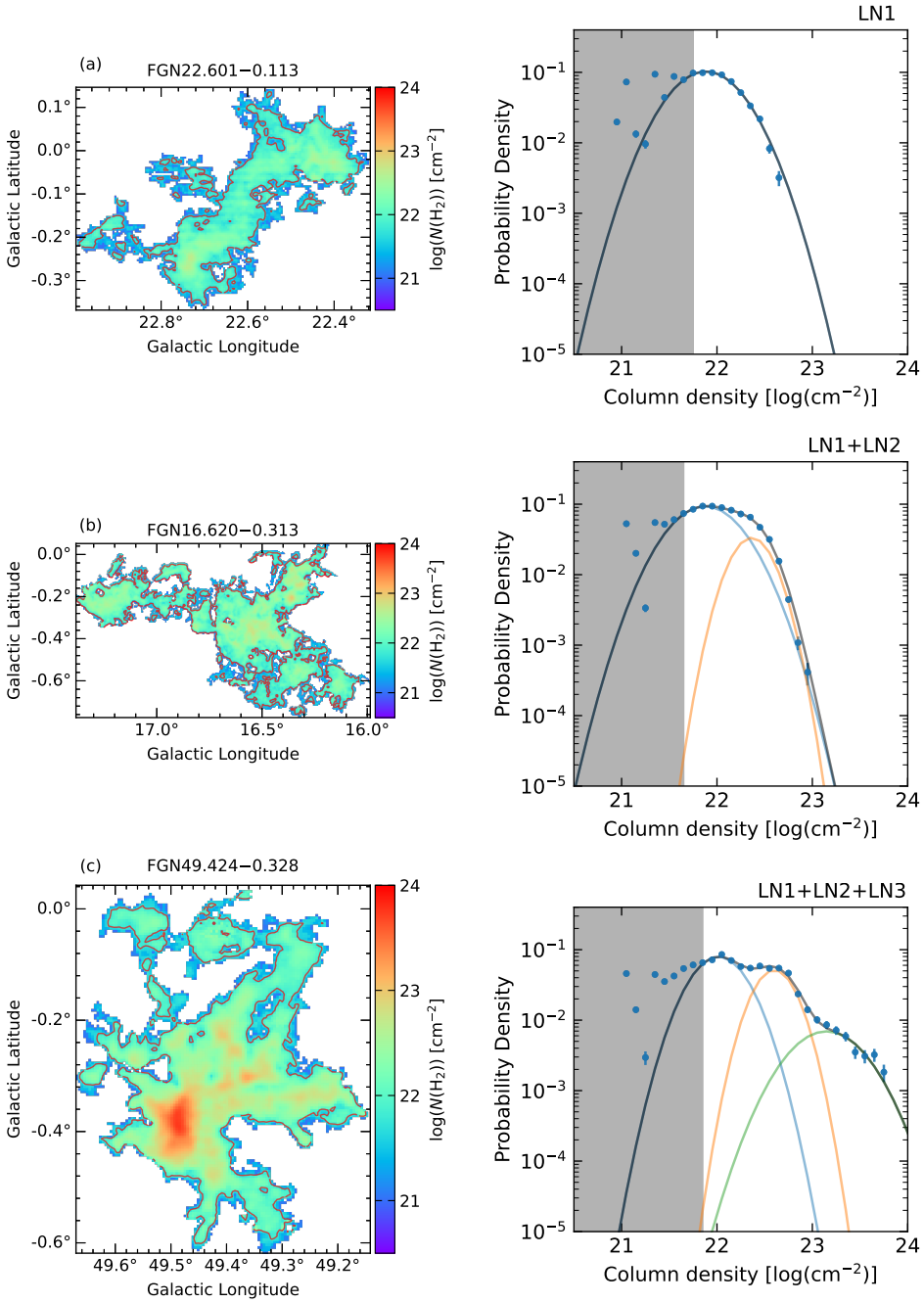

Figure 4.6: Examples of column density maps and N-PDFs of the types (a) LN1 type, (b) LN1+LN2 type, (c) LN1+LN2+LN3 type, and (d) UN-type, respectively. The red contours in the left panels indicate the completeness limit of H_2 column density. Blue, orange, and green curves in the right panels indicate LN1, LN2, and LN3 components, respectively. Black curves show the best-fit curve. The gray-shaded areas correspond to column densities out of the completeness limit.

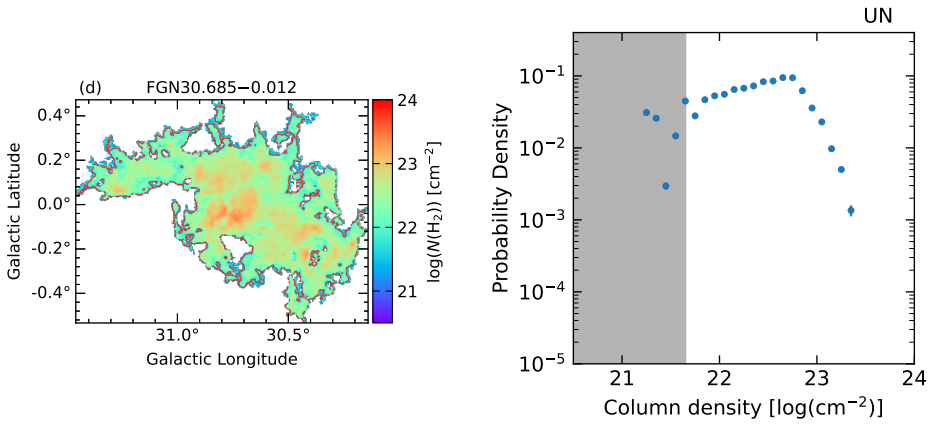

Figure 4.6: *continued.* All molecular clouds and N-PDFs are given in Figure C.1.

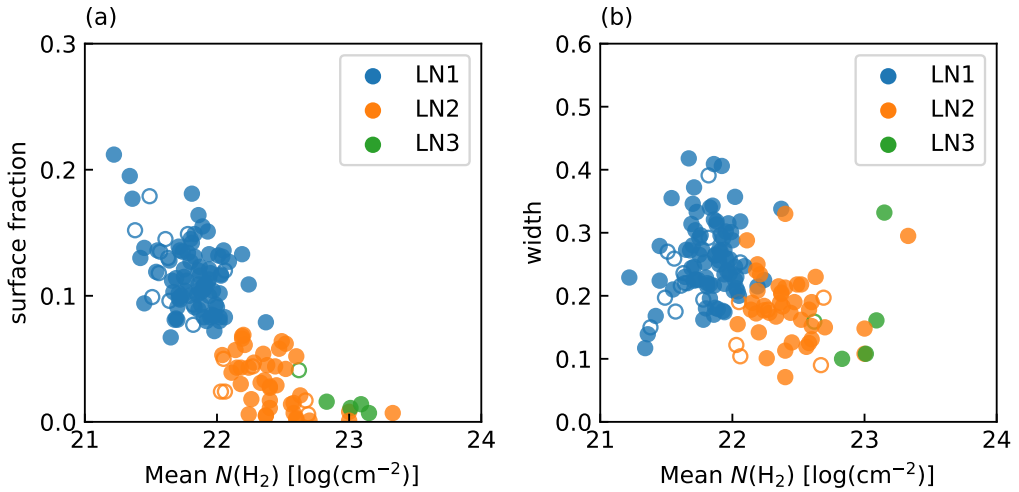

Figure 4.7: The correlation plots between the mean H_2 column density and (a) surface fraction, and (b) between the mean H_2 column density and half-width of LN components, respectively. Blue, orange, and green symbols indicate LN1, LN2, and LN3 components, respectively. The filled symbols indicate the clouds of which the completeness limit contours were closed, and the open symbols indicate the other clouds.

4.3 Discussion

We investigated the dependence of the statistical structure of MCs on the Galactic environment based on the longitude-velocity distribution of the N-PDF parameters obtained from Section 4.2.3. The colored lines in all

panels of Figure 4.8 indicate the spiral arms of the Milky Way shown by Reid et al. (2016). Our analysis region includes the spiral arms of Norma, Sagittarius, Scutum, and Perseus (Figure 4.1). Aquila Rift and Aquila Spur are recognized as near-solar and inter-arm regions, respectively.

As described in Section 4.2.2, the distance of MCs is an uncertain parameter in this study. The distance effect is expected to be stronger for smaller statistical structures (i.e., high column density regions). Therefore, we used the parameters of the LN1 component ($\bar{N}_1$ and σ_1), which is the largest statistical structure of the MC that is less affected by distance effects. Figure 4.8 shows the longitude velocity map of the parameters of the LN1 component. Since we identified clouds from the ^{13}COemission line, there is a bias toward clouds with relatively dense structures. Therefore, we emphasize that many identified clouds are located in the bar and galactic spiral arms.

Figure 4.8-(a) shows a longitude–velocity map of the number of LN components composing the N-PDF of each identified cloud. We suggested that the number of log-normal components composing a MC is independent of the Galactic environment. Figure 4.8-(a) shows that the proportions of LN1-type and LN1+LN2-type are almost the same in the arms other than Aquila Spur and Aquila Rift. We focused on the MC located around the terminal velocity. In the Aquila Spur, it was shown that there were more LN1-type clouds and fewer high-column density regions. This is consistent with the mass fraction of dense gas in MCs estimated in the C^{18}O (J=1–0) emission line (Torii et al., 2019).

As described in Section 3.4.2, the shape of the N-PDF is expected to be independent of star formation in the interior of clouds. However, the MCs with the densest log-normal component (LN3) are well-known active star formation and internal gas motion regions, such as M16, W33, W43, and W51 (i.e., HII regions, massive star-forming regions, and supernova remnants). It will still be essential to study the statistical structure of the cloud scales and their star formation activity.

Figures 4.8-(b) and (c) show the longitude-velocity maps of the N-PDF parameters, $\bar{N}_1$ and σ_1, respectively. The range of $\bar{N}_1$ was $10^{21.2} \sim 10^{22.2}$ cm^{-2} (Figure 4.7-(a)). We found that the mean LN1 column density is relatively low in the MCs on the Aquila Rift. On the other hand, the MCs located above $v_{\rm LSR} \sim 10$ km s^{-1} did not show any dependence on the Galactic environment. We suggested that this trend difference originated from the arms and inter-arm regions of the galaxy. Colombo et al. (2022)

have compared cloud properties in the spiral arms and inter-arm regions using ^{13}CO (J=2–1) data from the SEDIGISM (Structure, Excitation, and Dynamics of the Inner Galactic Interstellar Medium) survey (Schuller et al., 2017). They showed that the flux PDFs of ^{13}CO (J=2–1) from different galactic regions are not significantly different. On the other hand, they reported that the number of clouds per unit area and the gas mass is approximately a factor of 1.5 larger in the spiral arms than in the inter-arm regions. This is similar to other spiral-arm galaxies in the local universe (e.g., M 51: Hughes et al., 2013). As the GMCs generated in the spiral arms leave the arms, they are transformed into elongated structures such as spurs, feathers, and branches by the high shear of the rotating galactic disk, as predicted by the previous simulation (e.g. Dobbs & Pringle, 2013; Duarte-Cabral & Dobbs, 2016). This has been confirmed by high-resolution CO observations (Schinnerer et al., 2017). Therefore, we considered the MCs in the inter-arm region to have suppressed or dispersed high-density gas formation compared to other Galactic environments.

Finally, we compared the width of the LN1 component with the Galactic environment (Figure 4.8-(c)). We can find that the widths of the LN1 components range from about 0.1 to 0.4 (Figure 4.7-(b)). Consequently, the dependence of the width of the LN1 component on the Galactic environment could not be resolved. As described in Section 1.2.3, the width of the log-normal N-PDF was thought to be related to the turbulence in molecular clouds (see also Federrath et al., 2010). Our results suggest that turbulence in the relatively diffuse statistical structure of molecular clouds is a unique property independent of the Galactic environment.

In conclusion, we suggest that the diffuse structures that make up the bulk of molecular clouds have relatively consistent properties in the arms of the Milky Way. On the other hand, we found a trend toward lower mean column densities in the inter-arms. Our results suggest that the statistical structure of molecular clouds can be adapted from previous studies showing that the properties of molecular clouds in the inner-galactic plane are largely insensitive to the Galactic environment (e.g. Duarte-Cabral & Dobbs, 2016; Pettitt et al., 2018; Rigby et al., 2019; Colombo et al., 2022).

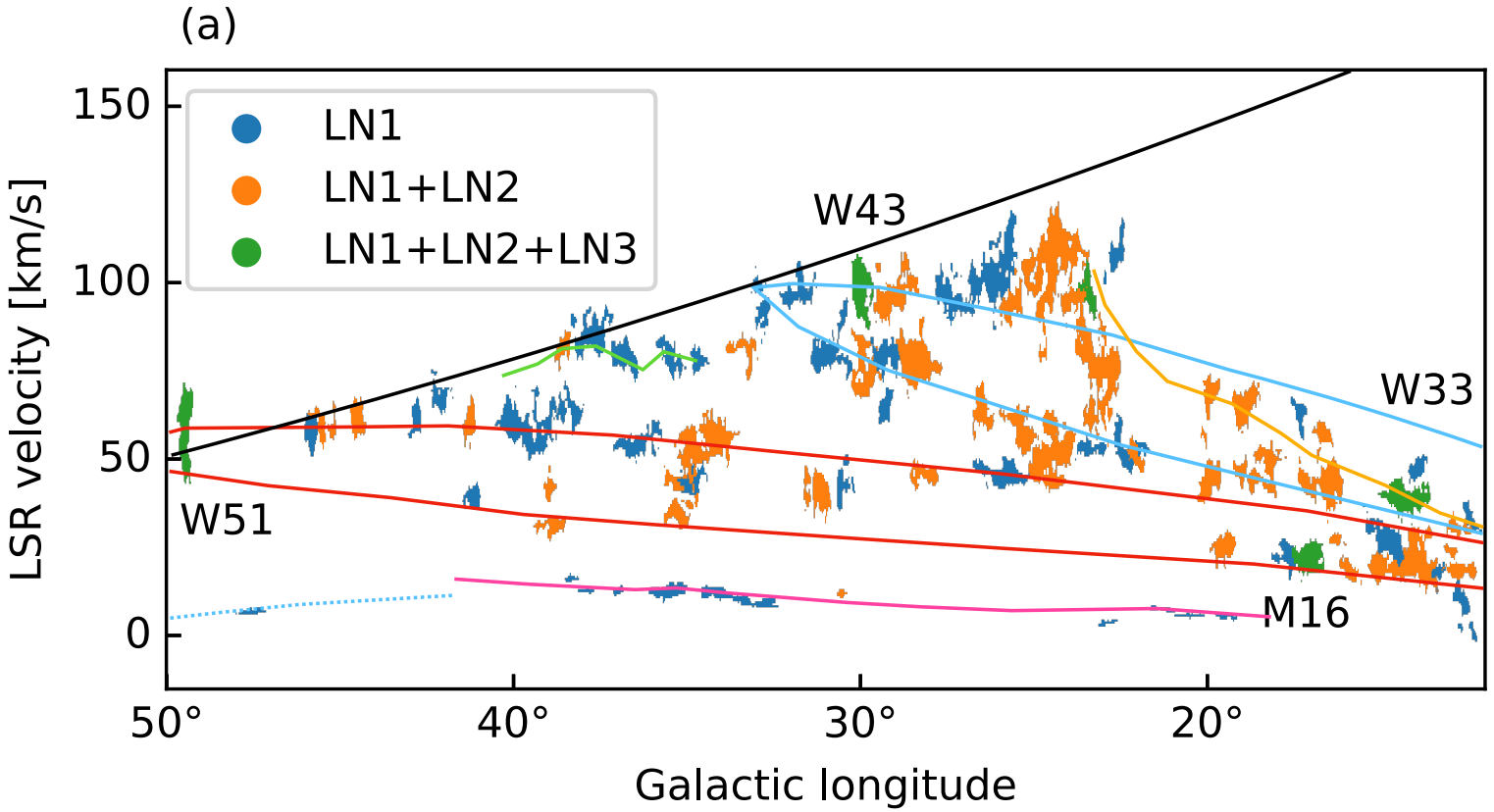

Figure 4.8: Longitude–velocity map of the N-PDF parameters obtained from identified clouds from the FUGIN survey. (a) The map of the number of LN components that compose the N-PDF of each identified cloud. Blue, orange and green indicate LN1 type, LN1+LN2 type, and LN1+LN2+LN3 type, respectively. UN type was excluded. The solid color lines are the same as in Figure 4.1.

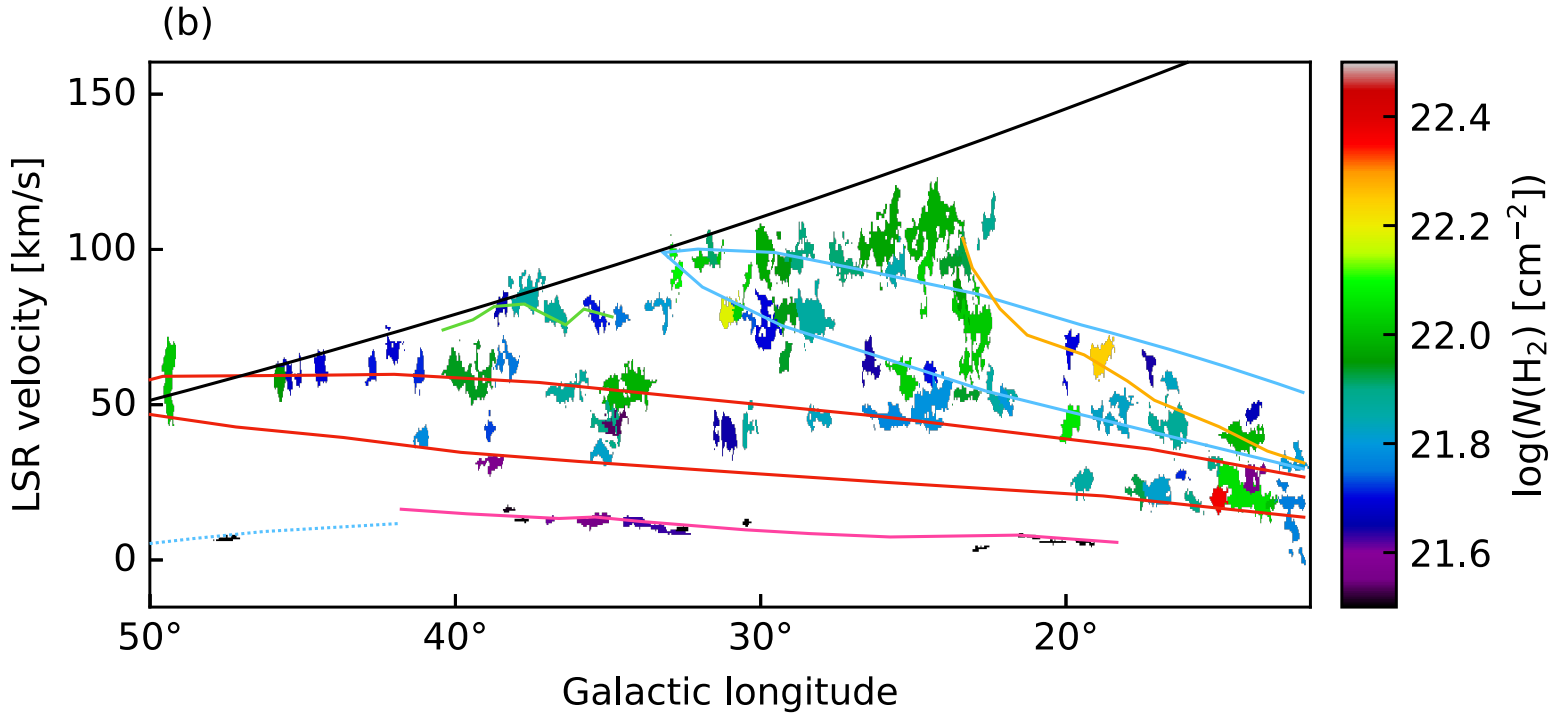

Figure 4.8: *continued.* (b) Longitude–velocity map of the mean column density of the LN1 component ($\bar{N}_1$). UN type was excluded. The solid color lines are the same as in Figure 4.1

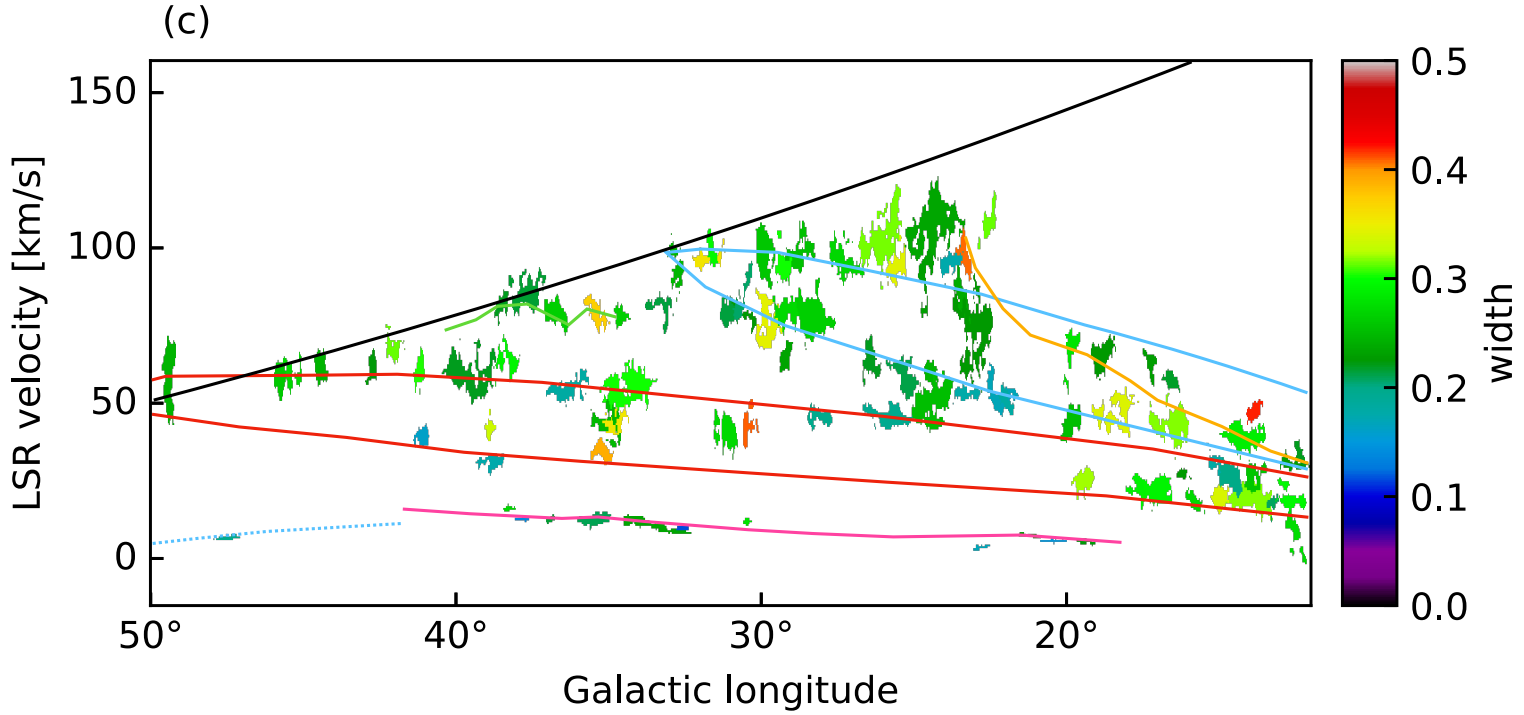

Figure 4.8: *continued.* (c) Longitude–velocity map of the width of the LN1 component (σ_1). UN type was excluded. The solid color lines are the same as in Figure 4.1

4.4 Conclusions

We present the statistical properties of MCs and their relation to the Galactic environment based on a multi-log normal analysis of molecular gas N-PDFs. Using DENDROGRAM and SCIMES algorithms, we performed source extraction on ^{13}CO (J=1–0) data obtained from the FUGIN project with the Nobeyama 45-m telescope. We identified 96 extended clouds ($>$ 4000 pixels) from the first quadrant ($12^\circ \leq l \leq 50^\circ$, $|b| \leq 1^\circ$) of the galaxy. These clouds are located in the Norma Arm, the Scutum Arm, the Sagittarius Arm, the Aquila Spur, and the Aquila Rift. Our main results can be summarized as follows:

1. The N-PDFs obtained from the identified clouds were well-fitted with at most three log-normal distributions. We named them LN1, LN2, and LN3, in order of the least dense log-normal distribution. In this analysis, 46 clouds were single LN type, 42 clouds were double LN type, 5 clouds were triple LN type, and 3 clouds had a complex shape.

2. In each arm, the MCs of single-LN type and double-LN type were almost the same proportion. Although the shape of the N-PDF has less correlation with star formation activity in the interior of the cloud (as shown in Section 3.4.2), the MCs with the densest log-normal component (LN3) were well-known regions with active star formation and internal gas motion, such as M16, W33, W43, and W51. Investigating the statistical structure of MCs and star formation activity will still be essential.

3. We have investigated the dependence of the diffuse statistical structure of MCs (LN1) on the Galactic environment using a longitude-velocity map of the N-PDF parameters. We found no dependence on the Galactic environment for MCs in the arm. In contrast, clouds in the Aquila Rift had a relatively low mean column density trend compared to other Galactic environments. This difference in mean column density could be originated from the Galactic environment (arm and inter-arm regions).

4. We found no dependence between the width of LN1 and the Galactic environment. The turbulence of the diffuse structures of the MCs

can be considered as a unique property independent of the Galactic environment.

In this study, we have revealed that cloud-scale structures are universally composed of multiple turbulent structures. This multiple turbulent structure is an essential feature that links the cloud scale to the star-forming scale. Still, it is challenging to resolve the origin of the turbulence structure with only the data used in this study. We expect that a comparison with large-scale extragalactic observations with pc-scale resolution will provide insight into the origin of the turbulent structure of MCs.

Chapter 5

Summary

Molecular gas is one of the major components in interstellar space and a key to understanding the evolution of the structure of the Milky Way through star formation. The spatial structure of a MC should provide a key to address this question. In previous studies, however, the discussion of the properties of a MC has been strongly biased toward formed stars and around them due to the technical limitations of observational studies. After understanding the final stage of star formation from the ISM, we should go ahead toward the diffuse gas and cloud formation from it. In this dissertation, we have studied the properties of a molecular cloud derived from molecular line observations. This dissertation is our first step to a total understanding of the ISM in the Milky Way.

First, we determined the spatial distribution of physical parameters throughout the MC to study the effect of star formation feedback from newly formed massive stars on the surrounding molecular gas. We made mapping observations in the metastable NH_3 inversion transitions towards the massive star-forming region W33 complex. We obtained data cubes covering dust clumps at different evolutionary stages of massive star formation. The distribution of the rotational temperature shows that the high-temperature regions are confined around the W33 Main, which is associated with the compact HII region. This suggests that the interaction between the compact HII region and the molecular gas is strongly spatially constrained and that the star formation feedback has less effect on the properties of the whole molecular cloud. On the contrary, the column density map showed no evidence of star formation feedback.

Next, we employed the N-PDF, which is the latest analysis method for

a cloud structure, to study the physical properties of individual clouds. We used J=1–0 transition lines of ^{12}CO and ^{13}CO obtained from the Nobeyama 45-m Cygnus-X CO survey and FUGIN survey data. We identify the MCs using the DENDROGRAM and SCIMES algorithms, which are also the latest cloud structure identification tools. From the fitting of the N-PDF, we found that the N-PDF can be well-fitted with multiple log-normal distributions. We also found that the shape of the N-PDF of a MC has little correlation with the star formation activity in it.

Finally, the study of this dissertation suggests that MCs are composed of multiple turbulent structures. The existence of this turbulent hierarchical structure is considered to be an essential feature connecting diffuse gas and dense gas. In addition, we found that the contribution of star formation feedback to cloud-scale physical properties is small. The features of the column density structures of MCs are considered to reflect the nature of the earlier stages of the star formation process than the traditional star formation studies. The study presented throughout this dissertation will push the envelope of ISM studies toward the earlier stages of evolution in the cosmic recycling.

References

Alves, J., Lombardi, M., & Lada, C. J. 2007, A&A, 462, L17, doi: 10.1051/0004-6361:20066389

—. 2017, A&A, 606, L2, doi: 10.1051/0004-6361/201731436

André, P., Men'shchikov, A., Bontemps, S., et al. 2010, A&A, 518, L102, doi: 10.1051/0004-6361/201014666

Armstrong, J. W., Rickett, B. J., & Spangler, S. R. 1995, ApJ, 443, 209, doi: 10.1086/175515

Astropy Collaboration, Robitaille, T. P., Tollerud, E. J., et al. 2013, A&A, 558, A33, doi: 10.1051/0004-6361/201322068

Astropy Collaboration, Price-Whelan, A. M., Sipőcz, B. M., et al. 2018, AJ, 156, 123, doi: 10.3847/1538-3881/aabc4f

Ballesteros-Paredes, J., Gazol, A., Kim, J., et al. 2006, ApJ, 637, 384, doi: 10.1086/498228

Ballesteros-Paredes, J., & Mac Low, M.-M. 2002, ApJ, 570, 734, doi: 10.1086/339624

Ballesteros-Paredes, J., Vázquez-Semadeni, E., Gazol, A., et al. 2011, MNRAS, 416, 1436, doi: 10.1111/j.1365-2966.2011.19141.x

Ballesteros-Paredes, J., Vázquez-Semadeni, E., Palau, A., & Klessen, R. S. 2018, MNRAS, 479, 2112, doi: 10.1093/mnras/sty1515

Ballesteros-Paredes, J., André, P., Hennebelle, P., et al. 2020, Space Sci. Rev., 216, 76, doi: 10.1007/s11214-020-00698-3

Bate, M. R. 2009, MNRAS, 392, 1363, doi: 10.1111/j.1365-2966.2008.14165.x

Bate, M. R., & Keto, E. R. 2015, MNRAS, 449, 2643, doi: 10.1093/mnras/stv451

Benjamin, R. A., Churchwell, E., Babler, B. L., et al. 2003, PASP, 115, 953, doi: 10.1086/376696

Bergin, E. A., & Langer, W. D. 1997, ApJ, 486, 316, doi: 10.1086/304510

Bertoldi, F. 1989, ApJ, 346, 735, doi: 10.1086/168055

Bertoldi, F., & McKee, C. F. 1990, ApJ, 354, 529, doi: 10.1086/168713

Billington, S. J., Urquhart, J. S., Figura, C., Eden, D. J., & Moore, T. J. T. 2019, MNRAS, 483, 3146, doi: 10.1093/mnras/sty3053

Blitz, L. 1993, in Protostars and Planets III, ed. E. H. Levy & J. I. Lunine, 125

Bobotsis, G., & Fich, M. 2019, ApJ, 884, 77, doi: 10.3847/1538-4357/ab3798

Bohlin, R. C., Savage, B. D., & Drake, J. F. 1978, ApJ, 224, 132, doi: 10.1086/156357

Bron, E., Le Bourlot, J., & Le Petit, F. 2014, A&A, 569, A100, doi: 10.1051/0004-6361/201322101

Burkhart, B., Collins, D. C., & Lazarian, A. 2015, ApJ, 808, 48, doi: 10.1088/0004-637X/808/1/48

Burns, R. A., Handa, T., Omodaka, T., et al. 2019, PASJ, 71, 91, doi: 10.1093/pasj/psz074

Caselli, P., & Myers, P. C. 1995, ApJ, 446, 665, doi: 10.1086/175825

Caswell, J. L. 1998, MNRAS, 297, 215, doi: 10.1046/j.1365-8711.1998.01468.x

Chabrier, G. 2003, PASP, 115, 763, doi: 10.1086/376392

Chabrier, G. 2005, in Astrophysics and Space Science Library, Vol. 327, The Initial Mass Function 50 Years Later, ed. E. Corbelli, F. Palla, & H. Zinnecker, 41, doi: 10.1007/978-1-4020-3407-7_5

Chen, H. H.-H., Burkhart, B., Goodman, A., & Collins, D. C. 2018, ApJ, 859, 162, doi: 10.3847/1538-4357/aabaf6

Chepurnov, A., & Lazarian, A. 2010, ApJ, 710, 853, doi: 10.1088/0004-637X/710/1/853

Chibueze, J. O., Imura, K., Omodaka, T., et al. 2013, ApJ, 762, 17, doi: 10.1088/0004-637X/762/1/17

Christie, H., Viti, S., Yates, J., et al. 2012, MNRAS, 422, 968, doi: 10.1111/j.1365-2966.2012.20643.x

Collins, D. C., Kritsuk, A. G., Padoan, P., et al. 2012, ApJ, 750, 13, doi: 10.1088/0004-637X/750/1/13

Colom, P., Lekht, E. E., Pashchenko, M. I., & Rudnitskij, G. M. 2015, A&A, 575, A49, doi: 10.1051/0004-6361/201323083

Colombo, D., Rosolowsky, E., Ginsburg, A., Duarte-Cabral, A., & Hughes, A. 2015, MNRAS, 454, 2067, doi: 10.1093/mnras/stv2063

Colombo, D., Rosolowsky, E., Duarte-Cabral, A., et al. 2019, MNRAS, 483, 4291, doi: 10.1093/mnras/sty3283

Colombo, D., Duarte-Cabral, A., Pettitt, A. R., et al. 2022, A&A, 658, A54, doi: 10.1051/0004-6361/202141287

Contreras, Y., Schuller, F., Urquhart, J. S., et al. 2013, A&A, 549, A45, doi: 10.1051/0004-6361/201220155

Dame, T. M., Hartmann, D., & Thaddeus, P. 2001, ApJ, 547, 792, doi: 10.1086/318388

Deharveng, L., Lefloch, B., Zavagno, A., et al. 2003, A&A, 408, L25, doi: 10.1051/0004-6361:20031157

Deharveng, L., Zavagno, A., Anderson, L. D., et al. 2012, A&A, 546, A74, doi: 10.1051/0004-6361/201219131

Deharveng, L., Zavagno, A., Samal, M. R., et al. 2015, A&A, 582, A1, doi: 10.1051/0004-6361/201423835

Dewangan, L. K., Baug, T., & Ojha, D. K. 2020a, MNRAS, doi: 10.1093/mnras/staa1526

Dewangan, L. K., Sharma, S., Pandey, R., et al. 2020b, ApJ, 898, 172, doi: 10.3847/1538-4357/ab9c27

Dobashi, K., Bernard, J.-P., & Fukui, Y. 1996, ApJ, 466, 282, doi: 10.1086/177509

Dobbs, C. L., & Pringle, J. E. 2013, MNRAS, 432, 653, doi: 10.1093/mnras/stt508

Dobbs, C. L., Krumholz, M. R., Ballesteros-Paredes, J., et al. 2014, in Protostars and Planets VI, ed. H. Beuther, R. S. Klessen, C. P. Dullemond, & T. Henning, 3, doi: 10.2458/azu_uapress_9780816531240-ch001

Downes, D., & Rinehart, R. 1966, ApJ, 144, 937, doi: 10.1086/148691

Draine, B. T. 2011, Physics of the Interstellar and Intergalactic Medium

Duarte-Cabral, A., & Dobbs, C. L. 2016, MNRAS, 458, 3667, doi: 10.1093/mnras/stw469

Duarte-Cabral, A., Colombo, D., Urquhart, J. S., et al. 2021, The SEDIGISM survey: molecular clouds in the inner Galaxy, Monthly Notices of the Royal Astronomical Society, Volume 500, Issue 3, pp.3027-3049, doi: 10.1093/mnras/staa2480

Dunham, M. K., Rosolowsky, E., Evans, Neal J., I., et al. 2010, ApJ, 717, 1157, doi: 10.1088/0004-637X/717/2/1157

Duronea, N. U., Cappa, C. E., Bronfman, L., et al. 2017, A&A, 606, A8, doi: 10.1051/0004-6361/201730528

Elmegreen, B. G. 2000, ApJ, 530, 277, doi: 10.1086/308361

Elmegreen, B. G., & Lada, C. J. 1977, ApJ, 214, 725, doi: 10.1086/155302

Elmegreen, B. G., & Scalo, J. 2004, ARA&A, 42, 211, doi: 10.1146/annurev.astro.41.011802.094859

Falgarone, E., Pety, J., & Hily-Blant, P. 2009, A&A, 507, 355, doi: 10.1051/0004-6361/200810963

Falgarone, E., Phillips, T. G., & Walker, C. K. 1991, ApJ, 378, 186, doi: 10.1086/170419

Federrath, C., & Klessen, R. S. 2013, ApJ, 763, 51, doi: 10.1088/0004-637X/763/1/51

Federrath, C., Klessen, R. S., & Schmidt, W. 2008, ApJ, 688, L79, doi: 10.1086/595280

Federrath, C., Roman-Duval, J., Klessen, R. S., Schmidt, W., & Mac Low, M. M. 2010, A&A, 512, A81, doi: 10.1051/0004-6361/200912437

Federrath, C., Rathborne, J. M., Longmore, S. N., et al. 2016, ApJ, 832, 143, doi: 10.3847/0004-637X/832/2/143

Feng, S., Li, D., Caselli, P., et al. 2020, ApJ, 901, 145, doi: 10.3847/1538-4357/abada3

Ferrière, K. M. 2001, Reviews of Modern Physics, 73, 1031, doi: 10.1103/RevModPhys.73.1031

Field, G. B. 1965, ApJ, 142, 531, doi: 10.1086/148317

Field, G. B., Goldsmith, D. W., & Habing, H. J. 1969, ApJ, 155, L149, doi: 10.1086/180324

Friesen, R. K., Pineda, J. E., co-PIs, et al. 2017, ApJ, 843, 63, doi: 10.3847/1538-4357/aa6d58

Fujita, S., Ito, A. M., Miyamoto, Y., et al. 2022, arXiv e-prints, arXiv:2212.06238. https://arxiv.org/abs/2212.06238

Galván-Madrid, R., Zhang, Q., Keto, E., et al. 2010, ApJ, 725, 17, doi: 10.1088/0004-637X/725/1/17

Girichidis, P., Offner, S. S. R., Kritsuk, A. G., et al. 2020, Space Sci. Rev., 216, 68, doi: 10.1007/s11214-020-00693-8

Glover, S. C. O. 2003, ApJ, 584, 331, doi: 10.1086/345684

Goldreich, P., & Kwan, J. 1974, ApJ, 189, 441, doi: 10.1086/152821

Goldsmith, P. F. 2001, ApJ, 557, 736, doi: 10.1086/322255

Goldsmith, P. F., Heyer, M., Narayanan, G., et al. 2008, ApJ, 680, 428, doi: 10.1086/587166

Goodman, A. A., Pineda, J. E., & Schnee, S. L. 2009, ApJ, 692, 91, doi: 10.1088/0004-637X/692/1/91

Gould, R. J., & Salpeter, E. E. 1963, ApJ, 138, 393, doi: 10.1086/147654

Güver, T., & Özel, F. 2009, MNRAS, 400, 2050, doi: 10.1111/j.1365-2966.2009.15598.x

Habing, H. J., & Israel, F. P. 1979, ARA&A, 17, 345, doi: 10.1146/annurev.aa.17.090179.002021

Habing, H. J., Israel, F. P., & de Jong, T. 1972, A&A, 17, 329

Haschick, A. D., & Ho, P. T. P. 1983, ApJ, 267, 638, doi: 10.1086/160900

Haschick, A. D., Menten, K. M., & Baan, W. A. 1990, ApJ, 354, 556, doi: 10.1086/168715

Hatchell, J., Wilson, T., Drabek, E., et al. 2013, MNRAS, 429, L10, doi: 10.1093/mnrasl/sls015

Heithausen, A., Bensch, F., Stutzki, J., Falgarone, E., & Panis, J. F. 1998, A&A, 331, L65

Henkel, C., Braatz, J. A., Menten, K. M., & Ott, J. 2008, A&A, 485, 451, doi: 10.1051/0004-6361:20079140

Hennebelle, P., & Chabrier, G. 2011, ApJ, 743, L29, doi: 10.1088/2041-8205/743/2/L29

Hennebelle, P., Commerçon, B., Lee, Y.-N., & Chabrier, G. 2020, ApJ, 904, 194, doi: 10.3847/1538-4357/abbfab

Hennemann, M., Motte, F., Schneider, N., et al. 2012, A&A, 543, L3, doi: 10.1051/0004-6361/201219429

Henning, T., Linz, H., Krause, O., et al. 2010, A&A, 518, L95, doi: 10.1051/0004-6361/201014635

Hernandez, A. K., & Tan, J. C. 2011, ApJ, 730, 44, doi: 10.1088/0004-637X/730/1/44

Heyer, M., & Dame, T. M. 2015, ARA&A, 53, 583, doi: 10.1146/annurev-astro-082214-122324

Heyer, M. H., & Brunt, C. M. 2004, ApJ, 615, L45, doi: 10.1086/425978

Heyer, M. H., Carpenter, J. M., & Snell, R. L. 2001, ApJ, 551, 852, doi: 10.1086/320218

Heyer, M. H., & Terebey, S. 1998, ApJ, 502, 265, doi: 10.1086/305881

Hildebrand, R. H. 1983, QJRAS, 24, 267

Hillenbrand, L. A., & Hartmann, L. W. 1998, ApJ, 492, 540, doi: 10.1086/305076

Hirota, T., Bushimata, T., Choi, Y. K., et al. 2007, PASJ, 59, 897, doi: 10.1093/pasj/59.5.897

Ho, P. T. P., & Townes, C. H. 1983, ARA&A, 21, 239, doi: 10.1146/annurev.aa.21.090183.001323

Högbom, J. A. 1974, A&AS, 15, 417

Hogge, T., Jackson, J., Stephens, I., et al. 2018, ApJS, 237, 27, doi: 10.3847/1538-4365/aacf94

Hogge, T. G., Jackson, J. M., Allingham, D., et al. 2019, ApJ, 887, 79, doi: 10.3847/1538-4357/ab5180

Hughes, A., Meidt, S. E., Schinnerer, E., et al. 2013, ApJ, 779, 44, doi: 10.1088/0004-637X/779/1/44

Humphreys, R. M. 1978, ApJS, 38, 309, doi: 10.1086/190559

Immer, K., Galván-Madrid, R., König, C., Liu, H. B., & Menten, K. M. 2014, A&A, 572, A63, doi: 10.1051/0004-6361/201423780

Immer, K., Reid, M. J., Menten, K. M., Brunthaler, A., & Dame, T. M. 2013, A&A, 553, A117, doi: 10.1051/0004-6361/201220793

Inoue, T., & Inutsuka, S.-i. 2012, ApJ, 759, 35, doi: 10.1088/0004-637X/759/1/35

Jaupart, E., & Chabrier, G. 2020, ApJ, 903, L2, doi: 10.3847/2041-8213/abbda8

Johnstone, D., Fich, M., Mitchell, G. F., & Moriarty-Schieven, G. 2001, ApJ, 559, 307, doi: 10.1086/322323

Johnstone, D., Wilson, C. D., Moriarty-Schieven, G., et al. 2000, ApJ, 545, 327, doi: 10.1086/317790

Jura, M. 1975, ApJ, 197, 575, doi: 10.1086/153545

Kainulainen, J., Beuther, H., Henning, T., & Plume, R. 2009, A&A, 508, L35, doi: 10.1051/0004-6361/200913605

Kalberla, P. M. W., & Kerp, J. 2009, ARA&A, 47, 27, doi: 10.1146/annurev-astro-082708-101823

Kamazaki, T., Okumura, S. K., Chikada, Y., et al. 2012, PASJ, 64, 29, doi: 10.1093/pasj/64.2.29

Kauffmann, J., Pillai, T., Zhang, Q., et al. 2017, A&A, 603, A89, doi: 10.1051/0004-6361/201628088

Kennicutt, R. C. 2005, in IAU Symposium, Vol. 227, Massive Star Birth: A Crossroads of Astrophysics, ed. R. Cesaroni, M. Felli, E. Churchwell, & M. Walmsley, 3–11, doi: 10.1017/S1743921305004308

Keown, J., Di Francesco, J., Rosolowsky, E., et al. 2019, ApJ, 884, 4, doi: 10.3847/1538-4357/ab3e76

Keto, E. R., & Ho, P. T. P. 1989, ApJ, 347, 349, doi: 10.1086/168123

Keto, E. R., Ho, P. T. P., & Haschick, A. D. 1987, ApJ, 318, 712, doi: 10.1086/165405

Khullar, S., Federrath, C., Krumholz, M. R., & Matzner, C. D. 2021, MNRAS, 507, 4335, doi: 10.1093/mnras/stab1914

Klessen, R. S. 2000, ApJ, 535, 869, doi: 10.1086/308854

Kobayashi, M. I. N., Inoue, T., Tomida, K., Iwasaki, K., & Nakatsugawa, H. 2022, ApJ, 930, 76, doi: 10.3847/1538-4357/ac5a54

Kohno, M., Torii, K., Tachihara, K., et al. 2018, PASJ, 70, S50, doi: 10.1093/pasj/psx137

Kohno, M., Nishimura, A., Fujita, S., et al. 2022, PASJ, 74, 24, doi: 10.1093/pasj/psab107

Kolmogorov, A. 1941, Akademiia Nauk SSSR Doklady, 30, 301

Könyves, V., André, P., Men'shchikov, A., et al. 2015, A&A, 584, A91, doi: 10.1051/0004-6361/201525861

Körtgen, B., Federrath, C., & Banerjee, R. 2019, MNRAS, 482, 5233, doi: 10.1093/mnras/sty3071

Kramer, C., Stutzki, J., Rohrig, R., & Corneliussen, U. 1998, A&A, 329, 249

Krieger, N., Ott, J., Beuther, H., et al. 2017, ApJ, 850, 77, doi: 10.3847/1538-4357/aa951c

Krieger, N., Bolatto, A. D., Koch, E. W., et al. 2020, ApJ, 899, 158, doi: 10.3847/1538-4357/aba903

Kritsuk, A. G., Norman, M. L., & Wagner, R. 2011, ApJ, 727, L20, doi: 10.1088/2041-8205/727/1/L20

Kroupa, P., Aarseth, S., & Hurley, J. 2001, MNRAS, 321, 699, doi: 10.1046/j.1365-8711.2001.04050.x

Kroupa, P., & Boily, C. M. 2002, MNRAS, 336, 1188, doi: 10.1046/j.1365-8711.2002.05848.x

Krumholz, M. R., McKee, C. F., & Bland-Hawthorn, J. 2019, ARA&A, 57, 227, doi: 10.1146/annurev-astro-091918-104430

Krumholz, M. R., Bate, M. R., Arce, H. G., et al. 2014, in Protostars and Planets VI, ed. H. Beuther, R. S. Klessen, C. P. Dullemond, & T. Henning, 243, doi: 10.2458/azu_uapress_9780816531240-ch011

Kuno, N., Takano, S., Iono, D., et al. 2011, in 2011 XXXth URSI General Assembly and Scientific Symposium, 1–4, doi: 10.1109/URSIGASS.2011.6051296

Kurtz, S. 2002, in Astronomical Society of the Pacific Conference Series, Vol. 267, Hot Star Workshop III: The Earliest Phases of Massive Star Birth, ed. P. Crowther, 81. https://arxiv.org/abs/astro-ph/0111351

Kutner, M. L., & Ulich, B. L. 1981, ApJ, 250, 341, doi: 10.1086/159380

Lada, C. J., Gull, T. R., Gottlieb, C. A., & Gottlieb, E. W. 1976, ApJ, 203, 159, doi: 10.1086/154058

Lada, C. J., & Lada, E. A. 2003, ARA&A, 41, 57, doi: 10.1146/annurev.astro.41.011802.094844

Larson, R. B. 1981, MNRAS, 194, 809, doi: 10.1093/mnras/194.4.809

Larson, R. B. 1994, in The Structure and Content of Molecular Clouds 25 Years of Molecular Radioastronomy, ed. T. L. Wilson & K. J. Johnston (Berlin, Heidelberg: Springer Berlin Heidelberg), 13–28

Larson, R. B. 1995, MNRAS, 272, 213, doi: 10.1093/mnras/272.1.213

Latter, W. B., & Black, J. H. 1991, ApJ, 372, 161, doi: 10.1086/169961

Lewis, J. A., Lada, C. J., & Dame, T. M. 2022, ApJ, 931, 9, doi: 10.3847/1538-4357/ac5d58

Li, C., Wang, H., Zhang, M., et al. 2018, ApJS, 238, 10, doi: 10.3847/1538-4365/aad963

Liu, X.-L., Xu, J.-L., Wang, J.-J., et al. 2021, A&A, 646, A137, doi: 10.1051/0004-6361/201935035

Lombardi, M., Alves, J., & Lada, C. J. 2010, A&A, 519, L7, doi: 10.1051/0004-6361/201015282

Lombardi, M., Bouy, H., Alves, J., & Lada, C. J. 2014, A&A, 566, A45, doi: 10.1051/0004-6361/201323293

Lombardi, Marco, Alves, João, & Lada, Charles J. 2015, A&A, 576, L1, doi: 10.1051/0004-6361/201525650

Ma, Y., Wang, H., Li, C., et al. 2021, ApJS, 254, 3, doi: 10.3847/1538-4365/abe85c

Ma, Y., Wang, H., Zhang, M., et al. 2022, ApJS, 262, 16, doi: 10.3847/1538-4365/ac7797

Ma, Y.-H., Wang, H.-C., Li, C., & Yang, J. 2020, Research in Astronomy and Astrophysics, 20, 060, doi: 10.1088/1674-4527/20/4/60

Mangum, J. G., Wootten, A., & Mundy, L. G. 1992, ApJ, 388, 467, doi: 10.1086/171167

Maschberger, T. 2013, MNRAS, 429, 1725, doi: 10.1093/mnras/sts479

Massey, P. 1998, in Astronomical Society of the Pacific Conference Series, Vol. 142, The Stellar Initial Mass Function (38th Herstmonceux Conference), ed. G. Gilmore & D. Howell, 17

Mazumdar, P. 2022, PhD thesis, Max-Planck-Institute for Radioastronomy, Bonn

McKee, C. F., & Ostriker, E. C. 2007, ARA&A, 45, 565, doi: 10.1146/annurev.astro.45.051806.110602

McKee, C. F., & Ostriker, J. P. 1977, ApJ, 218, 148, doi: 10.1086/155667

McKee, C. F., & Tan, J. C. 2003, ApJ, 585, 850, doi: 10.1086/346149

Mebold, U., Winnberg, A., Kalberla, P. M. W., & Goss, W. M. 1982, A&A, 115, 223

Menten, K. M. 1991, ApJ, 380, L75, doi: 10.1086/186177

Minamidani, T., Nishimura, A., Miyamoto, Y., et al. 2016, in Millimeter, Submillimeter, and Far-Infrared Detectors and Instrumentation for Astronomy VIII, Vol. 9914, 99141Z, doi: 10.1117/12.2232137

Mohan, R., Dwarakanath, K. S., & Srinivasan, G. 2004, Journal of Astrophysics and Astronomy, 25, 185, doi: 10.1007/BF02702371

Motte, F., Andre, P., & Neri, R. 1998, A&A, 336, 150

Motte, F., André, P., Ward-Thompson, D., & Bontemps, S. 2001, A&A, 372, L41, doi: 10.1051/0004-6361:20010543

Motte, F., Bontemps, S., Hennemann, M., et al. 2012, in SF2A-2012: Proceedings of the Annual meeting of the French Society of Astronomy and Astrophysics, ed. S. Boissier, P. de Laverny, N. Nardetto, R. Samadi, D. Valls-Gabaud, & H. Wozniak, 45–50

Motte, F., Zavagno, A., Bontemps, S., et al. 2010, A&A, 518, L77, doi: 10.1051/0004-6361/201014690

Muench, A. A., Lada, E. A., Lada, C. J., & Alves, J. 2002, ApJ, 573, 366, doi: 10.1086/340554

Murase, T., Handa, T., Hirata, Y., et al. 2022, MNRAS, 510, 1106, doi: 10.1093/mnras/stab3472

Murase, T., Handa, T., Maebata, M., et al. 2020, in Origins: From the Protosun to the First Steps of Life, ed. B. G. Elmegreen, L. V. Tóth, & M. Güdel, Vol. 345, 353–354, doi: 10.1017/S174392131900200X

Murray, C. E., Stanimirović, S., Goss, W. M., et al. 2015, ApJ, 804, 89, doi: 10.1088/0004-637X/804/2/89

Myers, A. T., McKee, C. F., Cunningham, A. J., Klein, R. I., & Krumholz, M. R. 2013, ApJ, 766, 97, doi: 10.1088/0004-637X/766/2/97

Myers, P. C. 1978, ApJ, 225, 380, doi: 10.1086/156500

Nakano, M., Soejima, T., Chibueze, J. O., et al. 2017, PASJ, 69, 16, doi: 10.1093/pasj/psw120

Nolan, C. A., Federrath, C., & Sutherland, R. S. 2015, MNRAS, 451, 1380, doi: 10.1093/mnras/stv1030

Offner, S. S. R., Clark, P. C., Hennebelle, P., et al. 2014, in Protostars and Planets VI, ed. H. Beuther, R. S. Klessen, C. P. Dullemond, & T. Henning, 53, doi: 10.2458/azu_uapress_9780816531240-ch003

Ohashi, S., Sanhueza, P., Chen, H.-R. V., et al. 2016, ApJ, 833, 209, doi: 10.3847/1538-4357/833/2/209

Oort, J. H., Kerr, F. J., & Westerhout, G. 1958, MNRAS, 118, 379, doi: 10.1093/mnras/118.4.379

Ostriker, E. C., Stone, J. M., & Gammie, C. F. 2001, ApJ, 546, 980, doi: 10.1086/318290

Padoan, P., & Nordlund, Å. 2002, ApJ, 576, 870, doi: 10.1086/341790

Palmeirim, P., André, P., Kirk, J., et al. 2013, A&A, 550, A38, doi: 10.1051/0004-6361/201220500

Pandey, R., Sharma, S., Dewangan, L. K., et al. 2022, ApJ, 926, 25, doi: 10.3847/1538-4357/ac41c3

Paron, S., Granada, A., & Areal, M. B. 2021, MNRAS, 505, 4813, doi: 10.1093/mnras/stab1646

Passot, T., Pouquet, A., & Woodward, P. 1988, A&A, 197, 228

Passot, T., & Vázquez-Semadeni, E. 1998, Phys. Rev. E, 58, 4501, doi: 10.1103/PhysRevE.58.4501

Pettitt, A. R., Egusa, F., Dobbs, C. L., et al. 2018, MNRAS, 480, 3356, doi: 10.1093/mnras/sty2040

Pickett, H. M., Poynter, R. L., Cohen, E. A., et al. 1998, J. Quant. Spec. Radiat. Transf., 60, 883, doi: 10.1016/S0022-4073(98)00091-0

Pineda, J. L., Goldsmith, P. F., Chapman, N., et al. 2010, ApJ, 721, 686, doi: 10.1088/0004-637X/721/1/686

Plume, R., Jaffe, D. T., Evans, Neal J., I., Martín-Pintado, J., & Gómez-González, J. 1997, ApJ, 476, 730, doi: 10.1086/303654

Pokhrel, R., Gutermuth, R., Ali, B., et al. 2016, MNRAS, 461, 22, doi: 10.1093/mnras/stw1303

Rebull, L. M., Wolff, S. C., & Strom, S. E. 2004, AJ, 127, 1029, doi: 10.1086/380931

Reid, M. J., Dame, T. M., Menten, K. M., & Brunthaler, A. 2016, ApJ, 823, 77, doi: 10.3847/0004-637X/823/2/77

Reid, M. J., Menten, K. M., Zheng, X. W., et al. 2009, ApJ, 700, 137, doi: 10.1088/0004-637X/700/1/137

Rigby, A. J., Moore, T. J. T., Plume, R., et al. 2016, MNRAS, 456, 2885, doi: 10.1093/mnras/stv2808

Rigby, A. J., Moore, T. J. T., Eden, D. J., et al. 2019, A&A, 632, A58, doi: 10.1051/0004-6361/201935236

Ripple, F., Heyer, M. H., Gutermuth, R., Snell, R. L., & Brunt, C. M. 2013, MNRAS, 431, 1296, doi: 10.1093/mnras/stt247

Rosolowsky, E., Dunham, M. K., Ginsburg, A., et al. 2010, ApJS, 188, 123, doi: 10.1088/0067-0049/188/1/123

Rosolowsky, E. W., Pineda, J. E., Kauffmann, J., & Goodman, A. A. 2008, ApJ, 679, 1338, doi: 10.1086/587685

Roy, N., Chengalur, J. N., & Srianand, R. 2006, MNRAS, 365, L1, doi: 10.1111/j.1745-3933.2005.00114.x

Rumble, D., Hatchell, J., Kirk, H., & Pattle, K. 2021, MNRAS, 505, 2103, doi: 10.1093/mnras/stab1354

Rumble, D., Hatchell, J., Gutermuth, R. A., et al. 2015, MNRAS, 448, 1551, doi: 10.1093/mnras/stu2695

Rumble, D., Hatchell, J., Pattle, K., et al. 2016, MNRAS, 460, 4150, doi: 10.1093/mnras/stw1100

Rygl, K. L. J., Brunthaler, A., Reid, M. J., et al. 2010, A&A, 511, A2, doi: 10.1051/0004-6361/200913135

Rygl, K. L. J., Brunthaler, A., Sanna, A., et al. 2012, A&A, 539, A79, doi: 10.1051/0004-6361/201118211

Salpeter, E. E. 1955, ApJ, 121, 161, doi: 10.1086/145971

Sawada, T., Ikeda, N., Sunada, K., et al. 2008, PASJ, 60, 445, doi: 10.1093/pasj/60.3.445

Scalo, J. 1990, in Astrophysics and Space Science Library, Vol. 162, Physical Processes in Fragmentation and Star Formation, ed. R. Capuzzo-Dolcetta, C. Chiosi, & A. di Fazio, 151–176, doi: 10.1007/978-94-009-0605-1_12

Schinnerer, E., Meidt, S. E., Colombo, D., et al. 2017, ApJ, 836, 62, doi: 10.3847/1538-4357/836/1/62

Schisano, E., Rygl, K. L. J., Molinari, S., et al. 2014, ApJ, 791, 27, doi: 10.1088/0004-637X/791/1/27

Schneider, N., Bontemps, S., Motte, F., et al. 2016a, A&A, 591, A40, doi: 10.1051/0004-6361/201628328

Schneider, N., Bontemps, S., Simon, R., et al. 2006, A&A, 458, 855, doi: 10.1051/0004-6361:20065088

Schneider, N., Simon, R., Bontemps, S., Comerón, F., & Motte, F. 2007, A&A, 474, 873, doi: 10.1051/0004-6361:20077540

Schneider, N., Bontemps, S., Simon, R., et al. 2011, A&A, 529, A1, doi: 10.1051/0004-6361/200913884

Schneider, N., Csengeri, T., Hennemann, M., et al. 2012, A&A, 540, L11, doi: 10.1051/0004-6361/201118566

Schneider, N., André, P., Könyves, V., et al. 2013, ApJ, 766, L17, doi: 10.1088/2041-8205/766/2/L17

Schneider, N., Bontemps, S., Girichidis, P., et al. 2015a, MNRAS, 453, L41, doi: 10.1093/mnrasl/slv101

Schneider, N., Ossenkopf, V., Csengeri, T., et al. 2015b, A&A, 575, A79, doi: 10.1051/0004-6361/201423569

Schneider, N., Csengeri, T., Klessen, R. S., et al. 2015c, A&A, 578, A29, doi: 10.1051/0004-6361/201424375

Schneider, N., Bontemps, S., Motte, F., et al. 2016b, A&A, 587, A74, doi: 10.1051/0004-6361/201527144

Schraml, J., & Mezger, P. G. 1969, ApJ, 156, 269, doi: 10.1086/149964

Schuller, F., Menten, K. M., Contreras, Y., et al. 2009, A&A, 504, 415, doi: 10.1051/0004-6361/200811568

Schuller, F., Csengeri, T., Urquhart, J. S., et al. 2017, A&A, 601, A124, doi: 10.1051/0004-6361/201628933

Scoville, N. Z. 2013, in Secular Evolution of Galaxies, ed. J. Falcón-Barroso & J. H. Knapen, 491

Scoville, N. Z., & Solomon, P. M. 1974, ApJ, 187, L67, doi: 10.1086/181398

Seifried, D., Sánchez-Monge, Á., Suri, S., & Walch, S. 2017, MNRAS, 467, 4467, doi: 10.1093/mnras/stx399

Shetty, R., Beaumont, C. N., Burton, M. G., Kelly, B. C., & Klessen, R. S. 2012, MNRAS, 425, 720, doi: 10.1111/j.1365-2966.2012.21588.x

Shimajiri, Y., Takahashi, S., Takakuwa, S., Saito, M., & Kawabe, R. 2008, ApJ, 683, 255, doi: 10.1086/588629

Shirley, Y. L., Evans, Neal J., I., Young, K. E., Knez, C., & Jaffe, D. T. 2003, ApJS, 149, 375, doi: 10.1086/379147

Solomon, P. M., Rivolo, A. R., Barrett, J., & Yahil, A. 1987, ApJ, 319, 730, doi: 10.1086/165493

Spilker, A., Kainulainen, J., & Orkisz, J. 2021, A&A, 653, A63, doi: 10.1051/0004-6361/202040021

Spitzer, Lyman, J. 1956, ApJ, 124, 20, doi: 10.1086/146200

Sridharan, T. K., Beuther, H., Schilke, P., Menten, K. M., & Wyrowski, F. 2002, ApJ, 566, 931, doi: 10.1086/338332

Stier, M. T., Jaffe, D. T., Rengarajan, T. N., et al. 1984, ApJ, 283, 573, doi: 10.1086/162342

Stutzki, J., Bensch, F., Heithausen, A., Ossenkopf, V., & Zielinsky, M. 1998, A&A, 336, 697

Stutzki, J., & Guesten, R. 1990, ApJ, 356, 513, doi: 10.1086/168859

Su, Y., Yang, J., Zhang, S., et al. 2019, ApJS, 240, 9, doi: 10.3847/1538-4365/aaf1c8

Sunada, K., Nakazato, T., Ikeda, N., et al. 2007, PASJ, 59, 1185, doi: 10.1093/pasj/59.6.1185

Tafalla, M., Myers, P. C., Caselli, P., Walmsley, C. M., & Comito, C. 2002, ApJ, 569, 815, doi: 10.1086/339321

Takekoshi, T., Fujita, S., Nishimura, A., et al. 2019, ApJ, 883, 156, doi: 10.3847/1538-4357/ab3a55

Tanaka, K., Nagai, M., Kamegai, K., Iino, T., & Sakai, T. 2020, ApJ, 903, 111, doi: 10.3847/1538-4357/abbcca

Tassis, K., Christie, D. A., Urban, A., et al. 2010, MNRAS, 408, 1089, doi: 10.1111/j.1365-2966.2010.17181.x

Thompson, M. A., Urquhart, J. S., Moore, T. J. T., & Morgan, L. K. 2012, MNRAS, 421, 408, doi: 10.1111/j.1365-2966.2011.20315.x

Torii, K., Fujita, S., Nishimura, A., et al. 2019, PASJ, 71, S2, doi: 10.1093/pasj/psz033

Toujima, H., Nagayama, T., Omodaka, T., et al. 2011, PASJ, 63, 1259, doi: 10.1093/pasj/63.6.1259

Traficante, A., Duarte-Cabral, A., Elia, D., et al. 2018, MNRAS, 477, 2220, doi: 10.1093/mnras/sty798

Tremblin, P., Schneider, N., Minier, V., et al. 2014, A&A, 564, A106, doi: 10.1051/0004-6361/201322700

Tursun, K., Esimbek, J., Henkel, C., et al. 2020, A&A, 643, A178, doi: 10.1051/0004-6361/202037659

Umemoto, T., Minamidani, T., Kuno, N., et al. 2017, PASJ, 69, 78, doi: 10.1093/pasj/psx061

Urquhart, J. S., Thompson, M. A., Morgan, L. K., et al. 2007, A&A, 467, 1125, doi: 10.1051/0004-6361:20077236

Urquhart, J. S., Hoare, M. G., Purcell, C. R., et al. 2009, A&A, 501, 539, doi: 10.1051/0004-6361/200912108

Urquhart, J. S., Morgan, L. K., Figura, C. C., et al. 2011, MNRAS, 418, 1689, doi: 10.1111/j.1365-2966.2011.19594.x

Urquhart, J. S., Csengeri, T., Wyrowski, F., et al. 2014, A&A, 568, A41, doi: 10.1051/0004-6361/201424126

Urquhart, J. S., Figura, C. C., Moore, T. J. T., et al. 2015, MNRAS, 452, 4029, doi: 10.1093/mnras/stv1514

Vázquez-Semadeni, E. 1994, ApJ, 423, 681, doi: 10.1086/173847

Vázquez-Semadeni, E. 1999, in Astrophysics and Space Science Library, Vol. 241, Millimeter-Wave Astronomy: Molecular Chemistry & Physics in Space., ed. W. F. Wall, A. Carramiñana, & L. Carrasco, 161, doi: 10.1007/978-94-011-4714-9_9

Vázquez-Semadeni, E., & García, N. 2001, ApJ, 557, 727, doi: 10.1086/321688

VERA Collaboration, Hirota, T., Nagayama, T., et al. 2020, PASJ, 72, 50, doi: 10.1093/pasj/psaa018

Walsh, A. J., Breen, S. L., Britton, T., et al. 2011, MNRAS, 416, 1764, doi: 10.1111/j.1365-2966.2011.19115.x

Wang, K., Testi, L., Ginsburg, A., et al. 2015, MNRAS, 450, 4043, doi: 10.1093/mnras/stv735

Wang, S., Ren, Z., Li, D., et al. 2020, MNRAS, 499, 4432, doi: 10.1093/mnras/staa3059

Ward-Thompson, D., Di Francesco, J., Hatchell, J., et al. 2007, PASP, 119, 855, doi: 10.1086/521277

White, R. L., Becker, R. H., & Helfand, D. J. 2005, AJ, 130, 586, doi: 10.1086/431249

Wienen, M., Wyrowski, F., Menten, K. M., et al. 2018, A&A, 609, A125, doi: 10.1051/0004-6361/201526384

Willacy, K., Langer, W. D., & Velusamy, T. 1998, ApJ, 507, L171, doi: 10.1086/311695

Williams, J. P., Blitz, L., & McKee, C. F. 2000, in Protostars and Planets IV, ed. V. Mannings, A. P. Boss, & S. S. Russell, 97. https://arxiv.org/abs/astro-ph/9902246

Williams, J. P., de Geus, E. J., & Blitz, L. 1994, ApJ, 428, 693, doi: 10.1086/174279

Wilson, R. W., Jefferts, K. B., & Penzias, A. A. 1970, ApJ, 161, L43, doi: 10.1086/180567

Wilson, T. L., Batrla, W., & Pauls, T. A. 1982, A&A, 110, L20

Wilson, T. L., Bieging, J., & Downes, D. 1978, A&A, 63, 1

Wilson, T. L., & Rood, R. 1994, ARA&A, 32, 191, doi: 10.1146/annurev.aa.32.090194.001203

Wolfire, M. G., McKee, C. F., Hollenbach, D., & Tielens, A. G. G. M. 2003, ApJ, 587, 278, doi: 10.1086/368016

Wright, N. J., Drew, J. E., & Mohr-Smith, M. 2015, MNRAS, 449, 741, doi: 10.1093/mnras/stv323

Wu, J., Evans, Neal J., I., Shirley, Y. L., & Knez, C. 2010, ApJS, 188, 313, doi: 10.1088/0067-0049/188/2/313

Yamagishi, M., Nishimura, A., Fujita, S., et al. 2018, ApJS, 235, 9, doi: 10.3847/1538-4365/aaab4b

Yoda, T., Handa, T., Kohno, K., et al. 2010, PASJ, 62, 1277, doi: 10.1093/pasj/62.5.1277

Yonekura, Y., Dobashi, K., Mizuno, A., Ogawa, H., & Fukui, Y. 1997, ApJS, 110, 21, doi: 10.1086/312994

Zhang, Q., & Ho, P. T. P. 1995, ApJ, 450, L63, doi: 10.1086/316772

Appendix A

All cloud parameters in Cygnus X complex identified with SCIMES

Table A.1: All cloud parameters identified from the Cygnus-X CO survey.

ID	l [deg.]	b [deg.]	$v_{\rm LSR}$ [km s^{-1}]	σ_v [km s^{-1}]	$S_{\rm exact}$ [pix.^{2}]
1	77.874	−0.477	−1.85	0.74	101
2	77.882	−1.270	−7.51	1.63	446
3	77.964	−0.437	−5.32	0.89	317
4	77.981	−0.397	+11.53	0.68	142
5	78.003	−1.064	+13.75	1.03	402
6	78.058	−0.459	−3.33	0.55	226
7	78.063	−1.009	−0.15	2.34	14202
8	78.065	−0.381	+13.25	0.34	68
9	78.122	−0.860	+14.51	0.63	296
10	78.157	−1.280	+14.00	1.00	485
11	78.166	+0.002	+0.73	1.06	213
12	78.203	−0.148	−7.99	1.56	102
13	78.218	−0.314	+13.69	0.47	357
14	78.226	+0.536	−0.59	2.78	3656
15	78.235	+0.234	+14.13	0.62	544
16	78.323	+0.370	−3.28	0.47	234
17	78.368	−0.476	+11.26	2.03	1870
18	78.403	−1.047	+12.86	1.42	478
19	78.408	−0.241	+13.47	0.38	139
20	78.438	+0.395	−0.94	1.71	379
21	78.475	+0.066	−6.98	1.10	310
22	78.479	+0.105	+8.63	1.30	5915
23	78.494	−1.256	+13.01	0.75	148
24	78.517	−0.328	+12.63	0.47	273
25	78.535	−0.852	+5.63	0.97	1499
26	78.553	+0.179	+4.11	0.55	232
27	78.568	−0.149	−6.77	1.02	82
28	78.572	−1.210	−0.47	1.96	238
29	78.606	+0.175	+1.77	0.41	200
30	78.632	+0.263	+8.70	0.55	283
31	78.639	+0.425	+3.02	0.54	131
32	78.657	+0.772	−5.54	1.24	2475
33	78.667	−1.026	+5.48	0.43	264
34	78.703	−0.055	+2.98	0.42	459
35	78.762	−1.120	+4.92	0.39	217

Table A.1: *continued.*

ID	l [deg.]	b [deg.]	$v_{\rm LSR}$ [km s^{-1}]	σ_v [km s^{-1}]	$S_{\rm exact}$ [pix.^{2}]
36	78.777	−1.109	−0.08	1.61	481
37	78.837	−0.902	+11.06	1.22	342
38	78.875	−0.735	−3.03	0.77	379
39	78.885	−0.615	+4.59	0.34	263
40	78.916	+0.223	+4.06	4.58	4492
41	78.929	−0.614	+8.05	1.08	335
42	78.993	+0.866	+9.20	0.42	177
43	78.996	+0.051	−4.18	1.31	232
44	79.005	+0.614	+6.37	1.03	532
45	79.057	+0.475	−2.61	0.84	290
46	79.077	−0.284	+12.53	0.50	245
47	79.080	−0.969	+12.71	0.97	337
48	79.107	−0.070	+8.29	0.55	89
49	79.181	+0.956	+7.21	0.88	1009
50	79.186	+0.428	+11.11	0.70	97
51	79.188	−1.013	+9.03	3.00	1053
52	79.195	+0.534	+10.23	0.64	422
53	79.199	+0.400	+8.29	0.68	370
54	79.235	−0.036	−0.16	2.92	21290
55	79.237	−0.789	+13.38	0.48	224
56	79.251	+0.803	+11.88	0.58	202
57	79.254	+0.104	−2.30	0.89	280
58	79.269	+0.250	+4.01	1.12	135
59	79.297	−0.528	+10.44	1.13	684
60	79.297	+0.916	+11.56	0.85	254
61	79.300	+0.049	+9.72	1.19	198
62	79.308	−0.260	−5.36	0.45	138
63	79.337	−1.020	+6.67	0.94	124
64	79.364	−0.472	+0.93	0.78	868
65	79.400	−0.636	+4.68	1.48	5631
66	79.422	−0.720	+12.94	0.98	625
67	79.457	+0.938	−2.32	1.08	3937
68	79.476	−0.041	+7.79	1.30	473
69	79.504	+0.970	+11.83	0.97	536
70	79.507	−0.979	+6.93	0.81	116

Table A.1: *continued.*

ID	l [deg.]	b [deg.]	$v_{\rm LSR}$ [km s^{-1}]	σ_v [km s^{-1}]	$S_{\rm exact}$ [pix.^{2}]
71	79.645	+0.346	+5.73	0.59	237
72	79.661	−0.721	+10.74	0.64	165
73	79.681	−0.360	+3.39	0.71	423
74	79.710	−0.884	−2.03	0.57	215
75	79.759	−0.636	−1.28	0.23	147
76	79.787	−0.482	+0.11	0.71	149
77	79.813	+1.010	−7.50	0.72	421
78	79.836	+0.890	+10.76	0.63	447
79	79.852	+0.834	−4.06	0.76	436
80	79.971	+1.179	+12.69	0.50	477
81	80.018	−0.403	+0.11	1.15	545
82	80.044	+0.571	+11.22	0.59	426
83	80.099	+0.617	+3.78	1.24	1064
84	80.165	−0.411	−1.21	0.68	146
85	80.314	+0.268	−1.09	1.06	407
86	80.334	+0.708	−1.66	0.82	196
87	80.347	+0.558	−4.10	0.97	254
88	80.377	+0.442	+8.37	0.87	137
89	80.388	+0.700	+5.57	0.77	171
90	80.451	+0.274	+7.34	0.67	793
91	80.561	+1.031	−1.75	0.92	419
92	80.599	+1.210	+13.45	0.35	422
93	80.719	+0.835	+3.68	1.01	484
94	80.736	−0.581	−4.45	0.97	748
95	80.776	+0.511	−1.97	1.40	4231
96	80.801	−0.337	+5.48	1.74	13787
97	80.811	+0.375	+5.66	0.68	420
98	80.850	+0.560	+11.88	0.99	143
99	80.853	−0.372	+11.01	0.75	339
100	80.905	−0.310	−2.74	1.63	643
101	80.931	+1.060	+9.64	0.67	118
102	80.936	+1.444	+6.56	0.78	154
103	81.066	+1.301	+3.81	0.62	192
104	81.142	+0.127	+10.06	0.89	709
105	81.145	+0.749	+2.47	0.47	241

Table A.1: *continued.*

ID	l [deg.]	b [deg.]	$v_{\rm LSR}$ [km s^{-1}]	σ_v [km s^{-1}]	$S_{\rm exact}$ [pix.^{2}]
106	81.181	+1.315	−0.89	0.47	438
107	81.243	+0.621	+7.89	4.90	14139
108	81.246	+1.437	+4.95	0.47	620
109	81.361	−0.029	−5.00	1.49	3786
110	81.370	+1.454	−3.96	0.63	283
111	81.371	+1.237	+10.29	1.69	184
112	81.423	−0.145	+11.30	0.48	153
113	81.428	+0.941	−5.27	0.59	131
114	81.482	−0.181	+5.53	0.55	403
115	81.482	+1.369	−4.25	0.39	274
116	81.523	+1.331	+11.77	1.06	297
117	81.547	−0.066	−0.70	0.86	104
118	81.631	−0.254	+4.74	0.40	356
119	81.734	+0.964	+0.11	3.04	11051
120	81.771	+0.344	−5.89	0.43	313
121	81.839	+0.255	+8.65	1.66	12211
122	81.851	+1.299	+11.30	1.10	1566
123	81.908	+0.082	+14.24	0.93	865
124	82.061	+0.924	−3.96	0.57	91

Appendix B

All cloud parameters from FUGIN survey identified with SCIMES

Table B.1: All cloud parameters identified from the FUGIN survey.

ID	l [deg.]	b [deg.]	$v_{\rm LSR}$ [km s^{-1}]	$\tau_{^{13}\rm CO}$	$T_{\rm ex}$ [K]	$S_{\rm exact}$ [pix.^{2}]
FGN12.405–0.814	12.405	−0.814	+34.15	0.479	11.67	4047
FGN12.589–0.358	12.589	−0.358	+8.58	0.431	10.05	6084
FGN12.711+0.549	12.711	+0.549	+19.32	0.406	14.61	14375
FGN12.738+0.497	12.738	+0.497	+31.34	0.52	10.72	7755
FGN12.943–0.260	12.943	−0.260	+36.39	0.55	15.46	19723
FGN13.315+0.207	13.315	+0.207	+18.33	0.375	15.52	4835
FGN13.910+0.160	13.910	+0.160	+47.46	0.392	12.24	5938
FGN13.916+0.817	13.916	+0.817	+26.80	0.407	9.59	9705
FGN14.083–0.543	14.083	−0.543	+20.00	0.367	16.97	26297
FGN14.226–0.210	14.226	−0.210	+39.50	0.483	15.05	22290
FGN14.710–0.152	14.710	−0.152	+26.46	0.505	11.01	13170
FGN15.039–0.610	15.039	−0.610	+19.91	0.237	24.72	5248
FGN15.252+0.009	15.252	+0.009	+31.36	0.506	11.12	5978
FGN15.869–0.640	15.869	−0.640	+18.85	0.28	18.0	4847
FGN16.249+0.630	16.249	+0.630	+27.62	0.296	14.31	4806
FGN16.620–0.313	16.620	−0.313	+41.29	0.393	13.09	37693
FGN16.628–0.138	16.628	−0.138	+57.58	0.386	11.37	5148
FGN17.042+0.614	17.042	+0.614	+22.40	0.315	18.1	21627
FGN17.321–0.726	17.321	−0.726	+62.72	0.447	9.27	5170
FGN17.716+0.232	17.716	+0.232	+23.25	0.417	13.01	7864
FGN18.412–0.236	18.412	−0.236	+47.76	0.412	15.2	14449
FGN18.890–0.441	18.890	−0.441	+65.02	0.406	14.9	13486
FGN19.440+0.039	19.440	+0.039	+25.59	0.435	11.37	8433
FGN19.479+0.285	19.479	+0.285	+5.91	0.452	10.15	7020
FGN19.892–0.729	19.892	−0.729	+43.89	0.363	13.33	10511
FGN19.916–0.235	19.916	−0.235	+67.42	0.409	11.03	7478
FGN20.419+0.679	20.419	+0.679	+6.09	0.467	9.79	12806
FGN21.314+0.504	21.314	+0.504	+7.84	0.323	11.25	10408
FGN22.035+0.235	22.035	+0.235	+51.22	0.385	11.26	7148
FGN22.201–0.570	22.201	−0.570	+52.75	0.515	9.61	11827
FGN22.601–0.113	22.601	−0.113	+108.51	0.492	9.99	5316
FGN22.825+0.105	22.825	+0.105	+4.17	0.703	7.78	6129
FGN23.042–0.319	23.042	−0.319	+73.30	0.461	13.45	22132
FGN23.275–0.103	23.275	−0.103	+53.46	0.662	9.66	5429
FGN23.399–0.179	23.399	−0.179	+98.98	0.533	12.25	6596

Table B.1: *continued.*

ID	l [deg.]	b [deg.]	$v_{\rm LSR}$ [km s^{-1}]	$\tau_{^{13}\rm CO}$	$T_{\rm ex}$ [K]	$S_{\rm exact}$ [pix.^{2}]
FGN23.513+0.136	23.513	+0.136	+87.90	0.436	13.04	4126
FGN23.889+0.427	23.889	+0.427	+95.36	0.467	10.28	7218
FGN24.414+0.216	24.414	+0.216	+109.37	0.469	11.88	30945
FGN24.451–0.090	24.451	−0.090	+50.05	0.484	11.06	31745
FGN24.504–0.535	24.504	−0.535	+60.37	0.459	10.45	7035
FGN24.631–0.204	24.631	−0.204	+92.42	0.357	13.19	4705
FGN25.314–0.388	25.314	−0.388	+58.27	0.447	10.61	14327
FGN25.607–0.173	25.607	−0.173	+94.24	0.375	13.02	10348
FGN25.842+0.679	25.842	+0.679	+46.12	0.492	9.44	22802
FGN26.086+0.038	26.086	+0.038	+104.03	0.384	12.23	23074
FGN26.459–0.616	26.459	−0.616	+65.05	0.349	11.39	8105
FGN27.370+0.105	27.370	+0.105	+96.12	0.422	11.84	12634
FGN28.139–0.366	28.139	−0.366	+45.97	0.507	10.52	6567
FGN28.393+0.000	28.393	+0.000	+78.27	0.504	10.11	26085
FGN28.859–0.014	28.859	−0.014	+95.94	0.45	12.86	16869
FGN29.267–0.139	29.267	−0.139	+79.57	0.355	13.76	12854
FGN29.279–0.625	29.279	−0.625	+64.36	0.449	11.12	6481
FGN29.349–0.297	29.349	−0.297	+95.41	0.343	15.67	4764
FGN29.820–0.554	29.820	−0.554	+75.99	0.388	11.68	14419
FGN29.944–0.120	29.944	−0.120	+99.43	0.367	15.88	13684
FGN30.461+0.028	30.461	+0.028	+42.91	0.337	12.98	4660
FGN30.486–0.436	30.486	−0.436	+12.17	0.479	13.22	5169
FGN30.585+0.566	30.585	+0.566	+86.53	0.344	14.15	5184
FGN30.661–0.790	30.661	−0.790	+78.89	0.464	9.94	5414
FGN30.685–0.012	30.685	−0.012	+95.47	0.407	18.62	24366
FGN31.093+0.227	31.093	+0.227	+79.66	0.376	15.23	8834
FGN31.188+0.001	31.188	+0.001	+40.91	0.332	13.29	9032
FGN31.662–0.346	31.662	−0.346	+100.43	0.372	12.88	5444
FGN31.812+0.148	31.812	+0.148	+96.72	0.424	16.54	5848
FGN32.631–0.221	32.631	−0.221	+10.09	0.354	9.98	4792
FGN32.783+0.018	32.783	+0.018	+93.44	0.41	13.6	5435
FGN33.301+0.039	33.301	+0.039	+80.87	0.548	9.52	5073
FGN33.914–0.370	33.914	−0.370	+11.81	0.53	9.55	43078
FGN34.438–0.767	34.438	−0.767	+56.97	0.34	10.72	6144
FGN34.487+0.258	34.487	+0.258	+54.80	0.514	10.14	28480

Table B.1: *continued.*

ID	l [deg.]	b [deg.]	$v_{\rm LSR}$ [km s^{-1}]	$\tau_{^{13}\rm CO}$	$T_{\rm ex}$ [K]	$S_{\rm exact}$ [pix.^{2}]
FGN34.655–0.086	34.655	−0.086	+78.22	0.444	9.62	5025
FGN34.810+0.102	34.810	+0.102	+43.85	0.366	11.2	7008
FGN35.061–0.454	35.061	−0.454	+45.71	0.433	13.01	22461
FGN35.226–0.805	35.226	−0.805	+34.86	0.461	13.17	9331
FGN35.357–0.024	35.357	−0.024	+13.33	0.496	9.17	36140
FGN35.475+0.157	35.475	+0.157	+79.70	0.354	11.17	5400
FGN36.415–0.139	36.415	−0.139	+54.80	0.465	10.19	14093
FGN36.781–0.196	36.781	−0.196	+79.25	0.452	10.23	10303
FGN36.921+0.807	36.921	+0.807	+13.07	1.219	5.88	4865
FGN37.647+0.027	37.647	+0.027	+85.92	0.488	9.00	15748
FGN37.896–0.339	37.896	−0.339	+13.06	0.724	7.02	5229
FGN38.311–0.250	38.311	−0.250	+63.76	0.505	8.77	6678
FGN38.320–0.873	38.320	−0.873	+16.56	0.426	10.13	4180
FGN38.519–0.009	38.519	−0.009	+81.78	0.566	8.00	4862
FGN38.826+0.780	38.826	+0.780	+31.41	0.603	7.53	8159
FGN38.906–0.457	38.906	−0.457	+41.66	0.378	12.77	6194
FGN39.614–0.327	39.614	−0.327	+60.30	0.404	10.43	20686
FGN41.093–0.072	41.093	−0.072	+39.25	0.417	9.53	7176
FGN41.211–0.252	41.211	−0.252	+59.49	0.334	12.38	5160
FGN42.063–0.472	42.063	−0.472	+68.21	0.464	9.64	7517
FGN42.785–0.252	42.785	−0.252	+61.81	0.438	9.72	4534
FGN44.458–0.286	44.458	−0.286	+61.59	0.611	8.96	6227
FGN45.446+0.085	45.446	+0.085	+59.53	0.450	10.91	5460
FGN45.805–0.355	45.805	−0.355	+58.62	0.966	7.12	6042
FGN47.489–0.849	47.489	−0.849	+7.05	0.525	8.94	6901
FGN49.424–0.328	49.424	−0.328	+58.44	0.422	14.59	7132

Table B.2: N-PDF fitting parameters of all selected clouds identified from the FUGIN survey.

ID	N-PDF type	p_1	$\bar{N}_1$	σ_1	p_2	$\bar{N}_2$	σ_2	p_3	$\bar{N}_3$	σ_3	Edge
FGN12.405–0.814	LN1	0.181	21.81	0.220	–	–	–	–	–	–	N
FGN12.589–0.358	LN1	0.112	21.77	0.274	–	–	–	–	–	–	N
FGN12.711+0.549	LN1+LN2	0.104	21.76	0.296	0.017	22.40	0.213	–	–	–	N
FGN12.738+0.497	LN1+LN2	0.127	21.80	0.229	0.007	22.58	0.125	–	–	–	N
FGN12.943–0.260	UN	–	–	–	–	–	–	–	–	–	N
FGN13.315+0.207	LN1	0.132	22.01	0.208	–	–	–	–	–	–	N
FGN13.910+0.160	LN1	0.103	21.67	0.418	–	–	–	–	–	–	N
FGN13.916+0.817	LN1+LN2	0.118	21.56	0.259	0.024	22.06	0.104	–	–	–	Y
FGN14.083–0.543	LN1+LN2	0.083	22.06	0.318	0.062	22.52	0.162	–	–	–	N
FGN14.226–0.210	LN1+LN2+LN3	0.091	22.00	0.288	0.044	22.44	0.173	0.016	22.83	0.100	N
FGN14.710–0.152	LN1	0.136	22.05	0.200	–	–	–	–	–	–	N
FGN15.039–0.610	LN1+LN2	0.079	22.37	0.338	0.007	23.33	0.295	–	–	–	N
FGN15.252+0.009	LN1	0.155	21.89	0.179	–	–	–	–	–	–	N
FGN15.869–0.640	LN1+LN2	0.083	21.90	0.273	0.047	22.28	0.173	–	–	–	N
FGN16.249+0.630	LN1+LN2	0.136	21.72	0.226	0.018	22.26	0.101	–	–	–	N
FGN16.620–0.313	LN1+LN2	0.093	21.88	0.318	0.033	22.36	0.189	–	–	–	N
FGN16.628–0.138	LN1+LN2	0.131	21.83	0.218	0.003	22.60	0.131	–	–	–	N
FGN17.042+0.614	LN1+LN2+LN3	0.077	21.82	0.292	0.044	22.27	0.178	0.041	22.62	0.159	Y
FGN17.321–0.726	LN1	0.128	21.64	0.230	–	–	–	–	–	–	N
FGN17.716+0.232	LN1	0.110	21.93	0.291	–	–	–	–	–	–	N
FGN18.412–0.236	LN1+LN2	0.091	21.83	0.340	0.028	22.40	0.330	–	–	–	N
FGN18.890–0.441	LN1+LN2	0.109	22.24	0.225	0.008	23.00	0.108	–	–	–	N
FGN19.440+0.039	LN1+LN2	0.109	21.86	0.321	0.027	22.40	0.071	–	–	–	N

Table B.2: *continued.*

ID	N-PDF type	p_1	$\bar{N}_1$	σ_1	p_2	$\bar{N}_2$	σ_2	p_3	$\bar{N}_3$	σ_3	Edge
FGN19.479+0.285	LN1	0.138	21.45	0.224	–	–	–	–	–	–	N
FGN19.892–0.729	LN1+LN2	0.120	22.06	0.253	0.017	22.67	0.090	–	–	–	Y
FGN19.916–0.235	LN1+LN2	0.091	21.70	0.280	0.043	22.18	0.172	–	–	–	N
FGN20.419+0.679	LN1	0.152	21.38	0.150	–	–	–	–	–	–	Y
FGN21.314+0.504	LN1	0.212	21.22	0.229	–	–	–	–	–	–	N
FGN22.035+0.235	LN1+LN2	0.145	21.80	0.180	0.006	22.24	0.177	–	–	–	N
FGN22.201–0.570	LN1	0.164	21.86	0.170	–	–	–	–	–	–	N
FGN22.601–0.113	LN1	0.103	21.88	0.313	–	–	–	–	–	–	N
FGN22.825+0.105	LN1	0.130	21.42	0.168	–	–	–	–	–	–	N
FGN23.042–0.319	LN1+LN2	0.083	22.02	0.225	0.058	22.47	0.190	–	–	–	N
FGN23.275–0.103	LN1	0.151	21.93	0.176	–	–	–	–	–	–	N
FGN23.399–0.179	LN1+LN2+LN3	0.080	21.92	0.406	0.021	22.63	0.230	0.011	23.01	0.108	N
FGN23.513+0.136	LN1+LN2	0.085	21.96	0.240	0.054	22.35	0.215	–	–	–	N
FGN23.889+0.427	LN1+LN2	0.100	21.94	0.174	0.011	22.40	0.113	–	–	–	N
FGN24.414+0.216	LN1+LN2	0.084	21.98	0.235	0.042	22.52	0.218	–	–	–	N
FGN24.451–0.090	LN1+LN2	0.100	21.79	0.253	0.057	22.14	0.178	–	–	–	N
FGN24.504–0.535	LN1+LN2	0.102	21.71	0.246	0.069	22.20	0.142	–	–	–	N
FGN24.631–0.204	LN1+LN2	0.117	22.03	0.230	0.002	22.60	0.152	–	–	–	N
FGN25.314–0.388	LN1+LN2	0.116	22.03	0.212	0.001	22.70	0.150	–	–	–	N
FGN25.607–0.173	LN1+LN2	0.101	21.85	0.343	0.014	22.56	0.119	–	–	–	N
FGN25.842+0.679	LN1	0.149	21.78	0.194	–	–	–	–	–	–	Y
FGN26.086+0.038	LN1	0.104	21.97	0.315	–	–	–	–	–	–	N
FGN26.459–0.616	LN1+LN2	0.096	21.64	0.220	0.050	22.05	0.190	–	–	–	Y

Table B.2: *continued.*

ID	N-PDF type	p_1	$\bar{N}_1$	σ_1	p_2	$\bar{N}_2$	σ_2	p_3	$\bar{N}_3$	σ_3	Edge
FGN27.370+0.105	LN1	0.107	21.91	0.271	–	–	–	–	–	–	N
FGN28.139–0.366	LN1+LN2	0.149	21.83	0.196	0.005	22.37	0.203	–	–	–	N
FGN28.393+0.000	LN1+LN2	0.105	21.87	0.265	0.043	22.24	0.184	–	–	–	N
FGN28.859–0.014	LN1+LN2	0.105	21.90	0.256	0.031	22.33	0.167	–	–	–	N
FGN29.267–0.139	LN1	0.121	21.94	0.273	–	–	–	–	–	–	N
FGN29.279–0.625	LN1	0.133	21.94	0.234	–	–	–	–	–	–	N
FGN29.349–0.297	LN1+LN2	0.083	21.95	0.302	0.045	22.38	0.183	–	–	–	N
FGN29.820–0.554	LN1+LN2	0.081	21.70	0.346	0.043	22.15	0.189	–	–	–	N
FGN29.944–0.120	LN1+LN2+LN3	0.072	21.98	0.258	0.064	22.49	0.218	0.014	23.09	0.161	N
FGN30.461+0.028	LN1	0.089	21.86	0.409	–	–	–	–	–	–	N
FGN30.486–0.436	LN1+LN2	0.094	21.45	0.279	0.039	22.11	0.288	–	–	–	N
FGN30.585+0.566	LN1	0.131	22.04	0.207	–	–	–	–	–	–	N
FGN30.661–0.790	LN1	0.135	21.74	0.225	–	–	–	–	–	–	N
FGN30.685–0.012	UN	–	–	–	–	–	–	–	–	–	N
FGN31.093+0.227	LN1	0.133	22.19	0.215	–	–	–	–	–	–	N
FGN31.188+0.001	LN1+LN2	0.067	21.65	0.273	0.066	22.19	0.250	–	–	–	N
FGN31.662–0.346	LN1	0.109	21.91	0.296	–	–	–	–	–	–	N
FGN31.812+0.148	LN1	0.102	22.02	0.357	–	–	–	–	–	–	N
FGN32.631–0.221	LN1	0.195	21.34	0.117	–	–	–	–	–	–	N
FGN32.783+0.018	LN1	0.127	22.09	0.247	–	–	–	–	–	–	N
FGN33.301+0.039	LN1+LN2	0.142	21.81	0.215	0.005	22.37	0.205	–	–	–	N
FGN33.914–0.370	LN1	0.130	21.63	0.236	–	–	–	–	–	–	Y
FGN34.438–0.767	UN	–	–	–	–	–	–	–	–	–	N

Table B.2: *continued.*

ID	N-PDF type	p_1	$\bar{N}_1$	σ_1	p_2	$\bar{N}_2$	σ_2	p_3	$\bar{N}_3$	σ_3	Edge
FGN34.487+0.258	LN1+LN2	0.093	21.99	0.301	0.001	23.00	0.148	–	–	–	N
FGN34.655–0.086	LN1	0.115	21.75	0.265	–	–	–	–	–	–	N
FGN34.810+0.102	LN1	0.119	21.54	0.355	–	–	–	–	–	–	N
FGN35.061–0.454	LN1+LN2	0.108	21.90	0.250	0.029	22.45	0.126	–	–	–	N
FGN35.226–0.805	LN1+LN2	0.093	21.82	0.391	0.006	22.69	0.197	–	–	–	Y
FGN35.357–0.024	LN1	0.136	21.55	0.210	–	–	–	–	–	–	N
FGN35.475+0.157	LN1	0.098	21.71	0.372	–	–	–	–	–	–	N
FGN36.415–0.139	LN1	0.123	21.87	0.181	–	–	–	–	–	–	N
FGN36.781–0.196	LN1	0.116	21.87	0.264	–	–	–	–	–	–	N
FGN36.921+0.807	LN1	0.145	21.61	0.216	–	–	–	–	–	–	Y
FGN37.647+0.027	LN1	0.120	21.86	0.216	–	–	–	–	–	–	N
FGN37.896–0.339	LN1	0.177	21.36	0.139	–	–	–	–	–	–	N
FGN38.311–0.250	LN1	0.121	21.75	0.292	–	–	–	–	–	–	N
FGN38.320–0.873	LN1	0.099	21.51	0.270	–	–	–	–	–	–	Y
FGN38.519–0.009	LN1+LN2	0.112	21.66	0.220	0.053	22.04	0.155	–	–	–	N
FGN38.826+0.780	LN1+LN2	0.135	21.57	0.175	0.024	22.03	0.122	–	–	–	Y
FGN38.906–0.457	LN1+LN2	0.100	21.73	0.333	0.015	22.58	0.178	–	–	–	N
FGN39.614–0.327	LN1	0.113	21.94	0.219	–	–	–	–	–	–	N
FGN41.093–0.072	LN1	0.134	21.78	0.162	–	–	–	–	–	–	N
FGN41.211–0.252	LN1+LN2	0.097	21.72	0.304	0.030	22.18	0.240	–	–	–	N
FGN42.063–0.472	LN1	0.114	21.69	0.314	–	–	–	–	–	–	N
FGN42.785–0.252	LN1	0.139	21.71	0.224	–	–	–	–	–	–	N
FGN44.458–0.286	LN1+LN2	0.082	21.69	0.244	0.068	22.19	0.208	–	–	–	N

Table B.2: *continued.*

ID	N-PDF type	p_1	$\bar{N}_1$	σ_1	p_2	$\bar{N}_2$	σ_2	p_3	$\bar{N}_3$	σ_3	Edge
FGN45.446+0.085	LN1+LN2	0.081	21.68	0.272	0.061	22.21	0.234	–	–	–	N
FGN45.805–0.355	LN1	0.118	21.95	0.260	–	–	–	–	–	–	N
FGN47.489–0.849	LN1	0.179	21.49	0.197	–	–	–	–	–	–	Y
FGN49.424–0.328	LN1+LN2+LN3	0.080	22.02	0.246	0.052	22.60	0.190	0.007	23.15	0.332	N

Appendix C

All cloud H_2 column density map and N-PDF identified from FUGIN survey

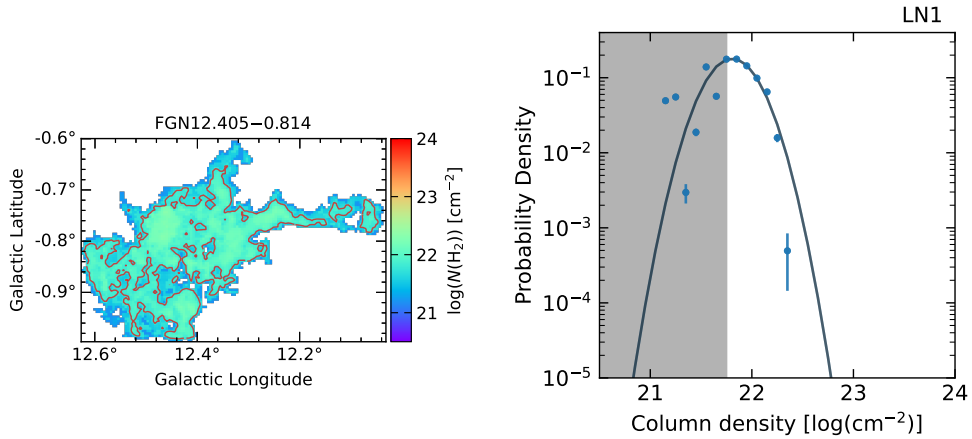

Figure C.1: Column density map (left panel) and N-PDF (right panel) for the identified molecular clouds from FUGIN survey. The red contours in the left panels indicate the completeness limit of H_2 column density. Blue, orange, and green curves in the right panels indicate LN1, LN2, and LN3, respectively. Black curves shows the best-fit curve. The grey-shaded areas correspond to column densities out of the completeness limit.

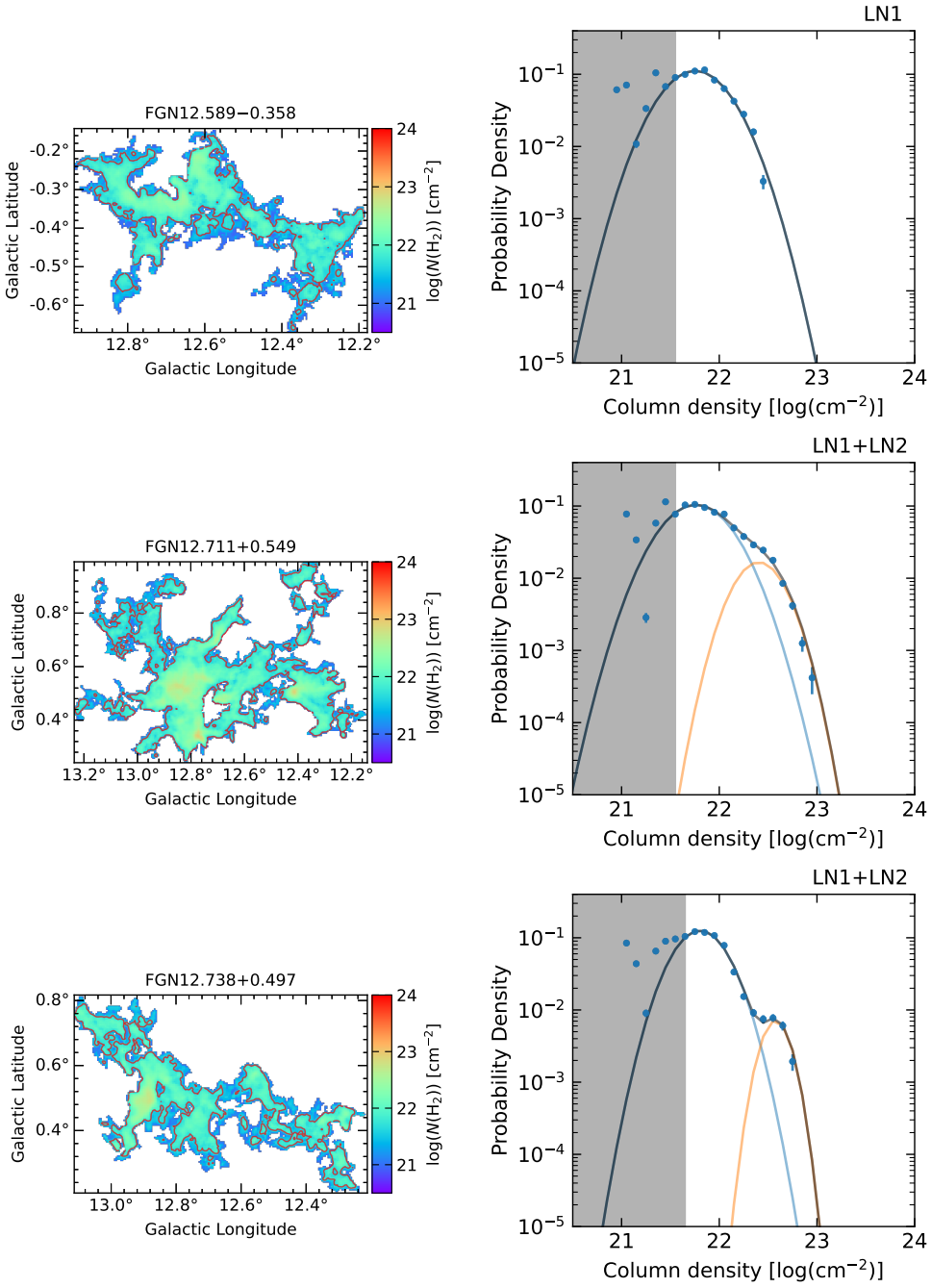

Figure C.1: *continued.*

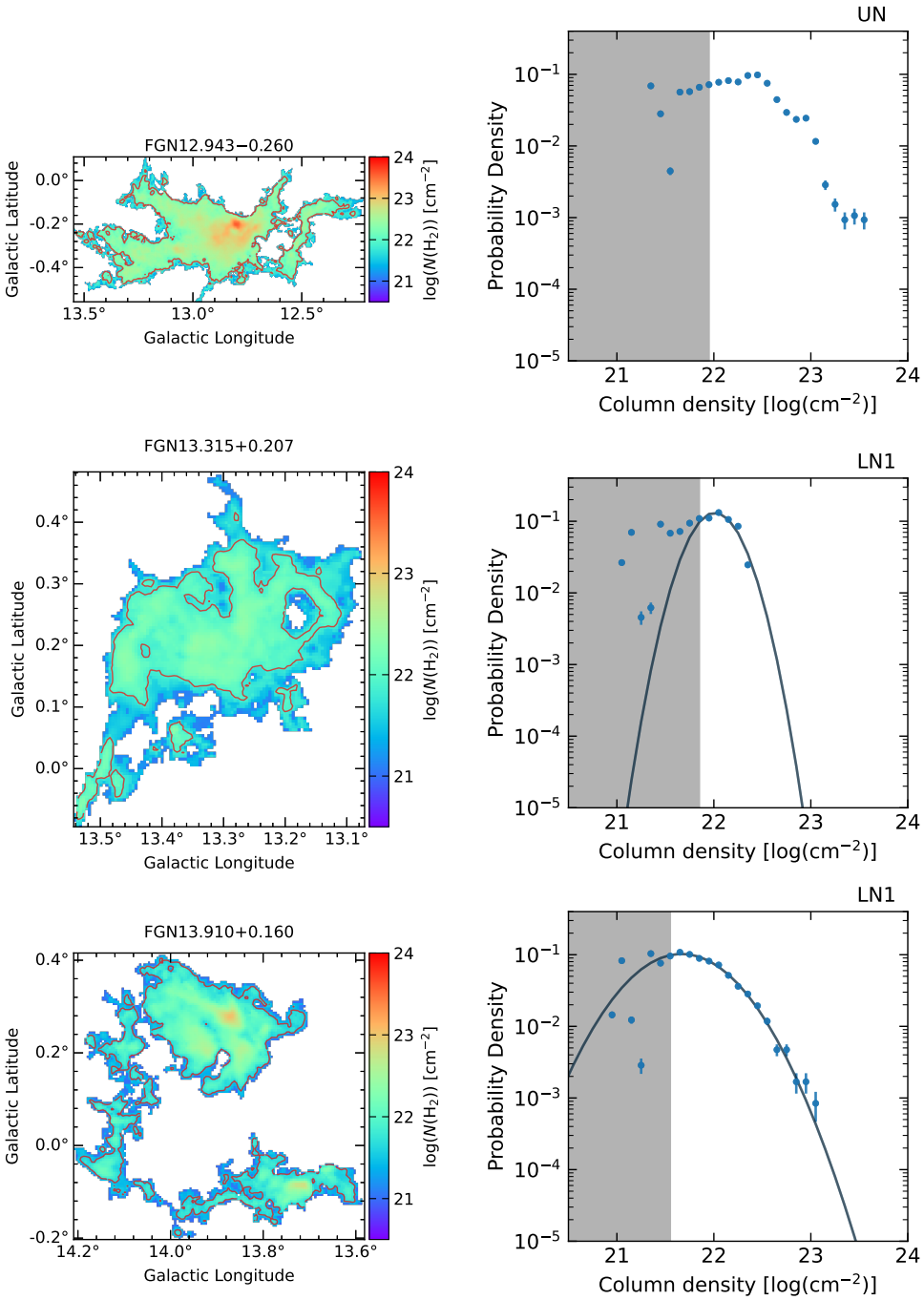

Figure C.1: *continued.*

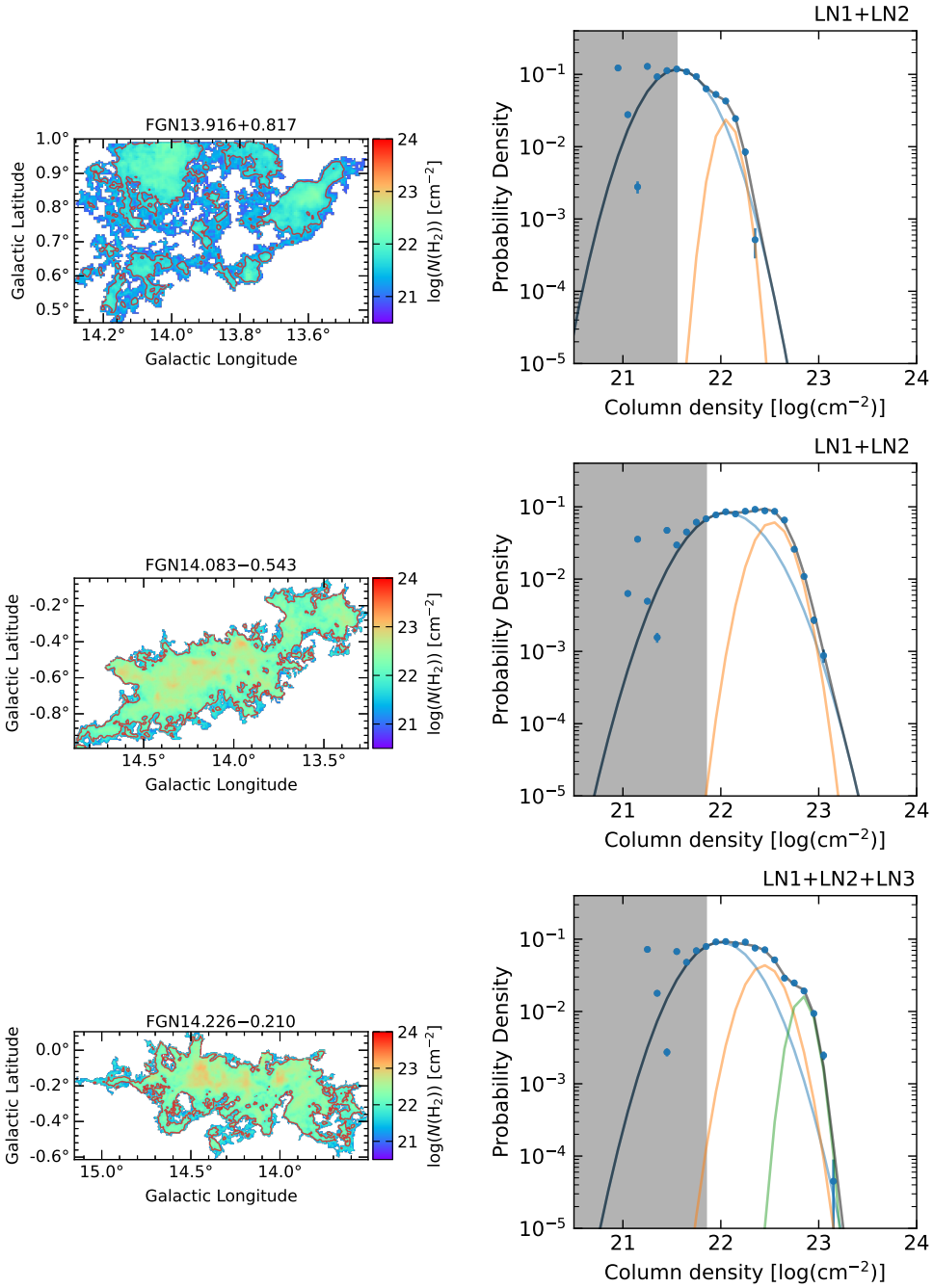

Figure C.1: *continued.*

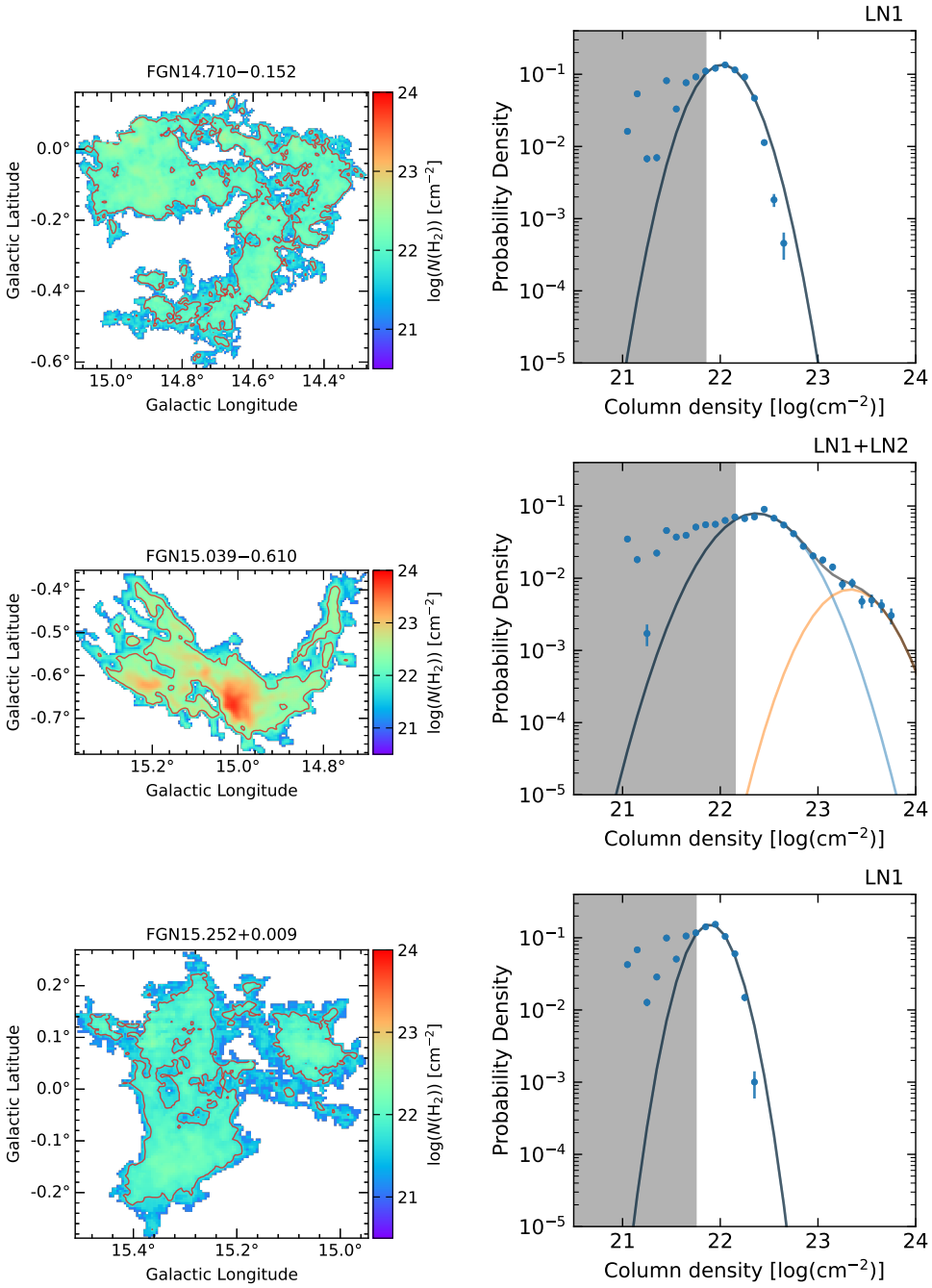

Figure C.1: *continued.*

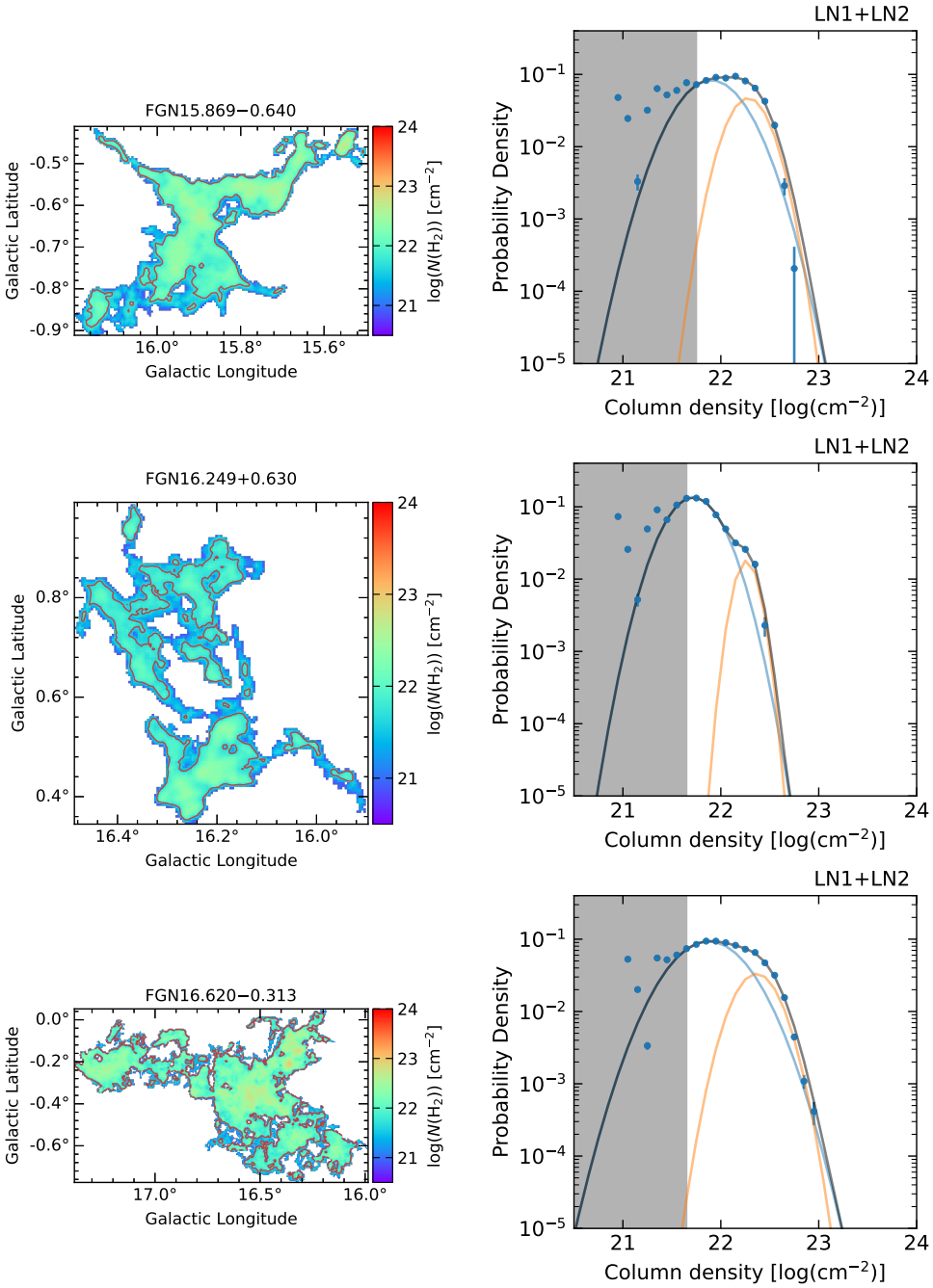

Figure C.1: *continued.*

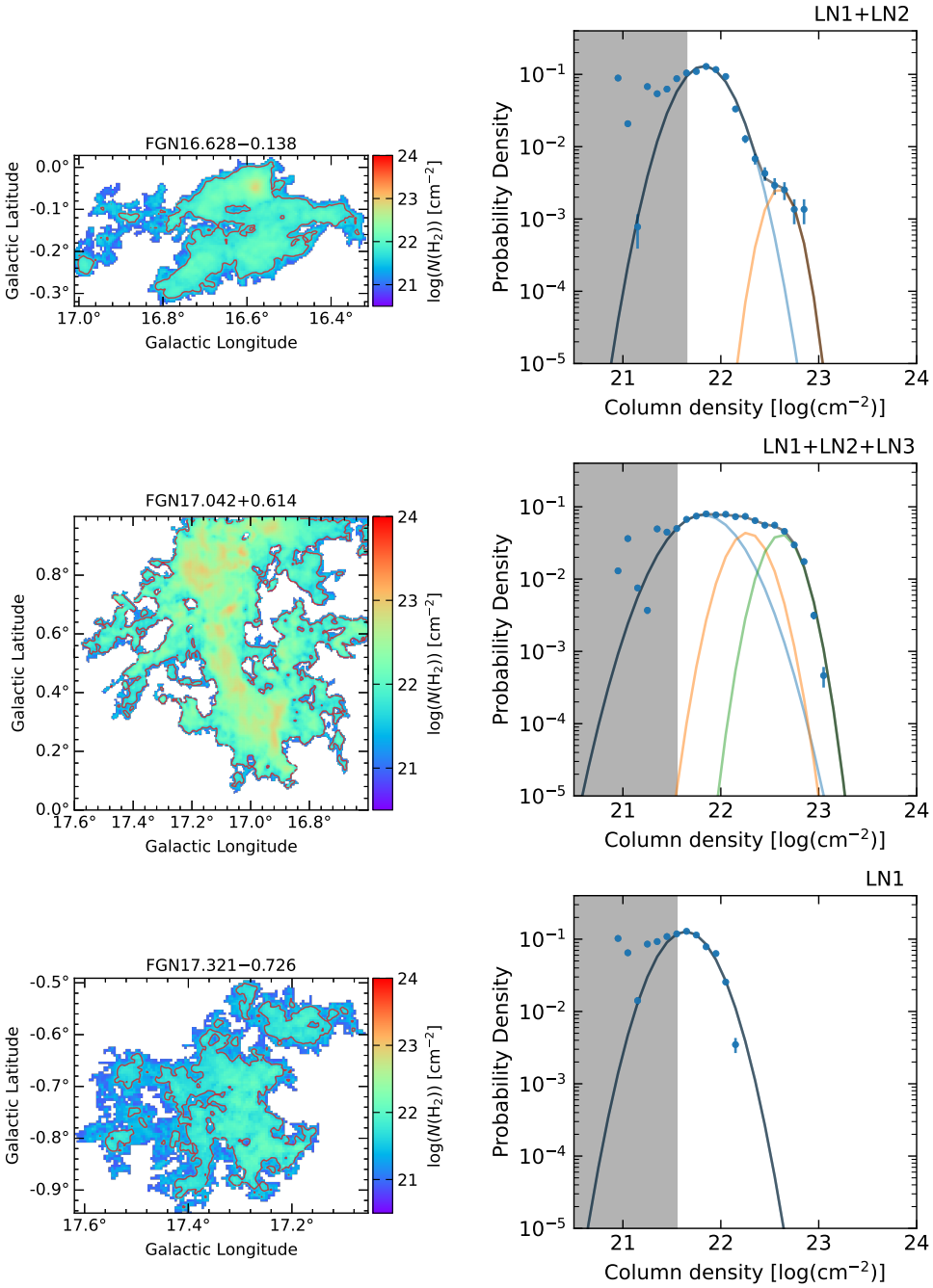

Figure C.1: *continued.*

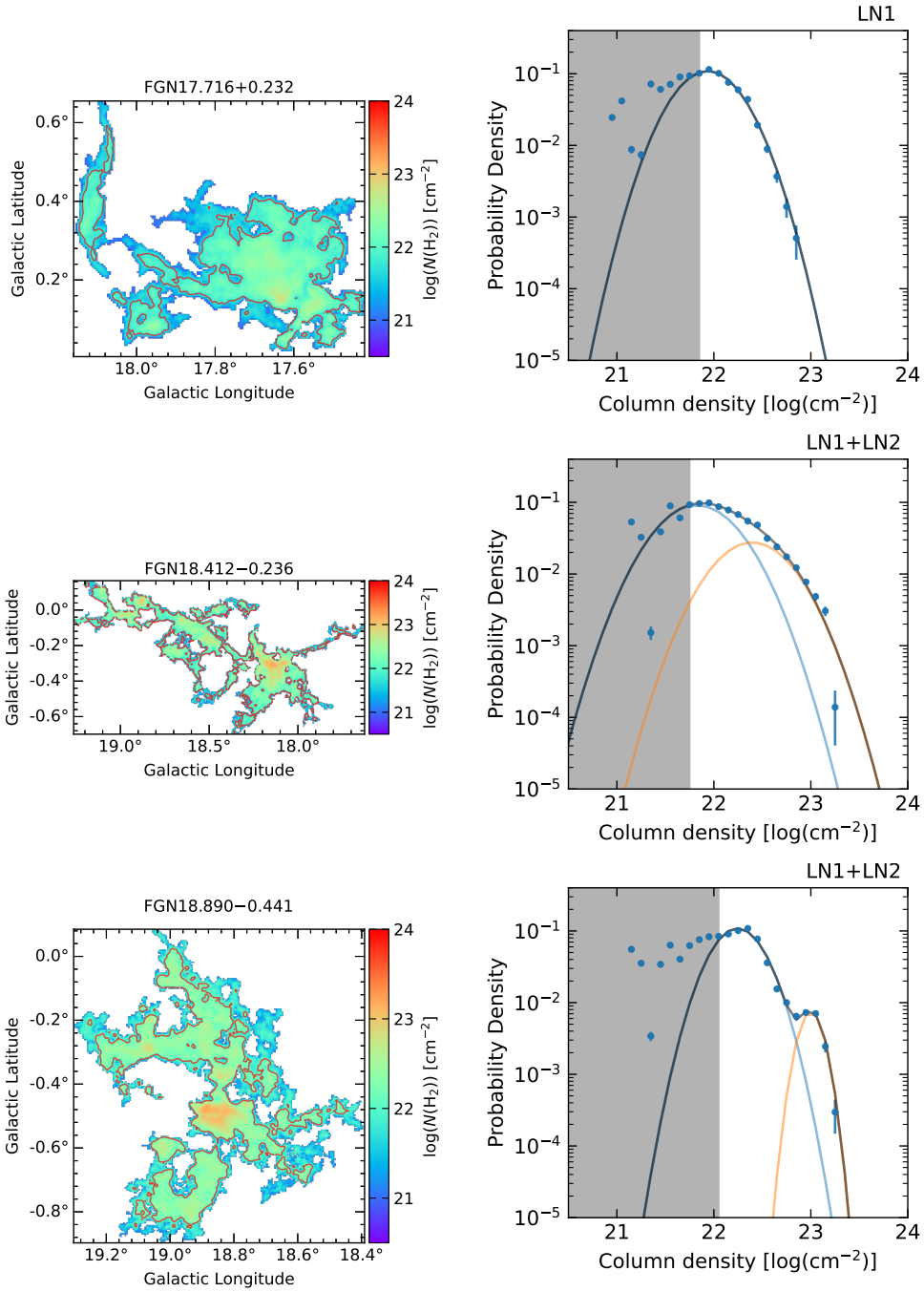

Figure C.1: *continued.*

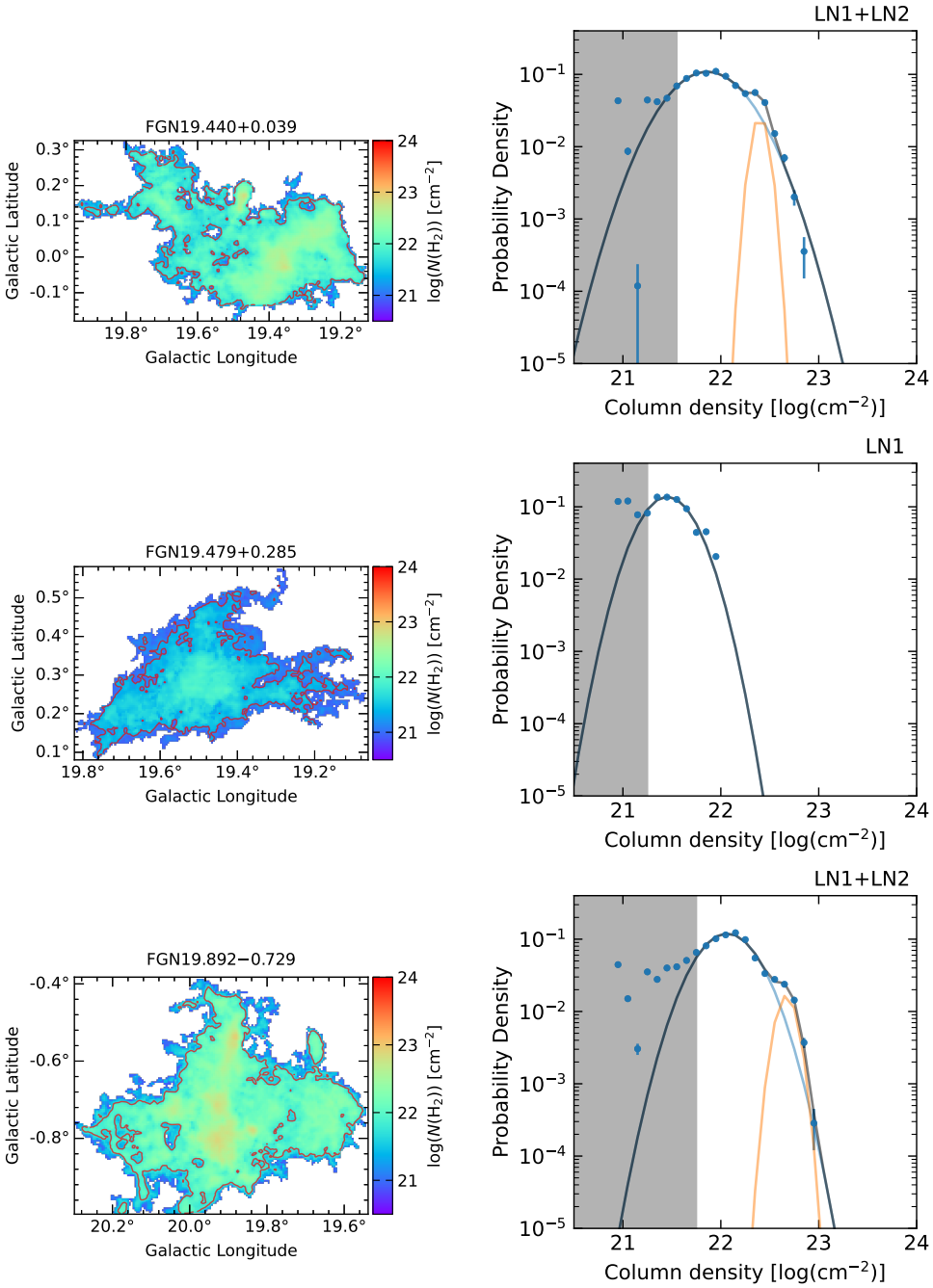

Figure C.1: *continued.*

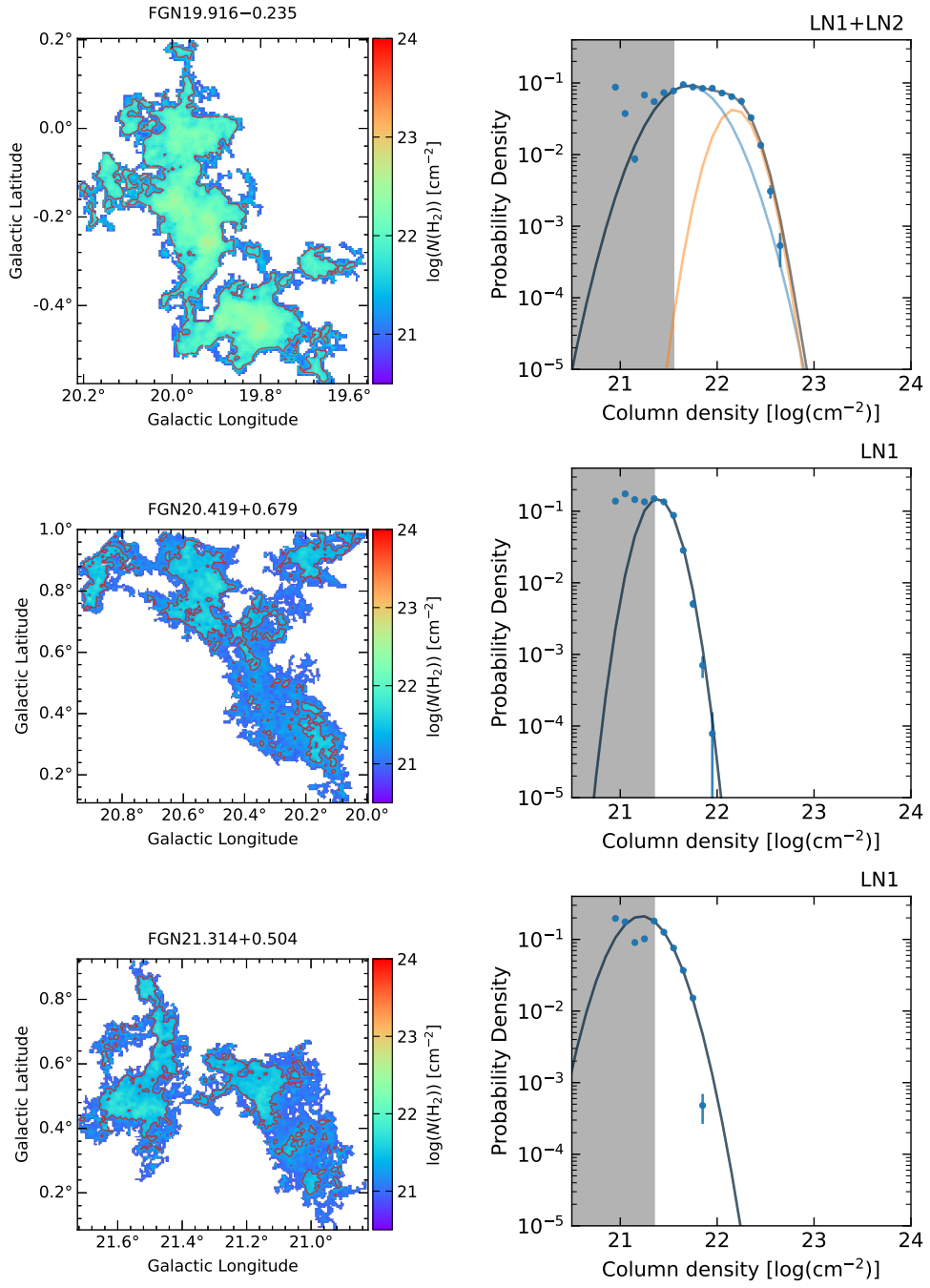

Figure C.1: *continued.*

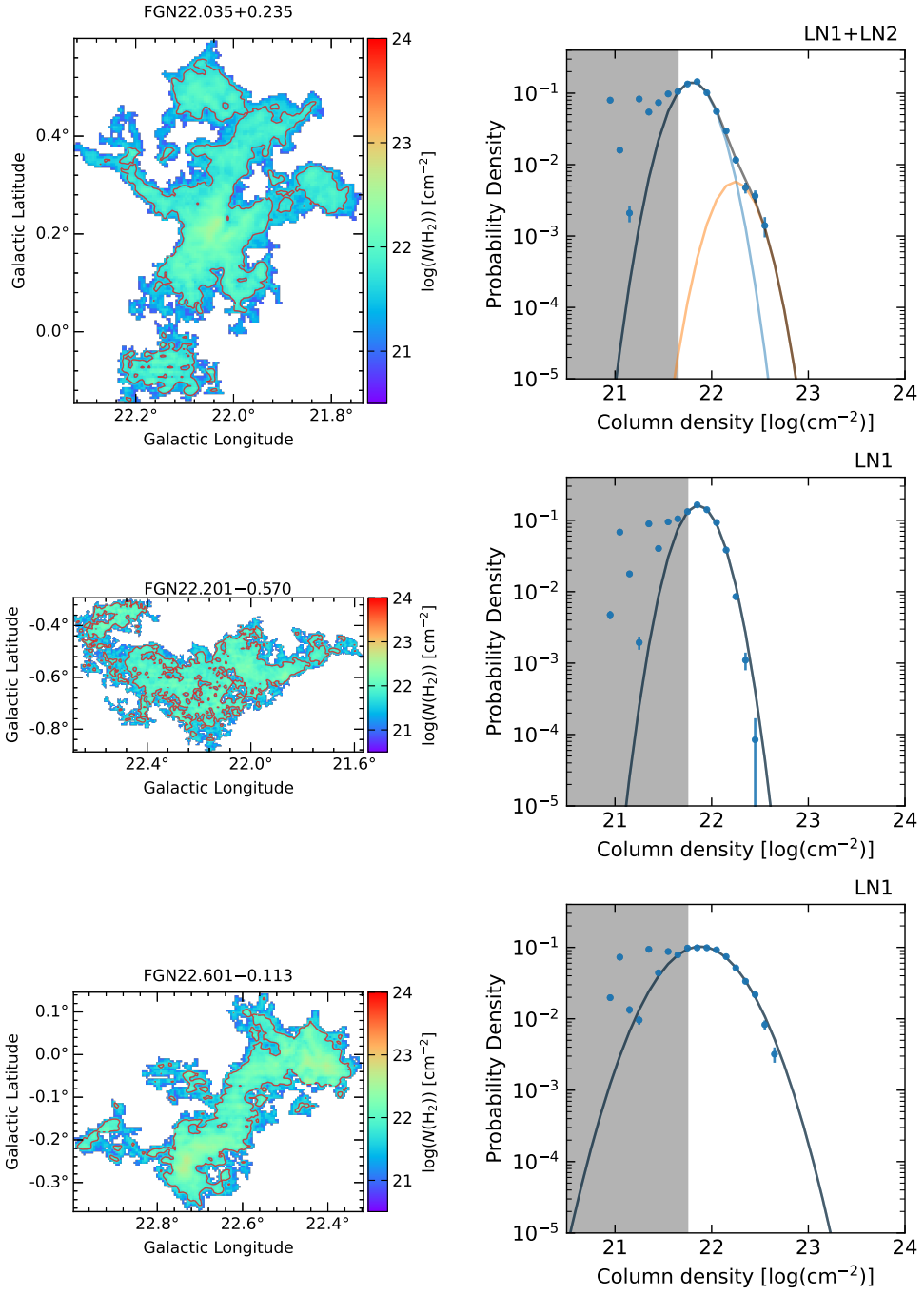

Figure C.1: *continued.*

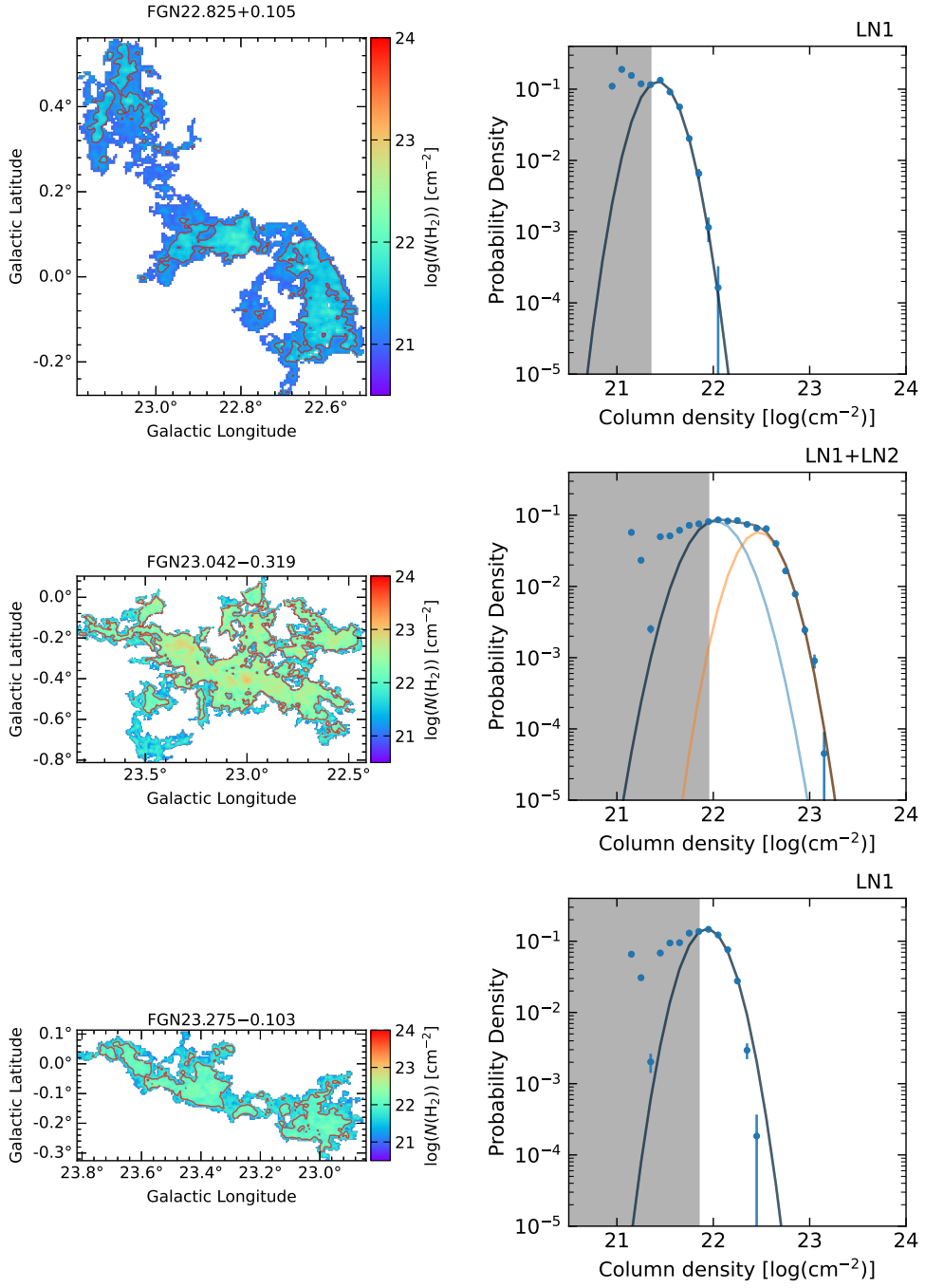

Figure C.1: *continued.*

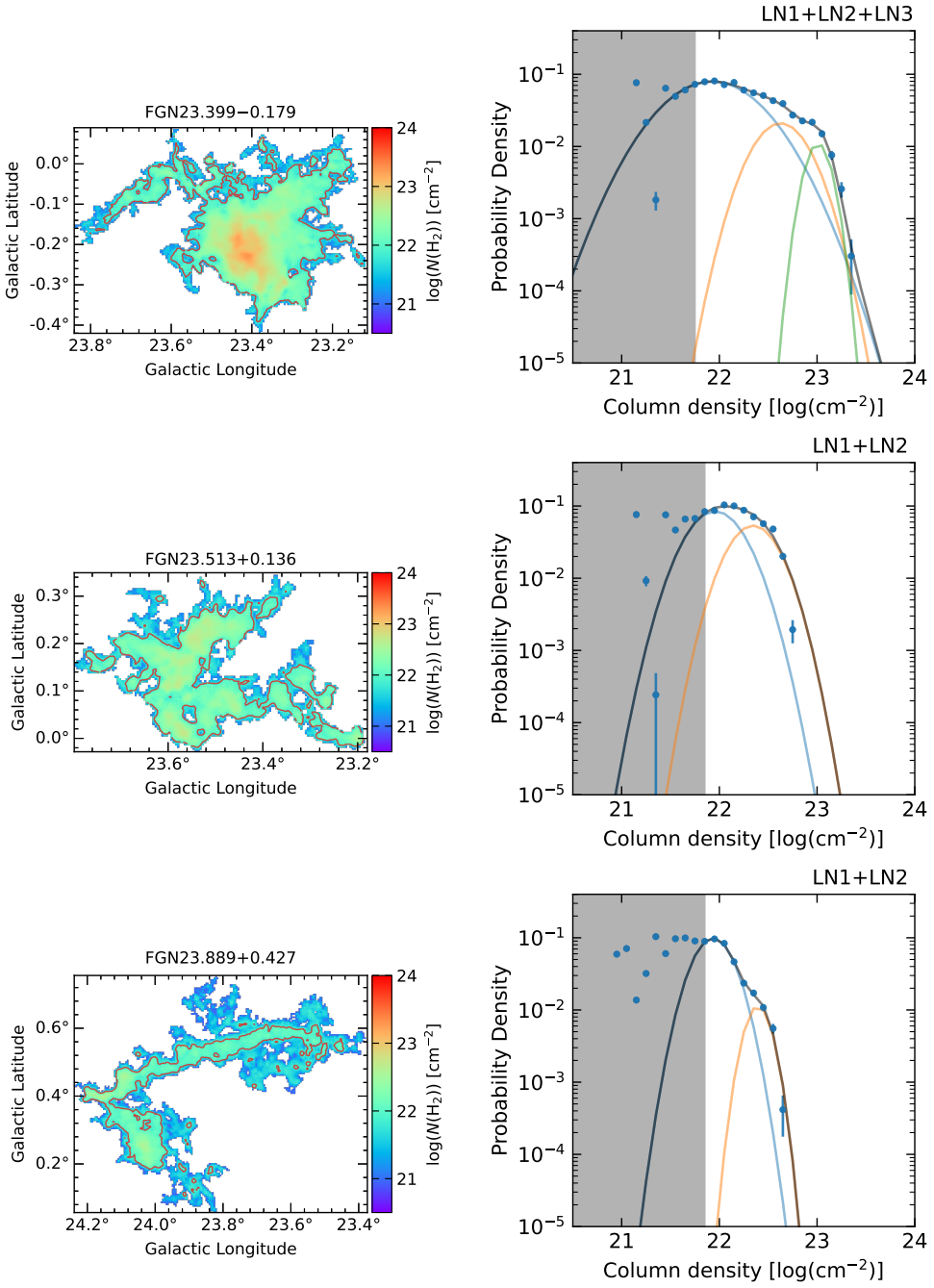

Figure C.1: *continued.*

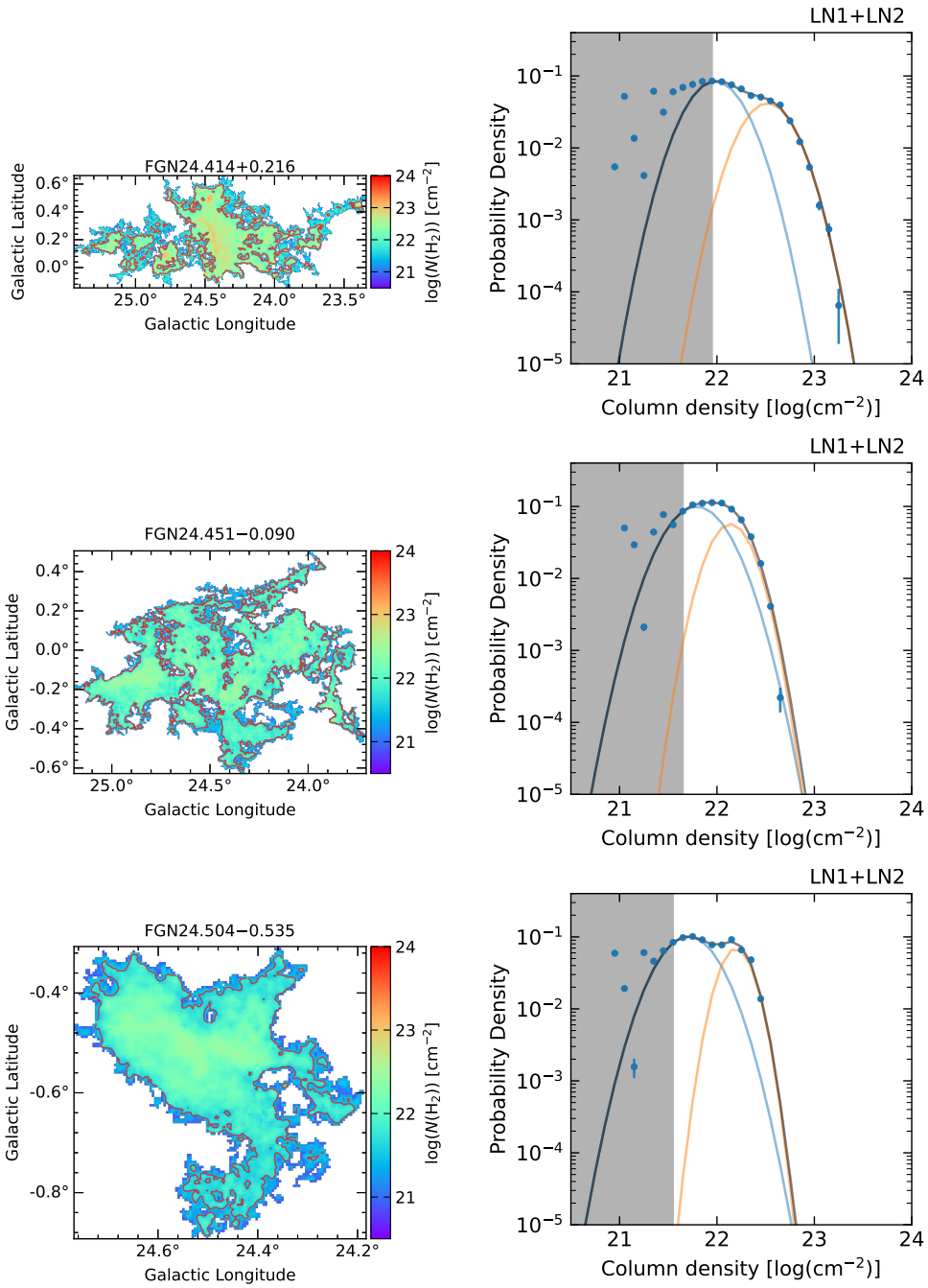

Figure C.1: *continued.*

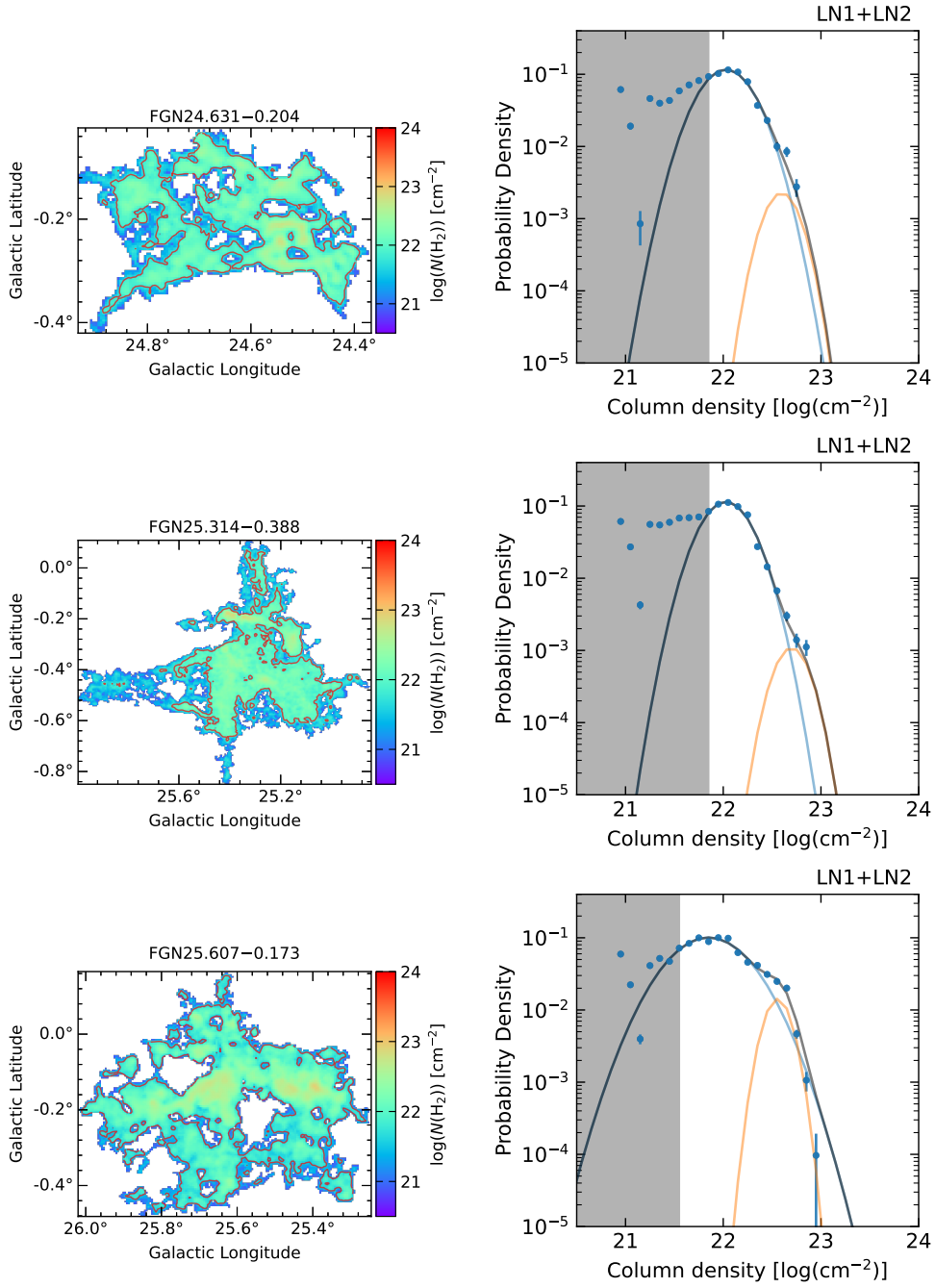

Figure C.1: *continued.*

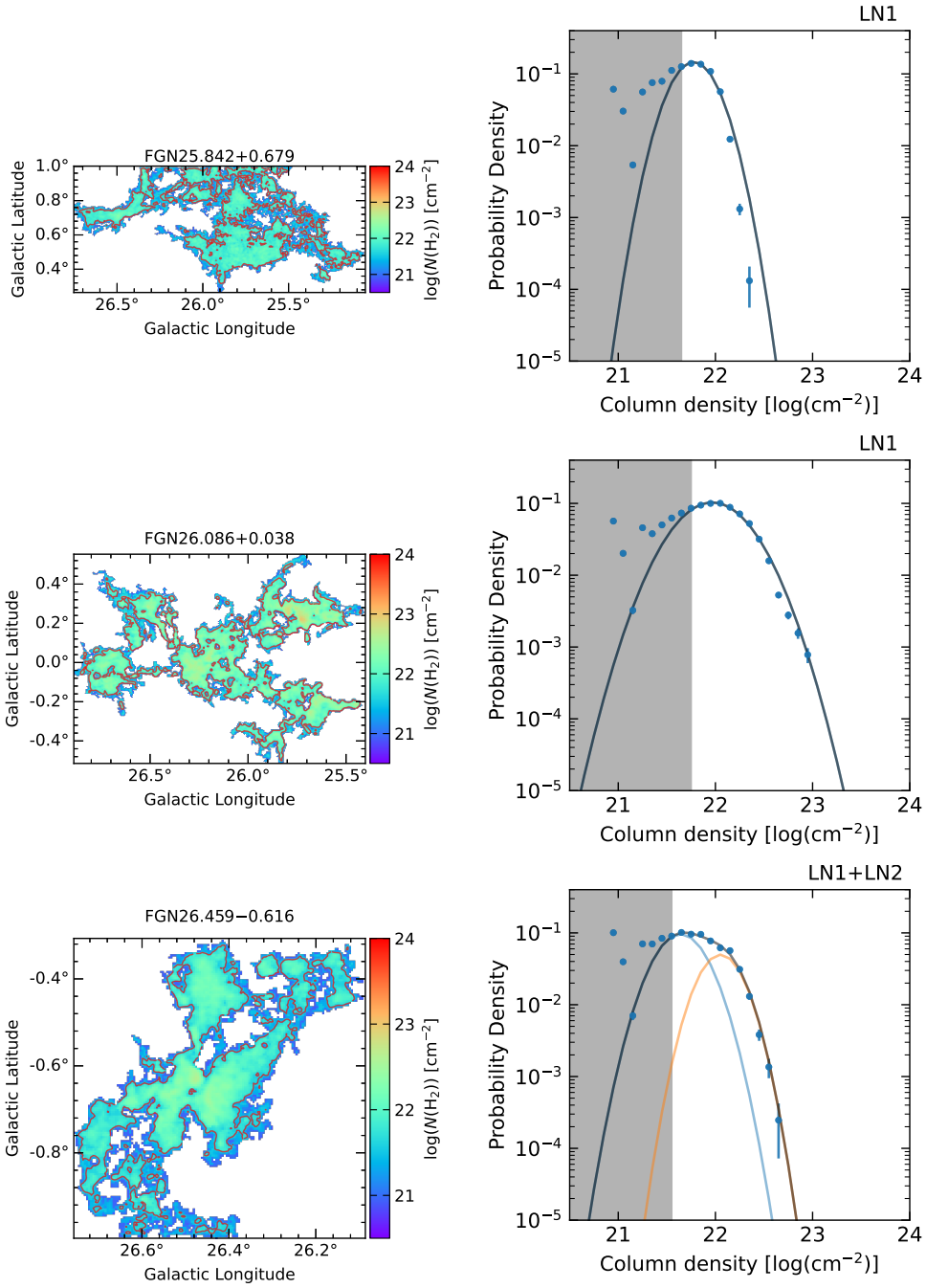

Figure C.1: *continued.*

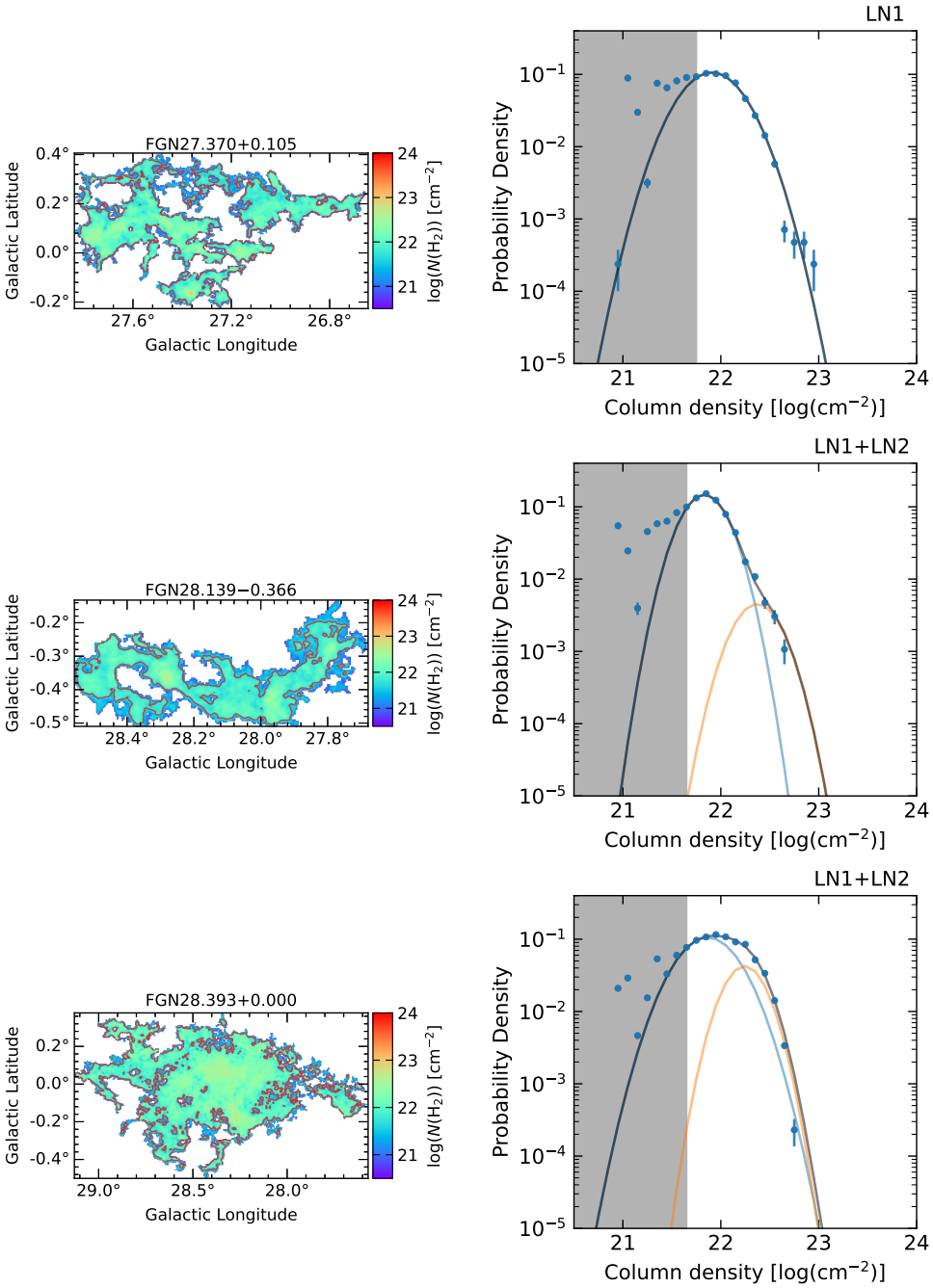

Figure C.1: *continued.*

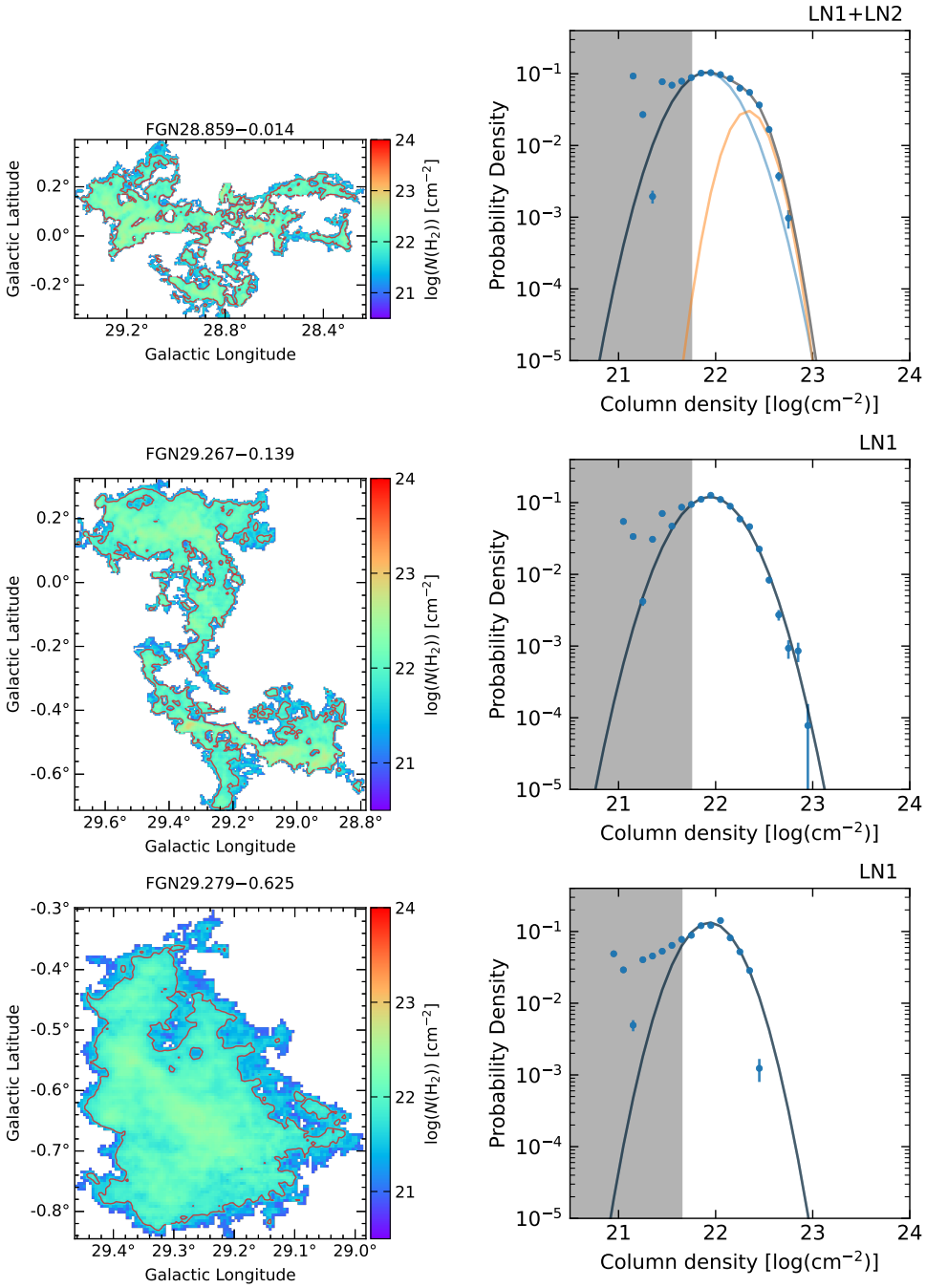

Figure C.1: *continued.*

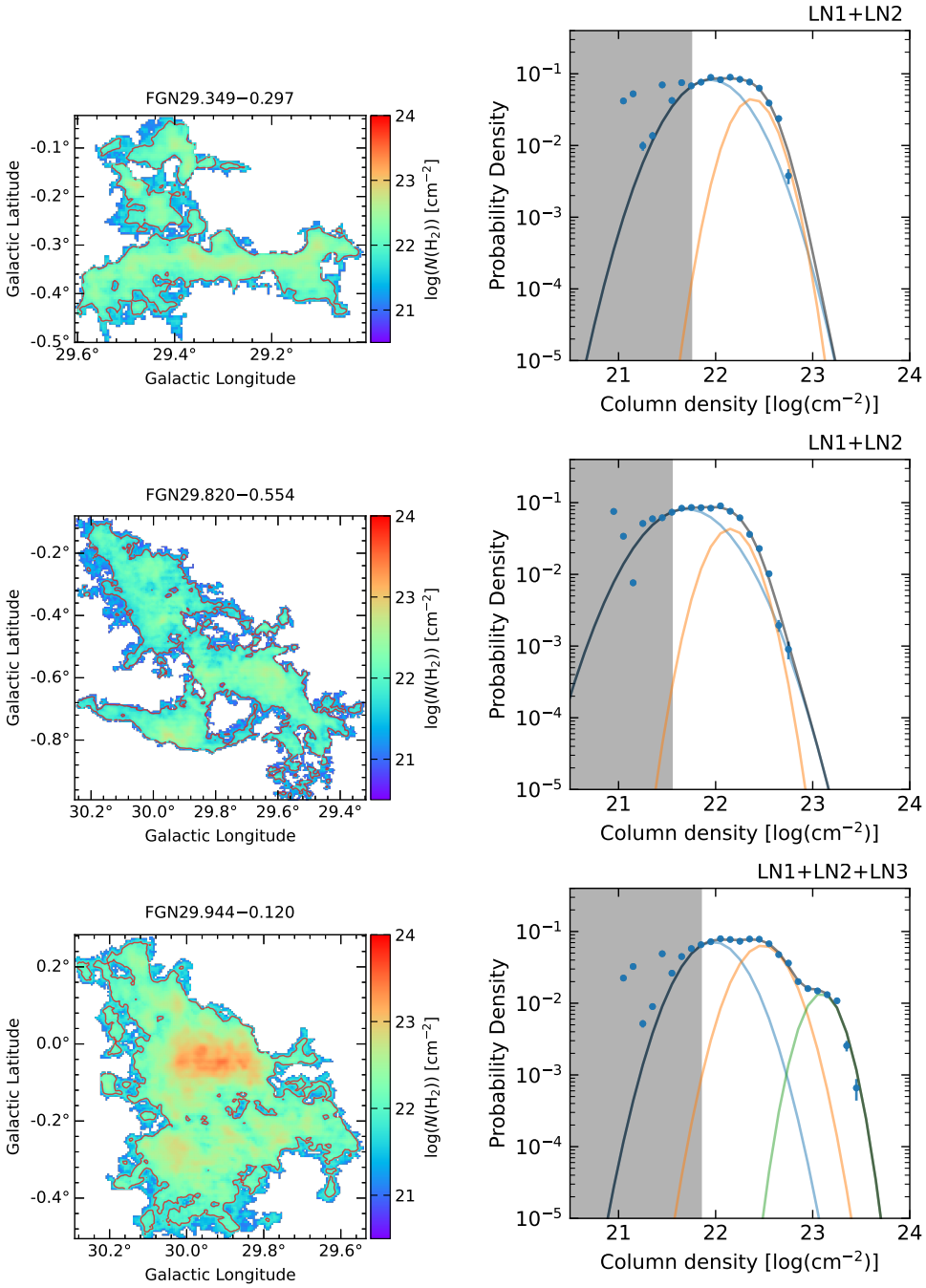

Figure C.1: *continued.*

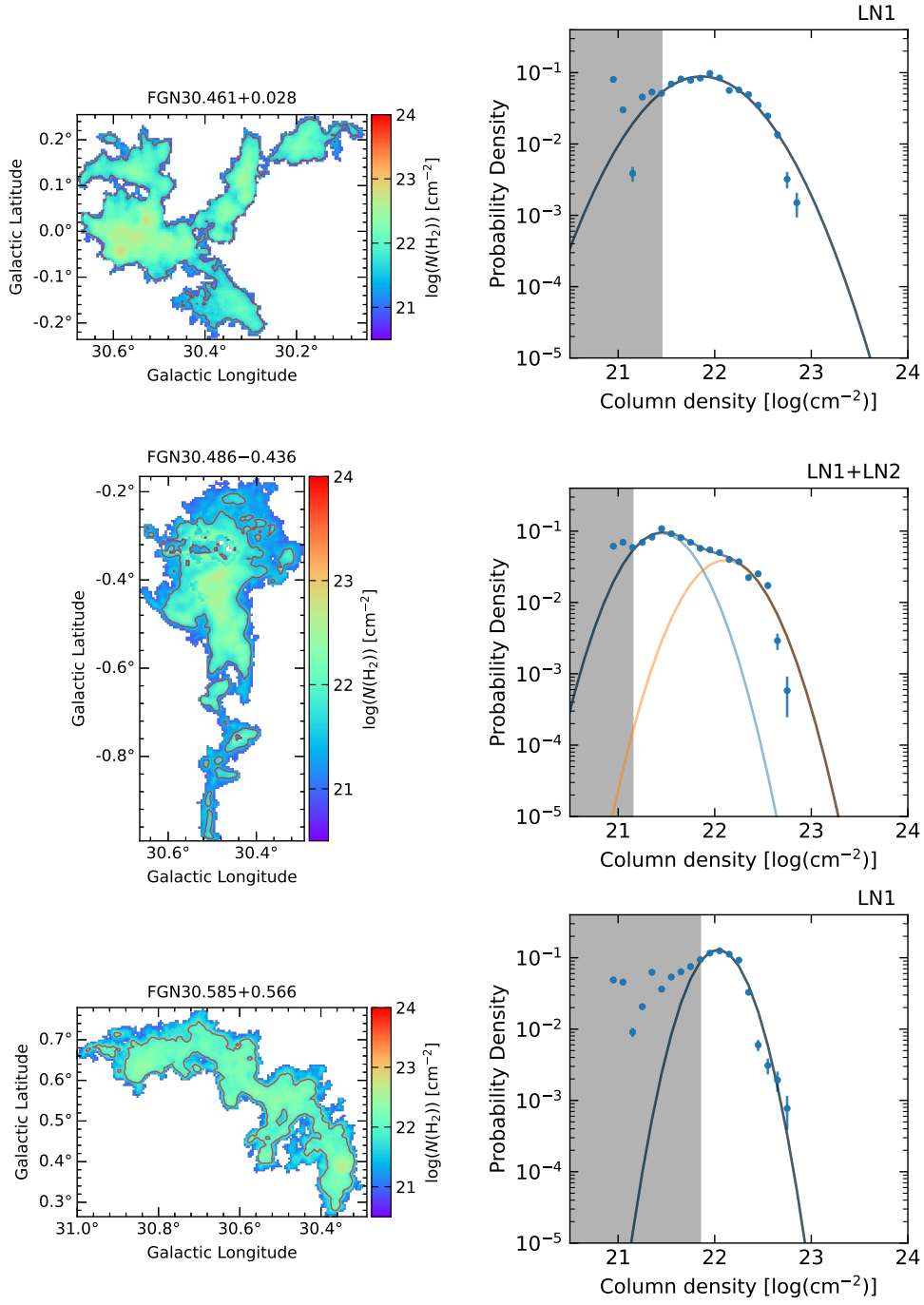

Figure C.1: *continued.*

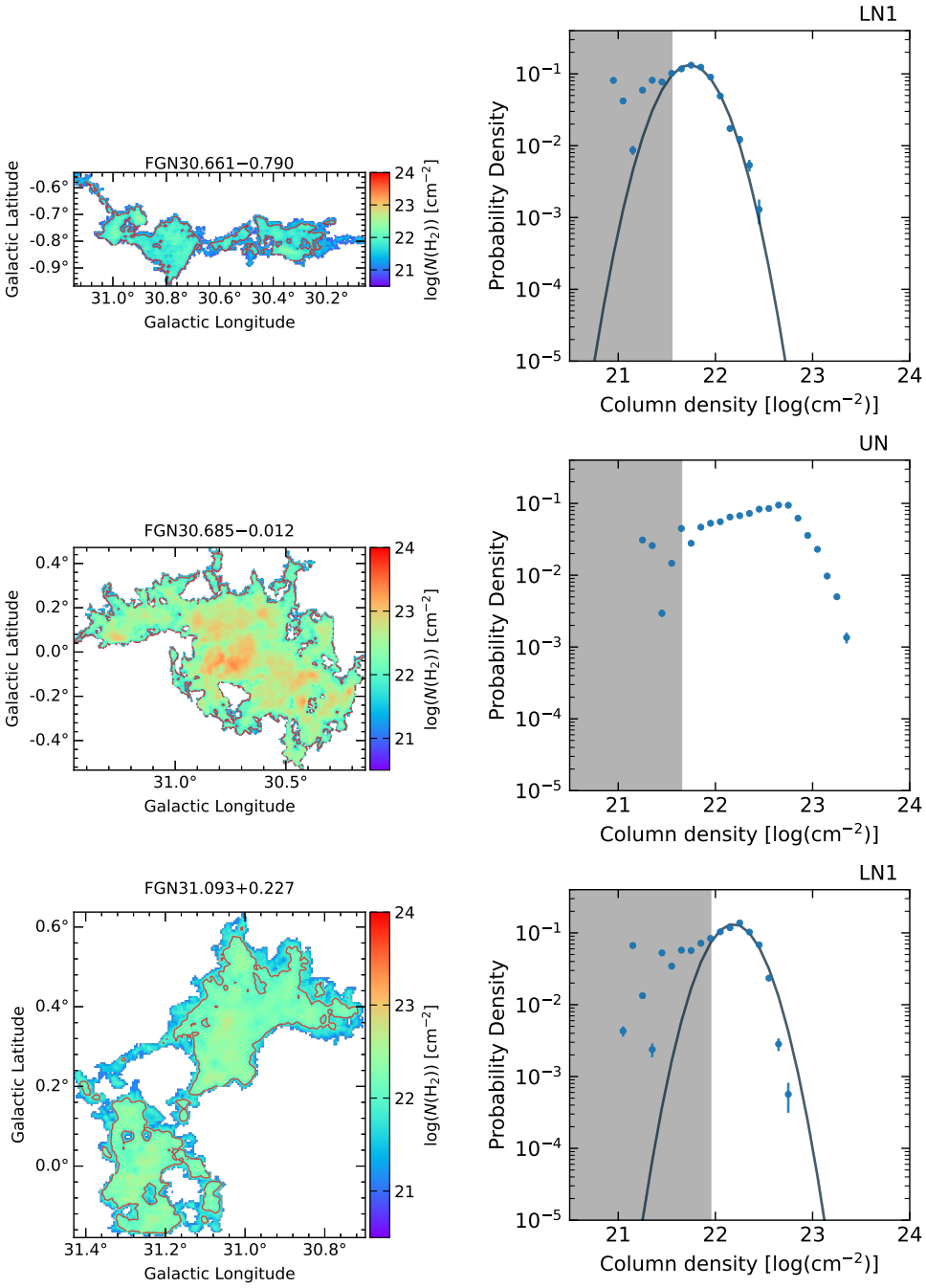

Figure C.1: *continued.*

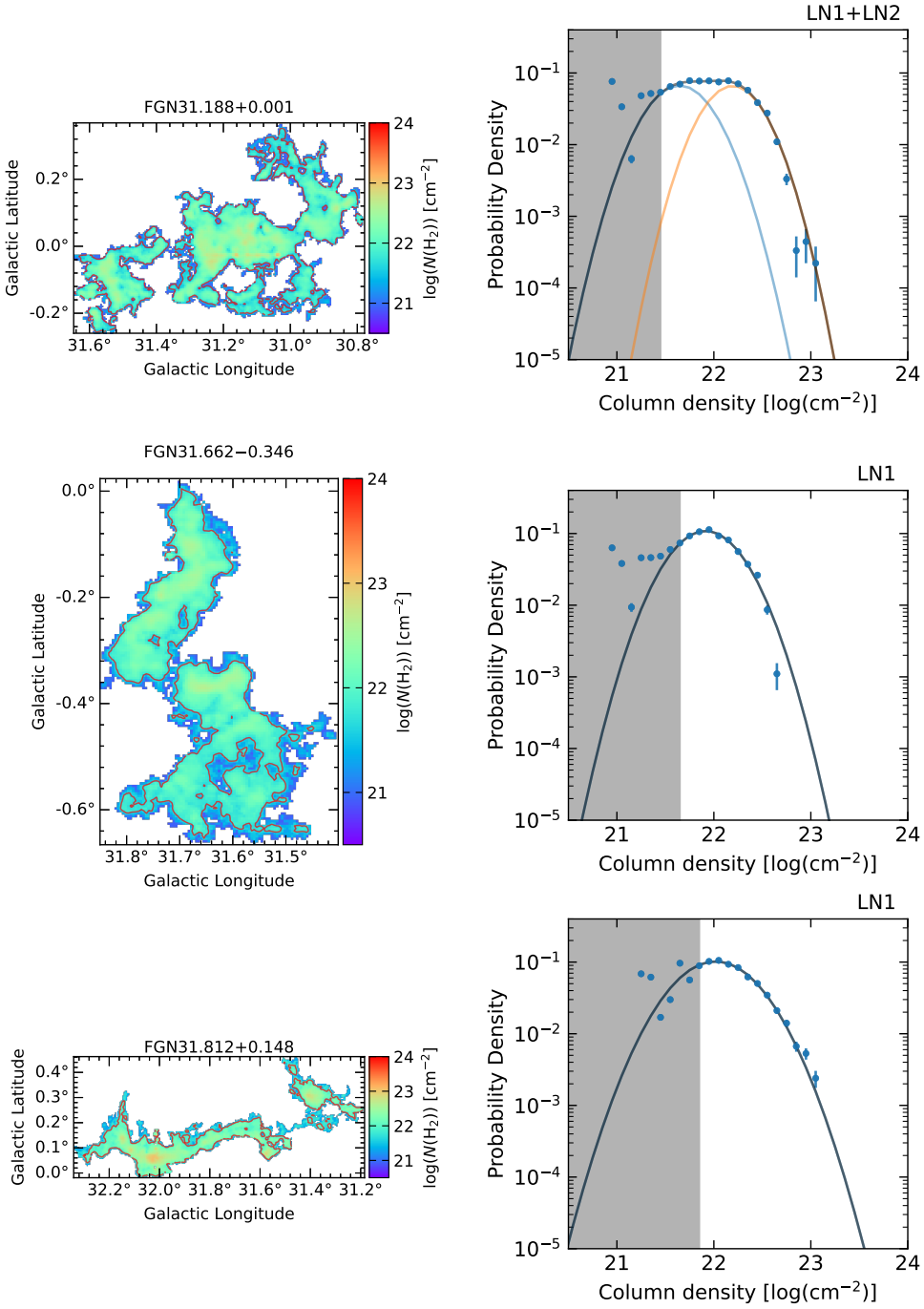

Figure C.1: *continued.*

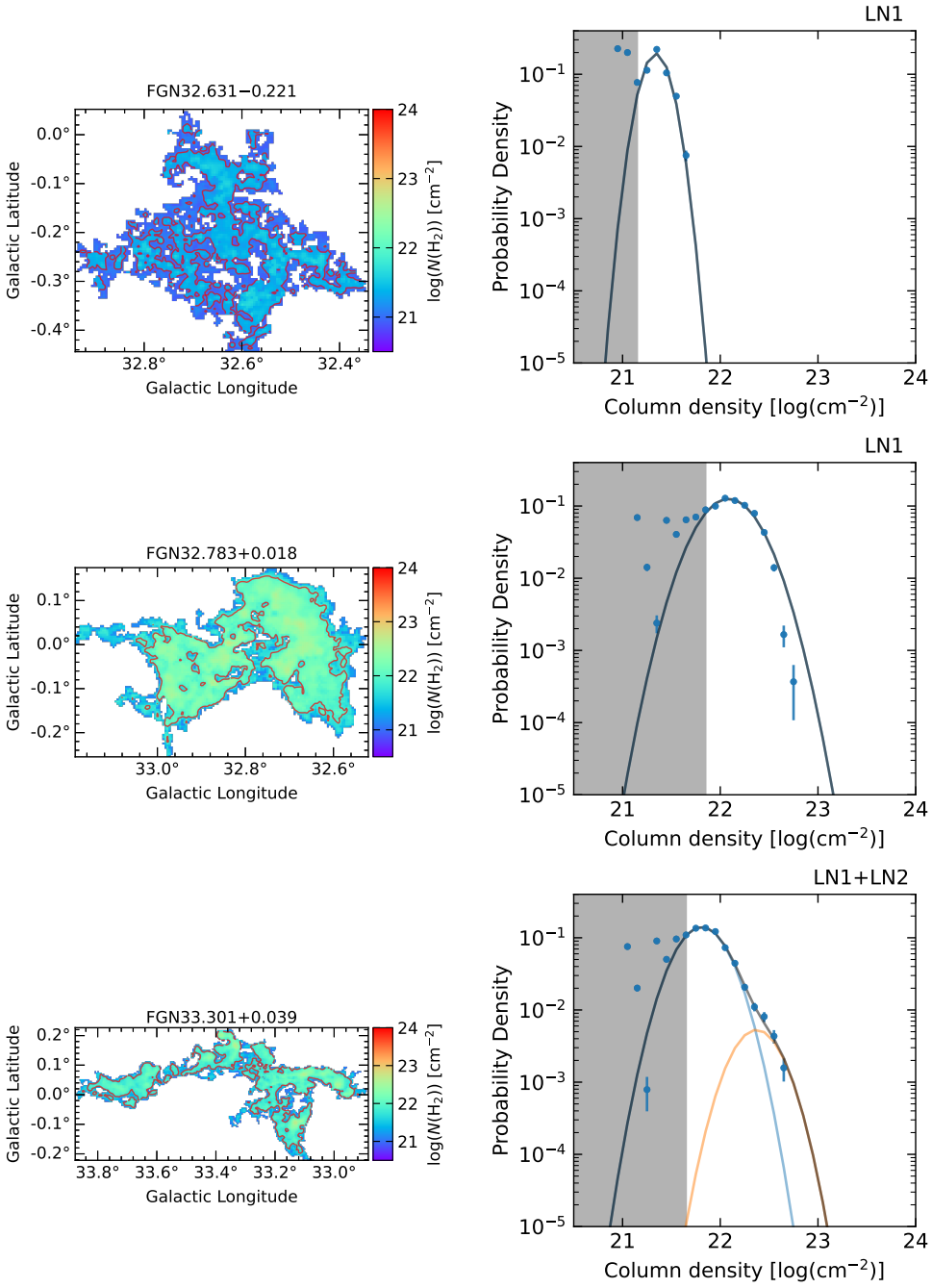

Figure C.1: *continued.*

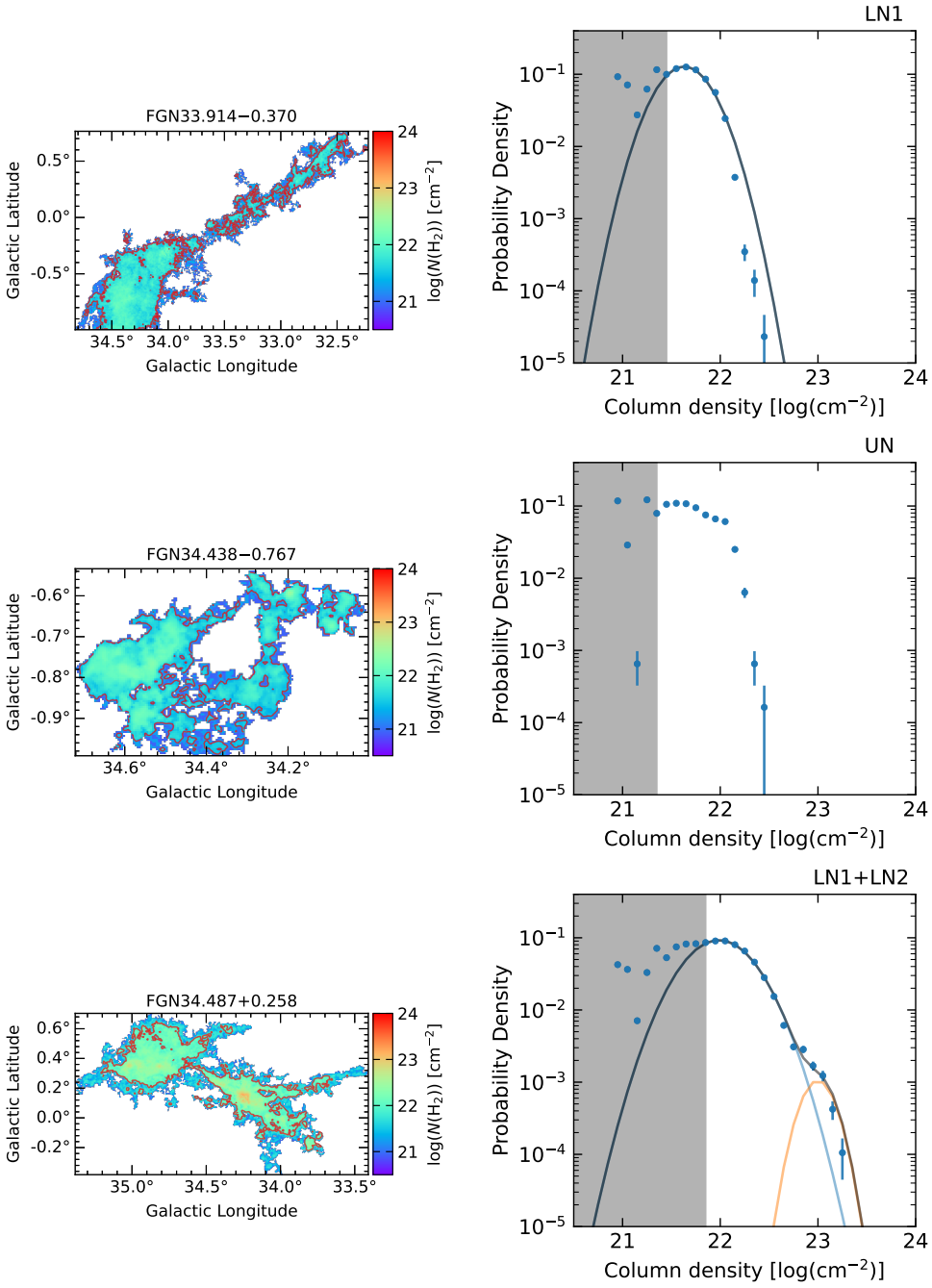

Figure C.1: *continued.*

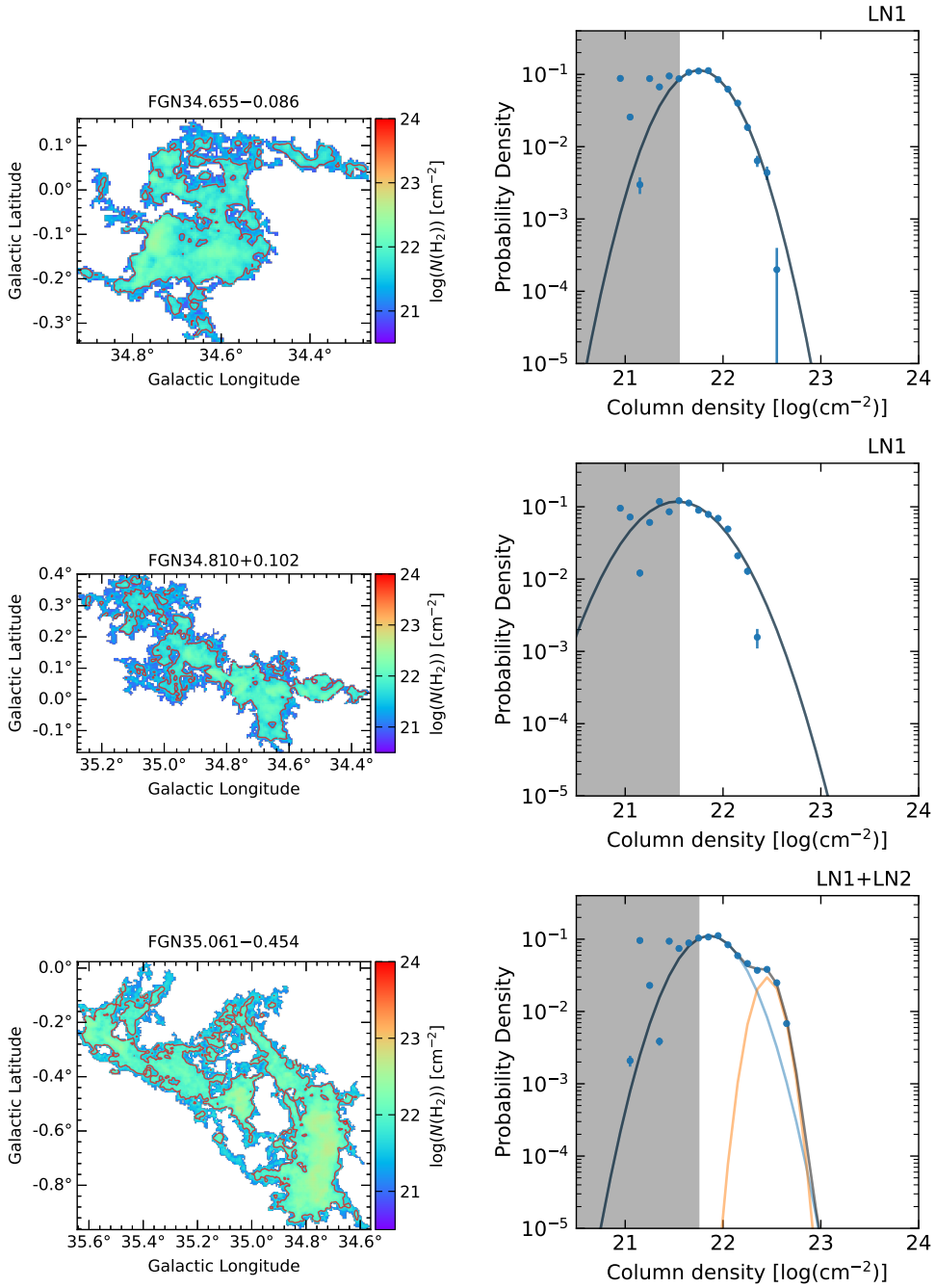

Figure C.1: *continued.*

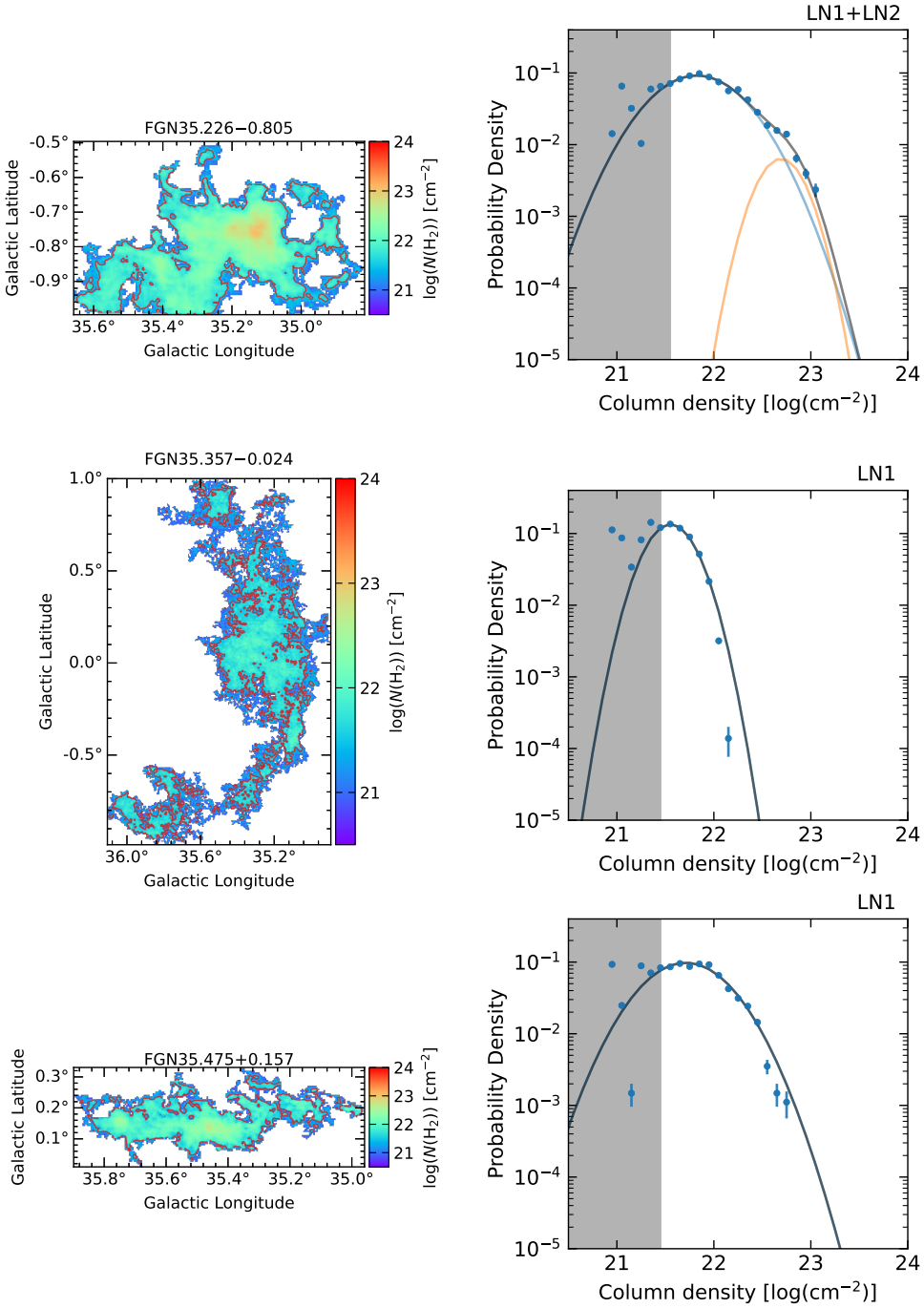

Figure C.1: *continued.*

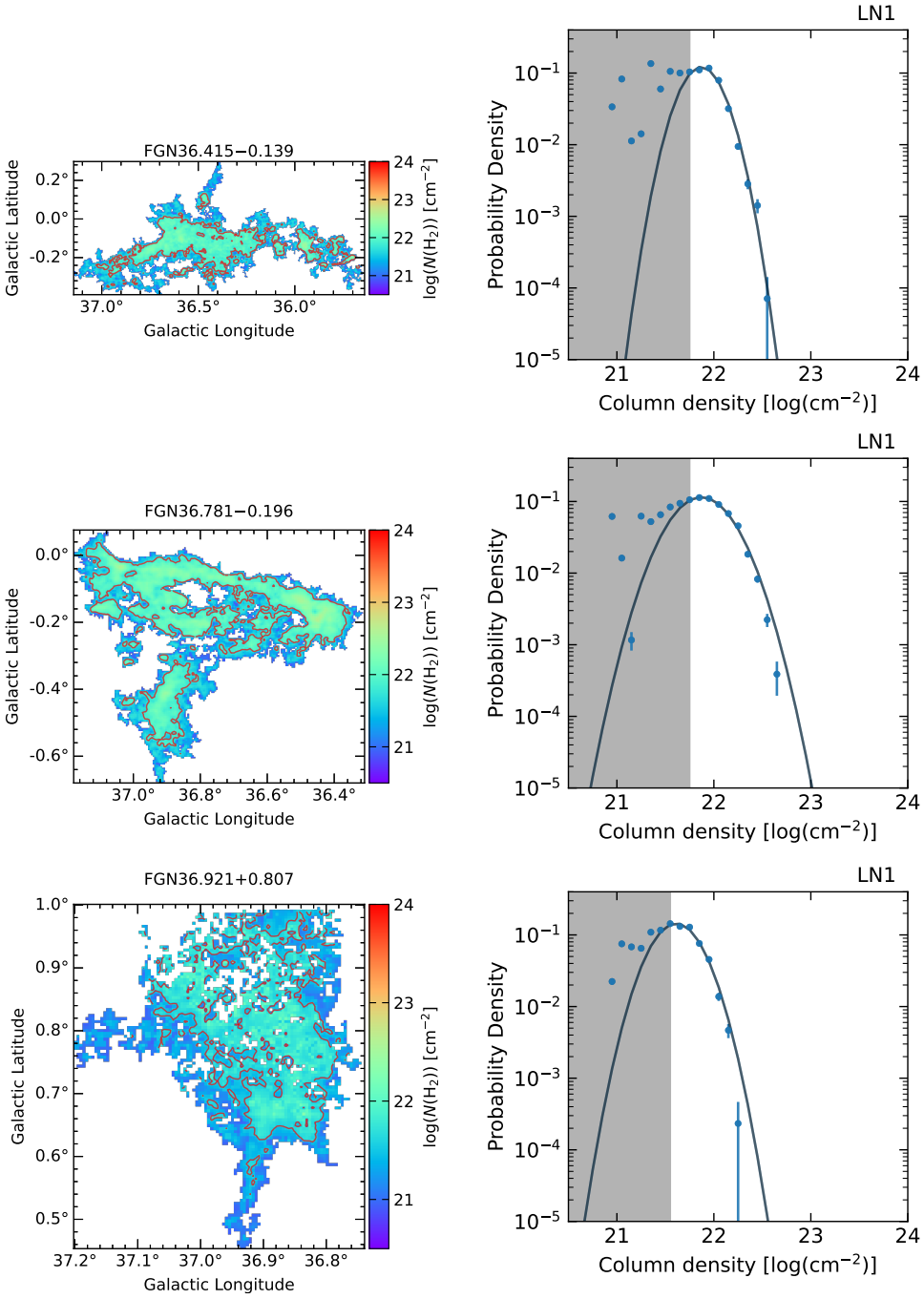

Figure C.1: *continued.*

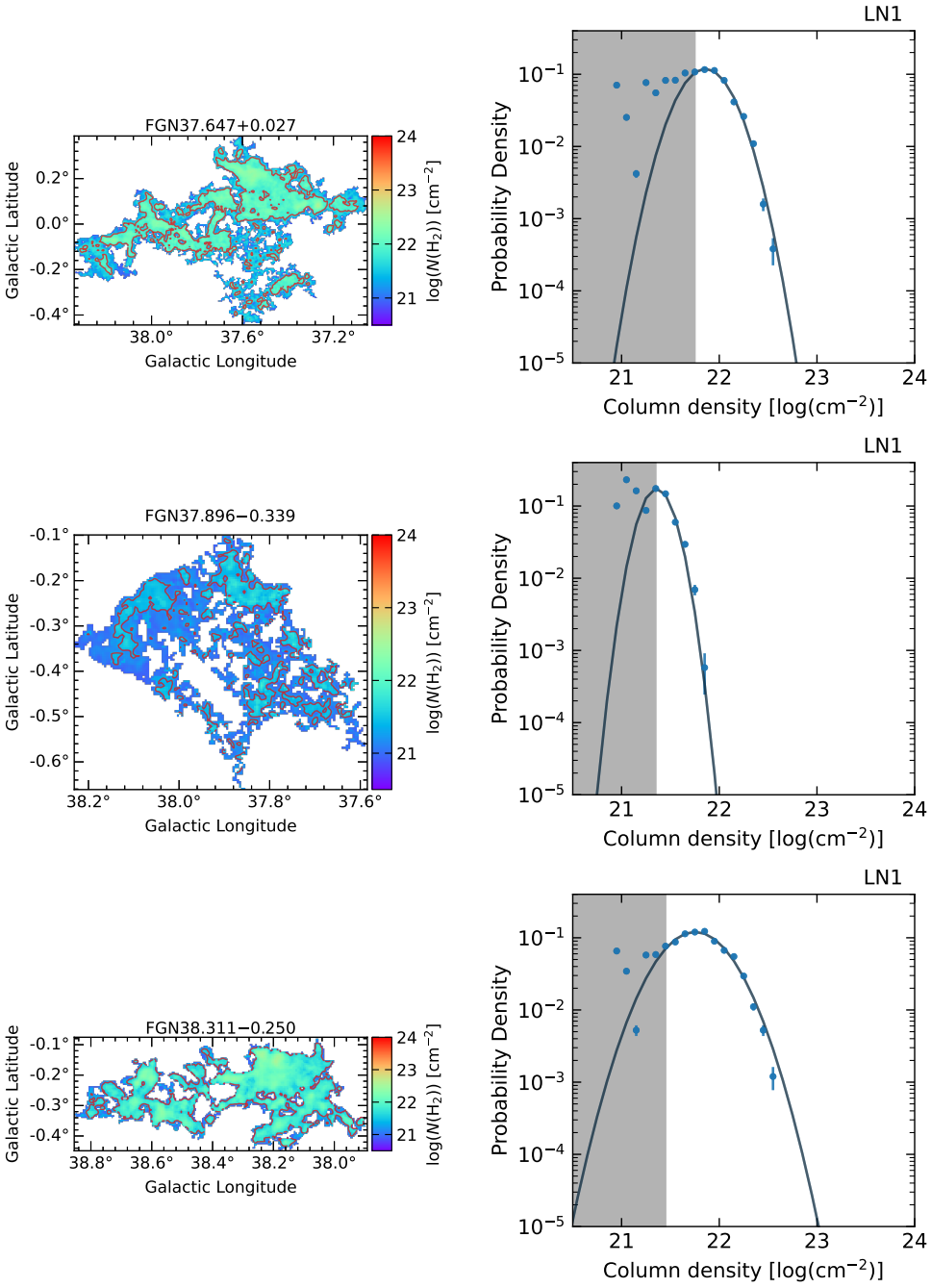

Figure C.1: *continued.*

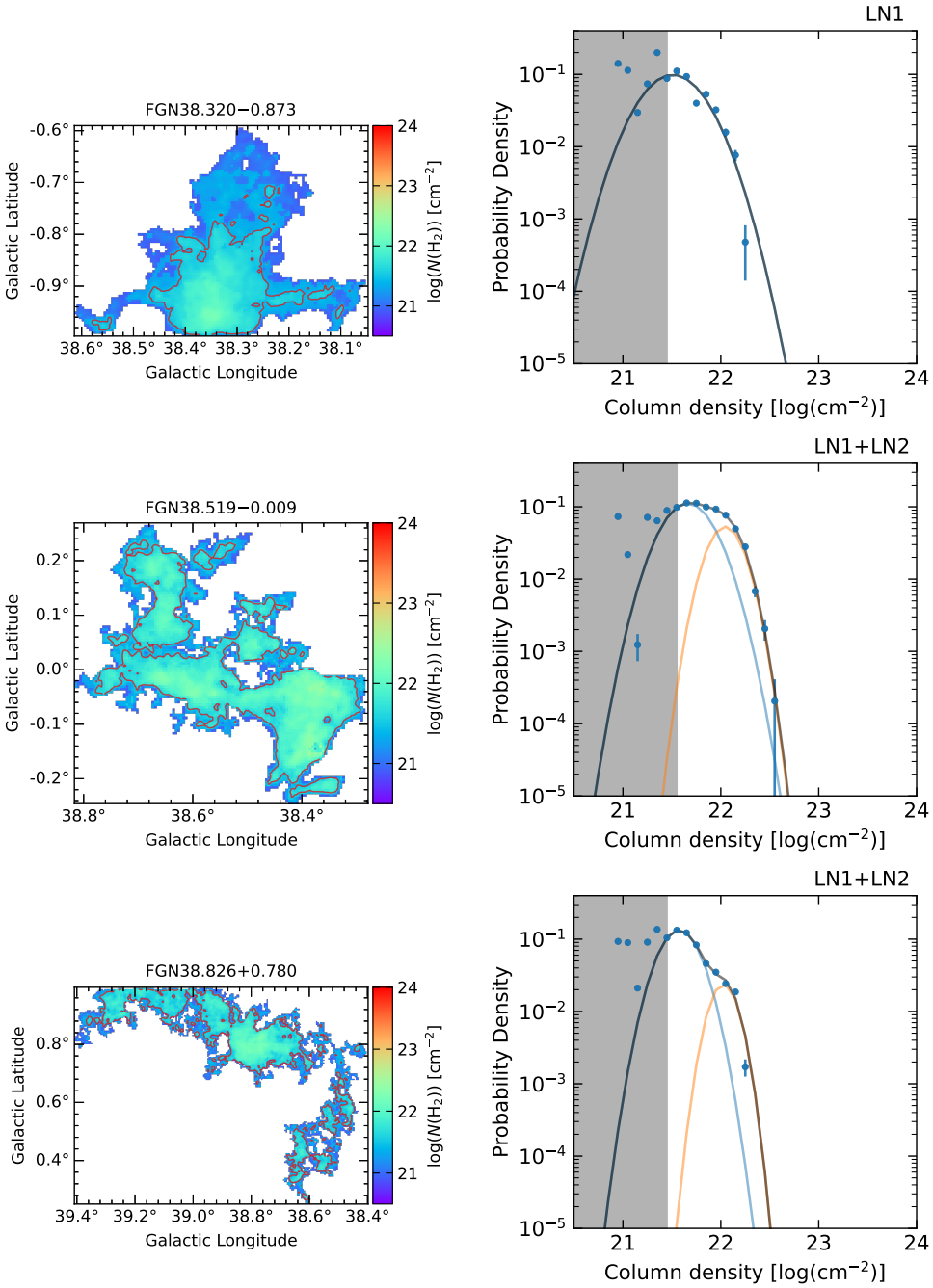

Figure C.1: *continued.*

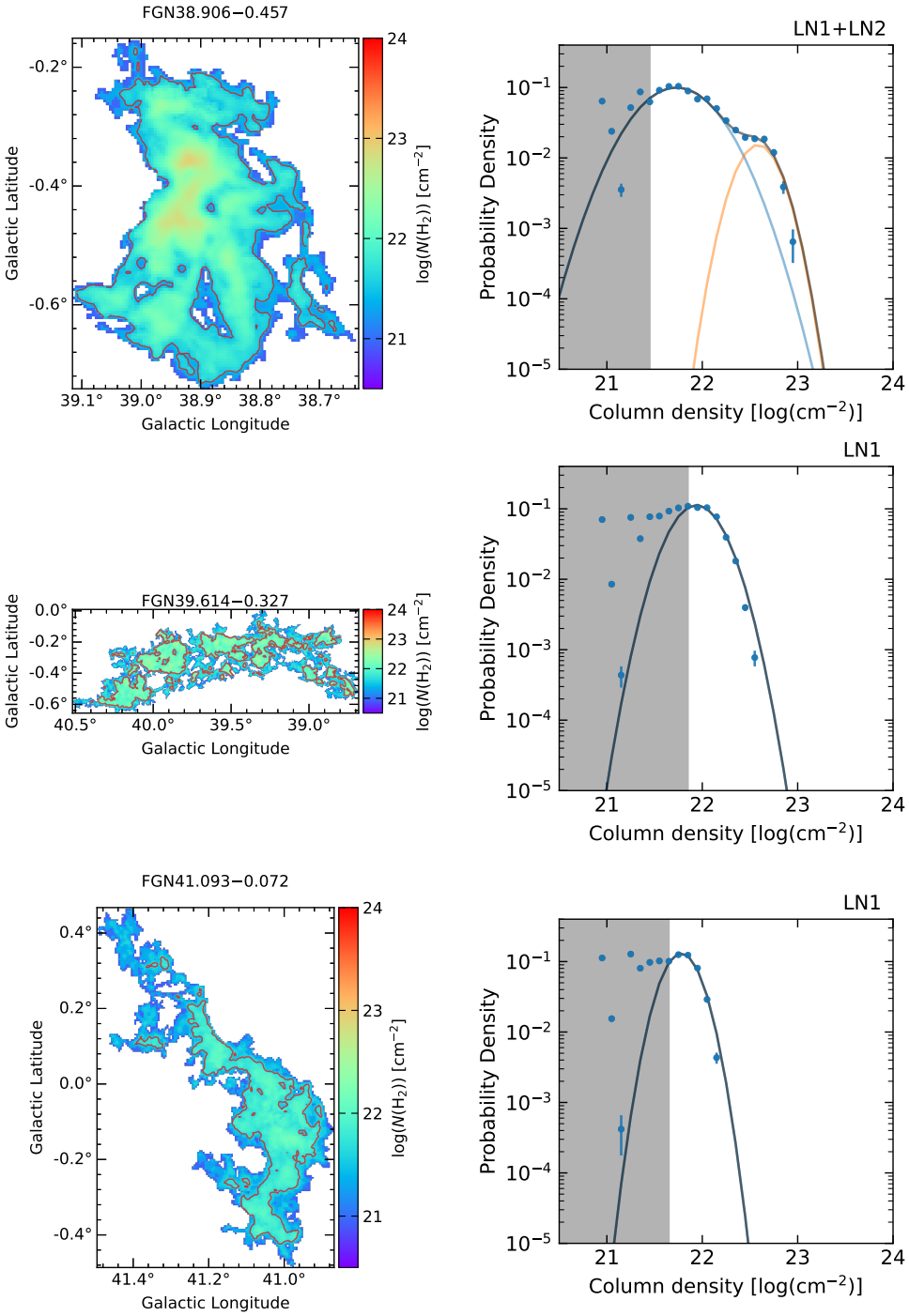

Figure C.1: *continued.*

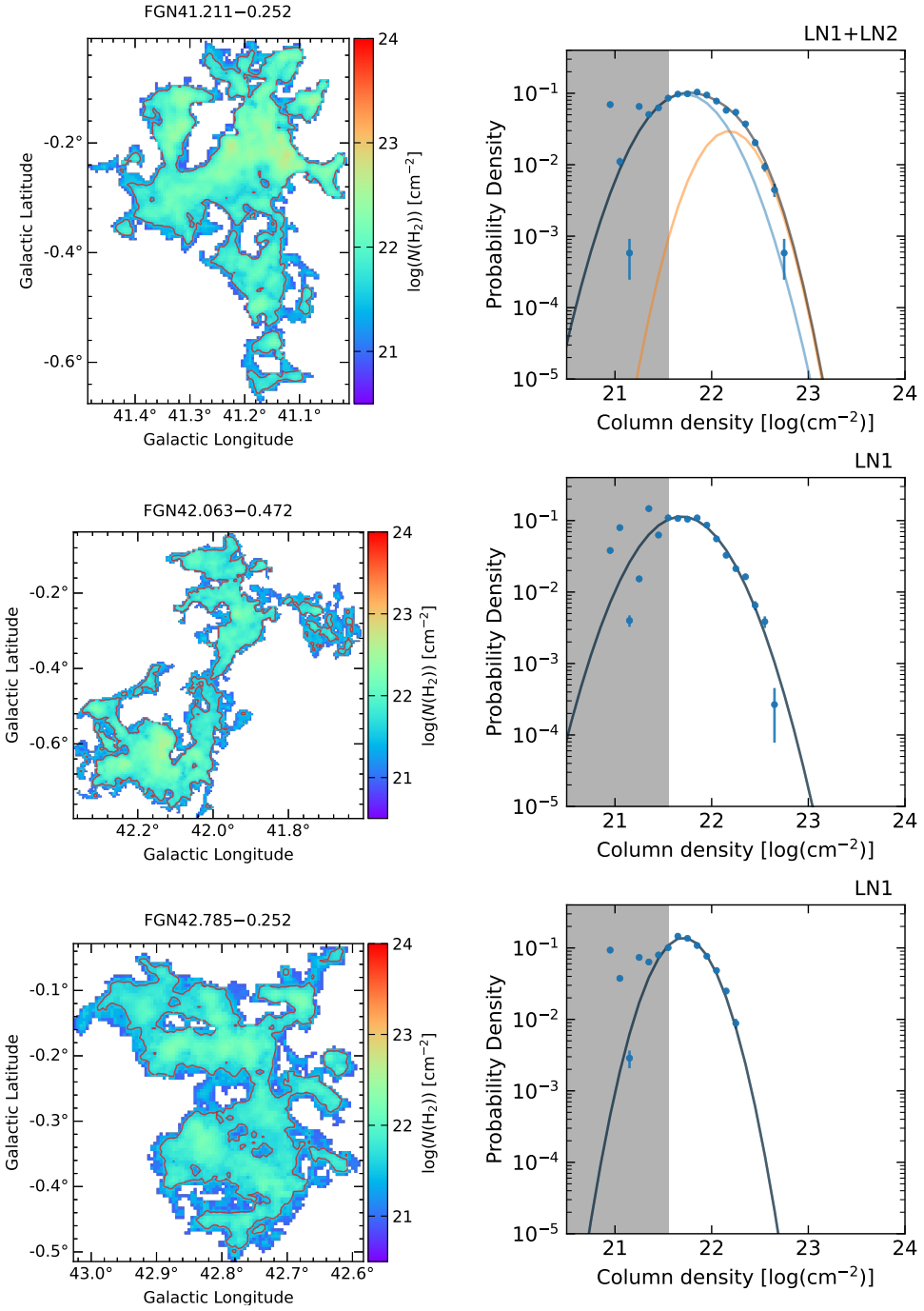

Figure C.1: *continued.*

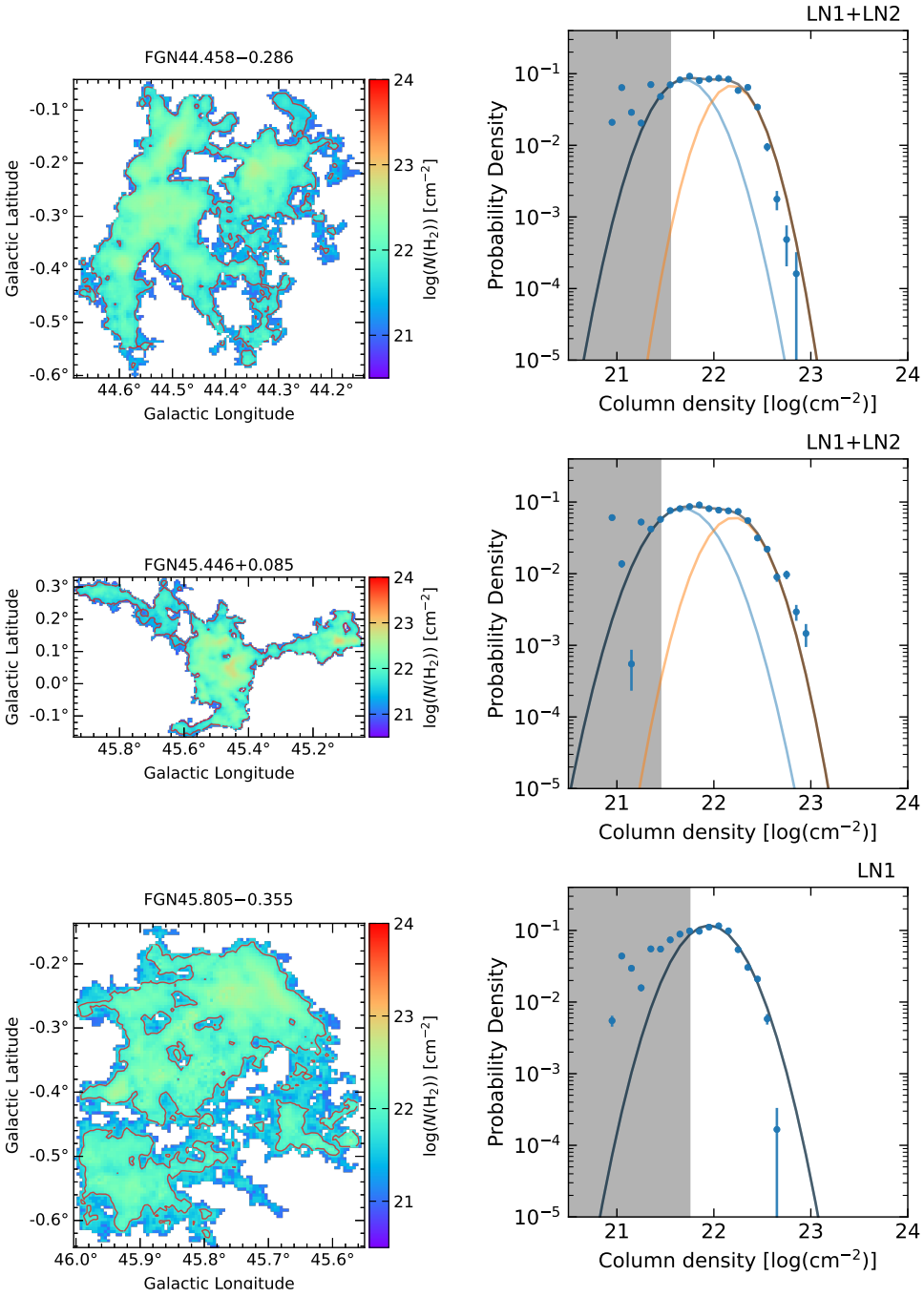

Figure C.1: *continued.*

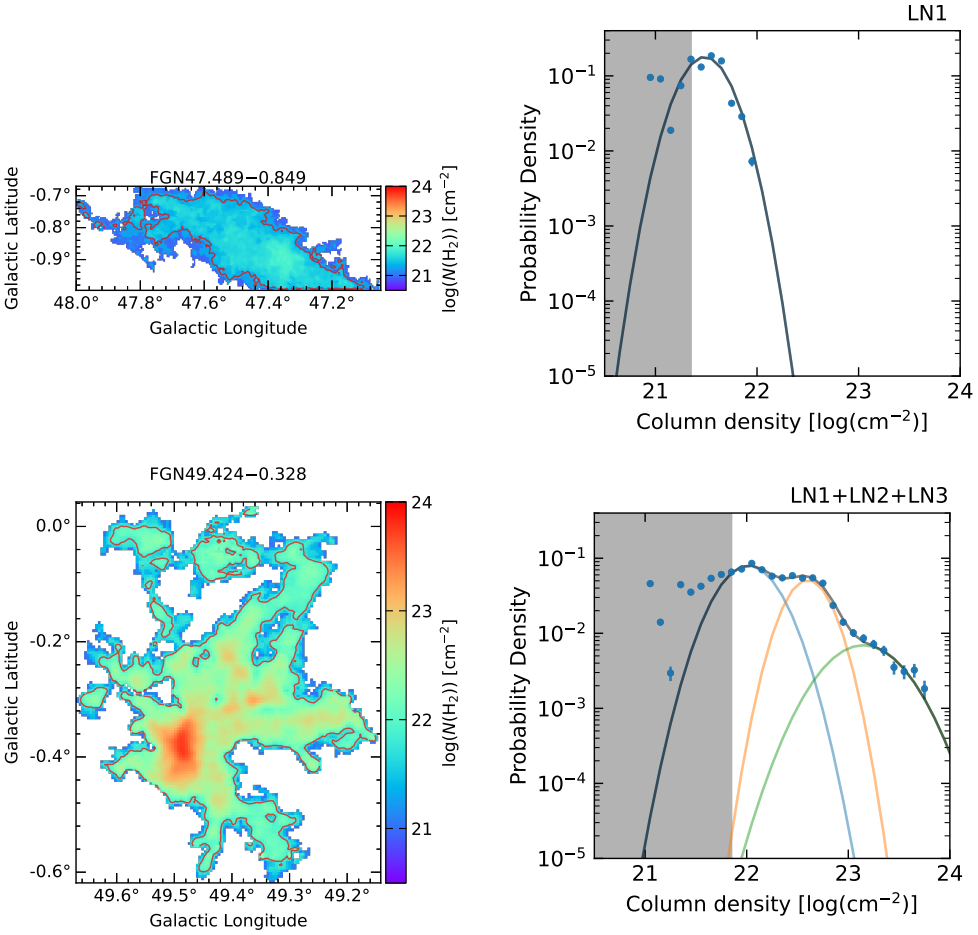

Figure C.1: *continued.*